Geochemistry and Evolution of the Earth's Mantle at the Hess Deep and the Mado Megamullion

By
Atlanta Sen

A dissertation submitted to the Department of Earth and Atmospheric Sciences,
College of Natural Science and Mathematics
in partial fulfillment of the requirements for the degree of

Doctor of Philosophy

in Geology

Chair of Committee: Alan Brandon

Co-Chair of Committee: Jonathan E. Snow

Committee Member: William W Sager

Committee Member: Qi Fu

Committee Member: Gelu Costin

University of Houston
December 2021

Dedicated to my parents and my husband

Acknowledgments

My advisor, Dr. Jonathan E. Snow transformed me from a student to a researcher. His enthusiasm and positive aura made challenging problems achievable. His critical insights and perspectives brought new dimensions into the projects. He was always a zoom-call away which made the distance between Louisiana State University and the University of Houston appear to be only a number. The constant support, encouragement and insights from Dr. Alan Brandon helped me become a better researcher. I thank Dr. William Sager and Dr. Qi Fu for their consent to be in my PhD committee.

I would like to acknowledge the co-operation of the RV Hakuho Maru, R/V Yokosuka, James Cook JC-21 and Shinkai 6500 pilots and staff. I thank our collaborators at the Hydrographic and Oceanographic Department of Japan, Tokyo, Nagoya University, Japan, University of Pavia, Italy and Cardiff University, United Kingdom for their critical inputs into the different projects that I had undertaken during my PhD. Dr. Yasuhiko Ohara at the Hydrographic and Oceanographic Department of Japan and Dr. Alessio Sanfilippo and Dr. Valentin Basch at the University of Pavia made the international collaborations seamless.

I would thank Dr. Gelu Costin for his insightful help with the Rice University electron probe facility, Dr. Barry Shaulis for his help with the LA-ICP-MS laboratory at the University of Arkansas and Dr. Christie Jilly-Rehak for helping at the SHRIMP facility at the University of Stanford and accessing these facilities in COVID times.

My husband, Sanket has been there with me through thick and thin. This PhD is not just a degree but a journey for the both of us. His belief in me has made this journey possible through a Trans-Atlantic long-distance marriage in these COVID times. My parents in India brought me up as an independent individual. I cannot thank them enough for that. Mental health issues have become very common in graduate students especially with the new challenges that COVID-19 has brought into our lives. My advisor, my husband and my parents have helped me overcome the phases of mental stress through these times. I dedicate this thesis to them.

Abstract

Mantle peridotites have been widely sampled in the ocean basins. These are considered residues of the melting process that ultimately results in the formation of the oceanic crust. However, the exact mechanism for their evolution has not been comprehensively understood. Plagioclase-bearing mantle rocks, for example, may be formed by fractional crystallization, melt-rock reaction and assimilation in the crust and shallow mantle. Nearly all mid-ocean ridge basalts (MORB) are believed to have at least some melt-rock reaction process in their evolutionary history. Yet, there is a lack of direct evidence that captures the reaction textures or intermediate compositions of the melt-rock reaction process.

Spreading centers and oceanic core complexes (OCC) provide a window to understand melt evolution processes in the lower crust and upper mantle. In this study we address the ongoing debate about the mechanism of melt transport in the mantle by textural and chemical analysis (major and trace elements) of samples from two unique tectonic regimes; a. the Hess Deep (fast spreading center in the Equatorial Pacific Ocean) and the Mado Megamullion (an OCC in the Shikoku back-arc basin). Magnetic anomaly data suggested that spreading in the Shikoku basin ceased after 15 Ma although the age of termination of spreading has not been constrained from geochronologic evidences until now. We integrated the model results with the natural samples to quantify the evolution of the peridotites. We dated zircons from amphibole-chlorite bearing veins that crosscut the peridotites of the Mado Megamullion. The U-Pb age of 13.37 ± 0.24 Ma and the trace and rare earth element (REE) chemistry of the zircons and the amphiboles suggests the possibility that magmatic activity and back-arc spreading at the Shikoku basin continued till 13 Ma. We could model the elevated TiO_2 content in melt-reacted plagioclase-bearing

peridotites from Hess Deep through assimilation fractional crystallization (AFC) process which could not be modelled by fractional crystallization process alone and has remained a topic of debate. Our results also show that back-arc basin peridotites at Mado Megamullion appear to have a unique petrographic and geochemical character that is distinct from those mid-ocean ridges or fore-arcs.

Table of Contents

LIST OF TABLES

List of Figures

Introduction

The nature of magmatic processes below oceanic ridges is important to understand the processes that form the oceanic crust. Deeper levels of the crust are generally not exposed at fast spreading ridges due to the continuous accretion of the oceanic crust in contrast to the slow spreading ridges, where tectonic stretching is significant, and lower crust and mantle rocks are exhumed in many areas. It is therefore important to explore the tectonic windows in fast spreading centers to understand the processes beneath them. Such unique and extensive lower crustal section is exposed at the Hess Deep (Francheteau et al., 1990; Rioux et al., 2012; Lissenberg et al., 2013; Gillis et al., 2013) at the northern edge of the Galapagos microplate.

In contrast to the tectonic setting of mid oceanic ridges, a significant fraction of the ocean floor is also created in back-arc basins. In contrast to the processes at mid oceanic ridges, water plays a major role in generating back-arc basin basalts. Much of the understanding the ocean crust comes from ophiolites (thought to be their on-land analogs) (Korenega et al., 1997; Godard at al., 2000; Kelemen et al., 2000; Hanghoj et al., 2010), most of which are largely attributed to supra subduction zone environment. Studying oceanic core complexes in back-arc basins are therefore important. These studies help us to understand the magmatic processes in the lower crust and upper the mantle that forms the oceanic crust in these tectonic settings.

The Hess Deep rift valley, exposed near the Galapagos microplate, is located at the triple junction between the Pacific, Cocos and Nazca plates (Hey et al., 1972, 1977; Holden and Dietz, 1972). Due to the westward propagation of the Cocos-Nazca plate at about half the spreading rate of the

East Pacific Rise (EPR) (~65 mm/yr), young (~1 Ma) lithosphere is being rifted ahead of the advancing Cocos-Nazca spreading ridge (Lonsdale, 1988).

Extensive multi-beam bathymetric mapping by Japan's continental shelf survey has revealed the presence of OCCs in several areas of the Philippine Sea Plate, such as in the Shikoku Basin, Kita-Daito Basin and West Philippine Basin (Ohara et al., 2015). These OCCSs have remained largely unsampled except only a few locations that were sampled as reconnaissance study sites (KH07-02-D27 and KH07-02-D28), which yielded serpentinized peridotites, confirming that these OCCs are in fact the detachment fault surfaces that exhumed oceanic lower crust and upper mantle. The Mado Megamullion in the Shikoku Basin is an oceanic core complex. YK-18-07, KH-18-02 therefore targeted the tectonic window of the Shikoku Basin OCCs to sample the lower crust and upper mantle lithologies. We examined the mantle lithologies to understand the magmatic processes in the back-arc spreading center in comparison to other OCCs in mid oceanic ridge systems like the Kane Megamullion in the Atlantic Ocean, and the only other studied back-arc OCC, the Godzilla Megamullion in the Parece-Vela basin (Sanfilippo et al., 2013; Michibayashi and Snow, 2016). Although the age of termination of back-arc spreading in the Shikoku Basin is considered to be at 15 Ma from magnetic anomaly data, this age is not well constrained by geochronologic evidence until now. We report ages of zircon from amphibole-chlorite bearing veins that crosscut the peridotites of the Mado Megamullion. In combination with trace element chemistry of zircons and amphiboles we try to constrain the process of mantle upwelling at the termination stage and the age of cessation of back-arc spreading at the Shikoku basin.

Chromian spinel is a ubiquitous accessory phase in crustal basalts and mantle peridotites (Dick and Bullen, 1984**).** The composition of spinel is sensitive to the bulk composition and petrogenesis of the host rocks (Irvine 1965, 1967; Evans and Frost, 1975**).** The constituent major elements in spinel behave differently during partial melting and fractional crystallization, which is also dependent on melting/crystallization temperatures and oxygen fugacities (fO_2) (Dick and Bullen, 1984**)**. Chromium spinels can be used as a petrogenetic indicator to understand the mantle melting and melt-rock reaction pathways. Melt-impregnated mantle rocks make up about 30% of all peridotites recovered from mid-ocean ridges (Dick, 1989). Chromian spinels with elevated Ti contents are thought to be diagnostic of such melt-reacted lithologies (Allan and Dick, 1996; Seyler and Bonatti, 1997; Warren and Shimizu, 2010). However, the mechanism of Ti enrichment in the spinel is not been well explained. We have examined a wide spectrum of peridotites ranging from harzburgites to plagioclase-bearing peridotites to understand the processes in the crust mantle transition zone which gives rise to the dynamic lithologies observed at different spreading centers. Clinopyroxenes and orthopyroxenes are the two major repositories of rare earth elements (REEs) in mantle peridotites. REEs strongly partition into clinopyroxene compared to orthopyroxene and olivine in spinel peridotites (Stosch 1982; Witt-Eickschen and O'Neill 2005; Lee et al. 2007; Liang et al. 2013; Sun and Liang 2014). The abundance of trace elements and REEs can be measured using different analytical techniques. Some of the conclusions based on the REE composition of clinopyroxenes in abyssal peridotites include, a. samples with depleted light rare earth element (LREE) resulted from fractional or near fractional melting **(**Johnson et al. 1990; Johnson and Dick 1992; Kelemen et al. 1997; Niu and Hékinian 1997; Shimizu 1998; Hellebrand

et al. 2001; Brunelli et al. 2006; Liang and Peng 2010; Warren 2016), b. samples with elevated LREE are affected by melt impregnation and melt–rock interaction **(**Elthon 1992; Hellebrand et al. 2002; Warren et al. 2009; Brunelli et al. 2014) which can be modelled by various open system models with different degree of mating and variable proportion of melt-influx rates, c. Elevated heavy rare earth element (HREE) and depleted LREE can be attributed to fractional melting in the garnet stability field (Johnson et al. 1990; Hellebrand et al. 2002; Brunelli et al. 2006). REE abundance in clinopyroxenes is therefore widely used to study partial melting, melt migration and melt–rock interaction processes in the mantle (Liang et al., 2021). We have examined and modelled the composition of the clinopyroxenes to quantify the evolution of the peridotites and the composition of the basaltic crust.

This study integrates the processes of melting and melt-rock reaction from the petrology and chemistry of abyssal peridotites recovered from spreading centers in different tectonic environments that ranges from the Hess Deep, which is a fast-spreading mid-oceanic ridge environment to the Mado Megamullion which is an OCC in the slow spreading back-arc of the Shikoku basin. The processes of melting and melt-rock interaction operating in the mantle dictates the composition of the melts that forms basaltic crust with its own unique geochemical signatures that distinguishes a mid-oceanic ridge basalt (MORB) from a back-arc or a fore-arc basin basalt.

Chapter 1: Formation of Plagioclase-bearing peridotites by Mantle assimilation-fractional crystallization at Hess Deep

1.1. Introduction

The reaction of basaltic melt with mantle rocks is a fundamental process in the evolution of the lower crust and upper mantle. These reactions transform mantle rocks into plagioclase-bearing varieties and control the composition of the primitive mid oceanic ridge basalts (MORB). The spinels in these plagioclase-bearing peridotites have an elevated TiO_2 content but the mechanism of formation of these peridotites is debated between fractional crystallization, melt-rock reaction and assimilation in the crust and shallow mantle. We have studied residual spinel peridotites and plagioclase-bearing peridotites recovered from Hess Deep (Equatorial Pacific Ocean). Evidence of the reactive origin of the plagioclase-bearing peridotite samples is present as symplectic intergrowth between plagioclase (altered) and spinel in the melt reaction pockets along with other replacement textures. In contrast the residual harzburgites have the typical holly-leaf and vermiform spinel morphology of mantle spinels. Compositionally the residual harzburgites have high Cr# (Cr/Cr+Al) ranging from 49 to 58 and very low TiO_2 content (<0.25%) while those from the plagioclase-bearing varieties have an elevated TiO_2 content up to 1.5 wt%. We have thermodynamically modelled the residual harzburgites by 20% partial melting of a fertile mantle composition. We found that the assimilation-fractional crystallization (AFC) reaction of the peridotites (after ~20% partial melting) with a primitive MORB (MgO 9.8-12.2 wt%) melt leads to progressive TiO_2-enrichment in spinels. There is a remarkable increase in the concentration of TiO_2 after plagioclase joins the AFC liquidus, which matches the compositional data from the Hess

Deep spinels from the plagioclase-bearing peridotites. These models are robust to changes in initial magma composition, fO_2 in the range of FMQ 0 to –1, and activity of H_2O in the magma source (up to 125 ppm in the source). These models also predict the appearance of early orthopyroxene in the AFC liquidus in a dry system that cannot be explained by a fractional crystallization alone. We suggest that the reaction of ascending basaltic melt with mantle peridotites is a dominating process that produces the chemistry of spinels in plagioclase-bearing peridotites and explains the appearance of orthopyroxene that is seen in different crustal sections from mid oceanic ridges.

Plagioclase-bearing peridotites have been recovered and studied from different spreading centers. They show evidence of melt impregnation into ultramafic lithologies, but the mechanism of transport of the melts remains debated (Kelemen et al., 1995; Kelemen and Dick, 1995; Liang et al., 2010) due to the scarcity of natural samples that show a direct record of these reaction textures or intermediate compositions.

Ultramafic lithologies were first recovered by Nautile Dive 17 at Hess Deep in the Equatorial Pacific Rise (EPR) (Francheteau et al., 1990). This was followed drilling expeditions, ODP leg 147 and IODP Expedition 345 (Site U1415) which intended to drill through the MOHO at the fast-spreading EPR (Dick and Natland, 1996; Gillis et al., 2014). Due to the high thickness of the EPR crust many of these expeditions could sample up to crustal depths and could not reach the mantle transition zone. Out of the 6 holes drilled in Site 895 (ODP Leg 147) harzburgites have been the dominant lithology from 3 holes, 895A, D, F. The drilled section in Hole 895D sampled harzburgite, dunite, troctolites gabbroic rocks and basalts (Edwards and Malpas, 1996). The ultramafic and related mafic rocks that have been recovered from all the 6 drill holes were similar

to the rocks from the transition zone of many ophiolite complexes and hence was considered to be lying close to the crust mantle transition zone (Dick and Natland, 1996; Gillis et al., 1993). IODP site U1415 (16 holes) drilled the plutonic crust and recovered mostly gabbros and troctolites from the lower crustal section (Gillis et al., 2014).

Porous flow is considered to be a major mechanism of melt transport and evolution in the upper mantle (Dick, 1977; Godard et al., 2000; Lissenberg et al., 2013; Quick, 1982). Abyssal peridotites and their on-land analogs (Batanova et al., 2011; Brunelli et al., 2014; Niu, 1997; Renna and Tribuzio, 2011) have not provided substantial direct evidence for the pathways of melt reaction, only the final reaction products. The main evidence for a hybridized rock in many of these studies has been inferred from the compositional reaction relationship between mantle harzburgite with melt which have together crystallized as troctolite (Bodinier et al., 1991; Constantin, 1999; Drouin et al., 2009; Natland and Dick, 1996; Sanfilippo et al., 2015). The presence of dunite channels as the final product in the Oman ophiolite (the best on-land analog of a fast-spreading center) have supported hydro-fracturing as the mechanism of melt transport (Kelemen et al., 2000; Kelemen and Aharonov, 1998; Korenaga and Kelemen, 1998). These require melt channels and a high melt/rock ratio. Melt-rock interaction is the other mechanism that is thought to be widespread in the ocean basins results in plagioclase-bearing (or “impregnated”) mantle peridotites at low melt fractions (Dick, 1989; Dick et al., 2010; Tartarotti et al., 2002).

The interpreted lithologic section in Hess Deep site 895 includes the presence of harzburgite, enclosing dunite. The dunites are enclosed by troctolites followed by olivine gabbro and gabbro-norite (Dick and Natland, 1996). This provided textural and chemical evidence that melts were not

in equilibrium with the wall rock and that the dunites were formed by melt rock reaction during melt migration from higher depths to the shallow mantle. The breakdown of mantle spinel to plagioclase has not been reported from crustal samples in these melt-reaction zones, but the partial resorption of spinel in plagioclase has been observed in Hess Deep troctolites (Edwards and Malpas, 1996). Melt-impregnated mantle rocks however make up about 30% of all peridotites recovered from mid-ocean ridges (Dick, 1989) making this reaction highly relevant to the overall mass balance of the crust, as some melt produced at depth stagnates in the upper mantle. Chromium spinels with elevated Ti contents are thought to be diagnostic of such reactions (Allan and Dick, 1996; Seyler and Bonatti, 1997; Warren and Shimizu, 2010), yet the mechanism of Ti enrichment in the spinel have not been well explained. Geophysical evidence also shows the presence of melt lenses below the Hess Deep ridge axis (discussed later). Fractional crystallization pathways would be dominant if melt transport was through hydro-fracturing. This would instead limit the extent of melt rock reaction. The appearance of orthopyroxene in the Hess Deep crust and other plutonic gabbros (Gillis et al., 2014; Kelemen et al., 1998) also cannot be explained by fractional crystallization alone (Gillis et al., 2014). Crystallization from a more oxidized parental magma than typical MORB or the influence of H_2O on the system (Berndt, 2004) are the existing theories to explain the process, but there is yet little direct evidence to test these processes (Saal et al., 2002).

1.2. Geological Setting

The East Pacific Rise is a fast-spreading end member of mid oceanic ridges with a half spreading rate of ~65 mm/year (Lonsdale, 1988). This forms a thick crust and therefore the deeper sections

of the crust and the upper mantle is difficult to access in contrast to the slow spreading ridges where lower crust and mantle rocks are exhumed. Geophysical evidence from seismic reflection studies show that the ridge axis is underlain by melt lenses (Detrick et al., 1987; Hooft et al., 1997; Hussenoeder et al., 1996). This is capped by a low velocity zone containing a higher and variable amount of partial melt (Crawford and Webb, 2002; Dunn et al., 2000). This evidence provide constraints to understand the method of melt transport with regards to porous flow (Dick, 1977; Godard et al., 2000; Lundstrom et al., 1995; Quick, 1982) suggesting melt-rock interaction as a dominating process.

Hess Deep is an accessible tectonic window in the fast-spreading lower crust. The rift valley is exposed near the Galapagos microplate and is located at the triple junction between the Pacific, Cocos and Nazca plates (Hey et al., 1972) (Figure 1-1A). The westward propagation of the Cocos-Nazca spreading center is half the spreading rate of the EPR. This exposes a 1 Ma young lithosphere at the Hess Deep (Rioux et al., 2012). The intra-rift ridge (a topographic high within the rift valley) provides a unique section of lower crustal rocks (Francheteau et al., 1990). This exposure has been studied to understand the magmatic processes in the fast-spreading center largely from primitive to evolved gabbroic rocks (Coogan et al., 2002; Dick and Natland, 1996; Hekinian et al., 1993; Lissenberg et al., 2013; Pedersen et al., 1996). ODP Site 895, Leg 147 sampled peridotites that have shown evidence of melt-rock interaction in the crust mantle transition zone (Edwards and Malpas, 1996). RSS JC 21 cruise mapped and sampled the intra-rift ridge in detail and sampled a wide range of mafic lithologies intercalated with ultramafic rocks (**Figure 1-1**B). At the southern slope of the of the intra-rift ridge predominantly melt-impregnated rocks

were recovered (olivine gabbros and melt impregnated dunites) while on the top of the slope were rocks of evolved composition (Eg: oxide gabbronorites). Residual peridotites were also recovered from the southern slope of the intra-rift ridge. The evolution of the melt has been studied from a fossilized melt lens (interpreted from the wide spectrum of gabbros that have been sampled by the cruise) in the lower oceanic crust (Lissenberg et al., 2013). We have studied the spectrum of peridotites (recovered by RSS JC 21) ranging from harzburgites to plagioclase-bearing peridotites (Table 1.1) to understand the processes in the crust mantle transition zone which gives rise to the dynamic lithologies observed at different spreading centers.

Table 1.1: Location and lithology of peridotites recovered by JC 21 cruise

Dive#	*Sample*	*Lat (deg)*	*Lat (min)*	*Long (deg)*	*Long (min)*	*Depth (m)*	*Rock type*
70	JC 21 70R-4	2	14.742	101	32.492	5194	Harzburgite
70	JC 21 70R-8	2	14.935	101	32.470	5038	Plagioclase-bearing peridotite
70	JC 21 70R-9	2	14.937	101	32.463	5039	Plagioclase-bearing peridotite
70	JC 21 70R-11	2	15.140	101	32.378	4900	Plagioclase-bearing peridotite
70	JC 21 70R-13	2	15.138	101	32.377	4901	Plagioclase-bearing peridotite
70	JC 21 70R-19	2	15.822	101	32.936	4405	Hybrid gabbro/peridotite
77	JC 21 77R-1	2	17.320	101	29.688	3745	Harzburgite
77	JC 21 77R-2	2	17.321	101	29.692	3737	Harzburgite
77	JC 21 77R-4	2	17.423	101	29.835	3590	Harzburgite
77	JC 21 77R-6	2	17.426	101	29.845	3585	Harzburgite
77	JC 21 77R-7	2	17.424	101	29.845	3585	Harzburgite
77	JC 21 77R-8	2	17.447	101	29.830	3547	Harzburgite

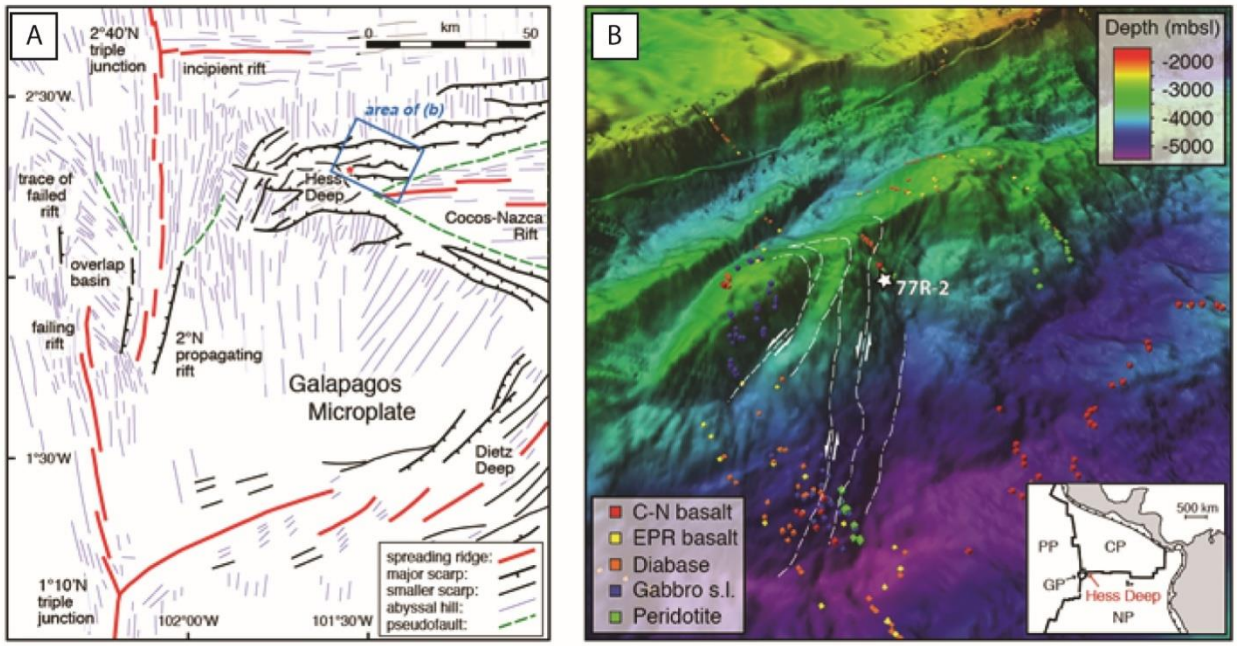

Figure 1-1: Tectonic setting of the Hess Deep. A. Distribution of tectonic plates showing the relative plate motions that generates the tectonic window at Hess Deep. B. Bathymetric map showing the sample locations of different lithologies sampled by the RSS JC 21 cruise

1.3. Petrography

This study includes 8 residual harzburgites, 4 melt impregnated plagioclase-bearing peridotites and a hybrid peridotite/gabbro or picrite sample. Textural relationships among the minerals were studied using LVPOL100 optical microscope under transmitted and reflected light.

1.3.1. Harzburgites:

Harzburgites are the residual mantle peridotites that are the products of melt extraction from the fertile mantle. These are therefore called residual peridotites. These are composed of altered

olivine (serpentinized) with some relict olivine grains, altered orthopyroxene (altered to amphibole or chlorite) and spinel. Clinopyroxene is present in some samples <5%. Spinel in these samples mostly holds the holly-leaf morphology which is typical of mantle spinels. They share inter-grain genetic relationships with olivine and orthopyroxene (Figure 1-2). Olivine is altered to serpentine but there are a few places where relict olivine grains are preserved. Overall, these samples exhibit signatures of extensive alteration, but spinels hold their primary morphology.

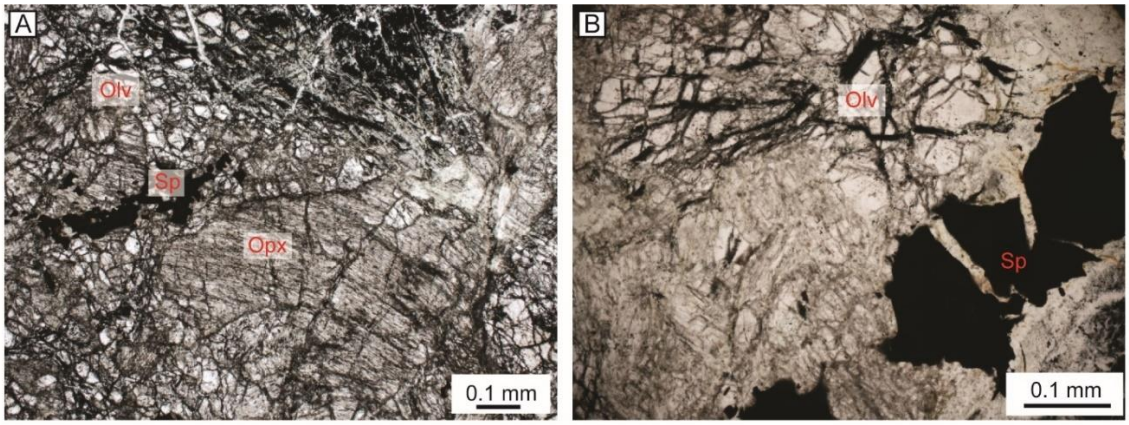

Figure 1-2: Representative photomicrographs of residual harzburgites and spinel morphology. A. Vermiform spinel in a harzburgite sample associated with olivine and orthopyroxene. B. Holly-leaf mantle spinel associated with altered olivine orthopyroxene

1.3.2. Plagioclase-bearing peridotites:

These are ultramafic rocks with pockets of impregnated melt that has crystallized and now characterize the presence of plagioclase-bearing lithologies in them. 4 samples exhibit melt impregnation signatures with differences in the quantity and extent of melt that has impregnated these samples (Figure 1-3). Most of the primary ultramafic phases in peridotites are altered and

can be identified by relict grain morphologies. The ultramafic lithologies are predominantly composed of serpentinized olivines. Spinel is the only primary mantle phase that holds its unaltered chemistry. The melt pockets consist of altered plagioclase (identified by its primary morphology) and spinel. The spinels in plagioclase-bearing zones exhibit signatures of melt-rock interaction (Figure 1-4). These spinels are rimmed/replaced by plagioclase (now altered) in places. Symplectic intergrowth between spinels and plagioclase is present in the melt impregnated zones that are dominantly composed of plagioclase melt pockets.

1.3.3. Hybrid mantle rock (hybrid gabbro/peridotite or picrite):

One sample cannot be clearly defined into a rock type based on its textural relationship or mineral compositions. It is divided into peridotitic (harzburgite) fractions composed of altered olivine, altered orthopyroxene and chrome-spinel as the primary magmatic minerals, and intruding gabbroic fractions composed of clinopyroxene, plagioclase, magnetite and Ti-oxides. There is a reaction zone between the spinels and the impregnating basaltic melt (that has now crystallized and contains clinopyroxene, plagioclase magnetite and Fe-Ti oxides). Similar reaction textures were seen in spinels in Hess Deep and termed as picrites (Allan et al., 1996). The name of this rock is controversial, and its origin is debated (Figure 1-4C).

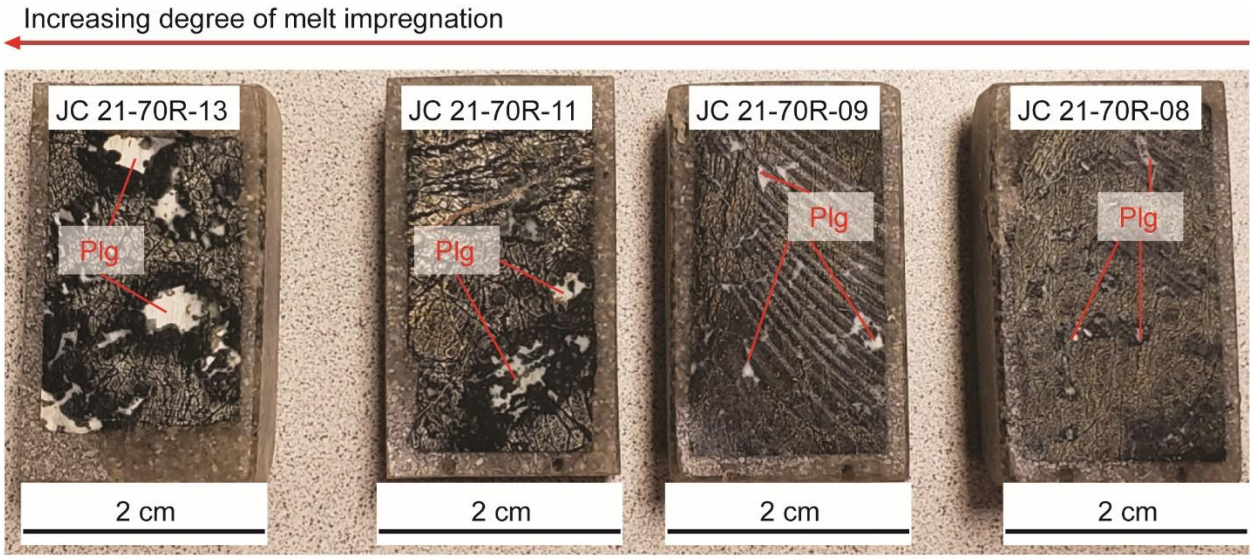

Figure 1-3: Plagioclase-bearing peridotite samples composed of altered plagioclase pockets in a serpentinized olivine bearing ultramafic assemblage. Note: the red arrow at top shows the increase in the molar proportion of altered plagioclase.

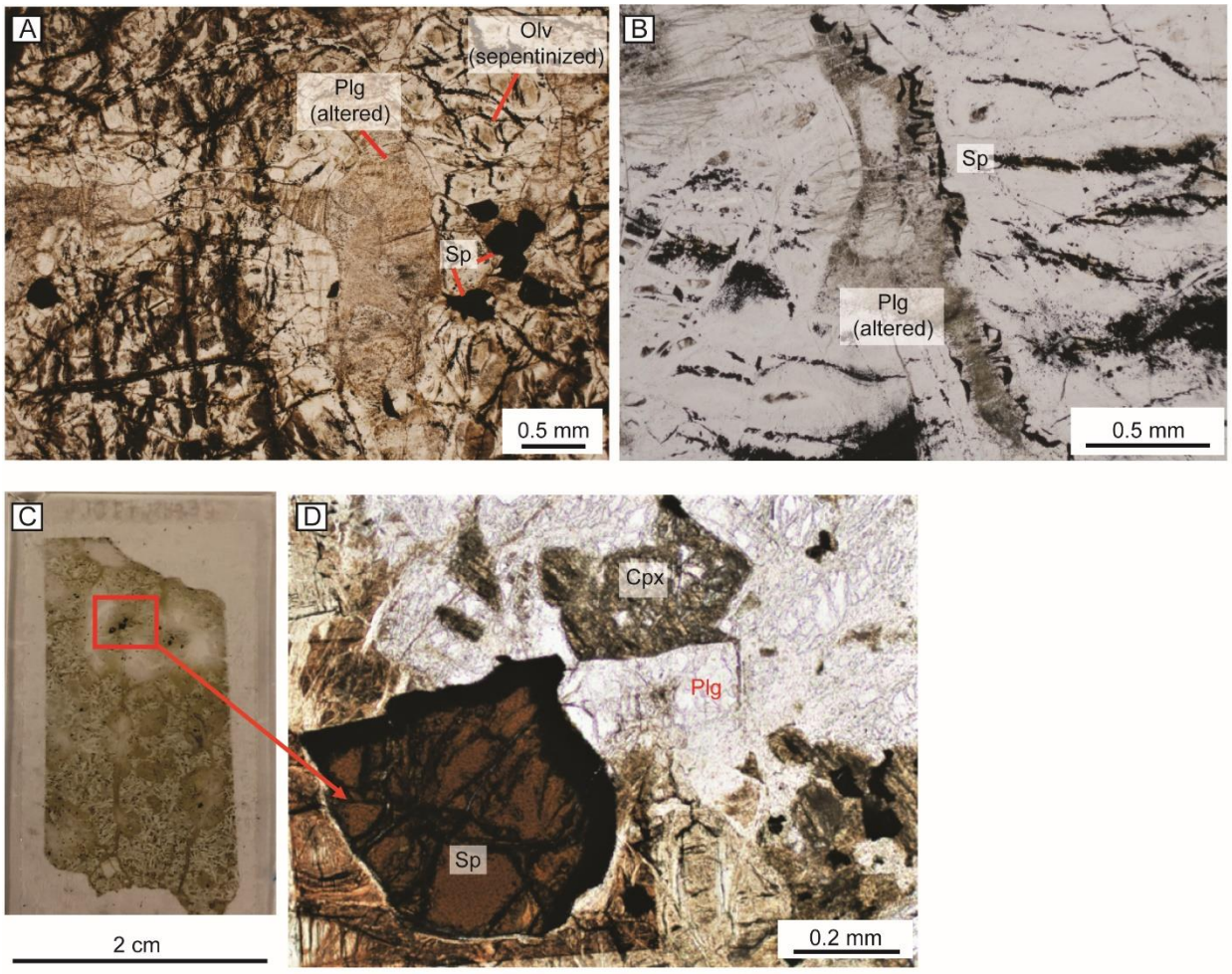

Figure 1-4: Mineral assemblage and textures from the plagioclase-bearing samples. A. Altered patches of plagioclase in an ultramafic assemblage associated with spinels. B. Altered plagioclase-spinel intergrowth in the melt-impregnated domain in the plagioclase-bearing peridotite. C. Thin section image of the hybrid sample. D. Photomicrograph of the region marked by the red box in C that shows the reaction zone between spinel and melt that has crystallized into a mafic (gabbroic) assemblage.

1.4. Major element analysis

We analyzed the major element concentration of silicates and spinel at Rice University by using a JEOL JXA 8530F Hyperprobe with a field emission assisted thermo-ionic (Schottky) emitter,

equipped with five Wavelength Dispersive Spectrometers (WDS). The analytical conditions employed for quantitative analysis of silicates at Rice University were 15 kV acceleration voltage, 20 nA beam current, ca. 300 nm beam size. The chemical composition of the minerals are shown in Supplementary Table S1 A-F.

1.5. Results

1.5.1. Orthopyroxene

Unaltered orthopyroxenes were found 3 residual harzburgite samples and 1 plagioclase-bearing peridotite sample. The Mg# (100*Mg/Mg+Fe) of these peridotites ranges from 88 to 92. The Al_2O_3wt% of the plagioclase-bearing peridotites are lower than the residual harzburgites. The peridotites plot in the lower range of abyssal peridotites Al_2O_3 towards the fore-arc peridotites field (Figure 1-5A). In terms of their Cr_2O_3 content the peridotites plot in the field of abyssal peridotites (Figure 1-5B). The plagioclase-bearing peridotites can be distinguished from the residual peridotites in terms of their Cr_2O_3 content (Figure 1-5B).

1.5.2. Clinopyroxene

Clinopyroxenes are mostly altered and present in very small volume percentage (<0.5). Relict primary clinopyroxene grains were analyzed from both the residual and the plagioclase-bearing peridotites. The residual peridotites can be distinguished from the melt impregnated ones on the basis of their Mg#, Al_2O_3 and TiO_2 content. The residual peridotites have high Mg# ranging between 90 and 94.6 and TiO_2<0.2 wt.% in contrast to the plagioclase-bearing peridotites with

Mg# 90 to 90.5 and TiO_2>0.25 wt.%. The Al_2O_3 in the residual peridotites have a wide range from 2 to 9 wt.% while those in the plagioclase-bearing samples range between 3-4 wt.% (Figure 1-5).

1.5.3. Olivine

Olivine in most of the samples were extensively altered to serpentine. Few microns sized relict olivine grains are present in some of the samples that could be analyzed in electron microprobe. There is a sharp contrast between the olivine Fo content (Mg/ Mg+Fe) in the harzburgites and the plagioclase-bearing peridotites (Figure 1-6B). The Mg# of the harzburgites ranges from 89-90 whereas those for the plagioclase-bearing peridotites is less than 89. The overall range for NiO varies between 0.13 to 0.45 weight% but the melt impregnated peridotites have a lower NiO content compared to the residual peridotites.

1.5.5. Spinel

Spinels show different compositional ranges in the residual peridotites and the melt reacted plagioclase-bearing peridotites. There is a dispersion of the spinel composition from the abyssal peridotite field in terms of the low Mg# (<0.5) and more iron-rich compositions in the plagioclase-bearing peridotites (Figure 1-6A). Residual harzburgite spinels are compositionally homogeneous with high Cr# (100*Cr/Cr+Al) ranging between 49 to 58 and negligible to very low TiO_2<0.3 weight%(Figure 1-7A). The spinel from the plagioclase-bearing peridotites form a separate cluster from the harzburgites, having an elevated TiO_2 ranging from 0.3 up to 1.5 weight%and a wider range of Cr# ranging from 32 to 56 (Figure 1-7B).

The hybrid mantle spinels in this sample are overall compositionally similar to plagioclase peridotite spinels (Hellebrand et al., 2001) with elevated TiO_2, and stand out from the compositions of refractory spinels of the spinel peridotites recovered from Hess Deep previously (Natland and Dick, 1996) and this study (Supplementary Table S1 E; Supplementary Figure S1 A). They exhibit a Cr-rich core (Zone 1) surrounded by successive mantles of complex compositional reverse zoning (Cr-Fe rich core and Mg-Al rich rim; Zone 2), a region of symplectic intergrowth between spinel and plagioclase (zone 3A, zone 3B). These numerous symplectite-bearing spinel grains are present on the boundary between clearly mantle-derived and gabbroic minerals. The outermost rims of these spinels trend toward a Ti-Cr-ulvöspinel composition (zone 3B) otherwise seen only in lherzolitic shergottites (Goodrich et al., 2003).

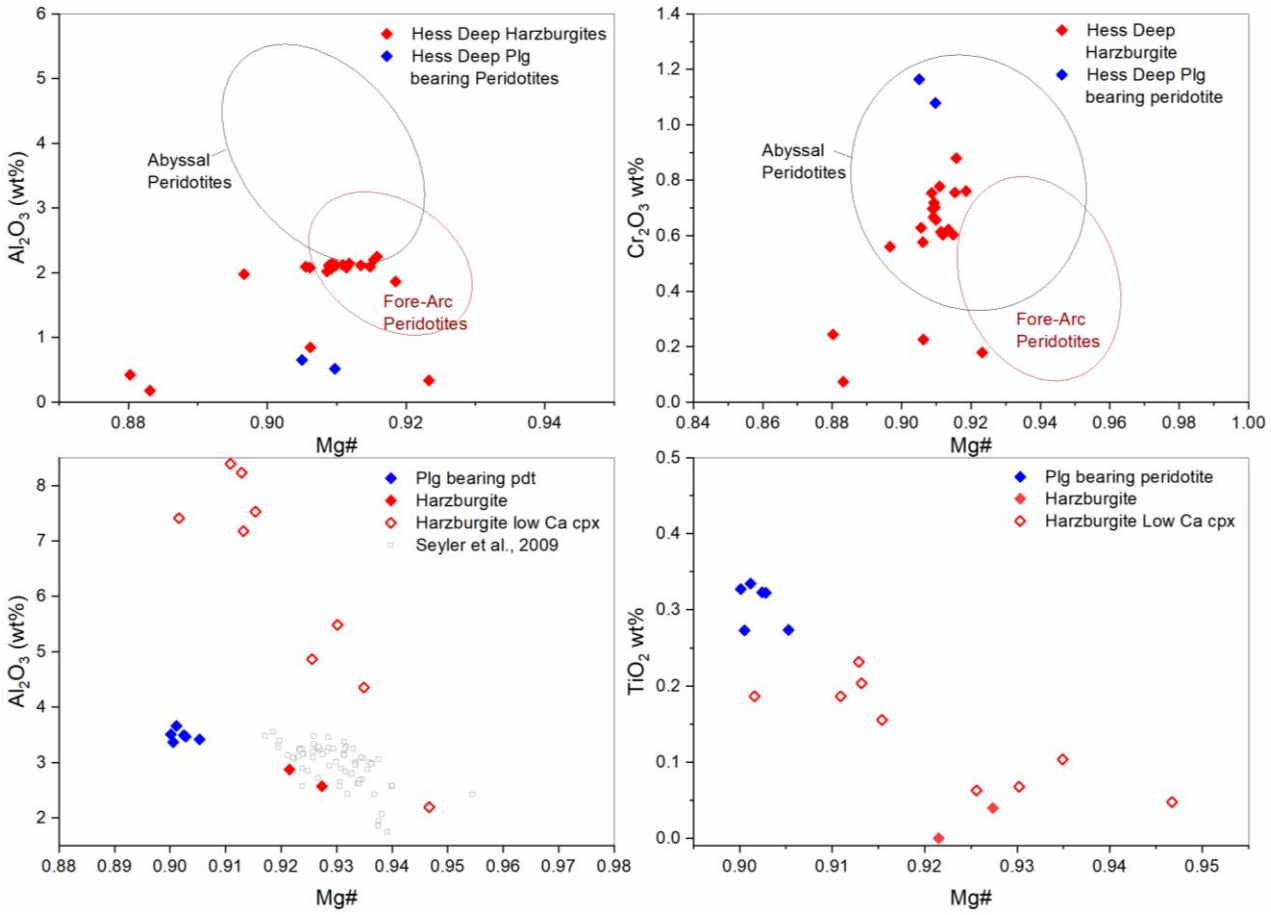

Figure 1-5: Major element chemistry of silicates in residual harzburgites and plagioclase-bearing peridotites. A. Plot of Mg# ($Mg/Mg+Fe^{2+}$) vs Al_2O_3 wt.% in orthopyroxenes show that the residual harzburgites have a lower Al_2O_3 content and mostly cluster towards the lower end of the abyssal peridotites field. B. Plot of Mg# ($Mg/Mg+Fe^{2+}$) vs Cr_2O_3 wt.% shows that the Hess Deep harzburgites are enriched in Cr_2O_3. C, D. Residual harzburgite clinopyroxenes define a separate cluster with respect to plagioclase-bearing peridotites in terms of their Mg#, Al_2O3 wt% and TiO_2 wt.%. The plagioclase-bearing peridotite clinopyroxenes have a lower Mg# and lower Al_2O_3 wt.% and are enriched in TiO_2.

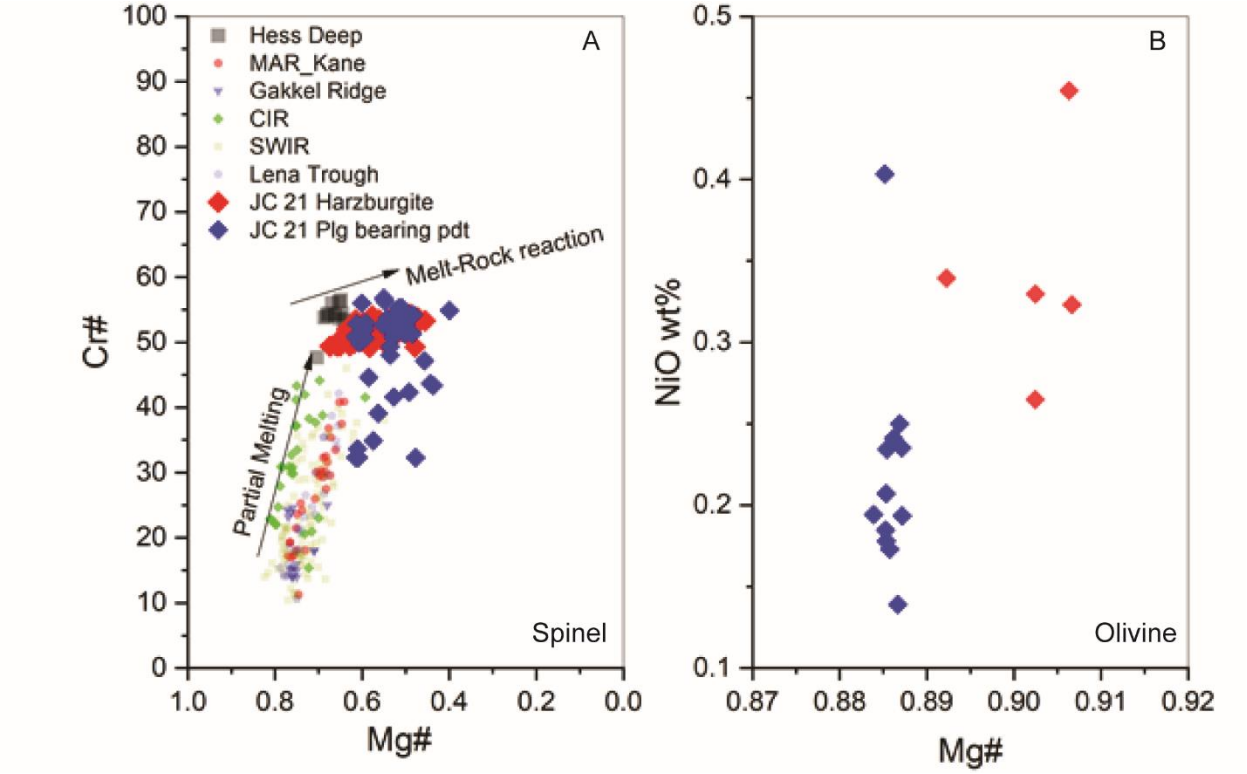

Figure 1-6: Major element composition of spinel and olivine. A. Mg# vs Cr# of spinels from Hess Deep that shows that high Mg# and Cr# for Hess Deep harzburgites while the plagioclase-bearing peridotites have a wider range. B. Mg# and Cr# vs NiO wt.% in olivines where plagioclase-bearing peridotites define a cluster at lower NiO wt.% and lower Mg#.

1.6. Discussion

1.6.1. Signatures of melt-rock reaction from mineral chemistry

The clinopyroxene TiO_2 weight% vs Mg# marks a different cluster for the plagioclase-bearing peridotites (Figure 1-5D). Higher values of TiO_2 wt% was previously observed and first reported in Hess Deep Site 895 troctolites and also in harzburgite samples adjacent to dunites (Edwards and Malpas, 1996). The partition coefficient (Kd) of Ti in cpx/opx increases with decrease in temperature (Hellebrand et al., 2005). The lower Mg# and NiO content in olivines from the

plagioclase-bearing peridotites (Figure 1-6A) can be attributed to Fe-Ti enrichment with progressively evolving melt composition. The higher TiO_2 content in clinopyroxene from the melt-impregnated rock could be a result of melt -rock interaction or lower equilibration temperatures. Similar trends of Fe-Ti enrichment have been reported from other studies of melt-impregnated harzburgites (Dick and Natland, 1996) in Hess Deep and Garrett Transform (Cannat et al., 1990; Hekinian et al., 1993).

plagioclase-bearingThe harzburgite spinels in this study show a more Fe-rich composition while the plagioclase-bearing peridotites exhibit a wider range in terms of their Cr# and Mg# (Figure 1-6A). The dispersion of the composition of the spinels from the harzburgite array to a more Fe-rich composition in Site 895 troctolites and gabbros was explained by olivine fractionation causing Fe enrichment in the melt and the drop in Cr# (troctolites and gabbros) by the early crystallization of clinopyroxene. Sub-solidus re-equilibration could also shift the composition of spinels to a more Fe rich composition. Since we do not see any notable variation in the Cr# for the harzburgites in our study this dispersion from the abyssal peridotite array can be attributed to either olivine fractionation (Edwards and Malpas, 1996) or subsolidus re-equilibration. Mg# of spinels in harzburgites could coincide with the melt-impregnated peridotites in terms of their Cr#, but can be distinguished based on their TiO_2 content (Hellebrand et al., 2001). Melt impregnated plagioclase-bearing peridotites have concentration of TiO_2 compared to residual rocks. A similar distinction has been noted in this study where the melt impregnated rocks are compositionally distinct based on their TiO_2 content (Figure 1-7B). TiO_2 acts as more robust indicator and separates the melt-reacted rocks from those that are residual.

1.6.2. Formation of plagioclase-bearing peridotites

There is a sharp difference between the mineralogy of the residual peridotites and the plagioclase-bearing peridotites. The harzburgites are dominated by the presence of altered olivine, orthopyroxene, minor clinopyroxene and spinel. Texturally the spinels in the harzburgites are typical of mantle spinels based on their shape and association with ultramafic minerals (olivine and orthopyroxene). The major element composition also reflects the distinct group of peridotites. The high Cr# and very low TiO_2 content of the spinels formed as a result of partial melting. The residual spinels have higher Cr number as Cr prefers to stay in the spinel being a compatible element. Al on the other hand partitions into the melt, thus elevating the Cr/Cr+Al value in the residual spinels. Ti being an incompatible element prefers the melt phase and thus depleting the residual peridotites in TiO_2 content. The very high Cr number in the peridotites is the result of high degrees of partial melting at Hess Deep (Dick and Natland, 1996; Gillis et al., 1993).

The plagioclase-bearing peridotites have zones or pockets of melt impregnation in the form of altered plagioclase. The composition of the spinel from these rocks have a wide range of Cr# as low as 27 and have TiO_2 up to 1.5 weight%. The texture in these rocks and the composition of the spinels indicates that these rocks have undergone reaction with a basaltic melt that is reflected in the chemistry of the spinels. The debated hybrid sample is dominated by replacement and symplectic intergrowth textures (Supplementary Table S1 A)**.** The symplectic intergrowth between plagioclase and spinel indicates that these crystallized in the presence of a melt that reacted with the ultramafic rocks. Symplectic intergrowth between spinel and plagioclase has been previously observed in metamorphic rocks (Liati and Seidel, 1996) or from lunar layered intrusions (Elardo

et al., 2012). Intergrowth between altered plagioclase and spinel has been observed in the Nain ophiolite (Pirnia et al., 2018). These were interpreted to be formed by the re-crystallization of spinel lherzolites in plagioclase facies conditions. Partially-resorbed spinel in plagioclase has been observed in the troctolites from Hess Deep Site 895 (Edwards and Malpas, 1996). These resorption textures in troctolites were interpreted to be a result of leaching of the melt with plagioclase in the liquidus. It is because plagioclase (the other aluminous phase other than spinel) incorporates Al in its structure forms a symplectic intergrowth with spinel. Spinel, therefore, starts to break down due to dis-equilibrium at lower pressure and change in silica activity in the presence of melt. In addition to the textures and compositions that represent the formation of plagioclase-bearing peridotites by melt-rock interaction we also ran several thermodynamic models using MELTS (Ghiorso et al., 2002; Ghiorso and Sack, 1995) to understand the evolution of spinel composition with melt stagnation.

To analyze our hypothesis about the formation of the residual peridotites and the plagioclase-bearing peridotites we ran MELTS (Workman and Hart, 2005) models partial melting and assimilation-fractional crystallization (AFC) models respectively.

1.6.3. MELTS Modelling

1.6.3.1. Bulk Mantle composition

It is essential to estimate the composition of the mantle (the starting composition in a melting model) to model a mantle harzburgite which is a result of partial melting of the mantle. Workman and Hart (2005) presents a 3% depleted primitive upper mantle composition (McDonough and Sun, 1995). This composition was calculated by extracting 3% MORB from the primitive mantle

composition (Dick and Natland, 1996). We ran several melting models using MELTS (Ghiorso and Sack 1995; Ghiorso et al., 2002) models with this composition and found that the starting melt composition has an elevated TiO_2 concentration at very low degrees of partial melting as compared to the data from global abyssal peridotites. We therefore reduced the TiO_2 percentage from the Workman and Hart (2005) composition. Also, MELTS partitions all the Cr_2O_3 from the bulk composition into spinels. We sequestered 0.02 weight% Cr_2O_3 from the original Workman and Hart (2005) composition to balance the partitioning effects in the model. After considering these 2 constraints for our estimated mantle composition we used this modified Workman and Hart (2005) **(**Table 1.2) composition as the bulk mantle composition in our melting models.

Table 1.2: Starting mantle composition for the melting model; assimilant and Hess Deep basalt composition used for AFC modelling

	Modified Workman and Hart 2005	*Composition of Assimilant*	*Hess Deep Basalt*
SiO_2	44.69	43.25	49.96
Al_2O_3	3.98		14.27
Fe_2O_3	0.19	0.1	11.68
FeO	8	8.34	8.74
MnO	0.13	0.16	0.2
MgO	38.71	45.56	7.35
CaO	3.17	0.79	11.7
Na_2O	0.28	-	2.53
Cr_2O_3	0.55	0.67	-
TiO_2	0.06	0	1.66
NiO	0.24	0.3	-
Total	100	100	100

1.6.3.2. Partial Melting

We ran a series of melting models, starting in the garnet and spinel stability fields. Since there is no prominent report of garnet bearing peridotite in the garnet stability field, we chose the condition of melting to begin in the spinel stability. On melting our estimated mantle composition by 20% (considering mantle upwelling as the process of partial melting in the mantle), the composition of the spinel in the residue aligns with the composition of spinel from Hess Deep (Uenver-Thiele et al., 2014) (Figure 1-7).

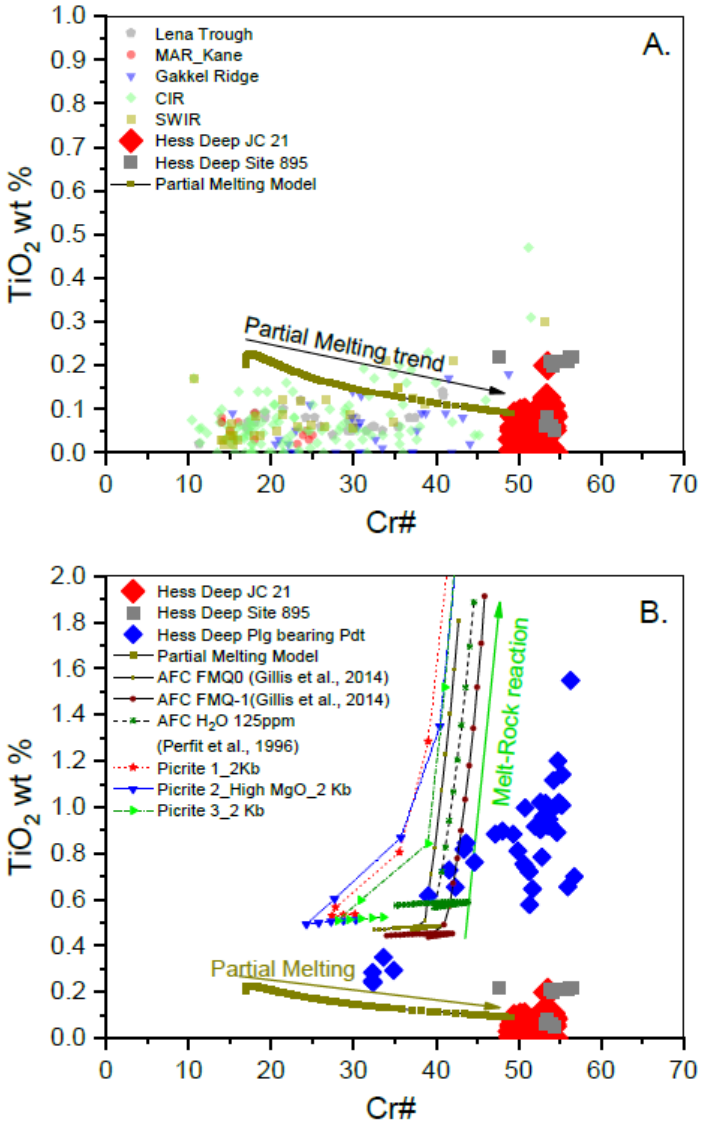

Figure 1-7: A. Chemistry of spinels in residual peridotites. Spinel peridotite data from other spreading centers is given for comparison (Dick et al., 2010; Dick and Natland, 1996; Hellebrand et al., 2002; Warren, 2016). The blue line indicates the compositional trend in spinels with increase in degree of partial melting of a fertile mantle (Workman and Hart, 2005). The Hess Deep spinel composition coincides with modeled spinels at ~20% meting. B: Spinel Cr# vs TiO_2 weight % in plagioclase-bearing peridotite from JC 21. They form a separate group with higher TiO_2 wt% than the residual peridotites of Hess Deep. The AFC model results and melt stagnation trends suggest that TiO_2 enrichment with progressive assimilation. The kink in the AFC model in terms of sharp increase in TiO_2 with the crystallization of plagioclase in the AFC liquidus.

1.6.4. AFC Model

1.6.4.1. P-T conditions

We took the solid residue after 20% melting as the composition of the assimilating solid as the assimilant in our AFC models. We ran MELTS assimilation models to assimilate the residual solid with a Hess Deep primitive basaltic melt at a shallow depth of 200 MPa. The formation of plagioclase is catalyzed at the expense of spinel occurs because the reaction takes place at a shallow depth, in the plagioclase stability field. This would correspond to about 200 MPa at the base of the oceanic crust. This could favour the formation of plagioclase-bearing lithologies and lead to the transition from spinel to plagioclase. We started the process at an elevated temperature, since it is important to completely assimilate the rock with the reacting melt, which needs a higher temperature above the liquidus temperature of basalts. The process of melting the solid assimilant is endothermic and this would require the additional heat to melt the assimilant. The temperature of the solid residue after 20% melting was 1296ºC in our partial melting model. We started our AFC process at this temperature.

1.6.4.2. Melt-Rock ratio

We have taken 6g of assimilant at each reaction step since the amount of the assimilant plays an important role as this determines the melt/rock ratio that the reactions are undergoing. At very low amounts of the assimilant the results are very similar to fractional crystallization trend as the melt/rock ratio is high in this case. Only higher proportion of assimilant can mimic a reactive porous flow process. We took different primitive melt compositions for Hess Deep basalts to get a more robust result from the models.

1.6.4.3. fO_2 and fH_2O

We ran a series of models varying oxygen fugacity of FMQ -1 to 0 as ambient mantle fO_2 (Uenver-Thiele et al., 2014). Any metasomatic event that increases the Fe+3 and hence the fO_2 above +1 values is not considered in this study. The amount of water is an important parameter as this could differentiate the melting process in a dry system with respect to a wet system. We took water up to 125 ppm (Hirth and Kohlstedt, 1996) to see if there is any notable change to the amount of water added during this process.

1.6.5. Melt-Rock reaction

All the models broadly predicted similar results. First, a significant change in TiO_2 concentration in the AFC modelled spinel with crystallization of plagioclase, at the invariant point. The invariant point where a majority of plagioclase crystallizes followed by clinopyroxene around 1232ºC shows a sharp increase in the TiO_2 and Cr_2O_3 content in the spinel. This trend also mimics the concentration of the oxides (spinel) in the AFC liquid. Since plagioclase (into which Ti or Cr does not partition) is the major crystallizing phase at this step, the concentration of these elements increases in the liquid, and the spinels that crystallize from it (Figure 1.8). The composition of these spinel nearly coincides with the spinel compositions from the plagioclase-bearing peridotite spinels and the hybrid sample (Supplementary Figure S1 D). Although the composition of all the plagioclase-bearing peridotite spinels does not exactly match the composition of the AFC evolution trend but the sharp increase in TiO_2 can explain the elevated Ti in melt reacted mantle spinels. It also explains the high concentration of TiO_2 in spinels in some of the global veined peridotites from different spreading centers.

1.6.6. Appearance of orthopyroxene early in the AFC liquidus

Hess Deep, being a fast-spreading ridge is believed to be a dry system of melting. There has not been any evidence of a feasible mechanism that can introduce large volumes of water in the partial melting processes operative at mid-oceanic ridges. The Oman ophiolite is considered a 'wet system' by some studies where subduction induced hydrous partial melting is a possibility. One of the arguments that explains the presence of the orthopyroxene layer in the Oman ophiolite is solved by the presence of water in the system. Our model results mark the appearance of orthopyroxene in the AFC liquidus prior to clinopyroxene. The crystallization sequence from the AFC models are olivine → olivine+ spinel → olivine + spinel + orthopyroxene → olivine + spinel + orthopyroxene + plagioclase→ olivine + spinel + orthopyroxene + plagioclase + clinopyroxene (Figure 1.8). Melt rock reaction at a lower melt/rock ratio can also explain the presence of orthopyroxene in the oceanic crust at different spreading centers without the involvement of water. Indeed, this seems the only way to explain the presence of olivine-orthopyroxene cumulates in the drilled section at Hess Deep IODP Site 1415 (Gillis et al., 2014) and Pito Deep (Perk et al., 2007) dredged samples. It also eases the restriction of olivine-orthopyroxene crystallizing magmas to subduction related hydrous partial melting of harzburgitic mantle, which had been a prime explanation for the formation of the parent magma to the Stillwater igneous complex (Boudreau et al., 1999), thus ironically connecting Harry Hess's Ph.D. field area high in the Beartooth Mountain range to the oceanic deep named in his honor (Hey et al., 1972).

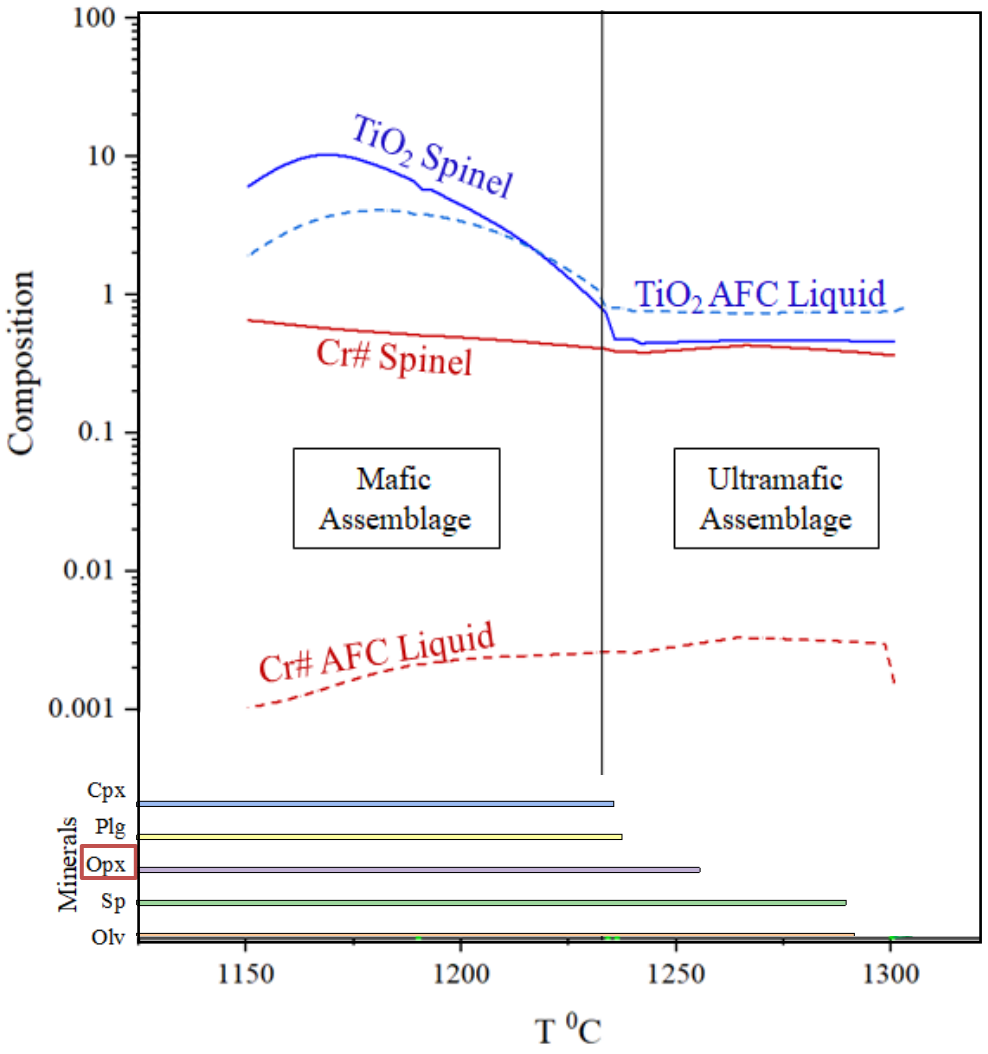

Figure 1.8: AFC model assemblages and appearance of minerals in the AFC liquidus. There is a marked increase in TiO_2 in spinels with the advent of crystallization of plagioclase. The AFC crystallization marks the appearance of orthopyroxene prior to clinopyroxene.

1.6.7. Crystallization of picritic melts and appearance of orthopyroxene

The symplectic intergrowth textures observed in the spinels from the hybrid sample in this study are similar to those observed in Site 894 Sample 147-894D-1R-CC, 4-6 cm (Allan et al., 1996). Based on the presence of large-rounded olivine phenocrysts (up to 6 mm), and their high abundance that constitutes 25-30% of the rock, this sample was interpreted as a picrite (Allan et al., 1996). To understand the evolution of a picritic magma we modelled picrites from the Siqueiros Transform **(**Table 1.3**)**. We took high MgO bearing picrites from recent volcanism at the Siqueiros transform (Perfit et al., 1996) and ran fractional crystallization models using MELTS. The spinels crystallizing from the picritic compositions have an elevated TiO_2 content (Figure 1.7B) but orthopyroxene appears much late in the liquidus at lower temperatures (Figure 1-9). Crystallization of a picritic magma also fails to explain the dis-equilibrium texture in the form of spinel-plagioclase intergrowth at the interface of spinel and basaltic melt (Supplementary Figure S1 C). A Magma mixing theory between a primitive melt and an evolved melt was proposed by Allan et al., 1996 regarding the genesis of Sample 147-894D-1R-CC, 4-6 cm. This is because of the presence fayalitic rims of olivines, resorbed margins of Cr-spinels and anorthitic plagioclase, all of which suggests dis-equilibrium between the phenocrysts and the melt. We propose melt-rock reaction instead of magma mixing as the possible mechanism for the formation of the plagioclase-bearing peridotites and the hybrid sample that preserves intermediate dis-equilibrium textures of melt-rock reaction. Our AFC models predict the composition of the spinels from the plagioclase-bearing peridotites as well as the early appearance of orthopyroxene in the AFC liquidus which is a ubiquitous phase in Hess Deep gabbros (Gillis et al., 2014).

Table 1.3: Composition of picritic basalts from the Siqueiros transform (Perfit et al., 1996)

	SiO2	*TiO2*	*Al2O3*	*FeO^T*	*MnO*	*MgO*	*CaO*	*Na2O*	*K2O*	*P2O5*	*Total*	*Mg#*
PB 1	47.05	0.88	16.11	7.96	0.15	12.78	11.13	2.18	0.039	0.077	98.37	76
PB 2	46.93	0.71	13.15	8.19	0.12	20.57	9.14	1.7	0.03	0.05	100.59	83.2
PB 3	47.9	0.85	16.18	7.92	0.1	14.24	10.64	2.16	0.03	0.07	100.09	76.1

1.6.8. Origin of the hybrid sample

The hybrid sample can be divided into peridotitic (harzburgite) fractions composed of olivine, orthopyroxene and chrome-spinel as the primary magmatic minerals, and intruding gabbroic fractions composed of clinopyroxene, plagioclase, magnetite and Ti-oxides (Supplementary Table S1 A). An extensive symplectic intergrowth is developed between numerous zoned spinels and a primitive melt, along with intermediate spinel and plagioclase feldspar compositions documenting its reaction pathway exceptionally clearly (Supplementary Figure S1 B; Supplementary Table S1 E).

The compositions of the melt-reacted spinels in this sample cannot be explained by simple partial melting the mantle (as noted in many other studies of plagioclase peridotites). The spinels preserve substantial intra-grain chemical heterogeneity that can be related to the evolution and reaction processes that such rocks have undergone (Supplementary Figure S1 B). Symplectic intergrowth between spinel and plagioclase has been previously observed either in metamorphic rocks (Liati et al., 1996; Scott et al., 2013) or from lunar layered intrusions (Elardo et al., 2012). The textural and compositional characteristic of spinel in the hybrid rock clearly indicate disequilibrium and breakdown of meta-stable spinel in a high thermal gradient (indicated by the presence of preserved symplectite), and in the presence of a melt. The presence of reverse zoning (Supplementary Figure

S1 B) is an indication of the evolution of melt during the re-crystallization of spinel, formed either as a result of disequilibrium between spinel crystal and the evolving silicate melt, re-equilibration and cation exchange at lower temperatures (Yang et al., 1993) or metasomatism of Cr rich spinel and diffusion of Cr in spinel due to a localized thermal event (Lenaz et al., 2016).

The presence of spinel and plagioclase in the symplectite zone suggests that the harzburgites (stable at higher pressure in the spinel stability field), containing the spinels became unstable due to change in pressure, in the presence of impregnating melt. The symplectites are thus a result of solid-state diffusion-limited reaction. The relative diffusion coefficients (D) of the constituent elements, $D_{(Al)} << D_{(Mg, Fe)}$ (Wan et al., 2008; Posner et al., 2016) are probably the reason why plagioclase (that incorporates Al) forms a symplectic intergrowth with the spinel. Also, the formation of plagioclase is catalyzed at the expense of spinel because the reaction takes place at a shallow depth, in the plagioclase stability field. This would correspond to about 200 MPa at the base of the oceanic crust. Spinel therefore starts to break down, due to dis-equilibrium at lower pressure and change in silica activity in the presence of a basaltic melt. The observed symplectite plagioclase becomes progressively albitic from core to rim of the spinel with the evolution of the infiltrating melt (Supplementary Figure S1 C; Supplementary Table S1 F). The Cr and Ti concentrations in spinel are elevated in the symplectite (Supplementary Figure S1 B) in Zone 3b because Cr cannot be accommodated in the structure of plagioclase, and the reacting melt becomes progressively Ti- rich with plagioclase crystallization. The reaction of chromium spinel with melt and crystallization of plagioclase and spinel in the symplectite, therefore increase the Cr and Ti content in spinel zone 3B. This would suggest that Ti-rich spinels in abyssal peridotites globally

do not simply absorb the Ti from an infiltrating melt as has been widely assumed, but instead are the products of re-precipitation of a high-Ti magmatic spinel from a melt that has concentrated Ti during the magmatic process. The composition of the Cr and Ti composition in the spinel follows the trend of evolution of the modeled melt by AFC process (described in section 1.6.5) (Supplementary Figure S1 D). Also, in this model, the sharp increase in the concentration of Cr and Ti in Zone 3B in the symplectite commences with the crystallization of plagioclase. The symplectite textures capture the reaction process and the fate of spinel present in the transition from the spinel to the plagioclase stability fields in the mantle. This observation addresses the ongoing debate of melt-rock reaction, as a major mechanism and fundamental process of melt transport under mid-ocean ridges because the rock preserves intermediate products of an on-going melt-rock interaction. Worldwide, mid-ocean ridge basalt is considered to be an aggregate of mantle partial melting processes combined with reactive porous flow in the shallow mantle. The relatively straight-forward AFC model explains both the mineral chemistry of reactively produced mantle spinels observed in plagioclase peridotites, and the liquidus relationships of the most refractory melts observed at mid-ocean ridges.

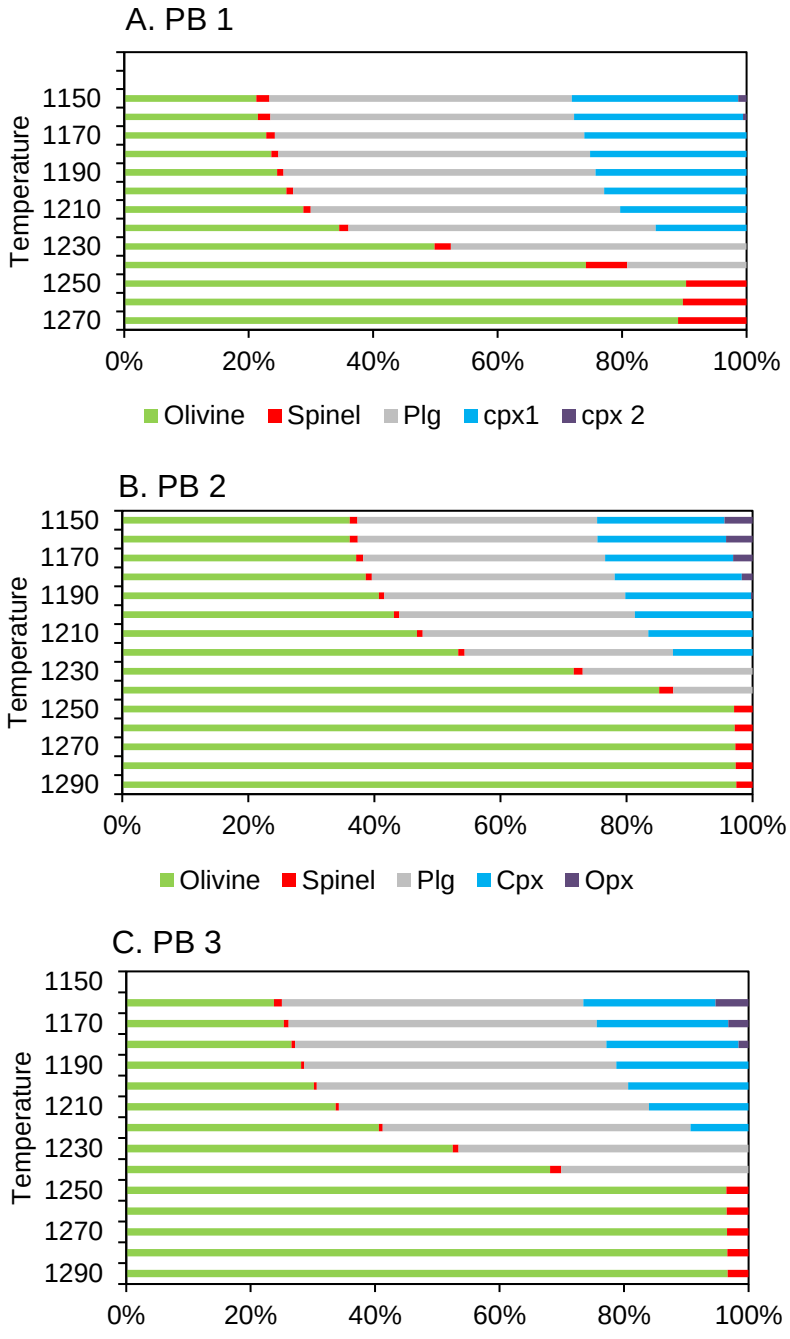

Figure 1-9: Crystallization sequence for picritic magma from the Siqueiros Transform. A, B, C. Appearance of mineral phases in the liquidus for picritic magma compositions PB-1, PB-2 and PB-3 respectively.

1.7. Conclusions

Plagioclase-bearing peridotites have been recovered from all spreading centers. These rocks ca be formed by melt-rock interaction. Our melt-impregnated samples exhibit symplectic intergrowth between spinels and altered plagioclase which is a product of such reactions. In addition to the textures, spinel composition reflects the process of melt stagnation in the form of enrichment in TiO_2 content.

The hybrid sample which is debated between a melt impregnated hybrid peridotite/gabbro and a picrite compositionally coincides with the rest of the plagioclase-bearing peridotite composition. This exhibits the presence of symplectites between spinel and plagioclase and can be a melt reacted mantle rock.

The composition of the residual peridotites from Hess Deep (Dick and Natland, 1996) and this study can be modelled by partial melting of a primitive upper mantle composition. The compositions show signatures of melt-rock reaction. Existing fractional crystallization models could not explain the evolution of these rocks. Our AFC model explains the TiO_2 enrichment trend in spinels form the melt-reacted rocks with the advent of plagioclase crystallization. The melt/rock ratio plays a significant role in distinguishing fractional crystallization to melt interaction processes.

The presence of water in a mid-oceanic ridge setup is debated and the amount of water (if present) is not well constrained. A mid-oceanic ridge is system is therefore considered to be dry in contrast to a wet hydrous partial melting system in a subduction zone setting. Our AFC models predicts the

early appearance of orthopyroxene in the AFC liquidus and explains the presence of orthopyroxene in the oceanic crust without the requirement of a hydrous partial melting process.

1.8. Supplementary Data 1

Supplementary Table S1 A: Major element composition of olivines

Sample No	*JC 21 70R-09*	*JC 21 70R-09*	*JC 21 70R-09*	*JC 21 70R-09*	*JC 21 70R-09*	*JC 21 70R-09*	*JC 21 70R-09*	*JC 21 70R-09*
SiO2	39.62	38.83	39.61	38.87	39.04	40.39	40.46	40.10
TiO2	0.02	0.00	0.01	0.01	0.00	0.00	0.03	0.00
Al2O3	0.00	0.01	0.00	0.00	0.00	0.01	0.00	0.00
FeO	11.10	11.21	11.31	11.10	11.26	11.00	11.16	11.08
MnO	0.17	0.19	0.15	0.16	0.16	0.18	0.16	0.14
MgO	47.92	48.66	48.91	48.63	48.72	48.41	48.66	48.78
CaO	0.08	0.07	0.05	0.08	0.06	0.07	0.08	0.12
Cr2O3	0.02	0.00	0.00	0.01	0.03	0.01	0.00	0.03
NiO	0.40	0.17	0.18	0.14	0.23	0.24	0.24	0.19
Na2O	0.04	0.00	0.00	0.02	0.03	0.00	0.01	0.00
K2O	0.00	0.02	0.00	0.00	0.00	0.00	0.01	0.00
Total	99.38	99.16	100.23	99.03	99.54	100.31	100.82	100.44
Mg#	0.89	0.89	0.89	0.89	0.89	0.89	0.89	0.89

Sample No	*JC 21 70R-09*	*JC 21 70R-09*	*JC 21 70R-09*	*JC 21 70R-09*	*JC 21 77R-1a*	*JC 21 77R-1a*	*JC 21 77R-1a*	*JC 21 77R-1a*	*JC 21 77R-1a*
SiO2	39.98	39.94	40.34	40.04	40.03	40.63	40.39	41.07	40.66
TiO2	0.02	0.01	0.00	0.00	0.02	0.00	0.00	0.00	0.00
Al2O3	0.02	0.01	0.00	0.09	0.02	0.00	0.01	0.05	0.00
FeO	11.23	11.15	11.24	11.37	10.58	9.63	9.25	9.17	9.66
MnO	0.16	0.21	0.16	0.14	0.16	0.11	0.15	0.14	0.11
MgO	48.52	48.95	48.59	48.47	49.06	49.89	50.11	49.87	50.04
CaO	0.07	0.08	0.07	0.09	0.02	0.00	0.06	0.32	0.03
Cr2O3	0.02	0.02	0.01	0.38	0.02	0.01	0.11	0.00	0.00
NiO	0.18	0.25	0.21	0.19	0.34	0.33	0.45	0.32	0.26
Na2O	0.00	0.00	0.01	0.00	0.00	0.01	0.00	0.00	0.00
K2O	0.02	0.00	0.01	0.01	0.01	0.00	0.00	0.00	0.00
Total	100.22	100.61	100.64	100.78	100.25	100.62	100.53	100.94	100.76
Mg#	0.89	0.89	0.89	0.88	0.89	0.90	0.91	0.91	0.90

Supplementary Table S1 B: Major element composition of orthopyroxenes

Sample No	*JC 21 70R-09*	*JC 21 70R-09*	*JC 21 77R-01b*	*JC 21 77R-01b*	*JC 21 77R-01b*	*JC 21 77R-01b*	*JC 21 77R-01b*	*JC 21 77R-01b*	*JC 21 77R-01b*	*JC 21 77R-01b*
SiO2	56.93	56.78	56.11	56.45	56.15	56.44	56.11	56.45	56.15	56.44
TiO2	0.11	0.08	0.00	0.02	0.01	0.01	0.00	0.02	0.01	0.01
Al2O3	0.52	0.65	2.09	2.09	2.14	2.08	2.09	2.09	2.14	2.08
FeO	6.25	6.64	5.73	6.39	5.97	6.03	5.73	6.39	5.97	6.03
MnO	0.25	0.18	0.13	0.14	0.09	0.15	0.13	0.14	0.09	0.15
MgO	35.07	35.23	34.25	34.11	34.38	34.54	34.25	34.11	34.38	34.54
CaO	0.53	0.66	1.54	1.53	1.50	1.46	1.54	1.53	1.50	1.46
Cr2O3	1.08	1.16	0.60	0.63	0.60	0.61	0.60	0.63	0.60	0.61
NiO	0.00	0.02	0.08	0.08	0.07	0.05	0.08	0.08	0.07	0.05
Na2O	0.06	0.08	0.03	0.02	0.01	0.00	0.03	0.02	0.01	0.00
K2O	0.00	0.00	0.02	0.00	0.01	0.00	0.02	0.00	0.01	0.00
Total	100.79	101.48	100.58	101.46	100.93	101.38	100.58	101.46	100.93	101.38
Mg#	0.91	0.91	0.91	0.91	0.91	0.91	0.91	0.91	0.91	0.91
Cr#	0.58	0.55	0.16	0.17	0.16	0.17	0.16	0.17	0.16	0.17

Sample No	*JC 21 77R-11*	*JC 21 77R-11*	*JC 21 77R-11*	*JC 21 77R-01a*	*JC 21 77R-01a*	*JC 21 77R-01a*	*JC 21 77R-01a*	*JC 21 77R-01a*	*JC 21 77R-01a*	*JC 21 70R-02*
SiO2	56.76	56.41	56.49	57.42	56.40	56.46	56.53	56.28	57.67	56.77
TiO2	0.00	0.01	0.03	0.04	0.01	0.03	0.01	0.04	0.00	0.00
Al2O3	2.10	2.06	2.08	0.18	2.11	2.14	2.11	2.11	0.84	2.25
FeO	6.04	6.03	6.36	8.27	5.80	6.08	6.05	6.14	6.64	5.68
MnO	0.15	0.14	0.19	0.22	0.14	0.16	0.18	0.15	0.16	0.15
MgO	33.85	33.63	34.18	34.79	34.10	33.95	34.01	34.11	35.72	34.40
CaO	1.68	1.95	1.30	0.13	1.52	1.61	1.46	1.53	0.16	1.32
Cr2O3	0.70	0.67	0.58	0.07	0.62	0.72	0.66	0.70	0.23	0.88
NiO	0.05	0.10	0.07	0.06	0.07	0.08	0.10	0.06	0.06	0.10
Na2O	0.00	0.00	0.00	0.00	0.00	0.00	0.03	0.00	0.02	0.00
K2O	0.00	0.01	0.00	0.00	0.00	0.00	0.00	0.00	0.00	0.00
Total	101.34	101.02	101.27	101.19	100.77	101.23	101.14	101.12	101.50	101.54
Mg#	0.91	0.91	0.91	0.88	0.91	0.91	0.91	0.91	0.91	0.92
Cr#	0.18	0.18	0.16	0.21	0.17	0.18	0.17	0.18	0.15	0.21

Sample No	JC 21 70R-02	JC 21 70R-02	JC 21 70R-02	JC 21 70R-02	JC 21 70R-02
SiO2	55.12	55.89	57.92	55.88	56.75
TiO2	0.00	0.02	0.00	0.01	0.04
Al2O3	2.02	2.20	0.34	2.12	1.86
FeO	6.14	5.73	5.49	6.01	5.59
MnO	0.17	0.12	0.09	0.13	0.13
MgO	33.99	34.50	36.79	34.21	35.08
CaO	0.86	1.31	0.11	1.20	1.16
Cr2O3	0.75	0.76	0.18	0.78	0.76
NiO	0.03	0.10	0.03	0.10	0.07
Na2O	0.00	0.02	0.00	0.00	0.00
K2O	0.01	0.01	0.00	0.03	0.00
Total	99.10	100.65	100.95	100.46	101.44
Mg#	0.91	0.92	0.92	0.91	0.92
Cr#	0.20	0.19	0.26	0.20	0.22

Supplementary Table S1 C: Major element composition of orthopyroxenes

Sample No	JC 21 70R-09	JC 21 70R-09	JC 21 70R-09	JC 21 70R-09	JC 21 70R-09	JC 21 70R-09	JC 21 70R-09	JC 21 70R-09	JC 21 70R-09
Comment									
SiO2	51.65	52.04	51.70	51.65	52.04	51.70	51.17	51.17	51.05
TiO2	0.32	0.27	0.33	0.32	0.27	0.33	0.32	0.27	0.33
Al2O3	3.47	3.42	3.66	3.47	3.42	3.66	3.49	3.37	3.51
FeO	3.25	3.14	3.26	3.25	3.14	3.26	3.20	3.70	3.32
MnO	0.10	0.11	0.13	0.10	0.11	0.13	0.09	0.09	0.10
MgO	16.81	16.71	16.55	16.81	16.71	16.55	16.48	18.65	16.66
CaO	23.07	23.25	23.02	23.07	23.25	23.02	22.28	19.76	22.25
Cr2O3	1.19	1.30	1.34	1.19	1.30	1.34	1.23	1.27	1.29
NiO	0.02	0.03	0.02	0.02	0.03	0.02	0.06	0.01	0.00
Na2O	0.22	0.26	0.24	0.22	0.26	0.24	0.24	0.27	0.32
K2O	0.00	0.03	0.00	0.00	0.03	0.00	0.00	0.00	0.00
Total	100.10	100.55	100.24	100.10	100.55	100.24	98.56	98.56	98.82
Mg#	0.90	0.91	0.90	0.90	0.91	0.90	0.90	0.90	0.90
Cr#	18.67	20.27	19.66	18.67	20.27	19.66	19.07	20.12	19.75

Sample No	*JC 21 70R-06*	*JC 21 70R-06*	*JC 21 70R-06*	*JC 21 70R-06*	*JC 21 77R-1a*	*JC 21 77R-1a*	*JC 21 77R-1a*	*JC 21 77R-1a*	*JC 21 77R-1a*
Comment					low Ca cpx	low Ca cpx	low Ca cpx	low Ca cpx	low Ca cpx
SiO2	53.14	52.14	53.14	52.14	53.08	52.88	56.01	54.12	50.43
TiO2	0.00	0.04	0.00	0.04	0.06	0.07	0.05	0.10	0.19
Al2O3	2.87	2.57	2.87	2.57	4.86	5.48	2.20	4.35	7.41
FeO	2.82	2.61	2.82	2.61	3.23	2.98	2.37	2.81	4.19
MnO	0.09	0.11	0.09	0.11	0.10	0.07	0.07	0.07	0.13
MgO	18.43	18.56	18.43	18.56	22.38	22.12	23.46	22.47	21.38
CaO	22.47	22.98	22.47	22.98	12.17	12.57	12.82	12.41	11.78
Cr2O3	0.95	0.98	0.95	0.98	1.44	1.33	0.73	0.82	1.04
NiO	0.05	0.01	0.05	0.01	0.09	0.09	0.07	0.09	0.05
Na2O	0.01	0.00	0.01	0.00	0.97	1.07	0.41	0.84	1.57
K2O	0.00	0.00	0.00	0.00	0.01	0.02	0.01	0.00	0.03
Total	100.83	100.00	100.83	100.00	98.40	98.67	98.19	98.10	98.21
Mg#	0.92	0.93	0.92	0.93	0.93	0.93	0.95	0.93	0.90
Cr#	18.16	20.30	18.16	20.30	16.59	13.98	18.20	11.24	8.62

Sample No	*JC 21 77R-1a*	*JC 21 77R-1a*	*JC 21 77R-1a*	*JC 21 77R-1a*
Comment	low Ca cpx	low Ca cpx	low Ca cpx	low Ca cpx
SiO2	50.11	51.35	50.97	50.23
TiO2	0.19	0.20	0.16	0.23
Al2O3	8.39	7.17	7.52	8.23
FeO	3.68	3.66	3.52	3.55
MnO	0.08	0.07	0.07	0.13
MgO	20.95	21.44	21.20	20.71
CaO	12.11	12.04	12.05	12.25
Cr2O3	1.24	1.07	0.95	1.06
NiO	0.08	0.04	0.09	0.08
Na2O	1.75	1.61	1.49	1.59
K2O	0.02	0.01	0.02	0.00
Total	98.60	98.66	98.05	98.06
Mg#	0.91	0.91	0.92	0.91
Cr#	9.01	9.09	7.84	7.94

Supplementary Table S1 D: Major element composition of spinels

Sample	*SiO_2*	*TiO_2*	*Al_2O_3*	*FeO*	*MnO*	*MgO*	*CaO*	*$Cr2O_3$*	*ZnO*	*NiO*	*V_2O_5*	*Total*	*Mg#*	*Cr#*
JC 21 77R-2a	0.00	0.03	25.02	21.00	0.22	11.31	0.00	41.93	0.25	0.13		100.08	0.53	0.53
JC 21 77R-2a	0.00	0.01	25.30	20.86	0.28	11.52	0.00	42.19	0.22	0.09		100.72	0.53	0.53
JC 21 77R-2a	0.00	0.04	26.40	20.23	0.33	12.10	0.00	40.73	0.24	0.08		100.36	0.51	0.55
JC 21 77R-2a	0.00	0.03	26.45	20.61	0.30	11.89	0.00	41.09	0.30	0.10		101.00	0.51	0.54
JC 21 77R-2a	0.00	0.02	22.19	26.22	0.40	8.63	0.00	41.66	0.22	0.10		99.61	0.56	0.42
JC 21 77R-2a	0.00	0.03	25.63	20.13	0.26	11.72	0.00	41.86	0.22	0.08		100.10	0.52	0.54
JC 21 77R-2a	0.00	0.01	25.96	20.73	0.32	11.81	0.00	41.68	0.22	0.13		101.06	0.52	0.54
JC 21 77R-2a	0.18	0.04	21.21	30.14	0.68	8.74	0.00	37.94	0.35	0.05		99.49	0.55	0.43
JC 21 77R-2a	0.00	0.02	25.60	21.31	0.29	11.61	0.00	40.72	0.15	0.10		99.99	0.52	0.54
JC 21 77R-2a	0.03	0.02	25.16	22.88	0.28	10.83	0.00	39.98	0.23	0.04		99.63	0.52	0.51
JC 21 77R-2a	0.00	0.04	24.93	22.39	0.30	10.59	0.00	41.26	0.17	0.10		99.99	0.53	0.49
JC 21 77R-2a	0.00	0.01	24.03	23.56	0.30	10.07	0.00	41.70	0.19	0.09		100.14	0.54	0.47
JC 21 77R-2b	0.01	0.02	25.69	19.19	0.26	12.43	0.00	42.19	0.21	0.06		100.26	0.52	0.57
JC 21 77R-2b	0.00	0.01	25.50	20.24	0.26	12.21	0.00	41.48	0.27	0.02		100.20	0.52	0.56
JC 21 77R-2b	0.00	0.07	25.89	20.95	0.28	11.63	0.00	41.30	0.27	0.11		100.69	0.52	0.54
JC 21 77R-2b	0.00	0.04	26.18	20.03	0.28	11.45	0.00	41.42	0.30	0.05		99.96	0.51	0.53
JC 21 77R-2b	0.01	0.01	25.94	20.97	0.28	11.88	0.00	40.12	0.21	0.07		99.75	0.51	0.55

Sample	*SiO_2*	*TiO_2*	*Al_2O_3*	*FeO*	*MnO*	*MgO*	*CaO*	*$Cr2O_3$*	*ZnO*	*NiO*	*V_2O_5*	*Total*	*Mg#*	*Cr#*
JC 21 77R-2b	0.04	0.06	25.73	20.95	0.25	11.77	0.00	39.96	0.26	0.10		99.31	0.51	0.55
JC 21 77R-2b	0.00	0.04	25.73	20.26	0.26	11.97	0.01	41.99	0.29	0.09		100.81	0.52	0.55
JC 21 77R-2b	0.00	0.06	25.71	20.42	0.29	11.93	0.00	42.12	0.18	0.04		100.94	0.52	0.54
JC 21 77R-2b	0.00	0.02	25.95	20.30	0.27	11.95	0.00	41.43	0.19	0.05		100.36	0.52	0.55
JC 21 77R-2b	0.00	0.06	26.00	20.05	0.27	12.20	0.00	41.38	0.18	0.09		100.46	0.52	0.56
JC 21 77R-2b	0.00	0.04	25.78	20.27	0.30	11.99	0.00	41.79	0.14	0.05		100.55	0.52	0.55
JC 21 77R-2b	0.01	0.05	26.36	19.90	0.30	12.41	0.00	41.12	0.27	0.11		100.76	0.51	0.57
JC 21 77R-2b	0.05	0.00	25.44	21.53	0.30	12.16	0.00	40.46	0.25	0.10		100.55	0.52	0.56
JC 21 77R-2b	0.00	0.03	26.05	20.65	0.28	12.20	0.00	41.41	0.28	0.08		101.22	0.52	0.56
JC 21 77R-2b	0.05	0.00	26.41	20.68	0.30	12.01	0.00	41.34	0.24	0.09		101.38	0.51	0.55
JC 21 77R-2b	0.00	0.03	25.98	20.95	0.28	11.99	0.00	41.16	0.22	0.07		100.86	0.52	0.55
JC 21 77R-2b	0.00	0.08	25.68	20.32	0.30	12.00	0.00	41.97	0.18	0.12		100.86	0.52	0.55
JC 21 77R-2b	0.03	0.05	25.77	20.01	0.29	11.80	0.00	41.70	0.24	0.10		100.18	0.52	0.54
JC 21 77R-2b	0.00	0.00	25.83	19.62	0.28	12.14	0.00	41.78	0.15	0.06		100.05	0.52	0.56
JC 21 77R-2b	0.03	0.05	25.94	19.93	0.31	12.33	0.00	41.50	0.20	0.06		100.56	0.52	0.56
JC 21 70R-11	0.33	0.89	21.60	23.59	0.30	11.52	0.00	38.82	0.14	0.19		97.61	0.55	0.54
JC 21 70R-11	0.00	0.92	22.83	24.24	0.32	12.07	0.01	39.28	0.23	0.16		100.34	0.54	0.55
JC 21 70R-11	0.00	0.90	23.61	22.66	0.24	13.16	0.00	39.13	0.10	0.22		100.26	0.53	0.59

Sample	*SiO_2*	*TiO_2*	*Al_2O_3*	*FeO*	*MnO*	*MgO*	*CaO*	*$Cr2O_3$*	*ZnO*	*NiO*	*V_2O_5*	*Total*	*Mg#*	*Cr#*
JC 21 70R-11	0.00	0.91	23.82	23.04	0.24	13.18	0.00	38.52	0.05	0.12		100.13	0.52	0.59
JC 21 70R-11	0.00	0.96	23.41	22.98	0.24	13.26	0.00	39.36	0.11	0.14		100.70	0.53	0.59
JC 21 70R-11	0.00	0.75	24.68	22.51	0.26	13.72	0.00	37.72	0.11	0.20		100.19	0.51	0.62
JC 21 70R-11	0.00	0.74	24.71	22.71	0.28	13.73	0.00	38.14	0.05	0.13		100.68	0.51	0.61
JC 21 70R-11	0.00	0.78	23.57	22.85	0.30	13.48	0.06	39.38	0.13	0.19		100.94	0.53	0.61
JC 21 70R-11	0.00	0.81	25.24	23.51	0.26	13.59	0.00	37.51	0.13	0.08		101.33	0.50	0.60
JC 21 70R-11	0.00	0.65	21.38	24.55	0.34	11.87	0.00	40.54	0.19	0.09		99.91	0.56	0.55
JC 21 70R-11	0.00	0.70	20.84	24.37	0.33	11.74	0.00	40.80	0.18	0.11		99.33	0.57	0.55
JC 21 70R-08	0.03	1.55	20.17	28.59	0.34	11.05	0.00	38.78	0.16	0.11		101.18	0.56	0.50
JC 21 70R-08	0.00	1.02	22.28	26.95	0.31	11.55	0.00	36.94	0.12	0.09		99.56	0.53	0.53
JC 21 70R-08	0.02	1.00	23.34	27.10	0.31	11.61	0.00	35.94	0.19	0.10		99.96	0.51	0.53
JC 21 70R-08	0.10	0.65	22.97	27.59	0.30	10.85	0.00	36.68	0.18	0.08		99.73	0.52	0.50
JC 21 70R-08	0.04	0.72	23.25	27.73	0.33	10.45	0.00	36.49	0.21	0.08		99.60	0.51	0.48
JC 21 70R-08	0.02	0.58	23.21	29.66	0.37	9.34	0.01	36.52	0.20	0.11		100.30	0.51	0.44
JC 21 70R-13	0.01	0.82	28.47	26.03	0.27	11.81	0.00	32.49	0.22	0.17		100.58	0.43	0.53
JC 21 70R-13	0.00	0.73	29.72	24.49	0.33	12.65	0.00	31.56	0.16	0.17		100.06	0.42	0.56
JC 21 70R-13	0.01	0.62	31.27	24.15	0.23	13.28	0.00	29.89	0.16	0.14		100.01	0.39	0.58
JC 21 70R-13	0.03	0.76	25.59	31.10	0.34	9.52	0.00	30.77	0.18	0.17		98.74	0.45	0.44

Sample	*SiO_2*	*TiO_2*	*Al_2O_3*	*FeO*	*MnO*	*MgO*	*CaO*	*$Cr2O_3$*	*ZnO*	*NiO*	*V_2O_5*	*Total*	*Mg#*	*Cr#*
JC 21 70R-13	0.02	0.85	27.30	27.80	0.29	10.81	0.00	31.57	0.17	0.18		99.25	0.44	0.49
JC 21 70R-13	0.00	0.65	28.36	26.82	0.28	10.33	0.00	31.03	0.25	0.12		98.09	0.42	0.48
JC 21 70R-13	0.00	0.24	36.00	23.71	0.22	14.21	0.00	25.62	0.18	0.23		100.67	0.32	0.61
JC 21 70R-13	0.00	0.24	35.18	24.25	0.25	14.04	0.00	25.12	0.17	0.27		99.78	0.32	0.61
JC 21 70R-13	0.00	0.25	36.14	23.56	0.22	14.15	0.00	25.69	0.17	0.17		100.64	0.32	0.61
JC 21 70R-13	0.39	0.35	34.15	24.87	0.26	13.94	0.00	25.82	0.18	0.15		100.34	0.34	0.61
JC 21 70R-13	0.05	0.28	34.66	25.27	0.25	12.93	0.00	24.66	0.24	0.19		98.80	0.32	0.57
JC 21 70R-13	0.54	0.29	31.38	29.89	0.45	9.81	0.00	25.07	0.39	0.02		98.11	0.35	0.46
JC 21 70R-13	0.00	0.88	25.46	27.12	0.26	11.84	0.00	33.92	0.17	0.22		100.15	0.47	0.54
JC 21 70R-13	0.00	0.90	24.85	26.80	0.35	11.74	0.00	34.27	0.13	0.18		99.50	0.48	0.53
JC 21 70R-13	0.00	0.88	23.88	27.01	0.29	11.40	0.00	34.69	0.22	0.13		98.78	0.49	0.53
JC 21 77R-08	0.01	0.11	23.94	21.88	0.32	11.27	0.00	40.92	0.12	0.03		98.93	0.53	0.53
JC 21 77R-08	0.00	0.13	24.01	22.29	0.35	10.79	0.00	41.04	0.25	0.07		99.23	0.53	0.51
JC 21 77R-08	0.00	0.08	24.53	21.93	0.31	11.85	0.00	40.62	0.10	0.09		99.81	0.53	0.55
JC 21 77R-08	0.02	0.02	24.27	22.54	0.33	10.78	0.00	40.01	0.16	0.08		98.51	0.53	0.51
JC 21 77R-08	0.00	0.07	24.48	20.78	0.27	12.42	0.00	41.71	0.17	0.07		100.29	0.53	0.57
JC 21 77R-08	0.00	0.10	24.47	20.89	0.33	12.30	0.00	41.21	0.21	0.06		99.90	0.53	0.57
JC 21 77R-07	0.04	0.01	26.17	19.51	0.28	12.79	0.00	41.31	0.24	0.08		100.70	0.51	0.58

Sample	SiO_2	TiO_2	Al_2O_3	FeO	MnO	MgO	CaO	$Cr2O_3$	ZnO	NiO	V_2O_5	Total	Mg#	Cr#
JC 21 77R-07	0.03	0.04	26.24	18.85	0.30	12.97	0.00	40.41	0.20	0.13		99.44	0.51	0.60
JC 21 77R-07	0.04	0.03	26.91	19.06	0.27	13.00	0.01	40.79	0.23	0.11		100.69	0.50	0.59
JC 21 77R-07	0.02	0.08	25.08	20.58	0.33	12.00	0.00	41.29	0.28	0.10		99.99	0.52	0.56
JC 21 77R-07	0.00	0.06	27.73	15.97	0.21	15.05	0.00	40.40	0.16	0.17		99.98	0.49	0.67
JC 21 77R-07	0.04	0.05	27.53	16.53	0.24	14.58	0.01	40.12	0.11	0.17		99.59	0.49	0.66
JC 21 77R-07	0.00	0.06	27.60	17.04	0.25	14.49	0.00	40.28	0.14	0.11		100.18	0.49	0.65
JC 21 77R-07	0.00	0.01	27.39	17.01	0.23	13.95	0.01	40.49	0.08	0.11		99.46	0.50	0.63
JC 21 77R-07	0.00	0.04	27.70	16.65	0.30	14.46	0.00	40.76	0.12	0.07		100.38	0.50	0.65
JC 21 77R-07	0.06	0.08	27.21	17.22	0.25	13.75	0.04	39.71	0.12	0.15		98.82	0.49	0.63
JC 21 77R-07	0.00	0.08	27.06	16.63	0.23	14.44	0.00	41.44	0.08	0.12		100.32	0.51	0.65
JC 21 77R-07	0.00	0.05	27.13	17.27	0.28	14.13	0.00	40.77	0.12	0.12		100.05	0.50	0.64
JC 21 77R-07	0.01	0.06	27.38	17.81	0.26	13.78	0.00	40.81	0.13	0.13		100.56	0.50	0.62
JC 21 77R-07	0.00	0.02	26.64	18.72	0.27	13.34	0.00	40.68	0.19	0.09		100.18	0.51	0.61
JC 21 77R-07	0.00	0.09	27.04	19.21	0.29	13.33	0.01	40.66	0.17	0.12		101.13	0.50	0.60
JC 21 77R-07	0.00	0.08	27.27	17.60	0.33	13.61	0.00	40.45	0.15	0.15		99.86	0.50	0.62
JC 21 77R-07	0.01	0.03	27.00	19.01	0.31	13.17	0.00	40.55	0.13	0.12		100.52	0.50	0.60
JC 21 77R-07	0.00	0.05	26.45	20.73	0.29	12.01	0.00	39.73	0.23	0.04		99.81	0.50	0.55
JC 21 77R-07	0.04	0.01	26.40	23.53	0.39	10.18	0.00	38.28	0.32	0.07		99.42	0.49	0.48

Sample	*SiO_2*	*TiO_2*	*Al_2O_3*	*FeO*	*MnO*	*MgO*	*CaO*	*$Cr2O_3$*	*ZnO*	*NiO*	*V_2O_5*	*Total*	*Mg#*	*Cr#*
JC 21 77R-07	0.00	0.03	27.34	19.53	0.32	12.76	0.00	39.49	0.23	0.08		100.01	0.49	0.58
JC 21 77R-07	0.00	0.08	26.67	19.97	0.27	12.08	0.00	40.62	0.18	0.05		100.16	0.51	0.55
JC 21 77R-04	0.01	0.06	25.48	18.35	0.23	13.61	0.00	41.77	0.17	0.12		100.09	0.52	0.62
JC 21 77R-04	0.03	0.03	25.68	18.47	0.28	13.29	0.00	42.43	0.05	0.12		100.59	0.53	0.60
JC 21 77R-04	0.02	0.06	25.87	18.71	0.31	13.80	0.00	42.26	0.11	0.10		101.54	0.52	0.62
JC 21 77R-04	0.11	0.04	24.90	19.45	0.23	12.46	0.00	42.07	0.14	0.08		99.73	0.53	0.58
JC 21 77R-04	0.05	0.06	24.11	18.89	0.30	12.29	0.00	42.32	0.17	0.06		98.49	0.54	0.58
JC 21 77R-04	0.02	0.03	25.43	18.16	0.25	13.63	0.00	42.09	0.11	0.06		100.01	0.53	0.62
JC 21 77R-04	0.36	0.05	24.77	21.46	0.27	10.87	0.00	38.74	0.27	0.03		97.02	0.51	0.52
JC 21 77R-04	0.01	0.04	25.87	18.24	0.26	13.92	0.00	41.96	0.17	0.10		100.83	0.52	0.63
JC 21 77R-04	0.01	0.01	26.16	17.79	0.23	14.15	0.00	42.36	0.12	0.09		101.14	0.52	0.63
JC 21 77R-04	0.08	0.04	25.07	21.43	0.32	11.17	0.00	40.43	0.32	0.08		99.17	0.52	0.53
JC 21 77R-04	0.03	0.05	25.94	20.71	0.32	11.48	0.00	40.73	0.21	0.09		99.80	0.51	0.53
JC 21 77R-04	0.01	0.05	24.94	20.93	0.35	11.31	0.00	41.72	0.24	0.03		99.85	0.53	0.53
JC 21 77R-04	0.06	0.04	24.30	22.72	0.31	10.63	0.00	41.20	0.37	0.09		99.99	0.53	0.50
JC 21 77R-04	0.06	0.00	24.68	23.09	0.34	10.12	0.00	41.04	0.40	0.05		100.00	0.53	0.48
JC 21 77R-04	0.02	0.00	24.63	19.53	0.29	12.05	0.00	42.21	0.27	0.01		99.21	0.53	0.56
JC 21 77R-04	0.15	0.02	25.04	20.37	0.26	12.26	0.00	41.73	0.28	0.04		100.39	0.53	0.56

Sample	*SiO_2*	*TiO_2*	*Al_2O_3*	*FeO*	*MnO*	*MgO*	*CaO*	*$Cr2O_3$*	*ZnO*	*NiO*	*V_2O_5*	*Total*	*Mg#*	*Cr#*
JC 21 70R-09	0.00	1.02	22.16	18.90	0.32	10.86	0.02	37.68	0.12	0.08	0.18	98.35	0.51	0.53
JC 21 70R-09	0.00	1.00	22.14	18.80	0.36	10.96	0.00	38.25	0.15	0.12	0.14	98.80	0.51	0.54
JC 21 70R-09	0.00	0.93	22.34	18.10	0.25	11.39	0.01	38.68	0.25	0.07	0.21	98.72	0.53	0.54
JC 21 70R-09	0.00	0.99	22.25	18.00	0.35	11.52	0.00	38.62	0.12	0.04	0.19	98.56	0.53	0.54
JC 21 70R-09	0.00	0.95	22.03	18.70	0.31	11.02	0.00	38.07	0.20	0.16	0.21	99.08	0.51	0.54
JC 21 70R-09	0.00	0.99	21.85	18.60	0.32	11.11	0.01	38.53	0.10	0.11	0.19	98.62	0.52	0.54
JC 21 70R-09	0.00	1.01	21.43	18.80	0.27	10.94	0.01	39.44	0.21	0.09	0.18	98.76	0.51	0.55
JC 21 70R-09	0.00	1.14	21.09	19.70	0.31	10.30	0.00	38.88	0.07	0.12	0.23	98.30	0.48	0.55
JC 21 70R-09	0.00	1.12	21.20	22.50	0.43	8.39	0.01	37.49	0.26	0.07	0.20	98.64	0.40	0.54
JC 21 70R-09	0.00	1.02	21.30	19.00	0.29	10.74	0.00	38.67	0.17	0.06	0.19	98.37	0.50	0.55
JC 21 70R-09	0.00	1.20	21.22	18.90	0.33	10.75	0.02	38.33	0.16	0.07	0.16	97.97	0.50	0.55
JC 21 70R-06	0.03	0.05	27.08	14.80	0.17	13.69	0.01	41.73	0.12	0.10	0.06	99.05	0.62	0.51
JC 21 70R-06	0.00	0.05	26.97	14.60	0.26	13.70	0.02	41.72	0.19	0.21	0.03	99.43	0.63	0.51
JC 21 70R-06	0.00	0.06	26.72	17.00	0.24	12.14	0.01	41.36	0.12	0.15	0.04	99.07	0.56	0.51
JC 21 70R-06	0.01	0.09	26.95	16.60	0.27	12.59	0.00	41.42	0.06	0.07	0.07	99.48	0.57	0.51
JC 21 77R-1b	0.00	0.09	24.35	19.00	0.29	10.57	0.01	42.79	0.23	0.09	0.08	99.27	0.50	0.54
JC 21 77R-1b	0.00	0.08	24.21	18.70	0.25	10.80	0.01	42.79	0.13	0.12	0.08	99.08	0.51	0.54
JC 21 77R-1b	0.00	0.06	24.68	19.30	0.30	10.42	0.00	41.93	0.11	0.10	0.07	98.97	0.49	0.53

Sample	*SiO_2*	*TiO_2*	*Al_2O_3*	*FeO*	*MnO*	*MgO*	*CaO*	*$Cr2O_3$*	*ZnO*	*NiO*	*V_2O_5*	*Total*	*Mg#*	*Cr#*
JC 21 77R-1b	0.00	0.04	24.84	19.50	0.26	10.22	0.00	41.62	0.18	0.14	0.12	99.03	0.48	0.53
JC 21 77R-1b	0.00	0.00	24.12	19.20	0.25	10.34	0.02	42.71	0.20	0.05	0.11	98.72	0.49	0.54
JC 21 77R-1b	0.00	0.05	24.15	18.90	0.30	10.40	0.00	42.44	0.11	0.14	0.10	98.25	0.50	0.54
JC 21 77R-1b	0.00	0.09	24.54	19.20	0.35	10.32	0.01	42.29	0.25	0.10	0.12	98.85	0.49	0.54
JC 21 77R-1b	0.03	0.08	23.88	20.20	0.32	9.45	0.01	40.62	0.25	0.01	0.14	97.53	0.45	0.53
JC 21 77R-1b	0.53	0.06	24.06	19.80	0.27	10.29	0.17	42.09	0.16	0.07	0.10	98.63	0.48	0.54
JC 21 77R-1b	0.00	0.06	24.28	19.30	0.32	10.18	0.01	42.40	0.15	0.14	0.06	98.32	0.48	0.54
JC 21 77R-1b	0.00	0.04	24.45	19.80	0.26	9.98	0.01	41.94	0.09	0.04	0.10	98.23	0.47	0.54
JC 21 77R-1b	0.01	0.07	24.25	19.80	0.32	9.93	0.02	42.01	0.04	0.05	0.13	98.35	0.47	0.54
JC 21 70R-19	0.07	0.32	37.87	10.80	0.16	17.37	0.01	28.74	0.14	0.22	0.13	98.29	0.74	0.34
JC 21 70R-19	0.06	0.28	38.39	10.90	0.17	17.52	0.00	28.67	0.00	0.15	0.13	98.58	0.74	0.33
JC 21 70R-19	0.07	0.27	41.90	11.00	0.16	18.19	0.00	25.71	0.16	0.28	0.09	100.95	0.75	0.29
JC 21 70R-19	0.00	0.29	36.37	11.20	0.19	17.02	0.00	31.08	0.00	0.17	0.11	98.33	0.73	0.36
JC 21 70R-19	0.04	0.26	38.44	11.10	0.18	17.56	0.00	29.79	0.08	0.21	0.12	100.00	0.74	0.34
JC 21 70R-19	0.06	0.28	40.22	12.20	0.21	17.04	0.01	26.49	0.00	0.22	0.12	99.66	0.71	0.31
JC 21 70R-19	0.03	0.24	36.69	10.70	0.18	17.41	0.03	30.70	0.07	0.18	0.11	99.02	0.74	0.36
JC 21 70R-19	0.06	18.83	2.35	45.50	1.31	0.58	0.01	0.07	0.00	0.04	0.65	93.37	0.02	0.02
JC 21 70R-19	0.05	0.30	31.59	13.70	0.21	14.84	0.00	35.20	0.11	0.19	0.10	98.25	0.66	0.43

Sample	*SiO_2*	*TiO_2*	*Al_2O_3*	*FeO*	*MnO*	*MgO*	*CaO*	*$Cr2O_3$*	*ZnO*	*NiO*	*V_2O_5*	*Total*	*Mg#*	*Cr#*
JC 21 70R-19	0.02	0.34	32.07	13.40	0.24	15.43	0.02	35.85	0.01	0.18	0.12	99.75	0.67	0.43
JC 21 70R-19	0.03	0.35	31.62	12.90	0.21	15.46	0.00	35.95	0.15	0.23	0.16	98.96	0.68	0.43
JC 21 70R-19	0.08	0.36	36.41	14.00	0.22	14.86	0.03	27.72	0.16	0.24	0.15	97.30	0.65	0.34
JC 21 70R-19	0.00	0.67	33.02	15.00	0.22	14.70	0.01	30.27	0.21	0.17	0.23	100.48	0.64	0.38
JC 21 70R-19	0.04	0.34	39.66	11.90	0.16	17.04	0.00	27.69	0.08	0.27	0.14	99.20	0.72	0.32
JC 21 70R-19	0.02	0.30	40.58	12.00	0.18	17.26	0.00	27.33	0.00	0.31	0.14	100.37	0.72	0.31
JC 21 70R-19	6.04	1.37	18.37	26.45	0.29	6.34	2.68	22.01	0.11	0.00	0.20	86.33	0.30	0.45
JC 21 70R-19	0.04	3.48	10.73	27.45	0.35	5.45	0.06	33.35	0.09	0.00	0.49	97.16	0.26	0.68
JC 21 70R-19	0.03	0.28	42.51	10.90	0.21	17.99	0.00	24.56	0.00	0.27	0.13	99.36	0.75	0.28
JC 21 70R-19	0.05	0.31	42.22	10.40	0.18	18.47	0.00	25.38	0.01	0.22	0.14	99.78	0.76	0.29
JC 21 70R-19	1.19	0.70	31.79	17.00	0.27	14.36	0.13	30.42	0.01	0.11	0.18	100.56	0.60	0.39
JC 21 77R-1a	0.00	0.10	24.49	19.20	0.27	10.45	0.00	42.28	0.03	0.12	0.27	98.54	0.49	0.54
JC 21 77R-1a	0.00	0.04	24.67	19.30	0.27	10.29	0.00	42.05	0.08	0.06	0.24	98.15	0.49	0.53
JC 21 77R-1a	0.00	0.11	24.73	19.30	0.27	10.36	0.00	41.64	0.21	0.10	0.24	98.79	0.49	0.53
JC 21 77R-1a	0.00	0.06	24.67	19.20	0.34	10.30	0.02	41.65	0.14	0.07	0.22	98.27	0.49	0.53
JC 21 77R-1a	0.00	0.06	25.03	19.10	0.27	10.41	0.00	41.38	0.11	0.10	0.27	98.12	0.49	0.53
JC 21 77R-1a	0.00	0.05	25.12	19.40	0.27	10.33	0.00	41.54	0.09	0.04	0.20	98.42	0.49	0.53
JC 21 77R-1a	0.01	0.04	24.48	19.50	0.30	10.08	0.00	41.16	0.23	0.12	0.30	98.66	0.48	0.53

Sample	*SiO_2*	*TiO_2*	*Al_2O_3*	*FeO*	*MnO*	*MgO*	*CaO*	*$Cr2O_3$*	*ZnO*	*NiO*	*V_2O_5*	*Total*	*Mg#*	*Cr#*
JC 21 77R-1a	0.00	0.03	20.48	20.70	0.35	8.71	0.01	42.54	0.32	0.05	0.17	97.88	0.43	0.58
JC 21 77R-1a	0.00	0.06	24.45	19.60	0.27	10.06	0.01	41.09	0.17	0.00	0.26	98.30	0.48	0.53
JC 21 77R-1a	0.00	0.07	24.52	19.70	0.27	10.11	0.00	41.39	0.21	0.09	0.20	99.03	0.48	0.53
JC 21 77R-1a	0.00	0.05	25.09	19.10	0.28	10.38	0.02	41.10	0.25	0.06	0.20	98.46	0.49	0.52
JC 21 77R-1a	0.00	0.04	25.12	19.20	0.27	10.57	0.00	41.59	0.24	0.08	0.24	99.63	0.50	0.53
JC 21 77R-1a	0.00	0.04	24.99	19.60	0.28	10.31	0.00	41.71	0.24	0.07	0.29	99.43	0.48	0.53
JC 21 77R-1a	0.00	0.05	24.67	19.20	0.35	10.31	0.02	41.39	0.29	0.00	0.24	98.81	0.49	0.53
JC 21 77R-1a	0.00	0.07	24.46	19.70	0.33	10.00	0.00	40.84	0.29	0.07	0.19	98.90	0.47	0.53
JC 21 77R-1a	0.00	0.05	24.68	18.30	0.30	11.10	0.02	42.22	0.18	0.04	0.27	99.23	0.52	0.53
JC 21 77R-1a	0.00	0.07	25.08	19.10	0.26	10.65	0.00	41.99	0.09	0.05	0.22	99.00	0.50	0.53
JC 21 77R-1a	0.00	0.07	24.87	18.80	0.28	10.67	0.00	41.53	0.17	0.11	0.19	98.76	0.50	0.53
JC 21 77R-1a	0.00	0.11	24.85	19.30	0.26	10.60	0.00	42.08	0.12	0.00	0.23	99.14	0.49	0.53
JC 21 77R-02	0.00	0.04	25.93	18.30	0.27	11.09	0.01	41.45	0.18	0.13	0.23	98.96	0.52	0.52
JC 21 77R-02	0.01	0.07	25.85	18.40	0.30	11.15	0.00	41.90	0.13	0.07	0.25	99.12	0.52	0.52
JC 21 77R-02	0.00	0.00	25.44	19.40	0.22	10.35	0.00	40.84	0.13	0.00	0.19	98.30	0.49	0.52
JC 21 77R-02	0.00	0.05	25.90	19.10	0.30	10.51	0.03	40.46	0.26	0.00	0.30	98.44	0.50	0.51
JC 21 77R-02	0.00	0.05	25.21	19.00	0.31	10.64	0.00	42.01	0.24	0.09	0.21	99.23	0.50	0.53
JC 21 77R-02	0.00	0.02	25.17	19.00	0.31	10.55	0.00	41.74	0.16	0.10	0.27	98.69	0.50	0.53

Sample	*SiO_2*	*TiO_2*	*Al_2O_3*	*FeO*	*MnO*	*MgO*	*CaO*	*$Cr2O_3$*	*ZnO*	*NiO*	*V_2O_5*	*Total*	*Mg#*	*Cr#*
JC 21 77R-02	0.01	0.06	25.15	19.00	0.30	10.64	0.00	41.74	0.02	0.10	0.27	98.60	0.50	0.53
JC 21 77R-02	0.00	0.04	25.42	19.30	0.29	10.62	0.00	42.54	0.24	0.07	0.21	100.05	0.50	0.53
JC 21 77R-02	0.03	0.08	24.98	19.30	0.30	10.51	0.00	41.81	0.38	0.06	0.23	99.73	0.49	0.53
JC 21 70R-04	0.00	0.04	25.17	15.50	0.26	12.92	0.01	42.24	0.06	0.03	0.24	98.36	0.60	0.53
JC 21 70R-04	0.00	0.04	24.84	14.80	0.28	13.26	0.00	42.50	0.23	0.07	0.25	98.76	0.61	0.53
JC 21 70R-04	0.89	0.03	23.95	17.10	0.54	12.33	0.01	39.59	0.12	0.08	0.25	98.77	0.56	0.53
JC 21 70R-04	0.00	0.04	25.46	15.20	0.27	13.24	0.00	42.61	0.17	0.09	0.22	99.37	0.61	0.53
JC 21 70R-04	0.00	0.07	25.67	15.10	0.23	13.33	0.02	42.53	0.17	0.12	0.27	99.55	0.61	0.53
JC 21 70R-19	0.03	0.31	30.62	12.60	0.15	15.59	0.00	36.35	0.02	0.23	0.14	98.74	0.69	0.44
JC 21 70R-19	0.04	0.67	27.70	14.90	0.25	13.75	0.00	33.68	0.03	0.10	0.20	97.36	0.62	0.45
JC 21 70R-19	0.05	0.31	31.41	13.10	0.19	15.20	0.01	34.88	0.13	0.17	0.11	98.38	0.67	0.43
JC 21 70R-19	0.05	0.27	30.98	13.10	0.17	15.20	0.00	35.61	0.10	0.18	0.19	98.45	0.67	0.44
JC 21 70R-19	0.06	0.33	30.23	12.50	0.20	15.59	0.00	36.42	0.00	0.22	0.12	98.40	0.69	0.45
JC 21 70R-19	0.06	0.33	31.32	12.50	0.25	15.81	0.00	36.00	0.07	0.22	0.10	99.42	0.69	0.44
JC 21 70R-19	0.05	0.28	33.08	13.00	0.21	15.68	0.00	33.40	0.00	0.21	0.18	99.15	0.68	0.40
JC 21 70R-19	0.03	0.29	41.26	12.80	0.17	16.84	0.00	24.67	0.11	0.22	0.06	100.15	0.70	0.29

Supplementary Table S1 E: Major element composition of spinel from the hybrid sample measured by EPMA

Zone	*SiO_2*	*CaO*	*ZnO*	*FeO*	*TiO_2*	*NiO*	*Al_2O_3*	*MgO*	*Cr_2O_3*	*MnO*	*V_2O_3*	*Total*	*Cr#*
1,2	0.07	0.01	0.14	10.8	0.318	0.22	37.87	17.37	28.74	0.16	0.13	98.29	0.34
1,2	0.06	0.00	0.00	10.9	0.284	0.15	38.39	17.52	28.67	0.17	0.13	98.56	0.34
1,2	0.07	0.00	0.16	11.0	0.274	0.28	41.9	18.19	25.71	0.16	0.09	100.94	0.29
1,2	0.00	0.00	0.00	11.2	0.290	0.17	36.37	17.02	31.08	0.19	0.11	98.33	0.36
1,2	0.04	0.00	0.08	11.1	0.256	0.21	38.44	17.56	29.79	0.18	0.12	100.00	0.34
1,2	0.06	0.01	0.00	12.2	0.280	0.22	40.22	17.04	26.49	0.21	0.16	99.66	0.31
1,2	0.03	0.03	0.07	10.7	0.242	0.18	36.69	17.41	30.7	0.18	0.11	99.02	0.36
1,2	0.05	0.00	0.11	13.7	0.299	0.19	31.59	14.84	35.2	0.21	0.10	98.25	0.43
1,2	0.02	0.02	0.01	13.4	0.338	0.18	32.07	15.43	35.85	0.24	0.12	99.75	0.43
1,2	0.03	0.00	0.15	12.9	0.353	0.23	31.62	15.46	35.95	0.21	0.16	98.96	0.43
1,2	0.08	0.03	0.16	14.0	0.364	0.24	36.41	14.86	27.72	0.22	0.15	97.30	0.34
3A	0.00	0.01	0.21	15.0	0.668	0.17	33.02	14.7	30.27	0.22	0.22	100.48	0.38
1,2	0.04	0.00	0.08	11.9	0.335	0.27	39.66	17.04	27.69	0.16	0.14	99.20	0.32
1,2	0.02	0.00	0.00	12.0	0.300	0.31	40.58	17.26	27.33	0.18	0.14	100.37	0.31
3B	0.04	0.06	0.09	27.5	3.480	-	10.73	5.45	33.35	0.35	0.48	97.16	0.66
1,2	0.03	0.00	0.00	10.9	0.280	0.27	42.51	17.99	24.56	0.21	0.13	99.36	0.28
1,2	0.05	0.00	0.01	10.4	0.314	0.22	42.22	18.47	25.38	0.18	0.14	99.78	0.29
3A	1.19	0.13	0.01	17.0	0.702	0.11	31.79	14.36	30.42	0.27	0.18	100.56	0.39
3A	0.07	0.02	0.16	13.2	0.632	0.13	33.31	15.64	29.55	0.21	0.19	98.80	0.37
1,2	0.03	0.00	0.02	12.6	0.306	0.23	30.62	15.59	36.35	0.15	0.14	98.74	0.44
3A	0.04	0.00	0.03	14.9	0.670	0.10	27.7	13.75	33.68	0.25	0.20	97.36	0.45
1,2	0.05	0.01	0.13	13.1	0.311	0.17	31.41	15.2	34.88	0.19	0.18	98.38	0.43

Zone	*SiO_2*	*CaO*	*ZnO*	*FeO*	*TiO_2*	*NiO*	*Al_2O_3*	*MgO*	*Cr_2O_3*	*MnO*	*V_2O_3*	*Total*	*Cr#*
1,2	0.05	0.00	0.10	13.1	0.265	0.18	30.98	15.2	35.61	0.17	0.19	98.45	0.43
1,2	0.06	0.00	0.00	12.5	0.328	0.22	30.23	15.59	36.42	0.20	0.12	98.40	0.45
1,2	0.06	0.00	0.07	12.5	0.326	0.22	31.32	15.81	36	0.25	0.10	99.42	0.44
1,2	0.05	0.00	0.00	13.0	0.279	0.21	33.08	15.68	33.4	0.21	0.18	99.15	0.40
1,2	0.03	0.00	0.11	12.8	0.287	0.22	41.26	16.84	24.67	0.17	0.06	100.15	0.29

Supplementary Table S1 F: Major element composition (mole%) of phases in the symplectite region marked in Supplementary Figure 3B measured by EDS

	Mineral	*SiO_2*	*Al_2O_3*	*FeO^T*	*MgO*	*CaO*	*Na_2O*	*Cr_2O_3*	*TiO_2*	*Total*
1	Spinel 1		27.53	22.36	33.29			16.82		100
2	Spinel 2		8.62	43.17	17.82			23.02	7.36	100
3	Plagioclase 3	58.45	21.89			15.60	4.06			100
4	Plagioclase 4	58.42	21.08			16.73	3.78			100
5	Plagioclase 5	55.39	21.56			20.33	2.73			

FeO^T = Total Fe as FeO

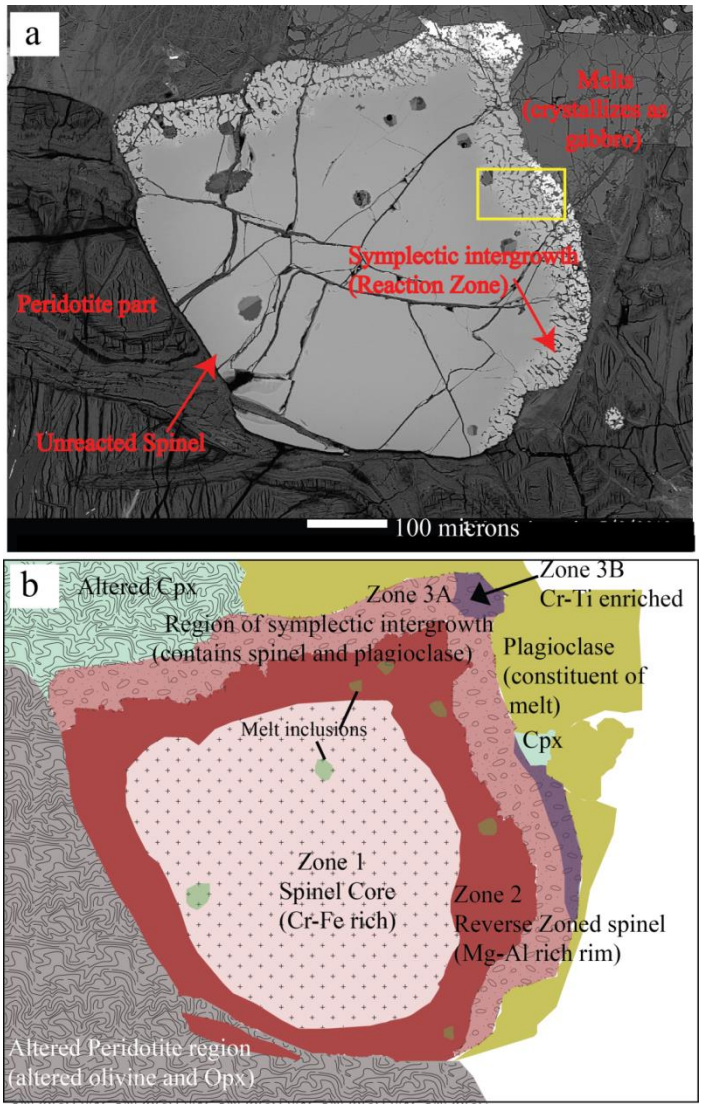

Supplementary Figure S1 A: BSE image of spinel from the hybrid sample JC 21 70R-19 showing the symplectic zone between spinel and plagioclase at the contact of the spinel with the gabbroic zone. The region towards the left which constitutes the peridotite fraction does not exhibit symplectic textures. B. Based on the heterogeneity in the spinels it is divided into different zones.

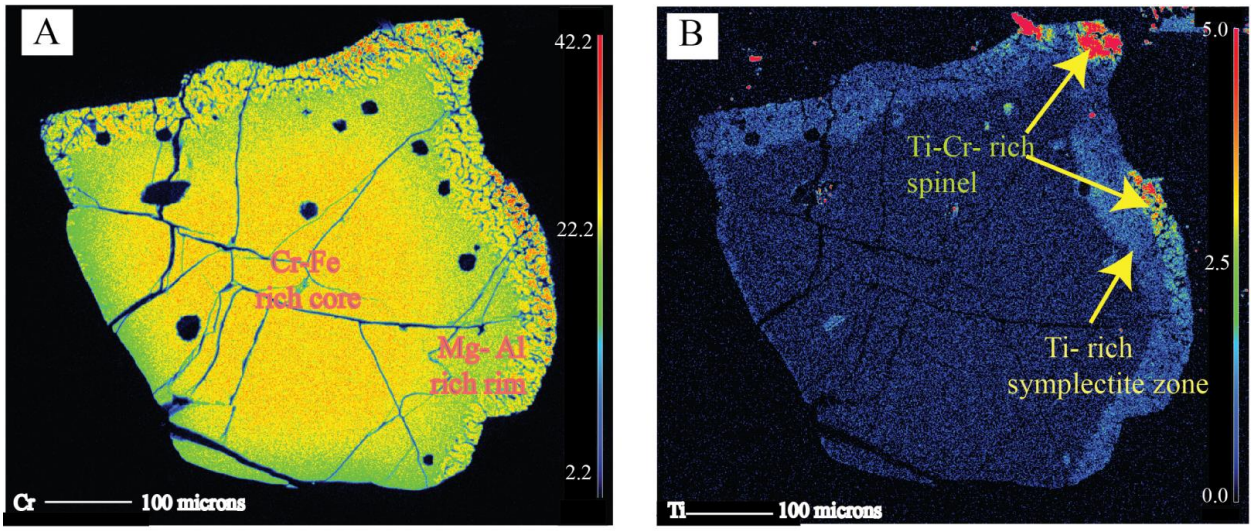

Supplementary Figure S1 B: X-Ray elemental maps of Cr and Ti respectively. The symplectite zone is enriched in Cr and Ti

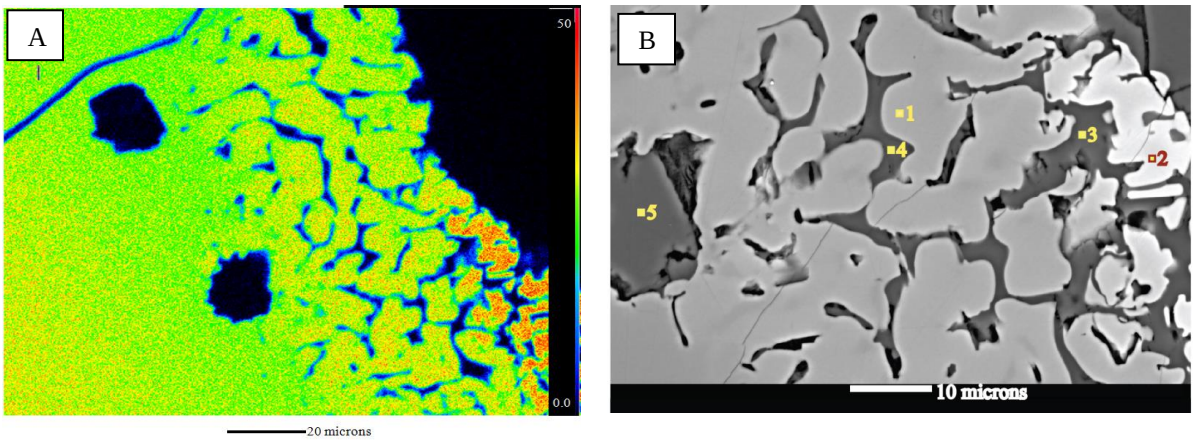

Supplementary Figure S1 C: Compositional range of phases in zone 3 marked by the yellow box in Figure 1. A. Variation in Cr_2O_3 content in the symplectite region. Remarkable compositional contrast is seen in zones 3A and 3B of the symplectite region. B. Composition of the minerals in the symplectite region analyzed by EDS (Energy dispersive spectrometers). The constituent minerals are spinel and plagioclase. There is difference in the composition of spinels and plagioclase in the different points marked in the figure. (Supplementary table S1F).

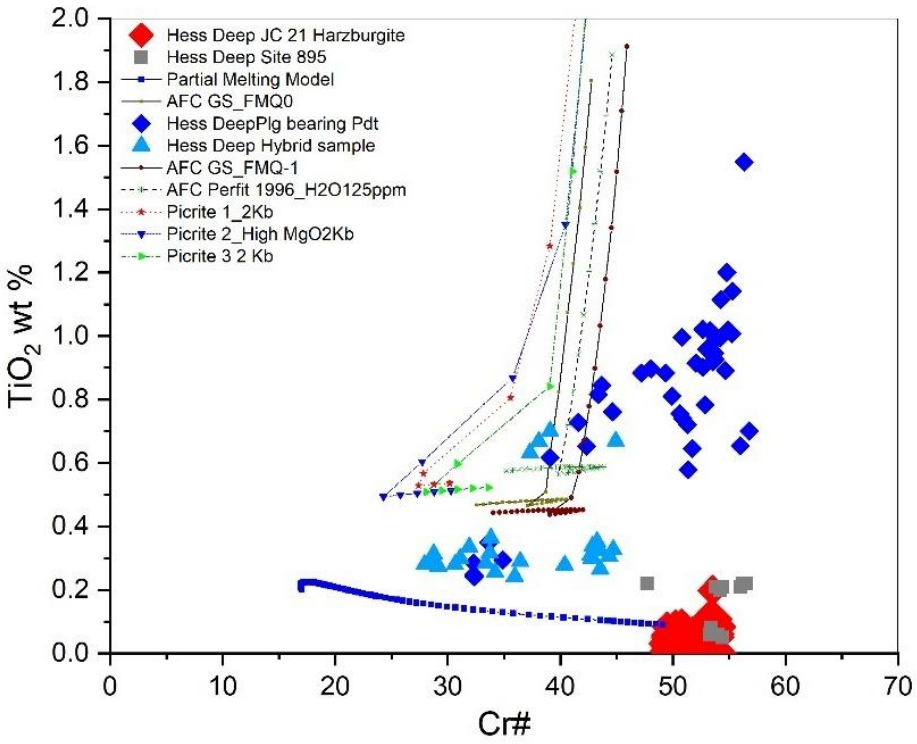

Supplementary Figure S1 D: Spinel Cr# vs TiO_2 weight% from residual peridotites, plagioclase-bearing peridotites and the hybrid sample JC 20 70R-19. Spinels from the hybrid sample has higher TiO_2 wt% than the residual peridotites in Hess Deep and coincides with the compositional trend of Hess Deep plagioclase-bearing peridotites.

Chapter 2: Melting and evolution of amphibole-rich back-arc abyssal peridotites at the Mado Megamullion, Shikoku Basin

Under review in *Geochemistry, Geophysics, Geosystems* as:
Sen, A., Snow, J. E., Ohara, Y., Hirauchi, K., Kouketsu, Y., Sanfilippo, A., Basch, V., Harigane, Y., Fujii, M., Okino, K., Akizawa, N. (2021). Melting and evolution of amphibole-rich back-arc abyssal peridotites at the Mado Megamullion, Shikoku Basin.

2.1. Introduction

The Mado Megamullion is an oceanic core complex (OCC) in the Shikoku back-arc basin within the Philippine Sea Plate. 27 mantle peridotite (serpentinized) samples were recovered by the KH-07-02, KH-18-02 and YK18-07 cruises. These peridotites exhibit signatures of extensive deformation. Amorphous pseudomorphs after plagioclase in many of the samples as well as plagioclase-spinel intergrowths are clear evidence of stagnation and melt-rock (mantle) reaction. Spinels show a wide range of compositions in terms of their Cr#, Mg# and TiO_2 content. The presence of apparently magmatic high-temperature pargasitic amphibole in veins and as replacement of clinopyroxene suggests that it may be a primary or near-primary mineral crystallized from a hydrous melt, unusual for abyssal peridotites. Two trace-element populations of clinopyroxenes are in equilibrium with depleted and enriched basaltic melts, respectively. Rare earth element (REE) in the most depleted clinopyroxenes are modelled by 10% fractional melting except for a ubiquitous La-Ce “kick”. Multiple models of open system melting combined with mixing of an enriched melt are sufficient to explain the REE data. Broadly it appears that the peridotites underwent variable degrees of partial melting with moderate influx of enriched melts, which agrees with the other textural and chemical evidence of melt-rock reaction and re-

fertilization. The compositions of the accumulated melts from the open system models reproduce the enrichments in fluid mobile elements (Ba, U, Pb) observed in basalts dredged from the Shikoku basin. Back-arc basin peridotites at Mado Megamullion appear to have a unique petrographic and geochemical character that is distinct from those of peridotites from mid-ocean ridges.

Oceanic core complexes (OCCs) are characterized by the presence of domal bathymetric highs with axis-normal striations (Cann et al., 1997; Escartín and Canales, 2011; Tucholke et al., 1998). These structures were first identified in the Mid-Atlantic Ridge at the 30°N Atlantis Fracture Zone (Blackman et al., 1998; Cann et al., 1997; Karson 1990; Tucholke et al., 1998). They are interpreted to be formed by the exhumation of the lithosphere along low-angle detachment faults at slow spreading rates ranging between 14 to 75 mm/year (Blackman et al., 2009). Gabbros and peridotites from the young lithosphere are exposed at the seafloor (Tucholke et al., 2008). These provide useful insights to understand the processes of crustal accretion, the architecture of the oceanic lithosphere and the mantle dynamics that connects magmatism to tectonics at mid-oceanic ridges (Escartín et al., 2003; Macleod et al., 2002). Peridotites exposed along detachment faults (Dick et al., 2010; Escartín et al., 2003; Warren and Shimizu, 2010) are characterized by the presence of deformation fabrics and alteration features (Harigane et al., 2011; Loocke et al., 2013; Macleod et al., 2002; Ohara, 2016). The detachment faulting is therefore thought to have initiated in the lower crust (melt-rich zone) and ceased during or prior to its exhumation (Blackman et al., 2005; Ildefonse et al., 2006). Prior studies on OCCs have mostly been conducted along slow-spreading Mid-Atlantic Ridge (Dick et al., 2008; Escartín et al., 2008; Blackman et al., 2006; Macleod et al., 2009; Parnell-Turner et al., 2018; Kelemen et al., 2004; Sdrolias et al., 2004; Smith

et al., 2008) and ultraslow-spreading Southwest Indian Ridge (Dick et al., 2002, 2019; Baines et al., 2003; Sauter et al., 2013). Other than mid-oceanic ridge settings, the Godzilla Megamullion (Ohara et al., 2001) in the Parece Vela Basin in the Philippine Sea remains the only OCC that has been extensively studied in a back-arc spreading environment until present (Harigane et al., 2008, 2011; Loocke et al., 2013; Michibayashi et al., 2014; Ohara et al., 2003, 2007; Okino et al., 1999; Spencer and Ohara, 2014; Sanfilippo et al., 2013; Tani et al., 2011). The study of OCCs in back-arc spreading environments helps understand mantle architecture, magmatic and tectonic evolution of global OCCs, and the evolutionary dynamics and processes that operate in back-arc environments.

In this study, we present data from mantle peridotites that were sampled from the Mado Megamullion, a recently discovered OCC in the back-arc spreading environment of the Shikoku Basin in the Philippine Sea (Ohara et al., 2018; Okino et al., 2019; Basch et al., 2020; Hirauchi et al., submitted; Akizawa et al., in prep.). This study focuses on the petrography and geochemical evolution of the peridotites in terms of the degree of partial melting, melt-rock reaction, and the role of water during its exhumation.

2.2. Geological Setting

The Philippine Sea Plate is a large and complex tectonic plate made of active and extinct back-arc basins, and arcs and remnant arcs in the Western Pacific region. The Parece Vela Basin, Shikoku Basin and West Philippine Basin are extinct back-arc basins whereas the Mariana Trough is an active back-arc (Kasuga and Ohara, 1997; Karig, 1975; Okino et al., 1999). The Parece Vela and Shikoku back-arc basins are inter-connected at ~25° N (Okino et al., 1999). They are located

between the Kyushu-Palau Ridge to the west and West Mariana Ridge and the Izu-Bonin Arc to the east (Okino et al., 1999) (Figure 2-1**A**). The two basins have a common evolutionary history. Magnetic anomaly data have revealed that both basins opened as a single back-arc system. Subsequently, after 19 Ma, there was a shift in the spreading direction and the extinct axes of the two basins show a different spreading orientation (Okino et al., 1999). The Shikoku Basin formed in two stages initiated by the subduction of the western margin of the Pacific Plate. In contrast to the Parece Vela Basin, spreading in the Shikoku Basin started at the northern end and propagated southward. The spreading direction changed from ENE-WSW to NE-SW. The axial zone is dominated by post-spreading volcanism known as the Kinan Seamount Chain in the Shikoku Basin while the Parece Vela Basin has a set of low-lying depressions also known as the Parece Vela Rift (Ohara et al., 2001; Okino et al., 1999).

The Godzilla Megamullion in the Parece Vela Basin (Harigane et al., 2008, 2011; Loocke et al., 2013; Michibayashi et al., 2014; Ohara et al., 2001; 2003, Ohara, 2016; Okino et al., 1999; Spencer and Ohara, 2014; Sanfilippo et al., 2013; Tani et al., 2011) has a corrugated morphology, which is typical of OCCs found along other slow-spreading ridges (Cannat et al., 1995; Dick et al., 2003; Blackman et al., 1998; Cann et al., 1997; Tucholke et al., 1998), and is the largest known OCC on Earth (Ohara, 2016). It is divided into proximal, medial, and distal regions and its development has been interpreted to be formed by melt-rock interaction resulting in detachment fault nucleation and weakening that may have exhumed large volumes of mantle rocks (Loocke et al., 2013). To date, it is the only well-studied OCC in a back-arc environment.

The Mado Megamullion was first sampled by the KH7-2 cruise in 2007 and further investigated by recent cruises (KH18-02, YK18-07 and YK19-04S; Basch et al., 2020; Ohara et al., 2019; Sen et al., 2020). Multibeam bathymetry and gravity studies revealed the presence of axis-parallel corrugations and high mantle Bouguer gravity anomaly (~20 mGal higher than the surroundings) in the Mado Megamullion and the Non-Transform Offset (NTO) massif (Ohara et al., 2018; Ohara et al., 2019; Okino et al., 2019) (Figure 2-1B). These geophysical observations are coupled with the presence of gabbros and peridotites sampled from the Mado Megamullion by dredges and Shinkai 6500 submersible dives (Basch et al., 2020; Ohara et al., 2019; Sen et al., 2020) (Figure 2-1B). The total area of the Mado Megamullion is ~550 km^2, which is much smaller in size than the Godzilla Megamullion (~7200 km^2) but is comparable to other OCCs such as the Kane Megamullion in the Mid-Atlantic Ridge (Karson and Dick 1983; Dick et al., 2008).

The cruise KH07-02 in 2007 recovered small amounts of serpentinized peridotite. This was followed by the KH18-02 dredging cruise and Shinkai 6500 diving expeditions YK18-07 in 2018 and YK19-04S in 2019 that extensively mapped and collected samples from the area. These cruises recovered a wide range of samples that include serpentinized peridotites, gabbros, dolerite intrusions, pillow basalts and sediments. In this study, we have focussed on the peridotites that were sampled by cruises KH07-02, YK18-07 and KH18-02.

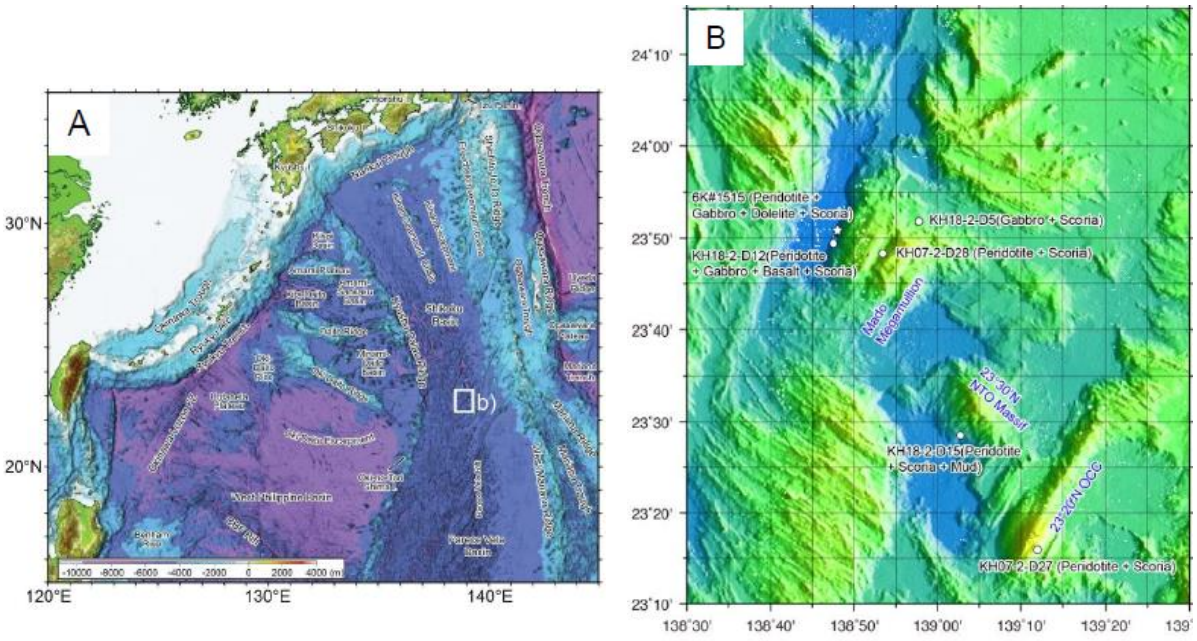

Figure 2-1: Bathymetric map of Philippine Sea plate comprising of different tectonic elements. A. The location of the Mado Megamullion is marked by white square. B. Dredge and dive site locations in a detailed map of the Mado Megamullion where most of the peridotite samples were recovered from the transform wall.

2.3. Samples

We have studied a total of 26 peridotite samples: 19 that were collected by the R/V Hakuho Maru KH18-02 dredging cruise in 2018. Dredge sites D12 and D15 recovered peridotites. The only peridotite recovered from D15 was highly altered and could only be used for elemental analysis of silicates. Our set of samples also includes 6 peridotites that were collected by R/V Yokosuka YK18-07 cruise using the DSV Shinkai 6500 submersible (at Dive 6K1515) and 1 peridotite recovered by the R/V Hakuho Maru KH07-02 dredging cruise in 2007 at dredge site D28 (Table 2.1).

Table 2.1: Location and lithology of peridotites from the Mado Megamullion. Classification is based on the petrography and chemistry of spinels

Cruise	*Sample No*	*Latitude(N)*	*Longitude(E)*	*Water Depth*	*Lithology*	*Comment*
KH18-02	D12-R34	23º49.306'	138º47.635'	5403	Dunite (serpentinized olivine)	Plg Present
KH18-02	D12-R17	23º49.306'	138º47.635'	5403	Lherzolite (Deformed)	Amp present
KH18-02	D12-R02	23º49.306'	138º47.635'	5403	Lherzolite(altered)	Plg present
KH18-02	D12-R12	23º49.306'	138º47.635'	5403	Serpentinized	
KH18-02	D12-R20	23º49.306'	138º47.635'	5403	Lherzolite	Plg present; Amp present
KH18-02	D12-R06	23º49.306'	138º47.635'	5403	Lherzolite	Plg present; Amp present
KH18-02	D12-R19	23º49.306'	138º47.635'	5403	Lherzolite	Amp present
KH18-02	D12-R08	23º49.306'	138º47.635'	5403	Lherzolite (Deformed)	Amp present
KH18-02	D12-R04	23º49.306'	138º47.635'	5403	Lherzolite(altered)	Amp present
KH18-02	D12-R11	23º49.306'	138º47.635'	5403	Lherzolite(altered)	Amp present
KH18-02	D12-R18	23º49.306'	138º47.635'	5403	Lherzolite (Deformed)	Amp present
KH18-02	D12-R14	23º49.306'	138º47.635'	5403	Lherzolite	
KH18-02	D12-R01	23º49.306'	138º47.635'	5403	Lherzolite	Plg present; Amp present
KH18-02	D12-R10	23º49.306'	138º47.635'	5403	Lherzolite (Deformed)	Amp present
KH18-02	D12-R07	23º49.306'	138º47.635'	5403	Lherzolite(altered)	Plg present
KH18-02	D12-R33	23º49.306'	138º47.635'	5403	Lherzolite (Deformed)	Amp present
KH18-02	D12-R05	23º49.306'	138º47.635'	5403	Lherzolite	Plg present; Amp present
KH18-02	D12-R15	23º49.306'	138º47.635'	5403	Lherzolite	Plg present; Amp present
KH18-02	D12-R03	23º49.306'	138º47.635'	5403	Lherzolite(altered)	Plg present;
YK18-07	6K-1515-R10	23º50.500'	138º48.257'	5295	Lherzolite	Peridotite with vein; Amp present
YK18-07	6K-1515-R09	23º50.500'	138º48.257'	5295	Lherzolite	Peridotite with vein; Amp present
YK18-07	6K-1515-R03	23º50.600'	138º48.089'	5680	Lherzolite (Deformed)	Amp present
YK18-07	6K-1515-R15	23º50.400'	138º48.437'	5025	Lherzolite	Amp present
YK18-07	6K-1515-R02	23º50.600'	138º47.923'	5673	Lherzolite	Amp present
YK18-07	6K-1515-R06	23º50.600'	138º48.089'	5483	Lherzolite(altered)	Peridotite with vein; Amp present
KH07-02	D28-001				Lherzolite	

2.3.1. Petrographic Analysis

The peridotites are mostly serpentinized (Hirauchi et al., 2021, submitted for publication) lherzolites and dunites containing clinopyroxene, orthopyroxene, serpentinized olivine, spinel and altered plagioclase (Figure 2-2). The modal proportion of clinopyroxenes in the lherzolites (fertile to depleted) varies from about 1 to 15%. Some of the lherzolites are highly altered where pyroxenes are replaced by secondary hydrous minerals although they preserve their primary morphology. The dunite sample contains olivine that has been completely serpentinized, spinel is the only primary mantle mineral that could be studied (Figure 2-2). Spinels are present either as holly-leaf morphology typical of mantle spinels (Figure 2-3A) or as worm-like intergrowths (Figure 2-3B). Altered plagioclase is present (as pseudomorphous material) as replacement coronas around spinels or clinopyroxenes but also as symplectite intergrowth with worm-like spinels (Figure 2-3B, C). As plagioclase is generally considered a characteristic related to melt stagnation, we classified the peridotites petrographically as *i)* plagioclase absent and *ii)* plagioclase present (Figure 2-3A-C).

Some of the lherzolites have been crosscut by different late-stage veins. Sulfide mineralization is observed in some of the veins of KH18-02-D12 samples (Figure 2-2D). The samples show signatures of deformation in the form of porphyroclastic textures and mylonitized fabrics (Figure 2-3D). Amphiboles are present in nearly all the samples as *i)* a replacement phase over pyroxenes or *ii)* within leucocratic veins. Late-stage amphibole-chlorite-Ti-oxide bearing leucocratic veins with traces of zircons and apatites are present in samples from both KH18-02 and YK18-07 cruises (Figure 2-2E). These samples are classified as peridotites with veins.

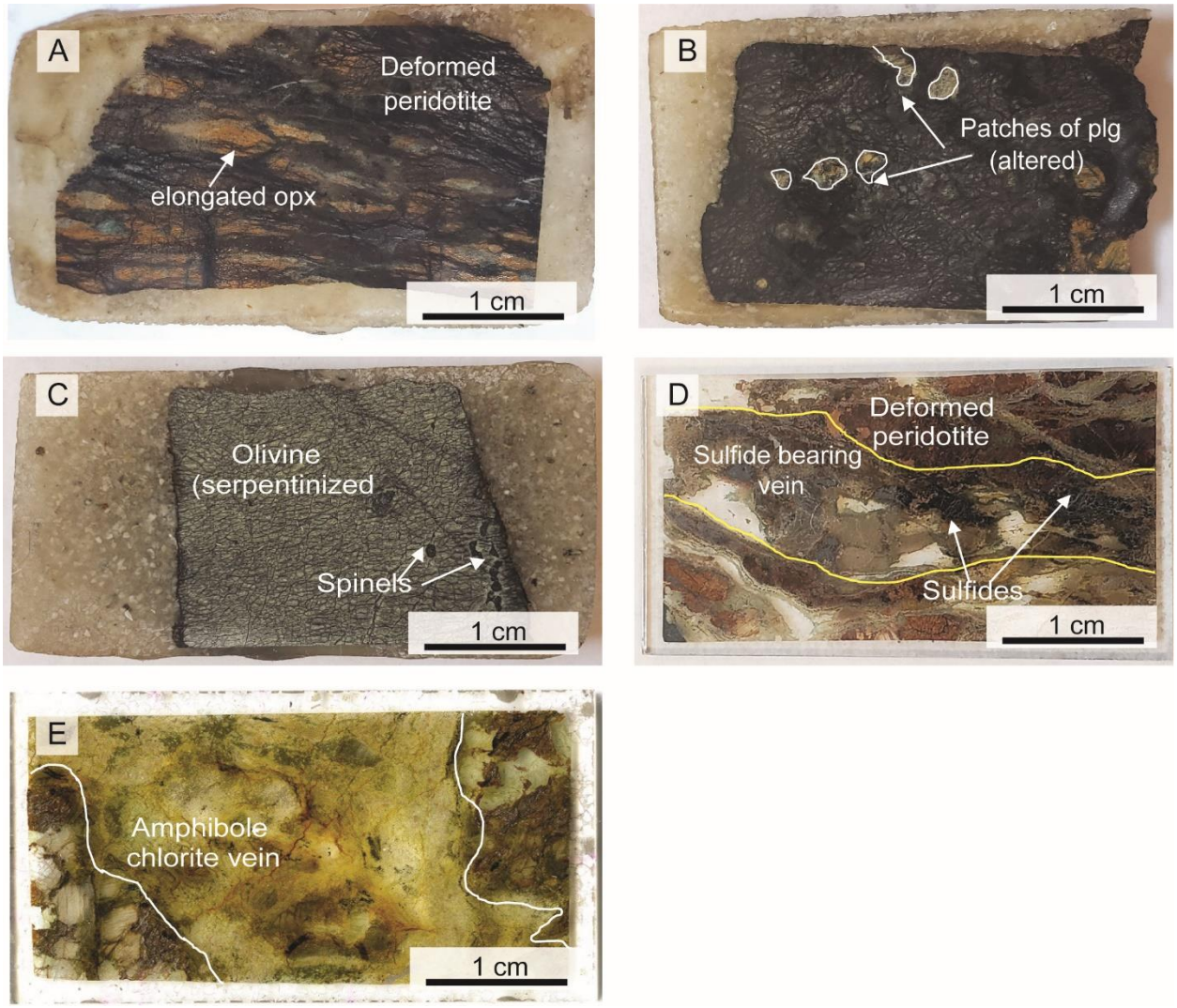

Figure 2-2: Photographs of billets and thin sections of representative samples. A. Dry peridotite containing elongated porphyroclasts of orthopyroxene along foliation planes. B. Melt reacted peridotite containing patches of altered plagioclase marked by the white dotted line. C. Dunite sample that has serpentinized olivine and spinel. D. Sulfide vein within peridotite where the sulfide bearing vein is marked by the dotted line. E. Zircon-apatite bearing chlorite-amphibole vein that cuts across peridotite.

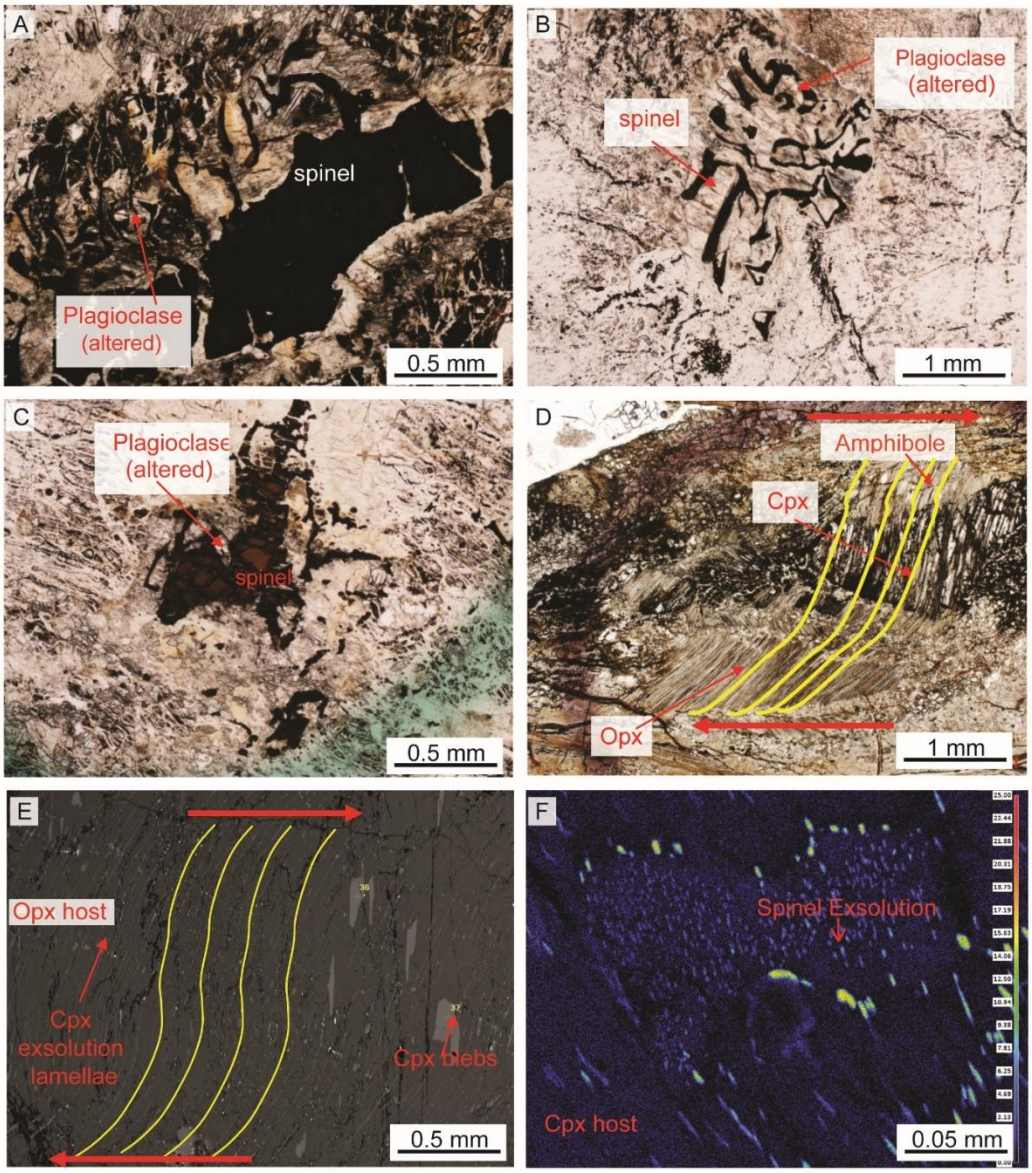

Figure 2-3: Photomicrographs, Back scattered electron (BSE) image and X-Ray elemental map of mineral phases and deformation fabrics. A. Holly-leaf like mantle spinels replaced by plagioclase (altered) along its boundary. B. Intergrowth between spinels and plagioclase (altered). C. Altered plagioclase along the boundary of spinels. D. Mylonitized and deformed fabrics in mantle pyroxenes. The yellow dotted lines define the deformation planes, and the heavy arrows mark the shear direction. E. BSE image showing exsolution lamellae of clinopyroxene (cpx) and presence of cpx blebs in a host orthopyroxene (opx). A deformation plane can be defined from the exsolution lamellae. F. X-Ray elemental map for Chromium showing exsolution of Cr rich oxides in a cpx host.

2.3.2. Clinopyroxene-orthopyroxene exsolution and spinel exsolution in clinopyroxene

The primary mantle minerals from KH18-02 cruise display extensive exsolution. Exsolution lamellae of clinopyroxene are present in orthopyroxene. These exsolution lamellae warp along the deformation or shear planes **(**Figure 2-3E). The clinopyroxenes contain exsolution lamellae of chromium-rich oxides (probably chrome spinels) **(**Figure 2-3F).

2.4. Analytical Methods

2.4.1. Major element analysis

We analyzed the major element concentration of silicates and spinel at Rice University by using a JEOL JXA 8530F Hyperprobe with a field emission assisted thermo-ionic (Schottky) emitter, equipped with five Wavelength Dispersive Spectrometers (WDS) and a JEOL JXA-8800R instrument at Nagoya University, Japan. The analytical conditions employed for quantitative analysis of silicates at Rice University were set to 15 kV acceleration voltage, 20 nA beam current, ca. 300 nm beam size, analytical conditions at Nagoya University were set to 15 kV accelerating voltage, 12 nA beam current, and ≤5 μm beam size. One sample was measured at the University of Houston using a CAMECA SX-50 at 15kV acceleration voltage and 20nA beam current, and beam size ≤5 μm.

2.4.2. Trace elements and REEs analysis

Laser ablation inductively coupled plasma mass spectrometry (LA-ICP-MS) analyses of clinopyroxenes from the peridotite samples were accomplished using a Thermo-iCAP Q

quadrupole mass spectrometer (Thermo Scientific, Bremen, Germany) coupled with a New Wave/ESI 193 nm laser ablation system (Elemental Scientific Lasers, Huntingdon, UK) at the University of Arkansas Trace Element and Radiogenic Isotope Laboratory (TRAIL). Laser ablation analyses utilized a 50 µm laser spot diameter, 10 Hz repetition rate over 20 s, laser fluence of ≈ 4.3 J/cm^2, and the application of a He carrier gas flow rate of 0.800 L/min. Instrumental settings were adjusted to maintain UO and ThO < 1.0%. The standard NIST 612 was used for calibration with 43Ca as the internal standard in all analyses. Standards NIST 610 and NIST 612 were measured prior to and at the end of each analytical session and were bracketed once more after each set of ten analyses during the analytical run. The investigated elements include the rare earth elements (REEs), Sr, Y, Zr, Nb, Cs, Ba, Hf, Pb, Th and U. Data reduction was carried out using the Iolite v4.4.3 software package (Iolite, Melbourne, Australia) **(**Paton et al., 2011**).**

2.5. Results

2.5.1. Mineral major element chemistry

Major element compositions of silicates (orthopyroxene, clinopyroxene, amphibole) and spinels are listed in Supplementary Table S2 A, B, D.

2.5.1.1. Pyroxenes

The orthopyroxenes are enstatite in composition. The Mg# (Mg# = Mg/(Mg+Fe) mol%) ranges between 0.88 to 0.94 and Cr# (Cr# = Cr/(Cr+Al) mol%) up to 0.2. In a Mg# vs. Al_2O_3 diagram the orthopyroxenes mostly plot in the field of abyssal peridotites (Lian et al., 2016; Pagé et al., 2008)

(Figure 2-4A; Supplementary Table S2 A). Some of the orthopyroxenes have lower Al_2O_3 content and plots outside the field of abyssal peridotites.

The clinopyroxenes are diopside to chromium-rich diopside in composition (Cpx data; Supplementary Table S2 B). They are present as individual mineral grains and as exsolutions lamellae and blebs in orthopyroxene. Their Mg# ranges between 0.90 to 0.95, their Cr# ranges between 0.08 to 0.32 and they contain up to 0.50 wt.% TiO_2 (Figure 2-4B, C; Supplementary Table S2 B). Exsolution of chromium-bearing oxides were found in some of the clinopyroxene grains. The clinopyroxenes exhibit a wide compositional range in terms of their Mg# and Al_2O_3 content. The average TiO_2 wt.% vs Na_2O wt. % plot (Figure 2-4C) shows that most of the samples fall in along a partial melting trend (Hellebrand et al., 2002) although there is a scatter towards higher Na_2O values at lower TiO_2 wt.% for some samples.

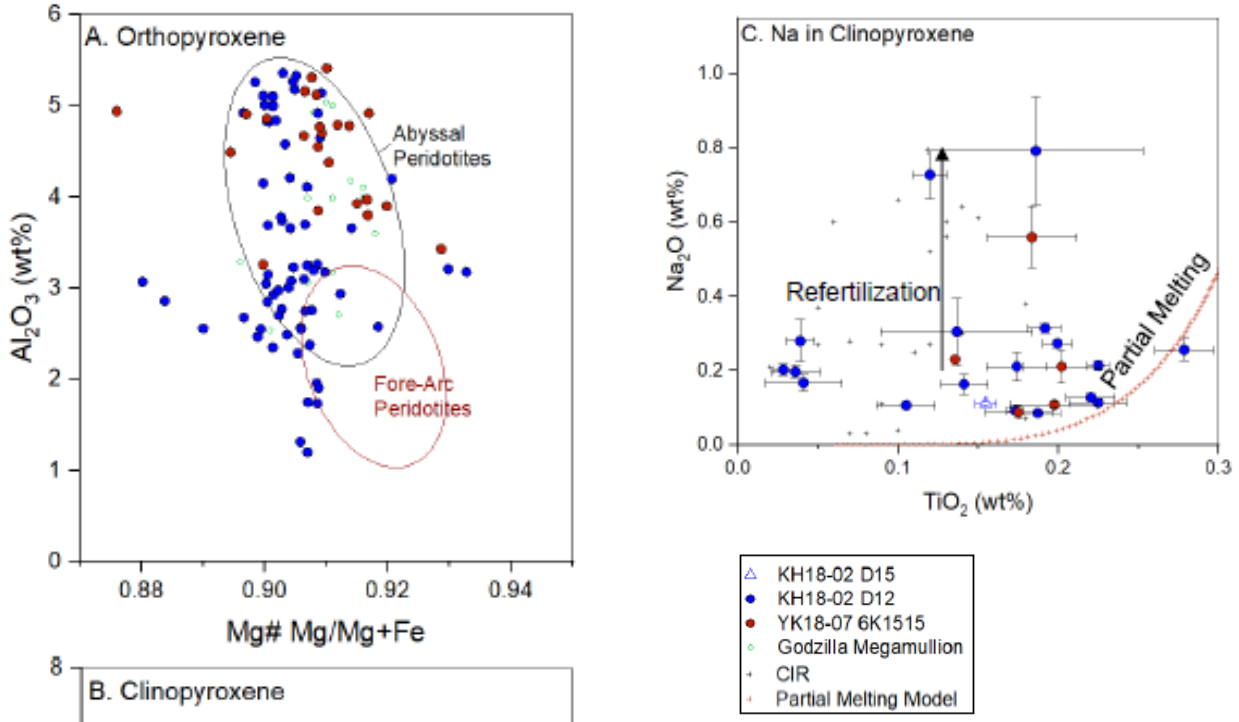

Figure 2-4: Major element compositional variation of mantle silicates in the peridotites A. Mg# vs Al_2O_3 wt.% plot for orthopyroxenes. The fields of fore-arcs and abyssal peridotites are from (Pagé et al., 2008) B. Clinopyroxene Mg# vs Al_2O_3 wt.%. For comparison the compositional field of highly refractory peridotites from the Mid Atlantic Ridge (ODP leg 209) is marked by the grey ellipse (Seyler et al., 2007); Godzilla Megamullion data from Ohara et al., 2003. e C. Clinopyroxene TiO_2 wt.% vs Na_2O wt.% plot; CIR data from Hellebrand et al., 2002.

2.5.1.2. Two-pyroxene geothermometer

Equilibration temperatures for mantle phases were calculated using the two-pyroxene geothermometer, considering that orthopyroxene and clinopyroxene (calcic diopside) were in equilibrium at upper mantle conditions (Bertrand and Mercier, 1985). For calculation of the temperature, homogeneous pyroxene grains and area that did not exhibit exsolution were chosen. This thermometer uses the M2 site occupancies in pyroxenes with corrections for Na. At pressures ranging between 1.5 to 2 kilobars, the calculated equilibrium temperature falls within 860 to 1140°C. This is well within the ambient temperature of the mantle. The results were compared using REE in two-pyroxene thermometer for mafic and ultramafic rocks (Liang et al., 2013**).** This thermometer yields temperatures between 1025 to 1491°C. The temperatures from REE in pyroxene thermometer are generally about 150-200° higher than the major element thermometer. This discrepancy could be a result of the difference in diffusion rate and closure temperature between the +2 and +3 cations in the pyroxenes (Liang et al., 2013).

2.5.1.3. Spinels

The Cr# in spinels shows a wide range of composition from 0.20 to 0.63 mol% and Mg# ranges from 0.15 to 0.73 mol% and TiO_2 up to 0.26 wt% in the peridotites where plagioclase is present (Figure 2-5A, B). The TiO_2 content of the spinels goes up to 0.46 wt% (Spinel data, Supplementary Table S2 C) in some of the peridotites which have been crosscut by late-stage veins. The spinels in these veins have Cr# as high as 0.81 mol% and TiO_2 up to 0.62 wt% (Figure 2-5A, B**)**. Concentric normal zoning (Dien et al., 2019; Mg-Al rich core and Cr-Fe^{2+} rich rim) is observed in spinel grains from sites KH18-02-D12 and YK18-07 6K1515. (Heterogeneous spinels;

Supplementary Table S2 F). These zoned spinels are present in the dry peridotite samples (Figure 2-6). The boundaries of these spinels are also marked by intergrowths with altered/metasomatized silicates (chlorite and amphibole).

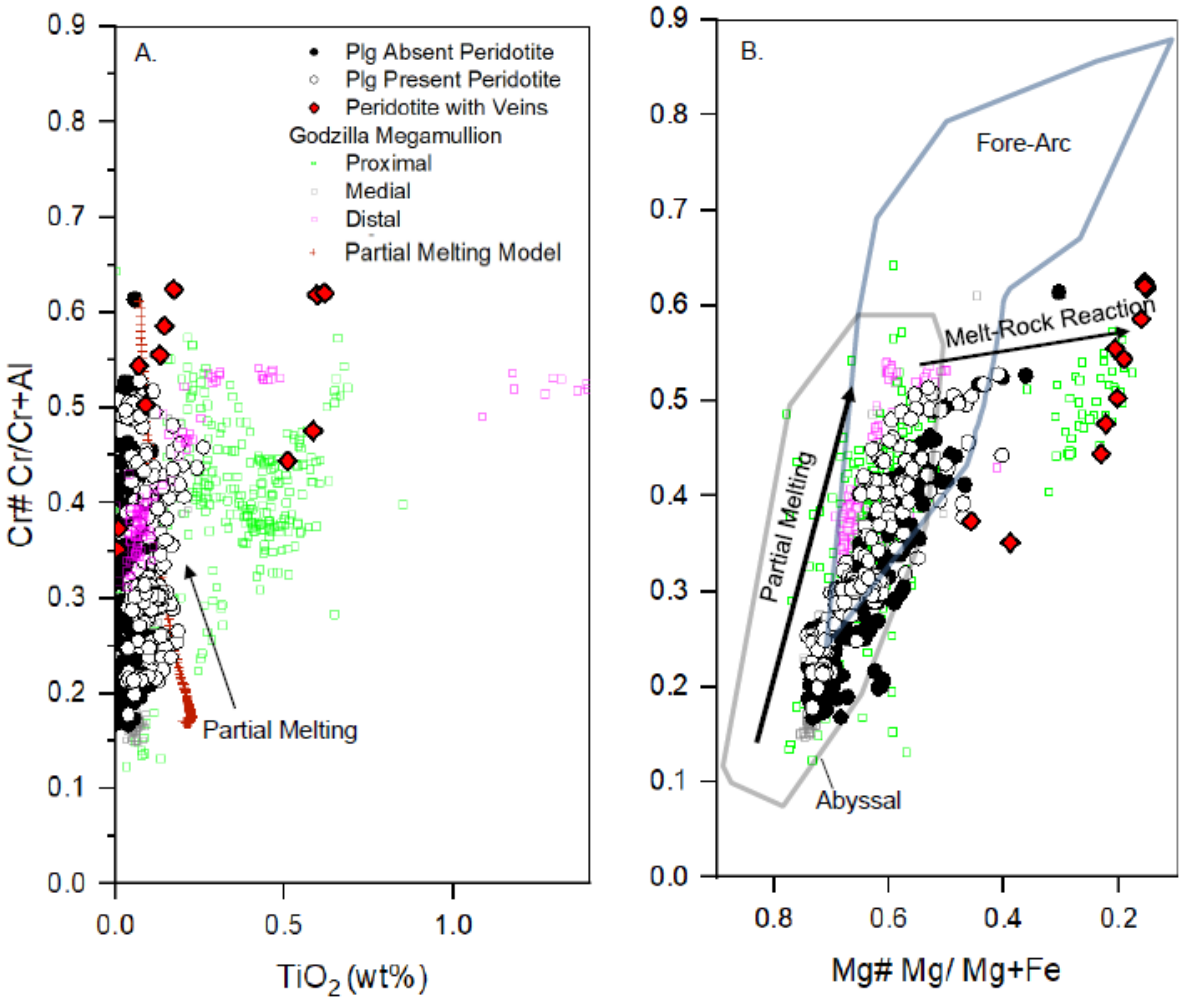

Figure 2-5: A. Cr# vs TiO_2 content of spinels from YK 18-07, KH 18-02 of residual peridotites, melt-reacted peridotites, and veined peridotite samples. B. Cr# vs Mg# of spinels from YK 18-07, KH 18-02 of peridotites, dunites, and veined peridotite samples from the Mado Megamullion. Proximal, media and distal region of the Godzilla Megamullion is from Loocke et al. (2013).

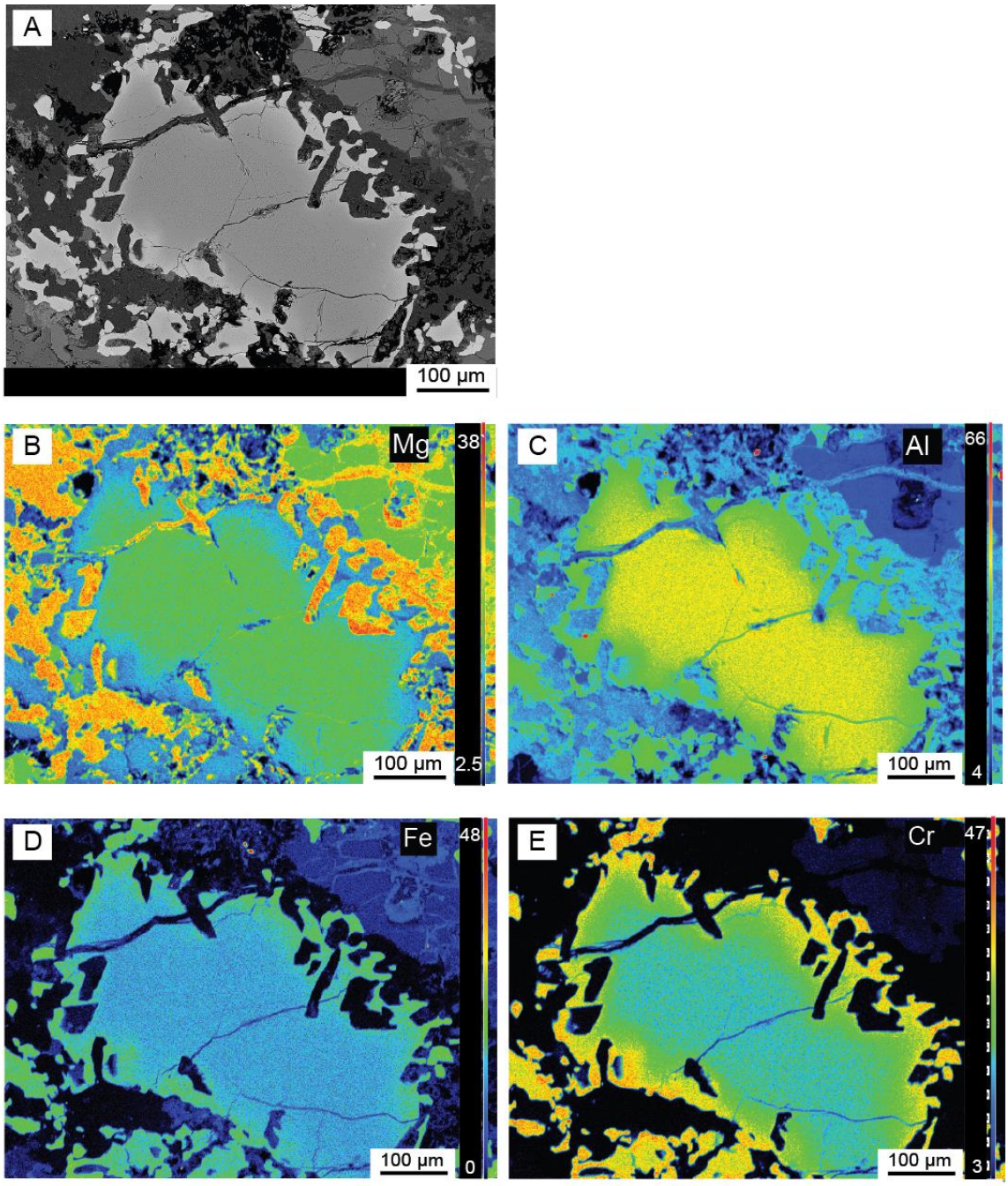

Figure 2-6: BSE and X-Ray elemental maps for a heterogeneous spinel grain. A. BSE image with darker core and brighter boundary. B-E. Mg-Al rich core and Fe-Cr rich boundary in the heterogeneous spinels.

2.5.1.4. Amphiboles

Brown-green pleochroic and colorless amphiboles are found in most of the samples, texturally replacing clinopyroxene (Figure 2-3D) and in leucocratic veins (Figure 2-2E). Most of the replacement amphiboles plot in the Edenite-Pargasite field (Leake et al., 1997) with a few crystals in the Edenite and Hornblende fields (Amphibole data; Supplementary Table S2 D). These amphiboles also coincide generally in composition with the magmatic amphiboles from the gabbros of the Mado Megamullion (Basch et al., 2020) (Figure 2-7A). The amphiboles can be chemically distinguished between vein and replacement types based on the distribution of TiO_2 and Cr_2O_3 weight %. The composition of the amphiboles in the veins is similar to the compositions of both the vein amphiboles and magmatic amphiboles from the Mado gabbros (Basch et al., 2020). The replacement amphiboles are lower in TiO_2 and have higher Cr_2O_3 content than the amphiboles in the veins. (Figure 2-7B). This would be consistent with a common origin, whereby the replacive amphiboles inherit immobile Cr from their host clinopyroxene.

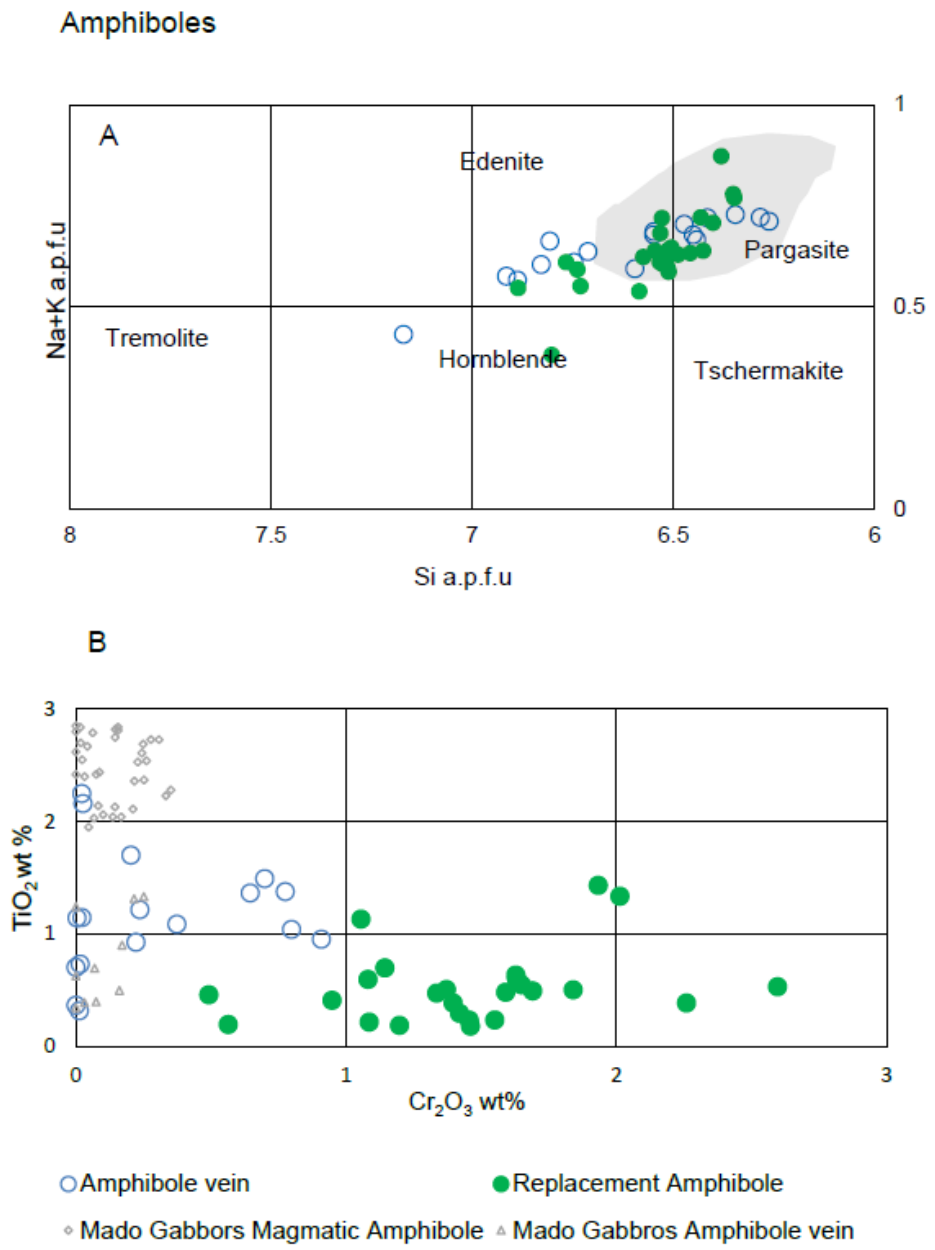

Figure 2-7: A. Si (atoms per formula unit) a.p.f.u vs Na+K a.p.f.u indicates that most of the amphiboles plot in the magmatic amphibole field. The gray area is the field of magmatic amphiboles in the gabbros of the Mado Megamullion (Basch et al., 2020). B. Cr_2O_3 wt% vs TiO_2 wt% plot for amphiboles where the replacement amphiboles have higher Cr_2O_3 wt% and lower TiO_2 wt% content than the amphibole in the veins.

2.5.2. Trace elements and REEs in clinopyroxenes

Trace elements and REEs were analyzed in clinopyroxenes in the peridotites. The concentration of the REEs (ppm) in clinopyroxenes is listed in Supplementary Table S2 E. Chondrite-normalized REE plots show that the clinopyroxene porphyroclasts from samples that do not exhibit deformation features show an LREE-depleted trend (Figure 2-8A). This LREE depleted trend is similar to those reported from depleted abyssal peridotites generally (Dick et al., 1984; Dick, 1989, Johnson et al., 1990; Michael and Bonatti, 1985). Simple melting models produce extreme LREE depletion trends and do not explain the inflection of LREEs seen in these residual clinopyroxenes (Figure 2-8A), also commonly observed in REE patterns from abyssal peridotite clinopyroxenes. Clinopyroxenes from the deformed peridotites or within deformed lamellae exhibit a flat REE pattern with a negative Eu anomaly (e.g., Figure 2-8A; enriched clinopyroxene). Similar REE patterns occur in the melt-impregnated peridotite samples of the Mariana Trough (Ohara et al., 2002**)** and the Parece Vela Rift (Ohara et al., 2003).

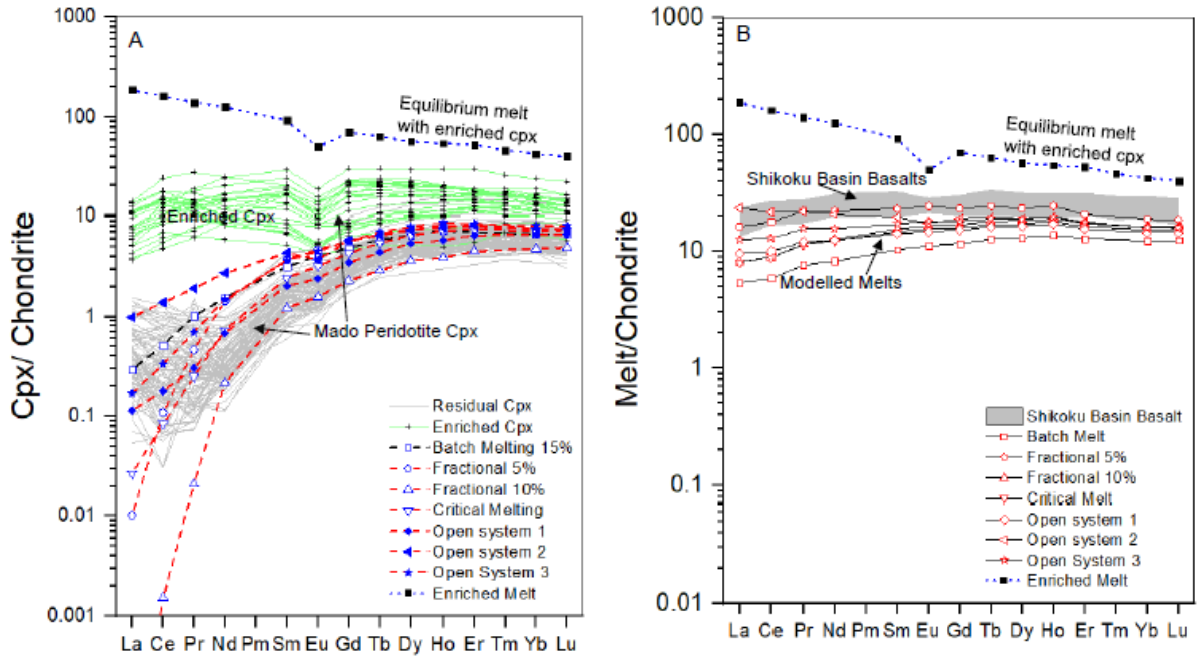

Figure 2-8: Chondrite normalized REE plot for clinopyroxenes and melt. A. Residual and enriched clinopyroxenes composition of Mado peridotites. The dashed lines indicate the composition of the pyroxenes from batch melting, fractional melting, critical melting and open system melting processes. The enriched melt composition is a derived melt in equilibrium with an enriched clinopyroxene. The LREE enrichment trend is not explained by fractional melting alone and invokes the idea of an open system melting process. B. REE Composition of accumulated melts from the different melting models (indicated by red symbols). The shaded area denotes the compositional filed of Shikoku basin basalts (Ishizuka et al., 2009). The open systems 2 and 3 closely approximates the composition of the basalts.

2.6. Discussion

2.6.1. Partial Melting

The spinels from the Mado peridotites plot within the normal range of abyssal peridotites (Dick and Bullen, 1984). Their wide compositional range in terms of the Cr# suggests that the Mado mantle has undergone variable degrees of partial melting (Figure 2-5A, B) (Hellebrand et al.,

2001). The presence of dunites and peridotites from the same dredge location indicates heterogeneous extraction, transport and reaction of melt (Kelemen et al., 1995; Niu et al., 1997). The heterogeneous spinels with increase in Cr towards the boundary (Figure 2-6) could be related to partial melting that removes Al^{3+} and increases Cr^{3+} in the residue (Dick and Bullen, 1984; Saumur and Hattori, 2013) at increasing degree of melting. The spreading rate and degree of melting are related (Niu and Hékinian, 1997), so initiation of normal detachment faulting after ca. 19 Ma might be related to a decrease in spreading rate to 3 cm/y (Okino, 2015) which resulted in an increase in the final depth of melting beneath the Shikoku Basin spreading axis.

To model the degree of partial melting we ran a series of models using pMELTS (Ghiorso et al., 2002; Ghiorso and Sack, 1995) in the spinel stability field. We selected a Depleted MORB Mantle (DMM) composition (Workman and Hart, 2005) as the starting material. We sequestered 18 wt% Cr_2O_3 from the DMM composition to account for the lack of a solution model for Cr in pyroxene of MELTS. This was based on the modal abundance of clinopyroxene in DMM (Workman and Hart, 2005) and the distribution coefficients between minerals and melt during mantle melting (Roux et al., 2015). We melted this modified DMM adiabatically in the spinel stability field starting at 18 kbar until the base of the crust at 2 kbar. The starting temperature of the model was taken as 1350°C. The composition of the peridotite spinels could be reproduced by a range of 7% to 21% partial melting. This agrees closely with Hellebrand et al. (2001)'s empirical calibration (degree of partial melting ranges from 6.28 to 17.66%) for the range of Cr# for the Mado Megamullion spinels. (Figure 2-5A).

Clinopyroxene and orthopyroxene compositions plot in the range of abyssal peridotites, while the samples with lower proportion of clinopyroxenes have a higher Mg# and lower Al_2O_3 content and are comparable to the most depleted abyssal peridotites (Figure 2-4A, B). The composition of these refractory clinopyroxenes from the Mado Megamullion coincides with the composition of the highly refractory clinopyroxenes from the Mid-Atlantic Ridge, ODP Leg 209 Site 1274 (Seyler at al., 2007). The clinopyroxene compositions of peridotites reflect the degree of depletion by melting from fertile to depleted peridotites (Dick et al., 1984) leading to very refractory compositions (Johnson et al., 1990). The presence of fertile to melt-depleted peridotites and the compositional variability of spinels and silicates suggests that the Mado mantle has undergone variable degrees of melt depletion. The REE trends (discussed below) of the clinopyroxenes fall within the compositional range of abyssal peridotites and do not exhibit the extreme signatures of depletion in REE reported from fore-arc regions.

2.6.2. Melt Stagnation and Reaction

Plagioclase is present in 30% of the Mado peridotites, pseudomorphously replaced either as rims on spinel or as symplectic intergrowths (Figure 2-3A-C). Fresh plagioclase is also found in some samples (Akizawa et al., in prep). The widely accepted mechanisms for the formation of plagioclase-bearing peridotites are the following: *i)* re-equilibration of an ascending mantle from the spinel stability field to the plagioclase stability field (Frost, 1976; Hamlyn and Bonatti, 1980) or *ii)* a melt-rock reaction mechanism driven by the impregnation of a melt into the residual peridotite (Dick, 1989; Dick and Bullen, 1984; Rampone et al., 2020). The spinels associated with the plagioclase-bearing peridotites exhibit an elevated content in TiO_2 and a wide range of

composition in terms of spinel Cr#. The proportion of plagioclase-bearing lithologies and the extent of plagioclase impregnation is less than documented in the proximal region of the Godzilla Megamullion (Loocke et al., 2013). The presence of plagioclase and the TiO_2 content in spinels are used as an indicator of melt stagnation and reaction and a cut off at 0.12 wt% (Dick et al., 2010; Cannat et al., 1990; Loocke et al., 2013; Tartarotti et al., 2002) is generally used to distinguish residual peridotites from melt-reacted peridotites (Ohara et al., 2003; Loocke et al., 2013; Sanfilippo et al., 2013). The TiO_2 content of the spinels from the plagioclase-bearing peridotites ranges up to 0.26 wt%, which is much less than the TiO_2 content of the spinels in plagioclase-bearing peridotites from the proximal region of the Godzilla Megamullion where the TiO_2 content reaches 1.56 wt%. The compositional range of spinels from the plagioclase-bearing peridotites in terms of their Cr# (0.18 to 0.53) and TiO_2 content (up to 0.26 wt%) coincides better with the compositional range of spinels from the distal region of the Godzilla Megamullion where Cr# ranges from 0.33 to 0.64 and TiO_2 up to 0.45 wt% (Loocke et al., 2013) (Figure 2-5A, B). Thus, the slightly elevated TiO_2 content (Figure 2-5A) in the associated spinels in the plagioclase-bearing peridotites indicates melt stagnation and melt-rock reaction, although the extent of these indicators is much lower than that seen in the proximal regions of the Godzilla Megamullion (Loocke et al., 2013).

The expected partial melting trend is observed for some of the samples in terms of the variation of TiO_2 and Na_2O content in clinopyroxenes while some samples have a much higher primary clinopyroxene Na_2O concentration than those calculated for partial melting trends at given TiO_2 values (Figure 2-4C). A similar feature was observed for residual peridotites from the Central

Indian Ridge (CIR) and was termed the “sodium problem” (Hellebrand & Snow, 2003). Partial melting would deplete the residue in Na which is more incompatible than Ti, as also seen in our partial melting model. The enrichment in Na in some samples could indicate re-fertilization of residual peridotites (Hellebrand et al., 2002).

2.6.3. Relationship between hydrous melt infiltration and exhumation

At decreasing temperatures, the complete solid-solution of pyroxenes changes to a limited solid-solution. As a result, the pyroxenes equilibrated at higher temperatures tend to assume ordered structure of separate phases (Ca-rich Cpx and Ca-poor Opx) in the form of exsolutions at lower temperatures (Poldervaart and Hess, 1951). Similar exsolution textures have been observed in ophiolites where mantle upwelling to shallower depths resulted in the formation of exsolutions (Basch et al., 2019; Kirby & Etheridge, 1981; Rehfeldt et al., 2007; Xiong et al., 2020). This suggests that the rocks that equilibrated at greater depths were emplaced at shallower depths because of exhumation of mantle rocks at a slow-spreading axis.

The presence of spinel exsolutions in pyroxene is not well constrained yet. A suggested mechanism for the presence of spinel exsolution in pyroxene is when there is no change in the oxygen framework but the spinel nuclei forms by the migration of cations from interstitial sites and tetrahedral sites (Okamura et al., 1976). The other possibility is a variation in the local oxidation state of the system. In the presence of magnetite and amphibole that consume O_2 and Fe^{3+} from the magmatic system, spinel may exsolve from the pyroxene structure (Zhu et al., 2018). The Mado peridotites have been crosscut by late-stage oxide-bearing amphibole-chlorite veins. The clinopyroxenes in the lherzolites contain amphiboles. Magmatic amphiboles are also ubiquitously

present in the Mado gabbros (Basch et al., 2020). This indicates that a late-stage process of melt percolation may have played a significant role for the exsolution of spinels from the structure of pyroxenes (Cr-diopsides). The textural relationships between magmatic veins rich in amphiboles (considered as late-stage hydrous melts) and the deformed pyroxenes indicate that melt was present during the deformation history that promoted the exhumation of the peridotites to the seafloor. These melts could have played a significant role in promoting detachment. The presence of mylonitized fabrics along the exsolution lamellae (Figure 2-3D, E) also indicates that the peridotites underwent crystal-plastic deformation during the slow exhumation of the mantle (Hirauchi et al., 2021 *submitted)* and formation of the OCC in the slow-spreading back-arc Shikoku basin.

2.6.4. Evolution in a water-rich environment

The presence of the different types of amphiboles in peridotites suggests the presence of water, at least in the late stages of the formation of the OCC (Harigane et al., 2019; Zhang et al., 2021). It cannot be definitively constrained whether there was sufficient water in the system during melting to crystallize amphibole as a primary mantle phase. However, the presence of magnetite, ilmenite and other Ti-bearing oxides in the amphibole veins and their crosscutting relationship with the peridotites (Figure 2-2E) suggest strongly that these amphiboles crystallized from a melt rich in incompatible elements and water, injected in a mantle sequence at the boundary between ductile and brittle regime. The compositional similarity between the pargasitic amphiboles in the veins within the peridotites and the magmatic amphiboles in the gabbros (Figure 2-7A, B**)** suggests that these amphiboles are genetically related. The higher Cr_2O_3 content in the replacement amphiboles

(Figure 2-7B) could indicate a reaction of Cr-rich pyroxenes with hydrous mafic melt (hydrous melt that formed the Mado gabbros; see Basch et al., 2020) or late-stage deuteric fluids to form the Cr-rich amphiboles. These high temperature pargasitic amphiboles have been identified from abyssal peridotites from very few localities (Melson et al., 1967; Seyler et al., 2004; Ohara et al., 2003); most of the amphiboles documented in abyssal peridotites are tremolitic. The presence of pargasitic amphiboles in peridotites from this study suggests that back-arc mantle could be hydrated/hydrous. This is unexpected as the mantle is generally considered to be free of high-temperature amphibole (pargasites) (Warren et al., 2016). Late-stage metasomatic effects are seen often in mantle rocks and these amphiboles corresponds to the presence of hydrous components in the mantle (Seyler et al., 2004; Basch et al., 2020). It is also observed from *in-situ* crystallization experiments that amphibole-bearing peridotites could form by reaction between lherzolites and hydrous partial melt (Wang et al., 2021**).** The replacement amphiboles from this study can be inferred to be reacted amphibole and this reaction product can lead to the hydration of the mantle in a back-arc environment. Amphiboles occurring in the Godzilla Megamullion peridotites (Ohara et al., 2003; Loocke at al 2013) have not yet been systematically studied, so it is not possible to say whether their occurrence or composition are consistent between the two complexes. It is possible that an increased influence of water-rich melts is a characteristic of back-arc abyssal peridotites as compared to those outcropping at mid-ocean ridges.

2.6.5. Evolution of the Depleted Clinopyroxenes

To model the trace element distribution in the most depleted clinopyroxenes, we have taken a DMM composition (Workman and Hart, 2005) as our starting mantle composition. We have

modelled the trace elements and REEs using equations for equilibrium melting (Shaw, 1970) and fractional melting (Johnson et al., 1990). The partition coefficients between clinopyroxene and liquid is taken from the new predictive model for partitioning of REE and Y between clinopyroxene and a basaltic melt (Sun and Liang, 2012) by least square analysis of available partitioning data based on the lattice strain model (Brice, 1975; Blundy and Wood, 1994) at 1300ºC**.** The partition coefficient of olivine (Stracke et al., 2003), orthopyroxene (Salters and Stracke, 2004) and spinel (Sobolev and Shimizu, 1992) is listed in Table 2.2. The initial mode (Sobolev and Shimizu, 1992), melting mode (Kinzler and Grove, 1992) and crystallization modes (Elthon 1992) used for the models are listed in Table 2.3. Although the batch melting models depletes the LREEs less than the fractional melting models, batch melting does not reach the observed depletion in incompatible trace elements in residual peridotite clinopyroxenes even with 15% melt extraction (Figure 2-8A). Fractional melting, on the other hand, satisfies the REE depletion trend for most elements, except for the La-Ce enrichment commonly seen in ocean floor peridotites (Johnson et al., 1990; Hellebrand et al., 2002; Ohara et al., 2002) (Figure 2-8A).

To better understand the process, we also used critical melting (Maaloe, 1982; Sobolev and Shimizu, 1992), where a residue of melting (α is the mass ratio of retained melt) is left behind in the pore spaces during partial melting and the REEs in the residual peridotites equilibrate with the melt. The critical melting model with α=0.01 and 10% fractional melting exhibits LREE enrichment as compared to the 10% fractional melting alone, but this still does not explain the higher LREE abundances in some of the residual clinopyroxenes.

Table 2.2: Mineral/melt partition coefficients used in the models

	Olivine[a]	Orthopyroxene[b]	Clinopyroxene	Spinel[e]
La	0.0002	0.0031	0.055[c]	
Ce	0.00007	0.004	0.0876[c]	0.0005
Pr			0.1318[c]	
Nd	0.00042	0.012	0.1878[c]	0.0008
Sm	0.0011	0.02	0.3083[c]	0.0009
Eu	0.0005		0.3638[c]	
Gd	0.0011	0.0065	0.4169[c]	0.0009
Tb			0.4645[c]	
Dy	0.0027	0.011	0.5034[c]	0.0015
Ho			0.5294[c]	
Er	0.0109	0.045	0.5437[c]	0.0045
Tm			0.5482[c]	
Yb	0.024	0.08	0.5453[c]	0.0045
Lu	0.02	0.12	0.5373[c]	
Rb	0.0003	0.0002	0.0004[d]	
Ba	0.000005	0.000006	0.0004[d]	
Th	0.00005	0.002	0.0059[d]	
U	0.00038	0.002	0.0094[d]	
Nb	0.0005	0.004	0.015[d]	
Ta	0.0005	0.004	0.015[d]	
K	0.00002	0.0001	0.001[d]	
Pb	0.003	0.009	0.012[d]	
Sr	0.00004	0.0007	0.091[d]	
Hf	0.0022	0.03	0.2835[d]	
Zr	0.005	0.0225	0.075[e]	0.05
Ti	0.008	0.0805	0.23[e]	0.1
Y			0.5219[c]	

[a] From from Stracke et al., 2003
[b] From Stracke et al., 2004
[c] From Sun and Liang., 2012
[d] From Salters and Stracke (2004)
[e] From Sobolev and Shimizu (1992)

Table 2.3: Modal proportions of the phases used in the models

	Initial Mode[a]	Melt mode[b]	Crystallization mode[c]
Olivine	0.58	-0.30	0.70
Orthopyroxene	0.26	0.40	
Clinopyroxene	0.13	0.82	0.30
Spinel	0.03	0.08	

[a] Sobolev and Shimizu (1992)
[b] Kinzler and Grove (1992)
[c] Elthon (1992)

2.6.6. Evolution of enriched signatures

The flat REE patterns in equilibrium with enriched melts from Mado clinopyroxene are associated with deformation and veining. The presence of the enriched clinopyroxenes in the deformed peridotites suggests the presence of an enriched melt. We therefore employed the open-system modelling mechanism (Dick et al., 1984; Ozawa and Shimizu, 1995). To estimate the composition of enriched melt, we used the enriched clinopyroxene composition from a typical deformed peridotite sample (KH18-02-D12-R17) and calculated the equilibrium melt composition using the partition coefficient between cpx and melt ($D^{cpx/liq}$) (Salters and Stracke, 2004; Sun and Liang, 2012). This composition compares closely to that of the hypothetical enriched component in the Mariana Trough peridotites (Ohara et al, 2002). We used this melt composition as the composition of the enriched metasomatic melt (Table 2.4). With a degree of fractional melting ranging from 7 to 10% and α=0.01 and influx rate (β) of 0.01, the clinopyroxenes in the residue exhibit more enrichment compared to the fractional or critical melting models (Figure 2-8A). After running the same model at a higher enriched melt influx rate (β=0.1), more enriched LREE patterns could be reproduced in the clinopyroxenes. The clinopyroxenes modelled by the mechanisms describe

above is given in Table 2.5. The HREE trends are primarily controlled by the degree of melting (F) and significant difference in the HREEs is not produced due to the melt fraction retained or the influx rate (β) of the LREE enriched melt (Ozawa and Shimizu, 1995). Although no significant change in the HREE pattern is observed in the fractional, critical or open system models, it is observed that the critical melting and the open system melting processes produce a higher HREE abundance at the same degree of partial melting.

Table 2.4: Composition of calculated influxed melt and modelled accumulated melts normalized to chondrite (Sun and McDonough, 1995)

	Enriched melt	*Batch melt*	*Fractional 5%*	*Fractional 10%*	*Critical Melting*	*Open System 1*	*Open System 2*	*Open System 3*
La	187.98	5.36	16.19	8.10	8.09	9.56	23.71	12.47
Ce	161.32	5.92	17.79	8.97	8.93	9.97	21.80	12.94
Pr	140.03	7.64	22.37	11.53	11.43	12.05	21.95	15.59
Nd	125.92	8.26	22.37	12.65	12.32	12.37	20.75	15.56
Sm	92.65	10.29	23.32	15.50	14.73	14.12	19.57	17.07
Eu	50.30	11.16	24.44	16.43	15.62	14.78	17.28	17.87
Gd	70.68	11.61	23.44	16.81	15.88	15.18	18.96	17.92
Tb	63.85	12.65	24.44	17.97	16.95	16.24	19.48	19.00
Dy	57.07	13.04	23.49	18.20	17.11	16.32	18.97	18.78
Ho	54.51	13.70	24.53	18.94	17.81	17.09	19.58	19.65
Er	53.18	12.82	20.83	17.30	16.28	15.50	17.72	17.38
Tm								
Yb	42.72	12.26	18.79	16.19	15.30	14.48	15.99	16.02
Lu	40.25	12.39	18.54	16.18	15.31	14.50	15.83	15.95

Critical melting F=0.10; α=0.01
Open system 1 F=0.10; α=0.01; β=0.01
Open system 2 F=0.10; α=0.01; β=0.1
Open system 3 F=0.07; α=0.01; β=0.0.01

Table 2.5: Composition of modelled clinopyroxenes normalized to chondrite (Sun and McDonough, 1995)

	Batch melting	*Fractional 5%*	*Fractional 10%*	*Critical Melting*	*Open System 1*	*Open System 2*	*Open System 3*
La	0.29	0.01	0.00	0.03	0.11	0.98	0.17
Ce	0.52	0.11	0.00	0.08	0.18	1.39	0.33
Pr	1.01	0.47	0.02	0.25	0.31	1.91	0.70
Nd	1.55	1.43	0.22	0.73	0.68	2.73	1.49
Sm	3.17	3.74	1.22	2.45	2.03	4.35	3.66
Eu	4.06	4.67	1.58	3.21	2.41	3.73	4.53
Gd	4.84	5.64	2.29	4.31	3.49	5.73	5.74
Tb	5.88	6.71	2.89	5.45	4.36	6.54	6.97
Dy	6.56	7.47	3.64	6.51	5.40	7.30	7.90
Ho	7.25	8.09	3.89	7.19	5.83	7.74	8.65
Er	6.97	7.87	4.52	7.39	6.52	8.16	8.47
Tm							
Yb	6.69	7.58	4.80	7.26	6.59	7.66	8.08
Lu	6.66	7.51	4.90	7.28	6.65	7.56	8.01

Model parameters same as Table 2.5

2.6.7. Modelled accumulated melts and Shikoku Basin basalts

Shikoku Basin back-arc basalts (Ishizuka et al., 2009) are enriched in LREE compared to N-MORB (Sun and McDonough, 1989). We modelled the accumulated melt compositions (Table 2.4) from batch melting, fractional melting, critical melting and open-system melting mechanisms (Figure 2-8B**).** Our models indicate that the compositions of the accumulated melts from the fractional melting (10%), batch melting, critical melting, and open system 1 with enriched melt influx rate (β) of 0.01, degree of melting (F) 10% and melt porosity (α)=0.01 (Figure 2-8B**)** processes do not show the enrichment documented in the Shikoku Basin basalts (Ishizuka et al., 2009). Only the accumulated melt compositions from the open system 2 process (with a higher enriched melt influx rate (β) of 0.1, α=0.01 at F=10%) and fractional melting (5%) shows a compositional similarity with the Shikoku Basin basalts. The open system 3 (F=7%, α=0.01,

β=0.01) plots slightly lower than the compositional field of the Shikoku Basin basalts (Figure 2-8B). In the extended spider diagram (Figure 2-9) it is seen that open system 2 estimates a higher proportion of fluid mobile elements (Ba, U, Pb) than that seen in the Shikoku Basin basalts as well as the Mado basalts (Basch et al., 2020). The composition predicted by open system 3 plots in the field of the Shikoku Basin basalts and closely estimates the analyzed trace element compositions (Figure 2-9).

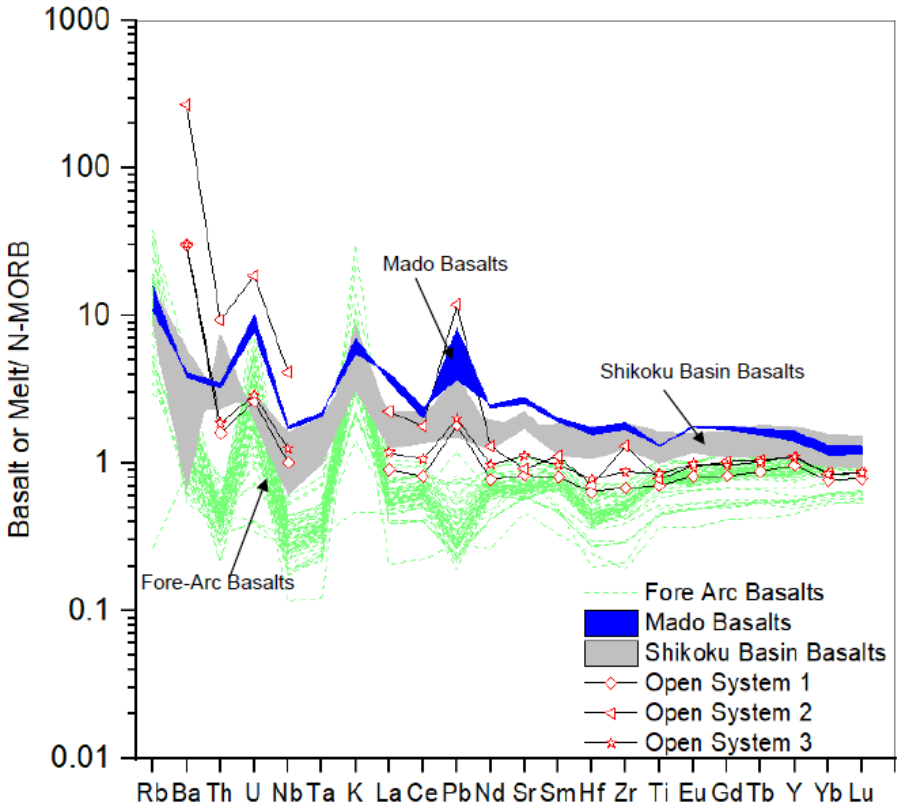

Figure 2-9: Multi-element spider diagram normalized to N-MORB (Sun and McDonough, 1989). The back-arc basalts from the Shikoku basin and Mado Megamullion shows distinct enrichment trends in comparison to fore arc basalts from the Izu-Bonin-Mariana arc. Our open system models for the accumulated melt compositions closely approximate the trends shown by the Shikoku basin basalts along with the enrichment trends in fluid mobile elements (Ba, U, Pb).

2.6.8. Tectonic Implications

The enrichment seen in the Shikoku Basin basalts was predicted by the open system 2 model in which the proportion of the influxing melt was higher (β=0.1). The feasibility of this higher melt influx rate is not well constrained in a back-arc spreading environment. The open system model 3 with 7% degree of melting and melt influx rate β=0.01 closely resembles the composition of the Shikoku Basin basalts. This rate of melt influx compared to the open system 2 seems to be a more realistic scenario as the Mado Megamullion formed at the final stages of back-arc spreading when the melt production rate decreased leading to moderate melt-rock reaction or re-fertilization of the residual clinopyroxenes which is also consistent with the melt-rock reaction textures and chemistry seen in the Mado spinels. The higher enrichment trends seen in the Mado Megamullion basalts in terms of the fluid-mobile elements respect to those predicted by our open system 3 model could be produced by the influx of a hydrous melt rich in fluid-mobile elements (Gale et al., 2013). Basalts from the Izu-Bonin-Mariana fore-arc region display distinctive geochemical signatures with an overall depletion in trace elements and REEs (Figure 2-9) compared to back-arc basalts or MORBs (Shervais et al., 2019). These depleted signatures reflect a higher degree of partial melting in a fore-arc region. A two-stage melting process was suggested (Shervais et al., 2019) in which shallow melting at higher potential temperatures (due to the presence of a hotspot) of an already depleted source led to these depletions. Thus, the source mantle in a back-arc spreading environment and a fore-arc region could be different. The domal structures that we see in OCCs have been discovered from slow- to ultraslow-spreading axes in the Southwest Indian Ridge, Mid-Atlantic Ridge, as well as back-arc basins. The recovery of serpentinized peridotites suggests that

the exhumation of the mantle rock was fault driven in a magma-starved condition (Tucholke et al., 1998). However, ODP and IODP holes from the Atlantis Bank in the Southwest Indian Ridge and the Atlantis Massif in the Mid-Atlantic Ridge has recovered thick layers of gabbroic rocks (Dick et al., 2019; Godard et al., 2009; Ildefonse et al., 2007). It has been suggested from numerical modelling that long-lived detachment faults could be formed by extension accommodated by magmatic accretion (Tucholke et al., 2008).

Hydrous open-system magmas are to be expected as a component in the petrogenesis of peridotite from back-arc basins. Their occurrence sets back-arc peridotites apart from the majority of mid-ocean ridge peridotites, where primary or near-primary amphibole is extremely rare, and the contribution of enriched metasomatic fluids are minor.

2.7. Conclusions

The deformation-related textures and chemistry of associated spinels and silicates suggest that the Mado Megamullion peridotites are residues of melting and melt-rock interactions with hydrous basaltic liquids probably equivalent to primitive back-arc basin basalts. The abundance of residual peridotites and the compositions of primary silicates and spinels that fall in the range of global abyssal peridotites suggest a relatively wide range of degrees of partial melting. The elevated content of TiO_2 in spinels from the plagioclase-bearing peridotites and the presence of residual and melt-reacted peridotites from the same dredge site requires the involvement of melt stagnation or melt-rock reaction. The composition of the spinels from the Mado Megamullion is similar to those of peridotites from the distal region of the Godzilla Megamullion, and the extent of melt stagnation is lower than the proximal Godzilla Megamullion. 10% fractional melting can

approximate the MREE-HREE compositions of the most depleted peridotite clinopyroxenes. The multiple generations of amphiboles suggest the involvement of water at different stages of exhumation of the OCC. The compositional similarity between the amphiboles in the veins to the magmatic amphiboles suggests a genetic relationship between them. Back-arc mantle could be hydrated by reaction of the peridotites with hydrous melt. Exsolution between orthopyroxene, clinopyroxene and Cr-bearing oxides suggests a change in oxygen fugacity and water content in the infiltrating melt compared to the host peridotite. The flat REE pattern of the clinopyroxenes in the deformed peridotites and along deformation planes indicates the presence of an enriched melt that was in equilibrium with these clinopyroxenes. The moderate enrichment "inflection" of LREEs in the residual clinopyroxenes cannot be reproduced by fractional melting alone and rather indicates the involvement of an enriched melt that reacted with the residual peridotite clinopyroxenes. Our open system models with moderate degrees of melting (between 7-10%) closely approximates the composition of the residual clinopyroxenes with moderate influx rates of β=0.01 and melt porosity α=0.01. The composition of the accumulated melts from these open system models also approximates the composition of Shikoku basin and Mado basalts. The enrichment in fluid mobile elements in the back-arc basalts with respect to N-MORB indicates the presence of hydrous melts in the system that acted as carriers of these fluid-mobile elements. We infer that reaction of refractory mantle with enriched hydrous melts played an important role in the evolution of the Mado Megamullion mantle peridotites and crustal basalts in the back-arc spreading system.

2.8. Supplementary Data 2

Supplementary Table S2 A: Major element composition of orthopyroxenes

Cruise ID	*Sample*	*SiO_2*	*TiO_2*	*Al_2O_3*	*FeO*	*MnO*	*MgO*	*CaO*	*Cr_2O_3*	*ZnO*	*NiO*	*Na_2O*	*K_2O*	*Total*	*Mg#*	*Cr#*	*Comment*
KH18-02	D12-R01	56.07	0.04	3.08	6.32	0.14	33.52	0.49	0.48		0.10	0.00	0.01	100.25	0.90	0.09	
KH18-02	D12-R01	55.11	0.05	4.15	6.46	0.13	32.54	0.67	0.76		0.09	0.09	0.01	100.05	0.90	0.11	
KH18-02	D12-R01	53.77	0.18	4.92	5.49	0.14	30.64	2.60	0.67		0.08	0.27	0.00	98.76	0.91	0.08	
KH18-02	D12-R01	56.50	0.08	2.49	6.45	0.16	33.92	0.42	0.31		0.05	0.00	0.00	100.39	0.90	0.08	
KH18-02	D12-R01	55.96	0.07	3.10	6.48	0.12	33.69	0.41	0.46		0.08	0.00	0.01	100.37	0.91	0.09	
KH18-02	D12-R01	55.75	0.05	3.69	6.52	0.16	33.13	0.43	0.59		0.06	0.02	0.00	100.40	0.90	0.10	
KH18-02	D12-R01	55.42	0.02	3.78	6.35	0.16	33.03	0.40	0.57		0.08	0.00	0.00	99.80	0.90	0.09	
KH18-02	D12-R01	56.02	0.01	2.75	6.51	0.15	33.75	0.32	0.43		0.09	0.00	0.01	100.04	0.91	0.09	
KH18-02	D12-R01	55.91	0.05	2.94	6.52	0.16	33.85	0.43	0.48		0.08	0.00	0.00	100.42	0.91	0.10	
KH18-02	D12-R01	56.80	0.02	2.57	6.24	0.18	33.68	0.37	0.66		0.08	0.00	0.00	100.60	0.91	0.15	
KH18-02	D12-R03	55.98	0.06	3.66	6.32	0.16	33.45	0.56	0.60		0.11	0.00	0.01	100.89	0.90	0.10	
KH18-02	D12-R03	55.94	0.07	3.74	6.40	0.13	33.36	0.57	0.66		0.12	0.00	0.01	101.00	0.90	0.11	
KH18-02	D12-R03	54.59	0.00	4.20	6.32	0.15	33.21	0.52	0.78		0.12	0.02	0.00	99.91	0.92	0.11	
KH18-02	D12-R03	55.32	0.04	3.70	6.44	0.12	33.22	0.49	0.66		0.13	0.01	0.01	100.14	0.91	0.11	
KH18-02	D12-R03	55.95	0.07	2.58	6.39	0.15	34.12	0.39	0.47		0.09	0.00	0.00	100.21	0.92	0.11	
KH18-02	D12-R03	56.46	0.05	2.70	6.51	0.22	33.75	0.37	0.50		0.07	0.00	0.01	100.64	0.90	0.11	
KH18-02	D12-R03	54.97	0.11	5.14	6.41	0.15	33.15	0.50	0.92		0.07	0.00	0.01	101.43	0.91	0.11	
KH18-02	D12-R03	54.98	0.03	4.58	6.24	0.12	32.71	0.49	0.84		0.08	0.00	0.01	100.09	0.90	0.11	
KH18-02	D12-R03	54.95	0.03	4.65	6.39	0.17	33.07	0.41	0.91		0.14	0.00	0.00	100.72	0.91	0.12	
KH18-02	D12-R03	55.51	0.04	4.11	6.35	0.13	33.34	0.55	0.81		0.07	0.00	0.00	100.91	0.91	0.12	
KH18-02	D12-R04	52.03	0.07	6.32	6.68	0.16	32.48	0.67	0.80		0.06	0.00	0.01	99.27	0.90	0.08	Exsolution of Cpx
KH18-02	D12-R04	55.81	0.02	4.21	6.37	0.14	33.70	0.50	0.59		0.14	0.00	0.00	101.49	0.90	0.09	Exsolution of Cpx
KH18-02	D12-R05	57.15	0.00	2.35	6.64	0.14	34.02	0.46	0.56	0.00	0.05	0.03	0.00	101.40	0.90	0.14	
KH18-02	D12-R05	56.85	0.00	2.56	6.74	0.14	33.81	0.38	0.50	0.00	0.05	0.02	0.00	101.04	0.90	0.12	

Cruise ID	*Sample*	*SiO_2*	*TiO_2*	*Al_2O_3*	*FeO*	*MnO*	*MgO*	*CaO*	*Cr_2O_3*	*ZnO*	*NiO*	*Na_2O*	*K_2O*	*Total*	*Mg#*	*Cr#*	*Comment*
KH18-02	D12-R05	56.74	0.02	2.85	6.61	0.15	33.58	0.65	0.51	0.00	0.08	0.01	0.00	101.19	0.90	0.11	
KH18-02	D12-R06	53.73	0.00	5.18	6.20	0.13	33.08	0.50	0.86		0.08	0.01	0.01	99.77	0.90	0.10	
KH18-02	D12-R06	53.97	0.06	5.27	6.27	0.12	33.37	0.52	0.83		0.09	0.00	0.00	100.50	0.90	0.10	
KH18-02	D12-R06	54.10	0.01	5.00	6.38	0.08	32.71	0.86	0.84		0.17	0.04	0.01	100.21	0.90	0.10	
KH18-02	D12-R06	53.86	0.04	5.33	6.15	0.10	32.90	0.75	0.90		0.08	0.02	0.00	100.12	0.91	0.10	
KH18-02	D12-R06	55.37	0.00	5.01	6.51	0.10	32.88	0.69	0.79	0.00	0.07	0.00	0.02	101.45	0.90	0.10	
KH18-02	D12-R06	54.74	0.07	5.36	5.85	0.09	30.53	3.79	0.84	0.00	0.06	0.04	0.00	101.36	0.90	0.10	
KH18-02	D12-R06	55.33	0.03	4.83	6.24	0.11	31.62	2.65	0.80	0.00	0.09	0.00	0.00	101.70	0.90	0.10	
KH18-02	D12-R06	55.17	0.02	4.82	6.52	0.12	33.20	0.61	0.72	0.00	0.08	0.03	0.00	101.29	0.90	0.09	
KH18-02	D12-R06	55.42	0.00	4.84	6.40	0.09	32.97	0.53	0.71	0.00	0.09	0.02	0.00	101.06	0.90	0.09	
KH18-02	D12-R07	55.63	0.10	3.23	6.18	0.13	32.90	0.60	0.97		0.08	0.02	0.02	99.85	0.90	0.17	
KH18-02	D12-R07	55.57	0.05	3.25	6.07	0.13	33.19	0.59	0.85		0.08	0.00	0.00	99.77	0.91	0.15	
KH18-02	D12-R07	55.52	0.10	3.18	6.10	0.16	33.40	0.59	0.82		0.12	0.01	0.00	99.99	0.91	0.15	
KH18-02	D12-R07	54.63	0.03	2.98	6.61	0.57	34.22	0.41	0.16		0.08	0.03	0.01	99.73	0.90	0.11	
KH18-02	D12-R07	54.54	0.04	3.15	6.57	0.49	33.37	0.44	0.14		0.09	0.00	0.00	98.84	0.90	0.09	
KH18-02	D12-R08	57.06	0.00	1.20	6.34	0.15	34.67	0.36	0.27		0.10	0.01	0.00	100.17	0.91	0.13	
KH18-02	D12-R08	55.79	0.01	2.93	6.54	0.14	33.57	0.35	0.77		0.09	0.00	0.01	100.21	0.90	0.15	
KH18-02	D12-R08	56.18	0.00	3.05	6.62	0.16	33.50	0.40	0.57		0.11	0.00	0.00	100.59	0.90	0.11	
KH18-02	D12-R08	56.05	0.06	2.77	6.56	0.16	34.16	0.40	0.72		0.07	0.01	0.01	100.96	0.90	0.15	
KH18-02	D12-R08	57.18	0.01	1.32	6.49	0.18	35.01	0.35	0.26		0.13	0.00	0.00	100.93	0.91	0.12	
KH18-02	D12-R08	56.56	0.02	2.29	6.39	0.19	34.30	0.43	0.65		0.09	0.00	0.01	100.93	0.91	0.16	
KH18-02	D12-R18	55.26	0.02	3.18	6.79	0.16	34.27	0.29	0.67		0.08	0.01	0.00	100.73	0.93	0.12	Exsolution of Cpx
KH18-02	D12-R18	55.78	0.02	3.21	6.73	0.17	34.20	0.63	0.46		0.08	0.11	0.02	101.40	0.93	0.09	Exsolution of Cpx
KH18-02	D12-R18	55.67	0.01	3.66	6.66	0.16	33.43	0.87	0.59		0.09	0.07	0.01	101.22	0.91	0.10	Exsolution of Cpx
KH18-02	D12-R18	55.21	0.06	2.86	9.44	0.24	32.42	0.27	0.51		0.06	0.00	0.00	101.07	0.88	0.11	Exsolution of Cpx
KH18-02	D12-R18	55.34	0.02	2.56	9.81	0.21	32.69	0.26	0.33		0.14	0.00	0.00	101.36	0.89	0.08	Exsolution of Cpx
KH18-02	D12-R18	55.14	0.09	3.07	9.71	0.23	32.14	0.28	0.62		0.17	0.00	0.05	101.50	0.88	0.12	Exsolution of Cpx

Cruise ID	*Sample*	*SiO_2*	*TiO_2*	*Al_2O_3*	*FeO*	*MnO*	*MgO*	*CaO*	*Cr_2O_3*	*ZnO*	*NiO*	*Na_2O*	*K_2O*	*Total*	*Mg#*	*Cr#*	*Comment*
KH18-02	D12-R19	56.08	0.04	2.68	6.95	0.17	33.82	0.38	0.39		0.08	0.10	0.02	100.72	0.90	0.09	
KH18-02	D12-R19	56.28	0.03	2.47	6.82	0.14	34.02	0.32	0.59		0.08	0.04	0.00	100.80	0.90	0.14	
KH18-02	D12-R20	56.44	0.06	3.26	6.11	0.16	34.06	0.61	0.51		0.13	0.02	0.01	101.37	0.91	0.09	
KH18-02	D12-R20	56.84	0.07	1.91	6.25	0.15	34.94	0.39	0.22		0.08	0.00	0.00	100.85	0.91	0.07	
KH18-02	D12-R20	56.01	0.08	3.01	6.47	0.13	34.14	0.66	0.64		0.14	0.01	0.01	101.31	0.90	0.12	
KH18-02	D12-R20	56.56	0.02	3.20	6.20	0.12	34.33	0.38	0.60		0.02	0.00	0.00	101.43	0.91	0.11	
KH18-02	D12-R20	56.95	0.04	2.55	6.35	0.13	34.30	0.39	0.37		0.05	0.01	0.01	101.16	0.91	0.09	
KH18-02	D12-R20	57.36	0.06	1.75	6.40	0.13	35.03	0.43	0.35		0.07	0.01	0.00	101.59	0.91	0.12	
KH18-02	D12-R20	57.21	0.03	1.74	6.26	0.14	34.91	0.44	0.29		0.11	0.00	0.00	101.13	0.91	0.10	
KH18-02	D12-R20	57.06	0.07	1.96	6.23	0.15	34.68	0.43	0.28		0.08	0.02	0.00	100.96	0.91	0.09	
KH18-02	D12-R20	56.14	0.06	2.76	6.22	0.12	34.29	0.42	0.44		0.09	0.00	0.00	100.54	0.91	0.10	
KH18-02	D12-R20	56.01	0.08	3.01	6.47	0.13	34.14	0.66	0.64		0.14	0.01	0.01	101.31	0.90	0.12	
KH18-02	D12-R20	56.56	0.02	3.20	6.20	0.12	34.33	0.38	0.60		0.02	0.00	0.00	101.43	0.91	0.11	
KH18-02	D12-R20	56.95	0.04	2.55	6.35	0.13	34.30	0.39	0.37		0.05	0.01	0.01	101.16	0.91	0.09	
KH18-02	D12-R20	56.90	0.02	2.38	6.29	0.15	34.55	0.40	0.27		0.13	0.00	0.00	101.08	0.91	0.07	
KH18-02	D12-R33	54.89	0.09	4.92	6.71	0.15	32.62	0.80	0.78	0.00	0.12	0.00	0.00	101.10	0.90	0.10	
KH18-02	D12-R33	55.01	0.09	5.26	6.55	0.15	32.50	0.92	0.81	0.01	0.09	0.02	0.00	101.41	0.90	0.09	
KH18-02	D12-R33	54.97	0.07	5.10	6.43	0.13	32.95	0.58	0.78	0.01	0.09	0.01	0.00	101.12	0.90	0.09	
KH18-02	D12-R33	55.07	0.05	5.11	6.51	0.15	32.80	0.61	0.81	0.00	0.08	0.02	0.00	101.22	0.90	0.10	
YK18-07	6K-1515-R02	54.42	0.05	4.67	6.41	0.66	32.60	0.54	0.17		0.08	0.02	0.01	99.62	0.91	0.10	
YK18-07	6K-1515-R02	54.65	0.03	4.38	6.63	0.63	33.08	0.36	0.14		0.01	0.01	0.00	99.91	0.91	0.10	
YK18-07	6K-1515-R02	54.84	0.04	3.85	6.29	0.58	32.95	0.61	0.11		0.09	0.02	0.01	99.40	0.91	0.10	
YK18-07	6K-1515-R02	55.20	0.07	3.93	6.54	0.52	33.22	0.83	0.21		0.09	0.04	0.00	100.65	0.92	0.09	
YK18-07	6K-1515-R02	54.44	0.08	4.86	6.21	0.64	31.48	1.72	0.17		0.11	0.19	0.04	99.92	0.90	0.09	
YK18-07	6K-1515-R02	54.97	0.06	3.90	6.31	0.55	33.49	0.52	0.12		0.10	0.00	0.00	100.02	0.92	0.09	
YK18-07	6K-1515-R02	54.88	0.06	3.43	6.68	0.42	33.61	0.74	0.16		0.03	0.02	0.00	100.02	0.93	0.08	Exsolution of Cpx

Cruise ID	*Sample*	*SiO_2*	*TiO_2*	*Al_2O_3*	*FeO*	*MnO*	*MgO*	*CaO*	*Cr_2O_3*	*ZnO*	*NiO*	*Na_2O*	*K_2O*	*Total*	*Mg#*	*Cr#*	*Comment*
YK18-07	6K-1515-R02	55.04	0.05	3.80	6.40	0.48	33.37	0.61	0.14		0.08	0.00	0.01	99.99	0.92	0.09	Exsolution of Cpx
YK18-07	6K-1515-R02	55.89	0.04	3.26	6.64	0.49	33.44	0.29	0.16		0.05	0.00	0.00	100.27	0.90	0.10	Exsolution of Cpx
YK18-07	6K-1515-R02	54.02	0.10	4.94	8.57	0.71	31.30	0.56	0.22		0.07	0.00	0.00	100.49	0.88	0.10	
YK18-07	6K-1515-R03	54.89	0.09	4.70	6.60	0.72	33.19	0.38	0.14		0.05	0.00	0.00	100.76	0.91	0.10	
YK18-07	6K-1515-R03	54.31	0.10	5.16	6.51	0.77	32.66	0.40	0.11		0.15	0.00	0.00	100.17	0.91	0.10	
YK18-07	6K-1515-R03	54.57	0.07	4.79	6.35	0.73	33.10	0.34	0.14		0.03	0.04	0.00	100.16	0.91	0.10	
YK18-07	6K-1515-R03	54.92	0.10	4.92	6.58	0.79	33.44	0.39	0.17		0.10	0.02	0.00	101.43	0.92	0.11	
YK18-07	6K-1515-R03	54.40	0.06	5.12	6.84	0.77	32.82	0.40	0.13		0.08	0.00	0.00	100.62	0.91	0.10	
YK18-07	6K-1515-R03	54.74	0.08	4.77	6.59	0.74	33.04	0.39	0.15		0.07	0.00	0.00	100.56	0.91	0.10	
YK18-07	6K-1515-R10	54.57	0.02	4.55	6.57	0.77	32.93	0.34	0.17		0.08	0.00	0.00	100.00	0.91	0.10	
YK18-07	6K-1515-R10	54.90	0.02	4.49	6.80	0.80	32.33	0.44	0.16		0.11	0.09	0.01	100.13	0.89	0.11	
YK18-07	6K-1515-R10	54.18	0.05	4.91	6.85	0.79	32.26	0.39	0.15		0.09	0.00	0.00	99.67	0.90	0.10	
YK18-07	6K-1515-R15	53.92	0.08	5.41	6.52	0.74	32.38	0.62	0.14		0.08	0.00	0.05	99.93	0.91	0.09	
YK18-07	6K-1515-R15	54.34	0.09	5.31	6.52	0.84	32.54	0.71	0.15		0.03	0.00	0.01	100.55	0.91	0.11	
YK18-07	6K-1515-R15	55.08	0.04	3.97	7.36	0.53	33.30	0.70	0.19		0.03	0.00	0.01	101.20	0.92	0.09	
YK18-07	6K-1515-R15	54.83	0.09	4.78	6.57	0.67	33.29	0.38	0.13		0.06	0.02	0.00	100.83	0.91	0.09	

Supplementary Table S2 B: Major element composition of clinopyroxenes

Cruise ID	*Sample*	*SiO2*	*TiO2*	*Al2O3*	*FeO*	*MnO*	*MgO*	*CaO*	*Cr2O3*	*ZnO*	*NiO*	*Na2O*	*K2O*	*Total*	*Mg#*	*Cr#*	*Comment*
KH18-02	D12-R01	52.96	0.19	1.67	2.15	0.05	17.42	23.98	0.81	0.06	0.02	0.08	0.00	99.39	0.94	0.25	
KH18-02	D12-R01	54.40	0.17	1.34	1.95	0.04	17.82	24.16	0.40	0.05	0.05	0.09	0.00	100.46	0.94	0.17	
KH18-02	D12-R01	54.51	0.17	1.60	1.99	0.04	17.53	24.22	0.41	0.01	0.04	0.10	0.00	100.61	0.94	0.15	
KH18-02	D12-R01	54.71	0.17	1.37	2.14	0.07	17.86	23.95	0.40	0.07	0.04	0.10	0.00	100.88	0.94	0.16	
KH18-02	D12-R01	53.90	0.15	1.63	2.01	0.02	17.34	23.97	0.48		0.05	0.13	0.00	99.68	0.94	0.16	
KH18-02	D12-R01	52.93	0.15	2.63	2.12	0.09	17.16	23.98	0.52		0.03	0.12	0.00	99.72	0.94	0.12	
KH18-02	D12-R01	53.17	0.26	2.18	2.08	0.05	16.89	23.89	0.42		0.06	0.15	0.00	99.16	0.94	0.12	
KH18-02	D12-R01	52.61	0.21	2.04	2.14	0.08	17.16	23.64	0.62		0.00	0.14	0.00	98.65	0.93	0.17	
KH18-02	D12-R01	53.94	0.11	1.47	2.07	0.10	17.30	23.89	0.42		0.05	0.13	0.00	99.48	0.94	0.16	
KH18-02	D12-R01	53.62	0.06	1.43	2.28	0.09	17.58	23.69	0.37		0.01	0.13	0.01	99.27	0.93	0.15	
KH18-02	D12-R01	54.13	0.11	1.45	2.09	0.13	17.45	23.70	0.42		0.03	0.17	0.00	99.68	0.94	0.16	
KH18-02	D12-R01	54.04	0.10	1.35	2.01	0.07	17.36	23.97	0.44		0.02	0.14	0.01	99.51	0.94	0.18	
KH18-02	D12-R01	54.27	0.08	1.60	2.13	0.07	17.34	23.45	0.23		0.02	0.10	0.00	99.29	0.94	0.09	
KH18-02	D12-R01	53.98	0.10	1.46	2.06	0.04	17.29	24.14	0.42		0.05	0.18	0.00	99.71	0.94	0.16	
KH18-02	D12-R01	53.62	0.13	2.10	2.17	0.05	17.15	23.70	0.60		0.07	0.15	0.00	99.74	0.93	0.16	
KH18-02	D12-R01	54.58	0.10	1.43	2.04	0.05	17.37	23.98	0.46		0.08	0.09	0.00	100.19	0.94	0.18	
KH18-02	D12-R01	54.28	0.11	1.73	2.12	0.01	17.32	23.96	0.57		0.04	0.12	0.00	100.25	0.94	0.18	
KH18-02	D12-R01	52.48	0.26	4.33	2.21	0.04	17.29	21.09	0.78		0.02	0.56	0.01	99.05	0.93	0.11	
KH18-02	D12-R01	53.15	0.16	2.50	2.02	0.08	16.62	23.89	0.84		0.01	0.14	0.00	99.41	0.94	0.18	
KH18-02	D12-R01	52.45	0.20	3.75	2.25	0.08	16.24	24.04	0.71		0.00	0.17	0.00	99.89	0.93	0.11	
KH18-02	D12-R01	54.86	0.11	1.34	2.11	0.05	17.47	23.99	0.39		0.05	0.16	0.00	100.55	0.94	0.16	
KH18-02	D12-R03	53.40	0.23	2.16	1.99	0.06	16.85	23.88	0.62		0.01	0.14	0.00	99.34	0.94	0.16	
KH18-02	D12-R03	53.29	0.23	2.27	2.09	0.07	16.99	23.98	0.61		0.05	0.08	0.00	99.66	0.94	0.15	
KH18-02	D12-R03	53.59	0.20	1.88	1.99	0.09	17.04	24.01	0.57		0.01	0.08	0.00	99.45	0.94	0.17	
KH18-02	D12-R03	53.96	0.19	1.70	2.00	0.07	17.29	24.27	0.56		0.10	0.11	0.01	100.25	0.94	0.18	
KH18-02	D12-R03	51.62	0.21	4.49	2.11	0.08	16.21	24.18	1.01		0.08	0.15	0.00	100.14	0.94	0.13	
KH18-02	D12-R03	51.73	0.33	5.24	2.12	0.04	16.09	23.57	1.21		0.05	0.17	0.01	100.57	0.93	0.13	
KH18-02	D12-R03	51.46	0.27	4.47	2.41	0.10	16.04	23.76	1.00		0.06	0.09	0.00	99.66	0.92	0.13	
KH18-02	D12-R03	52.59	0.15	3.72	2.29	0.09	16.37	23.91	0.85		0.05	0.18	0.00	100.20	0.93	0.13	
KH18-02	D12-R03	51.67	0.22	4.31	2.27	0.09	16.08	23.99	0.91		0.01	0.14	0.00	99.69	0.93	0.12	
KH18-02	D12-R03	51.01	0.18	5.21	2.20	0.06	15.89	23.99	1.29		0.05	0.14	0.00	100.02	0.93	0.14	Exsolved Cpx
KH18-02	D12-R03	51.73	0.21	4.49	2.25	0.06	16.03	24.02	1.14		0.01	0.14	0.00	100.08	0.93	0.15	Exsolved Cpx
KH18-02	D12-R04	53.18	0.23	3.42	2.22	0.08	17.03	23.35	0.64		0.09	0.11	0.00	100.35	0.93	0.11	Exsolved Cpx

Cruise ID	*Sample*	*SiO2*	*TiO2*	*Al2O3*	*FeO*	*MnO*	*MgO*	*CaO*	*Cr2O3*	*ZnO*	*NiO*	*Na2O*	*K2O*	*Total*	*Mg#*	*Cr#*	*Comment*
KH18-02	D12-R04	52.28	0.27	3.46	2.37	0.07	16.72	23.63	0.85		0.08	0.09	0.00	99.82	0.93	0.14	Exsolved Cpx
KH18-02	D12-R04	51.80	0.19	4.70	2.52	0.08	16.32	22.81	1.08		0.00	0.11	0.00	99.61	0.92	0.13	Exsolved Cpx
KH18-02	D12-R04	52.26	0.26	4.51	2.32	0.09	16.29	23.04	0.73		0.07	0.15	0.00	99.72	0.93	0.10	Exsolved Cpx
KH18-02	D12-R04	51.65	0.18	4.88	2.52	0.10	16.00	23.08	1.09		0.08	0.11	0.02	99.71	0.92	0.13	Exsolved Cpx
KH18-02	D12-R05	50.97	0.24	5.76	3.34	0.12	17.41	18.86	1.60	0.00	0.07	1.27	0.07	99.69	0.90	0.16	
KH18-02	D12-R05	53.73	0.05	1.83	3.12	0.17	16.55	23.00	0.83	0.03	0.04	0.43	0.01	99.78	0.90	0.23	
KH18-02	D12-R05	53.53	0.11	2.34	2.91	0.15	17.00	22.65	0.86	0.03	0.04	0.59	0.00	100.20	0.91	0.20	
KH18-02	D12-R05	52.92	0.09	3.44	2.35	0.10	17.26	21.82	1.09	0.05	0.05	0.78	0.04	99.97	0.93	0.17	
KH18-02	D12-R05	53.34	0.13	2.82	2.37	0.09	16.46	22.53	1.10	0.01	0.07	0.50	0.00	99.41	0.93	0.21	
KH18-02	D12-R05	51.65	0.50	4.86	2.77	0.09	17.39	19.54	1.20	0.00	0.03	1.17	0.11	99.31	0.92	0.14	
KH18-02	D12-R06	50.63	0.17	6.17	2.65	0.07	15.66	22.50	1.29		0.07	0.31	0.00	99.54	0.91	0.12	
KH18-02	D12-R06	50.72	0.20	5.95	2.38	0.06	15.91	22.47	1.31		0.03	0.24	0.00	99.27	0.92	0.13	
KH18-02	D12-R06	50.42	0.20	5.89	2.44	0.12	15.71	22.37	1.28		0.02	0.33	0.03	98.80	0.92	0.13	
KH18-02	D12-R06	51.25	0.19	5.73	2.25	0.06	16.00	22.42	1.35		0.03	0.37	0.01	99.65	0.93	0.14	
KH18-02	D12-R06	51.07	0.22	5.65	2.31	0.06	15.83	23.18	1.25		0.02	0.26	0.00	99.84	0.92	0.13	
KH18-02	D12-R06	51.48	0.23	4.93	2.23	0.10	16.27	22.97	1.13		0.06	0.22	0.00	99.61	0.93	0.13	
KH18-02	D12-R06	50.66	0.24	4.96	2.08	0.07	15.29	21.41	1.00		0.08	0.28	0.00	96.08	0.93	0.12	Exsolved Cpx
KH18-02	D12-R06	49.97	0.21	5.11	2.05	0.10	15.81	21.28	0.99		0.01	0.21	0.00	95.74	0.93	0.11	Exsolved Cpx
KH18-02	D12-R06	49.50	0.23	5.04	2.09	0.08	15.72	21.48	1.02		0.10	0.25	0.00	95.50	0.93	0.12	Exsolved Cpx
KH18-02	D12-R06	50.15	0.11	6.48	2.32	0.08	15.47	21.95	1.27		0.07	0.34	0.00	98.24	0.92	0.12	
KH18-02	D12-R06	49.86	0.19	6.23	2.53	0.11	15.70	22.05	1.25		0.10	0.32	0.01	98.36	0.92	0.12	
KH18-02	D12-R06	50.15	0.19	5.71	2.44	0.09	15.96	22.28	1.17		0.03	0.23	0.01	98.27	0.92	0.12	
KH18-02	D12-R06	50.56	0.15	6.22	2.49	0.08	15.60	22.09	1.24		0.03	0.26	0.00	98.72	0.92	0.12	
KH18-02	D12-R06	50.58	0.17	6.11	2.39	0.10	15.56	22.29	1.27		0.07	0.30	0.00	98.83	0.92	0.12	
KH18-02	D12-R06	50.42	0.17	6.28	2.56	0.06	15.45	22.30	1.35		0.06	0.22	0.00	98.86	0.91	0.13	
KH18-02	D12-R06	50.47	0.17	6.26	2.50	0.07	15.79	22.23	1.21		0.04	0.32	0.00	99.07	0.92	0.12	
KH18-02	D12-R06	50.48	0.21	5.67	2.22	0.07	15.98	22.38	0.96		0.09	0.28	0.00	98.33	0.93	0.10	
KH18-02	D12-R06	50.73	0.27	5.25	2.20	0.06	15.74	22.77	1.07		0.10	0.23	0.00	98.42	0.93	0.12	Exsolved Cpx
KH18-02	D12-R06	50.87	0.25	5.51	2.26	0.07	15.95	22.29	1.18		0.11	0.26	0.01	98.75	0.93	0.13	Exsolved Cpx
KH18-02	D12-R06	50.79	0.25	5.33	2.23	0.07	16.04	22.66	1.10		0.09	0.24	0.00	98.80	0.93	0.12	Exsolved Cpx

Cruise ID	*Sample*	*SiO2*	*TiO2*	*Al2O3*	*FeO*	*MnO*	*MgO*	*CaO*	*Cr2O3*	*ZnO*	*NiO*	*Na2O*	*K2O*	*Total*	*Mg#*	*Cr#*	*Comment*
KH18-02	D12-R06	53.93	0.16	2.11	2.00	0.04	16.95	23.35	0.88	0.00	0.04	0.27	0.01	99.73	0.94	0.22	
KH18-02	D12-R06	52.42	0.18	4.42	2.25	0.05	16.28	23.44	1.06	0.00	0.01	0.30	0.00	100.40	0.93	0.14	
KH18-02	D12-R06	53.59	0.18	3.10	2.26	0.07	16.80	22.96	1.09	0.00	0.02	0.29	0.00	100.35	0.93	0.19	
KH18-02	D12-R06	52.65	0.17	3.94	2.24	0.05	16.51	23.23	1.05	0.00	0.04	0.32	0.00	100.21	0.93	0.15	
KH18-02	D12-R06	51.81	0.23	4.70	2.24	0.04	15.81	23.01	1.15	0.00	0.02	0.34	0.01	99.36	0.93	0.14	
KH18-02	D12-R06	53.02	0.21	3.69	2.17	0.02	16.42	23.13	1.22	0.00	0.05	0.33	0.00	100.26	0.93	0.18	
KH18-02	D12-R06	52.82	0.22	4.63	2.30	0.06	16.28	22.98	1.17	0.00	0.04	0.36	0.00	100.85	0.93	0.14	
KH18-02	D12-R08	53.00	0.36	4.84	2.34	0.04	18.18	19.62	0.94		0.08	0.75	0.03	100.19	0.93	0.12	
KH18-02	D12-R08	53.68	0.12	1.83	2.05	0.09	17.69	22.58	0.58		0.05	0.26	0.02	98.95	0.94	0.18	
KH18-02	D12-R08	54.37	0.04	1.27	2.23	0.11	17.85	22.80	0.46		0.06	0.21	0.00	99.39	0.93	0.20	
KH18-02	D12-R08	53.13	0.14	3.36	2.29	0.06	16.52	23.08	0.91		0.10	0.21	0.00	99.81	0.93	0.15	Exsolved Cpx
KH18-02	D12-R08	53.60	0.07	2.59	2.23	0.09	16.97	23.26	0.78		0.11	0.24	0.00	99.93	0.93	0.17	Exsolved Cpx
KH18-02	D12-R08	54.44	0.09	1.45	2.08	0.08	17.47	23.16	0.51		0.03	0.16	0.00	99.47	0.94	0.19	Exsolved Cpx
KH18-02	D12-R10	54.10	0.05	1.62	2.06	0.08	17.29	23.66	0.56		0.03	0.26	0.01	99.71	0.94	0.19	
KH18-02	D12-R10	54.36	0.00	1.28	2.03	0.09	17.30	23.93	0.49		0.01	0.15	0.00	99.65	0.94	0.20	
KH18-02	D12-R10	54.36	0.02	1.18	1.99	0.04	17.50	23.90	0.50		0.00	0.15	0.03	99.67	0.94	0.22	
KH18-02	D12-R10	54.48	0.10	1.31	2.08	0.05	17.43	24.00	0.43		0.06	0.21	0.00	100.15	0.94	0.18	
KH18-02	D12-R10	54.72	0.04	1.46	2.16	0.10	17.17	23.47	0.49		0.08	0.20	0.00	99.90	0.93	0.18	
KH18-02	D12-R10	54.55	0.00	1.42	2.07	0.05	17.43	23.77	0.49		0.02	0.21	0.00	100.00	0.94	0.19	
KH18-02	D12-R11	54.76	0.05	0.68	1.94	0.05	18.31	23.57	0.23		0.10	0.19	0.01	99.89	0.94	0.18	Exsolved Cpx
KH18-02	D12-R11	54.22	0.01	0.77	2.06	0.06	18.25	23.18	0.22		0.05	0.20	0.00	99.02	0.94	0.16	Exsolved Cpx
KH18-02	D12-R11	54.57	0.04	0.70	2.02	0.07	18.33	23.43	0.24		0.03	0.16	0.00	99.59	0.94	0.19	Exsolved Cpx
KH18-02	D12-R11	54.80	0.04	1.03	1.97	0.06	18.09	23.56	0.61		0.04	0.19	0.00	100.38	0.94	0.28	Exsolved Cpx
KH18-02	D12-R11	54.80	0.02	1.11	2.06	0.03	17.73	23.38	0.79		0.06	0.27	0.00	100.25	0.94	0.32	Exsolved Cpx
KH18-02	D12-R11	54.96	0.01	1.08	2.03	0.07	18.22	23.37	0.66		0.09	0.20	0.01	100.70	0.94	0.29	Exsolved Cpx
KH18-02	D12-R17	54.09	0.07	0.58	1.87	0.19	17.93	24.93	0.06		0.01	0.15	0.00	99.87	0.94	0.18	
KH18-02	D12-R17	53.85	0.02	1.10	2.10	0.41	17.92	24.63	0.06		0.04	0.19	0.00	100.32	0.94	0.20	
KH18-02	D12-R18	53.33	0.12	3.10	2.47	0.07	18.39	21.14	0.68		0.02	0.63	0.08	100.04	0.93	0.13	
KH18-02	D12-R18	52.98	0.14	4.19	2.74	0.10	18.56	19.62	0.80		0.11	0.84	0.10	100.18	0.92	0.11	
KH18-02	D12-R18	53.21	0.10	3.33	2.48	0.07	18.32	20.62	0.70		0.05	0.71	0.07	99.67	0.93	0.12	
KH18-02	D12-R19	54.31	0.02	1.43	2.18	0.08	17.73	22.94	0.65		0.02	0.27	0.00	99.63	0.94	0.23	

Cruise ID	*Sample*	*SiO2*	*TiO2*	*Al2O3*	*FeO*	*MnO*	*MgO*	*CaO*	*Cr2O3*	*ZnO*	*NiO*	*Na2O*	*K2O*	*Total*	*Mg#*	*Cr#*	*Comment*
KH18-02	D12-R19	54.46	0.04	1.14	2.04	0.07	17.52	23.63	0.66		0.00	0.20	0.00	99.77	0.94	0.28	
KH18-02	D12-R19	54.68	0.05	1.26	2.20	0.09	17.54	23.11	0.66		0.04	0.21	0.00	99.85	0.93	0.26	
KH18-02	D12-R19	54.66	0.05	1.45	2.18	0.05	17.74	23.27	0.59		0.06	0.27	0.01	100.34	0.94	0.22	
KH18-02	D12-R19	54.94	0.03	1.03	2.13	0.06	17.68	23.57	0.43		0.00	0.15	0.01	100.03	0.94	0.22	
KH18-02	D12-R19	54.56	0.00	1.21	2.14	0.06	17.93	23.26	0.58		0.04	0.26	0.00	100.05	0.94	0.24	
KH18-02	D12-R19	53.88	0.07	2.29	2.33	0.06	18.38	20.89	0.67		0.11	0.60	0.00	99.28	0.93	0.16	
KH18-02	D12-R19	54.04	0.14	2.32	2.12	0.05	17.34	23.89	0.41	0.00	0.02	0.12	0.00	100.44	0.94	0.11	
KH18-02	D12-R19	54.30	0.11	2.02	2.14	0.03	17.46	23.78	0.34	0.00	0.00	0.10	0.00	100.27	0.94	0.10	
KH18-02	D12-R19	54.23	0.07	1.39	2.08	0.05	17.55	24.11	0.43	0.00	0.02	0.11	0.00	100.04	0.94	0.17	
KH18-02	D12-R20	51.78	0.17	3.23	2.57	0.11	17.27	22.45	1.03		0.06	0.05	0.00	98.72	0.92	0.18	
KH18-02	D12-R20	53.12	0.13	2.26	2.23	0.09	17.87	22.94	1.18		0.05	0.11	0.00	99.99	0.93	0.26	
KH18-02	D12-R20	53.25	0.21	3.03	2.15	0.12	17.04	23.30	0.72		0.10	0.10	0.00	100.02	0.93	0.14	Exsolved Cpx
KH18-02	D12-R20	53.58	0.16	2.83	2.17	0.09	17.07	23.38	0.66		0.06	0.09	0.00	100.09	0.93	0.14	Exsolved Cpx
KH18-02	D12-R20	52.73	0.17	3.25	2.10	0.09	17.02	22.98	0.74		0.06	0.09	0.00	99.23	0.94	0.13	Exsolved Cpx
KH18-02	D12-R20	53.00	0.24	3.35	2.26	0.12	17.18	23.03	0.86		0.04	0.10	0.00	100.18	0.93	0.15	Exsolved Cpx
KH18-02	D12-R20	51.70	0.23	4.16	2.51	0.05	17.36	22.67	1.15		0.11	0.06	0.00	100.00	0.92	0.16	Exsolved Cpx
KH18-02	D12-R33	52.93	0.24	2.53	2.15	0.10	17.19	23.47	0.99		0.07	0.20	0.01	99.86	0.93	0.21	
KH18-02	D12-R33	51.74	0.30	4.52	2.28	0.06	15.98	23.70	1.09		0.07	0.23	0.02	99.99	0.93	0.14	
KH18-02	D12-R33	51.73	0.32	5.20	2.18	0.07	15.40	23.44	1.17		0.06	0.26	0.00	99.83	0.93	0.13	
KH18-02	D12-R33	51.71	0.26	5.17	2.26	0.08	15.75	23.07	1.15		0.06	0.34	0.02	99.87	0.93	0.13	
KH18-02	D12-R33	54.92	0.10	2.37	3.04	0.07	22.31	18.04	0.28	0.00	0.02	0.07	0.00	101.20	0.93	0.07	
KH18-02	D12-R33	51.57	0.19	4.96	2.43	0.07	16.13	23.00	1.04	0.04	0.02	0.23	0.00	99.66	0.92	0.12	
KH18-02	D12-R33	50.95	0.17	5.13	2.43	0.06	15.53	23.15	1.07	0.00	0.02	0.28	0.00	98.78	0.92	0.12	
KH18-02	D12-R33	50.92	0.20	6.06	2.45	0.05	15.44	22.96	1.26	0.00	0.04	0.26	0.00	99.63	0.92	0.12	
KH18-02	D12-R33	50.96	0.20	6.03	2.50	0.07	15.64	22.94	1.25	0.02	0.00	0.23	0.00	99.84	0.92	0.12	
KH18-02	D12-R33	50.51	0.20	5.91	2.38	0.11	15.44	23.15	1.25	0.02	0.06	0.28	0.00	99.31	0.92	0.12	
KH18-02	D12-R33	51.14	0.20	6.01	2.43	0.08	15.39	22.87	1.30	0.07	0.08	0.26	0.01	99.84	0.92	0.13	
KH18-02	D12-R33	51.94	0.24	3.83	2.17	0.08	16.21	23.58	0.96	0.04	0.04	0.21	0.02	99.33	0.93	0.14	
KH18-02	D12-R33	52.31	0.23	4.08	2.26	0.08	16.30	23.35	0.85	0.02	0.06	0.17	0.01	99.72	0.93	0.12	
KH18-02	D12-R33	50.60	0.25	4.56	2.23	0.09	16.10	23.46	1.00	0.04	0.05	0.23	0.01	98.61	0.93	0.13	
KH18-02	D12-R33	53.48	0.24	3.08	2.21	0.06	16.81	23.41	0.56	0.09	0.04	0.22	0.02	100.21	0.93	0.11	
KH18-02	D12-R33	52.67	0.22	3.64	2.28	0.07	16.57	23.33	0.82	0.08	0.03	0.19	0.01	99.90	0.93	0.13	
KH18-02	D12-R33	51.91	0.24	3.95	2.21	0.06	16.35	23.23	0.85	0.06	0.07	0.17	0.01	99.11	0.93	0.13	
KH18-02	D12-R33	50.97	0.21	6.08	2.45	0.10	15.55	23.02	1.25	0.08	0.06	0.20	0.00	99.96	0.92	0.12	

Cruise ID	Sample	SiO2	TiO2	Al2O3	FeO	MnO	MgO	CaO	Cr2O3	ZnO	NiO	Na2O	K2O	Total	Mg#	Cr#	Comment
KH18-02	D15-R01	53.95	0.12	2.49	2.33	0.05	16.81	23.26	0.60		0.03	0.05	0.00	99.70	0.93	0.14	
KH18-02	D15-R01	53.40	0.13	3.04	2.62	0.13	17.02	22.65	0.84		0.06	0.12	0.01	100.02	0.92	0.16	
KH18-02	D15-R01	53.73	0.13	1.67	1.89	0.07	17.46	23.64	0.51		0.00	0.13	0.00	99.22	0.94	0.17	
KH18-02	D15-R01	53.37	0.13	2.62	2.02	0.09	17.15	23.39	0.89		0.00	0.14	0.00	99.81	0.94	0.19	
KH18-02	D15-R01	54.05	0.13	1.67	2.05	0.08	17.73	23.56	0.28		0.03	0.09	0.00	99.66	0.94	0.10	
KH18-02	D15-R01	53.40	0.11	2.56	2.20	0.08	17.10	23.43	0.56		0.03	0.09	0.01	99.58	0.93	0.13	
KH18-02	D15-R01	52.61	0.15	3.48	2.09	0.08	16.88	23.29	0.99		0.05	0.12	0.00	99.75	0.94	0.16	
KH18-02	D15-R01	51.98	0.14	4.05	2.31	0.10	16.48	23.20	0.99		0.08	0.12	0.00	99.45	0.93	0.14	
KH18-02	D15-R01	52.31	0.17	3.91	2.21	0.04	16.57	23.19	1.07		0.06	0.19	0.01	99.72	0.93	0.15	
KH18-02	D15-R01	54.13	0.10	2.10	1.77	0.09	17.33	23.44	0.44		0.05	0.11	0.00	99.56	0.95	0.12	
KH18-02	D15-R01	53.19	0.13	2.19	2.12	0.08	17.53	22.87	0.68		0.03	0.11	0.01	98.94	0.94	0.17	
KH18-02	D15-R01	53.74	0.12	2.08	2.26	0.07	17.48	23.38	0.63		0.04	0.09	0.00	99.89	0.93	0.17	
KH18-02	D15-R01	53.97	0.15	1.84	2.00	0.06	17.59	23.25	0.50		0.04	0.10	0.02	99.53	0.94	0.15	
KH18-02	D15-R01	51.61	0.18	4.94	2.18	0.08	15.84	23.30	1.46		0.07	0.12	0.01	99.78	0.93	0.17	
KH18-02	D15-R01	51.15	0.20	5.07	2.06	0.08	15.86	23.42	1.31		0.05	0.09	0.00	99.30	0.93	0.15	
KH18-02	D15-R01	51.27	0.16	5.26	2.12	0.03	15.61	23.42	1.47		0.03	0.13	0.01	99.51	0.93	0.16	
KH18-02	D15-R01	51.34	0.21	5.09	2.33	0.06	15.84	23.05	1.32		0.02	0.12	0.00	99.36	0.92	0.15	
KH18-02	D15-R01	51.65	0.25	4.86	2.06	0.04	15.89	23.36	1.57		0.08	0.12	0.00	99.86	0.93	0.18	
KH18-02	D15-R01	50.99	0.23	5.53	2.31	0.04	15.45	23.06	1.60		0.00	0.13	0.01	99.35	0.92	0.16	
KH18-02	D15-R01	51.04	0.21	5.43	2.72	0.07	17.02	21.08	1.62		0.01	0.12	0.00	99.32	0.92	0.17	
KH18-02	D15-R01	51.30	0.20	5.44	2.28	0.06	16.13	22.84	1.48		0.05	0.15	0.00	99.92	0.93	0.15	
KH18-02	D15-R01	53.25	0.13	3.41	2.43	0.06	17.09	22.87	0.89		0.05	0.13	0.00	100.31	0.93	0.15	
KH18-02	D15-R01	52.94	0.13	3.19	2.82	0.10	17.36	22.99	1.01		0.00	0.13	0.00	100.67	0.92	0.17	
KH18-02	D15-R01	51.80	0.14	3.80	2.32	0.09	16.80	23.09	0.98		0.02	0.15	0.00	99.19	0.93	0.15	
KH18-02	D15-R01	53.03	0.17	2.86	2.66	0.09	17.31	22.66	1.01		0.05	0.10	0.00	99.95	0.92	0.19	
KH18-02	D15-R01	53.61	0.20	2.73	2.71	0.07	17.16	23.35	0.89		0.00	0.10	0.00	100.81	0.92	0.18	
KH18-02	D15-R01	53.61	0.17	2.61	2.13	0.07	17.55	23.56	0.66		0.09	0.08	0.00	100.54	0.94	0.15	
KH18-02	D15-R01	53.71	0.10	1.89	2.40	0.11	17.91	23.03	0.62		0.02	0.09	0.01	99.89	0.93	0.18	
KH18-02	D15-R01	53.04	0.17	3.10	2.55	0.07	17.10	23.20	0.91		0.07	0.08	0.00	100.28	0.92	0.16	
KH18-02	D15-R01	51.44	0.15	5.22	2.50	0.07	16.22	22.85	1.43		0.08	0.10	0.00	100.07	0.92	0.16	
KH18-02	D15-R01	51.64	0.13	4.95	2.51	0.06	16.56	22.45	1.35		0.08	0.10	0.00	99.83	0.92	0.15	
KH18-02	D15-R01	51.64	0.16	5.06	2.34	0.05	15.94	22.97	1.37		0.01	0.11	0.00	99.64	0.92	0.15	
KH18-02	D15-R01	51.60	0.09	5.14	2.40	0.05	15.62	23.03	1.46		0.07	0.11	0.00	99.58	0.92	0.16	
YK18-07	6K-1515-R02	50.75	0.15	5.98	2.55	1.19	15.94	22.48	0.11		0.06	0.11	0.01	99.33	0.92	0.12	
YK18-07	6K-1515-R02	51.08	0.16	5.14	2.28	1.14	15.64	24.43	0.09		0.04	0.11	0.00	100.11	0.94	0.13	
YK18-07	6K-1515-R02	50.66	0.22	5.96	2.41	1.08	15.24	24.03	0.10		0.08	0.05	0.00	99.83	0.92	0.11	

Cruise ID	Sample	SiO2	TiO2	Al2O3	FeO	MnO	MgO	CaO	Cr2O3	ZnO	NiO	Na2O	K2O	Total	Mg#	Cr#	Comment
YK18-07	6K-1515-R03	51.89	0.21	4.39	2.13	1.04	16.46	24.32	0.05		0.03	0.18	0.00	100.69	0.95	0.14	Exsolved Cpx
YK18-07	6K-1515-R03	49.38	0.28	4.99	5.43	1.11	15.49	22.89	0.06		0.01	0.28	0.00	99.92	0.92	0.13	Exsolved Cpx
YK18-07	6K-1515-R03	50.98	0.33	5.80	2.20	1.09	15.55	23.74	0.07		0.07	0.17	0.01	100.01	0.93	0.11	Exsolved Cpx
YK18-07	6K-1515-R03	51.50	0.25	4.82	2.14	1.09	16.14	24.22	0.10		0.00	0.15	0.00	100.42	0.94	0.13	Exsolved Cpx
YK18-07	6K-1515-R03	53.07	0.15	2.93	2.04	0.68	16.77	24.09	0.06		0.04	0.12	0.00	99.96	0.94	0.13	
YK18-07	6K-1515-R03	51.99	0.18	3.97	2.17	0.88	16.54	23.86	0.10		0.02	0.16	0.00	99.87	0.93	0.13	
YK18-07	6K-1515-R03	53.74	0.05	1.69	2.00	0.38	17.57	24.07	0.06		0.10	0.08	0.01	99.76	0.94	0.13	
YK18-07	6K-1515-R03	53.14	0.16	2.86	2.09	0.71	16.98	24.37	0.09		0.02	0.10	0.01	100.53	0.94	0.14	
YK18-07	6K-1515-R03	52.37	0.23	4.06	2.13	0.90	16.74	23.14	0.03		0.05	0.34	0.00	100.00	0.93	0.13	
YK18-07	6K-1515-R03	52.72	0.19	3.70	2.22	0.65	17.94	20.95	0.10		0.07	0.54	0.00	99.07	0.94	0.11	
YK18-07	6K-1515-R03	52.77	0.19	2.69	2.30	0.77	16.97	23.84	0.06		0.07	0.20	0.00	99.86	0.93	0.16	
YK18-07	6K-1515-R09	54.10	0.14	1.03	2.26	0.52	17.31	24.08	0.09		0.01	0.23	0.00	99.76	0.93	0.25	Exsolved Cpx
YK18-07	6K-1515-R10	52.46	0.24	3.16	2.16	0.96	17.71	21.80	0.05		0.05	0.66	0.02	99.27	0.94	0.17	
YK18-07	6K-1515-R10	52.68	0.15	3.04	2.11	0.85	17.49	22.40	0.08		0.09	0.62	0.00	99.51	0.94	0.16	
YK18-07	6K-1515-R10	53.06	0.16	2.56	2.16	0.86	17.26	23.27	0.03		0.00	0.40	0.01	99.78	0.93	0.18	
YK18-07	6K-1515-R15	51.41	0.17	5.19	2.20	0.97	15.89	23.24	0.09		0.06	0.22	0.00	99.44	0.93	0.11	Exsolved Cpx
YK18-07	6K-1515-R15	51.13	0.14	5.27	2.50	0.99	16.43	23.11	0.08		0.02	0.09	0.00	99.75	0.93	0.11	Exsolved Cpx
YK18-07	6K-1515-R15	51.37	0.25	5.55	2.33	1.01	15.80	23.54	0.09		0.06	0.11	0.01	100.12	0.92	0.11	Exsolved Cpx
YK18-07	6K-1515-R15	50.98	0.27	5.56	2.11	1.06	15.96	23.93	0.07		0.07	0.08	0.00	100.10	0.94	0.11	Exsolved Cpx
YK18-07	6K-1515-R15	51.19	0.23	5.53	2.28	1.04	15.87	23.91	0.07		0.06	0.11	0.00	100.30	0.93	0.11	Exsolved Cpx

Supplementary Table S2 C: Major element composition of spinels

Cruise ID	*Sample*	*Lab*	*SiO_2*	*TiO_2*	*Al_2O_3*	*FeO**	*MnO*	*MgO*	*CaO*	*Cr_2O_3*	*Fe_2O_3*	*ZnO*	*V_2O_3*	*NiO*	*Na_2O*	*K_2O*	*Total*	*Mg#*	*Cr#*
KH07-02	D28-001	UH	0.00	0.08	46.70	11.13	0.07	17.85	0.02	19.67	2.62	0.21		0.20			98.54	0.74	0.22
KH07-02	D28-001	UH	0.00	0.05	44.44	11.62	0.10	17.40	0.02	21.71	3.23	0.10		0.21			98.89	0.73	0.25
KH07-02	D28-001	UH	0.00	0.05	44.05	11.67	0.09	17.42	0.01	22.87	2.86	0.26		0.11			99.39	0.73	0.26
KH07-02	D28-001	UH	0.03	0.00	43.46	11.19	0.06	17.59	0.00	22.75	3.32	0.17		0.14			98.72	0.74	0.26
KH07-02	D28-001	UH	0.02	0.00	43.30	11.65	0.05	17.02	0.00	22.23	2.94	0.25		0.08			97.54	0.72	0.26
KH07-02	D28-001	UH	0.03	0.05	43.39	11.54	0.04	17.41	0.00	22.48	3.53	0.05		0.18			98.67	0.73	0.26
KH07-02	D28-001	UH	0.00	0.08	44.07	12.01	0.10	17.13	0.00	22.52	2.81	0.24		0.15			99.11	0.72	0.26
KH07-02	D28-001	UH	0.04	0.06	43.68	11.48	0.11	17.39	0.00	22.55	3.28	0.24		0.17			98.99	0.73	0.26
KH18-02	D12-R01	Rice	0.05	0.09	28.78	23.11	0.33	9.84	0.26	35.96		0.30	0.32				99.04	0.46	0.46
KH18-02	D12-R01	Rice	0.28	0.11	30.47	22.38	0.46	10.83	0.00	34.36		0.29	0.18				99.36	0.50	0.43
KH18-02	D12-R01	Rice	0.34	0.13	30.22	22.41	0.40	10.78	0.00	33.88		0.29	0.21				98.66	0.50	0.43
KH18-02	D12-R01	Rice	0.00	0.12	37.64	18.22	0.24	14.41	0.01	29.29		0.12	0.26				100.30	0.62	0.34
KH18-02	D12-R01	Rice	0.00	0.12	30.76	20.10	0.26	12.81	0.00	35.56		0.18	0.26				100.05	0.57	0.44
KH18-02	D12-R01	Rice	0.00	0.02	27.07	21.37	0.27	11.45	0.03	38.97		0.46	0.11				99.75	0.53	0.49
KH18-02	D12-R01	Rice	0.00	0.01	25.97	21.86	0.28	11.30	0.01	40.01		0.46	0.09				100.00	0.53	0.51
KH18-02	D12-R01	Rice	0.00	0.04	25.80	22.62	0.33	10.35	0.01	39.39		0.35	0.12				99.01	0.49	0.51
KH18-02	D12-R01	Rice	0.01	0.13	33.38	21.57	0.32	11.38	0.01	32.53		0.47	0.21				100.02	0.51	0.40
KH18-02	D12-R01	Rice	0.00	0.16	32.78	20.90	0.28	11.77	0.01	33.34		0.45	0.25				99.93	0.53	0.41
KH18-02	D12-R01	Rice	0.00	0.15	34.23	19.55	0.24	12.96	0.01	31.71		0.36	0.25				99.46	0.58	0.38
KH18-02	D12-R01	Rice	0.00	0.12	46.57	14.97	0.13	17.53	0.00	21.59		0.13	0.15				101.19	0.71	0.24
KH18-02	D12-R01	Rice	0.00	0.10	45.95	15.31	0.17	17.47	0.00	21.50		0.12	0.18				100.80	0.71	0.24
KH18-02	D12-R01	Rice	0.00	0.10	46.15	15.18	0.14	17.51	0.00	21.47		0.11	0.14				100.80	0.71	0.24
KH18-02	D12-R01	Nagoya	0.02	0.14	37.15	20.98	0.32	12.57	0.02	27.94		0.72		0.31	0.04	0.03	100.23	0.55	0.34
KH18-02	D12-R01	Nagoya	0.03	0.13	36.74	19.61	0.27	13.47	0.04	28.91		0.61		0.30	0.03	0.04	100.18	0.59	0.35
KH18-02	D12-R01	Nagoya	0.02	0.15	35.72	20.17	0.26	13.17	0.03	30.06		0.68		0.29	0.04	0.04	100.62	0.58	0.36
KH18-02	D12-R02	Rice	0.00	0.07	38.98	16.01	0.22	15.83	0.00	28.68		0.39	0.26	0.10			100.53	0.67	0.33
KH18-02	D12-R02	Rice	0.00	0.10	36.22	16.65	0.22	14.76	0.00	30.96		0.25	0.21	0.13			99.49	0.64	0.36
KH18-02	D12-R02	Rice	0.00	0.09	39.42	17.20	0.23	14.94	0.00	27.54		0.39	0.27	0.07			100.15	0.64	0.32
KH18-02	D12-R02	Rice	0.00	0.14	32.57	18.93	0.27	12.94	0.00	33.77		0.37	0.25	0.03			99.28	0.58	0.41
KH18-02	D12-R02	Rice	0.00	0.08	37.85	16.54	0.29	15.00	0.00	29.00		0.31	0.27	0.11			99.47	0.65	0.34
KH18-02	D12-R02	Rice	0.14	0.01	36.07	17.01	0.25	14.73	0.01	31.39		0.33	0.22	0.03			100.19	0.64	0.37
KH18-02	D12-R02	Rice	0.01	0.12	33.00	18.58	0.22	13.63	0.00	34.21		0.09	0.26	0.11			100.22	0.60	0.41
KH18-02	D12-R02	Rice	0.02	0.11	32.79	18.42	0.25	13.54	0.00	33.89		0.33	0.28	0.14			99.76	0.60	0.41
KH18-02	D12-R02	Rice	0.58	0.07	30.30	22.54	0.53	12.66	0.00	32.22		0.31	0.23	0.11			99.55	0.58	0.42
KH18-02	D12-R02	Rice	0.00	0.11	45.32	13.36	0.13	17.86	0.00	23.22		0.18	0.14	0.16			100.47	0.73	0.26
KH18-02	D12-R02	Rice	0.00	0.14	45.69	13.40	0.10	18.26	0.02	23.16		0.36	0.13	0.16			101.43	0.74	0.25
KH18-02	D12-R02	Rice	0.00	0.18	45.87	13.66	0.22	18.11	0.00	23.27		0.19	0.10	0.25			101.83	0.73	0.25

Cruise ID	Sample	Lab	SiO_2	TiO_2	Al_2O_3	FeO*	MnO	MgO	CaO	Cr_2O_3	Fe_2O_3	ZnO	V_2O_3	NiO	Na_2O	K_2O	Total	Mg#	Cr#
KH18-02	D12-R02	Rice	0.00	0.08	42.82	15.07	0.22	16.71	0.00	25.63		0.20	0.11	0.11			100.95	0.69	0.29
KH18-02	D12-R02	Rice	0.00	0.10	39.53	15.57	0.20	15.90	0.00	28.00		0.25	0.22	0.20			99.97	0.68	0.32
KH18-02	D12-R02	Rice	0.02	0.12	39.82	16.25	0.23	15.77	0.01	27.41		0.15	0.16	0.17			100.12	0.67	0.32
KH18-02	D12-R02	Rice	0.00	0.13	40.38	16.61	0.23	15.77	0.01	27.43		0.23	0.14	0.10			101.02	0.66	0.31
KH18-02	D12-R02	Rice	0.03	0.11	37.92	17.17	0.24	14.83	0.00	28.75		0.41	0.26	0.07			99.79	0.64	0.34
KH18-02	D12-R02	Rice	0.14	0.03	33.79	18.59	0.34	13.50	0.00	32.26		0.34	0.22	0.05			99.25	0.60	0.39
KH18-02	D12-R02	Rice	0.01	0.12	32.06	19.11	0.29	12.83	0.00	34.04		0.26	0.29	0.09			99.09	0.58	0.42
KH18-02	D12-R02	Rice	0.01	0.06	33.93	18.55	0.26	13.45	0.00	32.94		0.41	0.28	0.05			99.93	0.60	0.39
KH18-02	D12-R02	Rice	0.00	0.08	41.15	15.54	0.19	15.69	0.01	26.06		0.14	0.17	0.18			99.19	0.67	0.30
KH18-02	D12-R02	Rice	0.00	0.14	36.75	16.13	0.24	14.59	0.01	30.64		0.16	0.18	0.10			98.93	0.64	0.36
KH18-02	D12-R02	Rice	0.04	0.10	43.17	14.57	0.18	16.28	0.01	24.77		0.24	0.21	0.13			99.68	0.68	0.28
KH18-02	D12-R02	Rice	0.05	0.09	39.39	17.46	0.29	14.39	0.00	27.14		0.25	0.18	0.13			99.37	0.62	0.32
KH18-02	D12-R02	Rice	0.00	0.10	45.89	13.90	0.17	17.15	0.01	22.25		0.14	0.12	0.15			99.86	0.71	0.25
KH18-02	D12-R02	Rice	0.07	0.07	45.29	13.73	0.19	17.74	0.02	22.39		0.21	0.14	0.11			99.95	0.73	0.25
KH18-02	D12-R02	Rice	0.00	0.14	46.09	13.81	0.22	18.06	0.00	22.50		0.15	0.15	0.18			101.30	0.73	0.25
KH18-02	D12-R02	Rice	0.00	0.09	42.96	16.21	0.22	15.80	0.01	24.20		0.30	0.17	0.15			100.10	0.67	0.27
KH18-02	D12-R02	Rice	0.00	0.06	40.59	15.69	0.21	15.61	0.00	26.61		0.24	0.16	0.16			99.33	0.67	0.31
KH18-02	D12-R02	Rice	0.00	0.05	41.28	14.82	0.19	16.61	0.00	26.22		0.20	0.18	0.12			99.67	0.70	0.30
KH18-02	D12-R03	Rice	0.32	0.07	32.33	25.74	0.36	10.33	0.01	29.28		0.69	0.15				99.27	0.47	0.38
KH18-02	D12-R03	Rice	0.04	0.06	26.67	30.16	0.41	8.39	0.00	31.61		0.54	0.21				98.10	0.40	0.44
KH18-02	D12-R03	Rice	0.02	0.05	31.67	25.75	0.33	10.26	0.01	30.50		0.44	0.14				99.18	0.47	0.39
KH18-02	D12-R03	Rice	0.00	0.04	44.39	17.51	0.23	15.68	0.02	21.83		0.35	0.16				100.20	0.66	0.25
KH18-02	D12-R03	Rice	0.46	0.04	36.86	19.25	0.28	12.79	0.01	25.76		0.32	0.10				95.88	0.57	0.32
KH18-02	D12-R03	Rice	0.00	0.05	39.81	18.36	0.27	14.17	0.02	26.79		0.36	0.18				100.01	0.61	0.31
KH18-02	D12-R03	Rice	0.00	0.08	41.42	17.45	0.25	14.71	0.02	26.14		0.26	0.22				100.56	0.62	0.30
KH18-02	D12-R03	Rice	0.01	0.10	41.11	17.68	0.21	14.66	0.01	25.80		0.25	0.22				100.04	0.62	0.30
KH18-02	D12-R03	Rice	0.00	0.09	30.78	21.71	0.27	10.97	0.02	35.11		0.40	0.19				99.54	0.50	0.43
KH18-02	D12-R03	Rice	0.00	0.07	35.09	17.84	0.19	13.66	0.00	31.74		0.19	0.24				99.02	0.60	0.38
KH18-02	D12-R03	Rice	0.01	0.13	36.04	17.65	0.22	13.63	0.00	31.37		0.32	0.26				99.64	0.60	0.37
KH18-02	D12-R03	Rice	0.04	0.12	33.43	19.03	0.26	12.60	0.02	32.36		0.28	0.20				98.33	0.57	0.39
KH18-02	D12-R03	Rice	0.00	0.06	39.05	18.77	0.26	14.21	0.00	26.36		0.27	0.16				99.14	0.62	0.31
KH18-02	D12-R03	Rice	0.02	0.05	31.00	20.86	0.28	11.60	0.00	33.75		0.36	0.27				98.19	0.53	0.42
KH18-02	D12-R03	Rice	0.01	0.04	35.56	17.55	0.22	14.01	0.02	31.11		0.26	0.24				99.02	0.62	0.37
KH18-02	D12-R04	Rice	0.00	0.05	47.51	15.10	0.19	16.94	0.00	20.21		0.19	0.10	0.17			100.46	0.69	0.22
KH18-02	D12-R04	Rice	0.01	0.02	47.16	14.58	0.13	17.00	0.00	20.98		0.22	0.15	0.30			100.56	0.70	0.23
KH18-02	D12-R04	Rice	0.06	0.00	40.88	18.84	0.23	13.78	0.12	25.00		0.29	0.09	0.15			99.44	0.60	0.29
KH18-02	D12-R04	Rice	0.11	0.05	33.23	19.71	0.34	12.88	0.01	32.25		0.41	0.22	0.12			99.32	0.58	0.39
KH18-02	D12-R05	Rice	0.03	0.08	26.60	18.87	0.29	11.55	0.00	41.86		0.18	0.22				99.67	0.53	0.51

Cruise ID	*Sample*	*Lab*	*SiO_2*	*TiO_2*	*Al_2O_3*	*FeO**	*MnO*	*MgO*	*CaO*	*Cr_2O_3*	*Fe_2O_3*	*ZnO*	*V_2O_3*	*NiO*	*Na_2O*	*K_2O*	*Total*	*Mg#*	*Cr#*
KH18-02	D12-R05	Rice	0.01	0.07	27.76	18.56	0.23	12.06	0.01	39.97		0.11	0.24				99.02	0.55	0.49
KH18-02	D12-R05	Rice	0.00	0.06	26.66	19.15	0.31	12.07	0.02	40.81		0.21	0.22				99.51	0.56	0.51
KH18-02	D12-R05	Rice	0.00	0.15	46.48	13.41	0.15	17.68	0.00	23.02		0.28	0.20				101.37	0.72	0.25
KH18-02	D12-R05	Rice	0.00	0.13	45.79	13.33	0.12	17.60	0.03	24.07		0.24	0.16				101.47	0.71	0.26
KH18-02	D12-R05	Rice	0.00	0.17	28.52	19.09	0.26	12.46	0.03	39.46		0.16	0.18				100.34	0.56	0.48
KH18-02	D12-R05	Rice	0.00	0.17	30.55	18.10	0.26	13.07	0.00	37.85		0.23	0.20				100.42	0.58	0.45
KH18-02	D12-R05	Rice	0.00	0.17	31.82	17.80	0.21	13.98	0.06	36.65		0.21	0.19				101.09	0.61	0.44
KH18-02	D12-R05	Rice	0.00	0.19	29.84	18.43	0.27	13.36	0.05	38.19		0.20	0.19				100.72	0.59	0.46
KH18-02	D12-R05	Rice	0.00	0.14	47.54	13.52	0.15	17.84	0.01	22.11		0.30	0.11				101.72	0.72	0.24
KH18-02	D12-R05	Rice	0.00	0.16	47.68	13.53	0.17	18.17	0.01	22.23		0.26	0.11				102.32	0.72	0.24
KH18-02	D12-R05	Rice	0.00	0.18	44.71	14.41	0.21	16.91	0.01	24.11		0.29	0.13				100.96	0.70	0.27
KH18-02	D12-R05	Rice	0.00	0.17	42.45	14.76	0.17	16.50	0.03	26.45		0.28	0.14				100.95	0.69	0.29
KH18-02	D12-R05	Rice	0.03	0.26	30.28	16.74	0.25	13.43	0.04	38.23		0.12	0.15				99.53	0.60	0.46
KH18-02	D12-R05	Rice	0.00	0.24	31.84	16.42	0.23	13.71	0.04	36.82		0.28	0.14				99.72	0.61	0.44
KH18-02	D12-R06	Rice	0.02	0.07	45.26	13.03	0.13	17.30	0.00	23.12		0.24	0.18	0.22			99.57	0.72	0.26
KH18-02	D12-R06	Rice	0.00	0.12	47.87	12.86	0.16	17.66	0.00	19.51		0.19	0.15	0.28			98.80	0.73	0.21
KH18-02	D12-R06	Rice	0.00	0.06	47.35	13.19	0.14	17.40	0.00	19.76		0.20	0.15	0.20			98.46	0.72	0.22
KH18-02	D12-R06	Rice	0.04	0.15	45.20	13.25	0.15	17.16	0.03	21.71		0.19	0.13	0.18			98.20	0.72	0.24
KH18-02	D12-R06	Rice	0.01	0.14	43.88	13.25	0.14	16.68	0.02	23.19		0.17	0.16	0.13			97.77	0.71	0.26
KH18-02	D12-R06	Rice	0.03	0.07	43.38	13.50	0.12	16.78	0.02	24.09		0.14	0.21	0.21			98.55	0.71	0.27
KH18-02	D12-R06	Rice	0.01	0.20	32.01	18.72	0.27	12.60	0.00	32.70		0.19	0.31	0.04			97.05	0.58	0.41
KH18-02	D12-R06	Rice	0.01	0.17	31.81	18.52	0.27	12.58	0.00	33.44		0.30	0.28	0.03			97.41	0.57	0.41
KH18-02	D12-R06	Nagoya	0.01	0.06	48.48	13.01	0.15	18.26	0.00	19.95		0.18		0.31	0.00	0.01	100.42	0.74	0.22
KH18-02	D12-R06	Nagoya	0.02	0.03	48.58	12.75	0.15	17.98	0.00	20.06		0.15		0.33	0.01	0.02	100.08	0.73	0.22
KH18-02	D12-R06	Nagoya	0.01	0.13	48.57	12.98	0.13	17.99	0.00	19.67		0.16		0.33	0.01	0.00	99.96	0.73	0.21
KH18-02	D12-R06	Nagoya	0.01	0.14	47.12	13.13	0.15	17.95	0.00	20.38		0.23		0.27	0.01	0.02	99.40	0.73	0.22
KH18-02	D12-R06	Nagoya	0.02	0.12	48.31	13.00	0.17	18.03	0.00	19.85		0.24		0.31	0.00	0.01	100.05	0.73	0.22
KH18-02	D12-R06	Nagoya	0.24	0.10	44.99	13.63	0.14	17.13	0.01	22.21		0.23		0.27	0.01	0.00	98.96	0.71	0.25
KH18-02	D12-R06	Nagoya	0.04	0.12	42.00	14.46	0.17	16.49	0.02	25.56		0.20		0.27	0.00	0.01	99.35	0.69	0.29
KH18-02	D12-R06	Nagoya	0.02	0.07	47.87	13.08	0.17	17.74	0.00	19.37		0.18		0.31	0.00	0.01	98.81	0.73	0.21
KH18-02	D12-R06	Nagoya	0.01	0.07	48.82	12.65	0.14	17.17	0.00	19.98		0.20		0.34	0.00	0.00	99.37	0.70	0.22
KH18-02	D12-R06	Nagoya	0.05	0.04	48.21	12.80	0.15	18.10	0.00	19.90		0.17		0.26	0.00	0.01	99.69	0.73	0.22
KH18-02	D12-R06	Nagoya	0.01	0.09	48.79	12.71	0.16	17.95	0.01	19.99		0.19		0.33	0.00	0.00	100.22	0.73	0.22
KH18-02	D12-R06	Nagoya	0.00	0.03	48.92	12.82	0.16	18.20	0.00	19.73		0.13		0.31	0.00	0.01	100.30	0.73	0.21
KH18-02	D12-R06	Nagoya	0.01	0.06	48.60	12.79	0.13	18.19	0.00	19.86		0.15		0.34	0.00	0.00	100.11	0.73	0.22
KH18-02	D12-R06	Nagoya	0.02	0.06	49.50	13.43	0.13	17.95	0.00	18.33		0.18		0.34	0.01	0.01	99.95	0.72	0.20
KH18-02	D12-R06	Nagoya	0.01	0.05	48.54	13.35	0.17	17.55	0.00	19.47		0.21		0.28	0.00	0.02	99.64	0.71	0.21
KH18-02	D12-R06	Nagoya	0.00	0.04	51.54	12.81	0.16	18.39	0.00	16.67		0.21		0.30	0.00	0.01	100.13	0.73	0.18

Cruise ID	*Sample*	*Lab*	*SiO_2*	*TiO_2*	*Al_2O_3*	*FeO**	*MnO*	*MgO*	*CaO*	*Cr_2O_3*	*Fe_2O_3*	*ZnO*	*V_2O_3*	*NiO*	*Na_2O*	*K_2O*	*Total*	*Mg#*	*Cr#*
KH18-02	D12-R06	Nagoya	0.01	0.09	47.93	13.52	0.11	17.42	0.00	19.84		0.22		0.30	0.00	0.02	99.46	0.71	0.22
KH18-02	D12-R06	Nagoya	0.03	0.04	47.60	13.41	0.15	17.48	0.00	20.33		0.16		0.29	0.00	0.01	99.49	0.71	0.22
KH18-02	D12-R06	Nagoya	0.01	0.10	48.14	13.48	0.11	17.67	0.00	20.04		0.16		0.28	0.00	0.01	100.01	0.72	0.22
KH18-02	D12-R06	Nagoya	0.00	0.04	48.05	13.90	0.15	17.58	0.00	19.66		0.24		0.34	0.00	0.02	99.98	0.71	0.22
KH18-02	D12-R06	Nagoya	0.02	0.08	48.40	13.88	0.13	17.51	0.00	19.66		0.26		0.29	0.01	0.01	100.24	0.71	0.21
KH18-02	D12-R06	Nagoya	0.02	0.05	47.28	14.16	0.14	17.41	0.00	19.20		0.19		0.26	0.01	0.01	98.74	0.72	0.21
KH18-02	D12-R07	Rice	0.00	0.11	33.02	18.99	0.28	12.92	0.00	33.54		0.20	0.18				99.24	0.58	0.41
KH18-02	D12-R07	Rice	0.02	0.20	30.73	20.37	0.31	12.09	0.00	35.92		0.22	0.15				100.00	0.54	0.44
KH18-02	D12-R07	Rice	0.01	0.13	33.18	17.29	0.24	14.26	0.01	35.33		0.20	0.20				100.86	0.62	0.42
KH18-02	D12-R07	Rice	0.00	0.14	32.80	18.19	0.28	13.87	0.00	34.78		0.21	0.18				100.45	0.61	0.42
KH18-02	D12-R07	Rice	0.00	0.09	33.67	16.69	0.22	14.39	0.00	34.84		0.27	0.14				100.31	0.63	0.41
KH18-02	D12-R07	Rice	0.02	0.14	33.34	16.76	0.24	14.33	0.00	35.48		0.19	0.16				100.66	0.63	0.42
KH18-02	D12-R07	Rice	0.00	0.19	33.15	16.31	0.22	14.78	0.00	35.68		0.13	0.17				100.63	0.64	0.42
KH18-02	D12-R07	Rice	0.00	0.11	33.15	16.18	0.19	14.84	0.00	35.90		0.09	0.14				100.60	0.64	0.42
KH18-02	D12-R07	Rice	0.00	0.11	34.65	15.61	0.25	15.10	0.00	34.75		0.13	0.20				100.79	0.65	0.40
KH18-02	D12-R07	Rice	0.01	0.06	34.41	16.05	0.24	15.00	0.00	34.52		0.12	0.16				100.58	0.65	0.40
KH18-02	D12-R07	Rice	0.00	0.09	34.14	16.56	0.20	14.38	0.00	34.39		0.18	0.14				100.08	0.63	0.40
KH18-02	D12-R07	Rice	0.00	0.08	29.00	17.52	0.27	13.33	0.04	39.95		0.14	0.17				100.50	0.60	0.48
KH18-02	D12-R07	Rice	0.00	0.09	30.40	18.62	0.26	12.48	0.00	37.25		0.32	0.20				99.62	0.56	0.45
KH18-02	D12-R07	Rice	0.02	0.06	28.50	17.83	0.27	12.85	0.02	40.63		0.17	0.14				100.48	0.58	0.49
KH18-02	D12-R07	Rice	0.02	0.05	30.99	16.17	0.22	14.11	0.00	37.82		0.07	0.19				99.64	0.63	0.45
KH18-02	D12-R07	Rice	0.05	0.06	31.40	16.46	0.26	13.89	0.01	36.98		0.18	0.17				99.46	0.62	0.44
KH18-02	D12-R07	Rice	0.00	0.05	31.02	16.47	0.24	14.28	0.00	37.75		0.10	0.17				100.08	0.63	0.45
KH18-02	D12-R08	Rice	0.00	0.06	34.10	18.28	0.21	13.46	0.00	32.23		0.20	0.10	0.15			98.79	0.60	0.39
KH18-02	D12-R08	Rice	0.00	0.05	34.04	18.38	0.25	13.38	0.00	32.39		0.34	0.13	0.12			99.09	0.60	0.39
KH18-02	D12-R08	Rice	0.03	0.04	38.41	16.42	0.18	14.91	0.01	28.59		0.28	0.15	0.17			99.18	0.65	0.33
KH18-02	D12-R08	Rice	0.00	0.11	35.04	17.30	0.24	14.23	0.00	31.55		0.25	0.21	0.12			99.04	0.63	0.38
KH18-02	D12-R08	Rice	0.00	0.05	46.03	14.57	0.13	17.31	0.00	22.09		0.16	0.17	0.20			100.72	0.71	0.24
KH18-02	D12-R08	Rice	0.00	0.06	37.09	16.64	0.25	14.93	0.00	29.69		0.20	0.25	0.18			99.28	0.65	0.35
KH18-02	D12-R08	Rice	0.00	0.04	45.77	14.84	0.15	17.16	0.00	21.44		0.15	0.18	0.26			100.00	0.71	0.24
KH18-02	D12-R08	Rice	0.03	0.11	29.44	20.09	0.24	11.91	0.01	36.65		0.15	0.28	0.10			99.01	0.54	0.46
KH18-02	D12-R08	Rice	0.02	0.06	29.75	19.80	0.28	12.11	0.05	35.95		0.24	0.22	0.10			98.58	0.56	0.45
KH18-02	D12-R10	Rice	0.00	0.07	44.37	15.16	0.14	16.80	0.01	23.04		0.22	0.18				100.00	0.70	0.26
KH18-02	D12-R10	Rice	0.00	0.03	46.51	15.04	0.17	17.73	0.00	21.33		0.33	0.16				101.29	0.72	0.24
KH18-02	D12-R10	Rice	0.00	0.03	46.34	14.87	0.17	17.49	0.00	21.42		0.15	0.19				100.67	0.71	0.24
KH18-02	D12-R10	Rice	0.00	0.04	43.38	15.05	0.15	16.47	0.01	23.82		0.30	0.17				99.40	0.69	0.27
KH18-02	D12-R10	Rice	0.02	0.06	30.24	20.38	0.28	12.40	0.03	36.29		0.37	0.14				100.22	0.56	0.45
KH18-02	D12-R10	Rice	0.00	0.03	29.86	20.42	0.28	12.09	0.00	36.04		0.29	0.15				99.17	0.55	0.45

Cruise ID	Sample	Lab	SiO_2	TiO_2	Al_2O_3	FeO*	MnO	MgO	CaO	Cr_2O_3	Fe_2O_3	ZnO	V_2O_3	NiO	Na_2O	K_2O	Total	Mg#	Cr#
KH18-02	D12-R10	Rice	0.00	0.08	39.80	15.64	0.23	15.92	0.01	28.75		0.31	0.20				100.94	0.67	0.33
KH18-02	D12-R10	Rice	0.00	0.10	37.95	15.97	0.21	15.17	0.00	30.74		0.29	0.26				100.69	0.65	0.35
KH18-02	D12-R10	Rice	0.01	0.11	38.06	16.34	0.17	15.14	0.00	28.72		0.21	0.23				98.99	0.65	0.34
KH18-02	D12-R10	Rice	0.00	0.06	32.70	18.99	0.24	12.79	0.02	33.79		0.29	0.20				99.08	0.57	0.41
KH18-02	D12-R10	Rice	0.02	0.04	29.10	20.99	0.32	11.47	0.10	36.75		0.24	0.25				99.28	0.53	0.46
KH18-02	D12-R10	Rice	0.01	0.04	29.41	20.76	0.32	11.35	0.02	37.24		0.22	0.18				99.55	0.52	0.46
KH18-02	D12-R11	Rice	0.00	0.00	31.15	20.46	0.24	12.22	0.01	34.19		0.45	0.10	0.14			98.94	0.56	0.42
KH18-02	D12-R11	Rice	0.00	0.01	32.05	19.39	0.26	12.56	0.01	34.22		0.43	0.12	0.10			99.16	0.57	0.42
KH18-02	D12-R11	Rice	0.01	0.00	29.07	20.69	0.29	11.45	0.02	37.09		0.47	0.13	0.12			99.33	0.53	0.46
KH18-02	D12-R11	Rice	0.02	0.04	27.16	20.58	0.31	11.15	0.06	38.75		0.36	0.09	0.08			98.61	0.52	0.49
KH18-02	D12-R11	Rice	0.00	0.05	32.75	19.79	0.22	12.63	0.00	32.81		0.42	0.07	0.12			98.87	0.57	0.40
KH18-02	D12-R11	Rice	0.00	0.04	33.55	19.19	0.23	13.22	0.00	31.96		0.40	0.13	0.16			98.87	0.59	0.39
KH18-02	D12-R11	Rice	0.00	0.04	31.36	19.82	0.26	12.70	0.00	34.07		0.39	0.15	0.12			98.91	0.58	0.42
KH18-02	D12-R11	Rice	0.02	0.06	31.15	19.93	0.28	12.70	0.00	34.24		0.47	0.10	0.17			99.11	0.58	0.42
KH18-02	D12-R11	Rice	0.02	0.04	28.53	21.52	0.27	11.41	0.02	36.69		0.49	0.14	0.06			99.19	0.53	0.46
KH18-02	D12-R11	Rice	0.01	0.03	26.31	22.20	0.30	10.56	0.04	38.52		0.34	0.15	0.09			98.56	0.50	0.50
KH18-02	D12-R11	Rice	0.00	0.02	26.22	22.48	0.27	10.61	0.07	38.09		0.47	0.18	0.02			98.42	0.50	0.49
KH18-02	D12-R12	Rice	0.00	0.03	39.02	19.21	0.21	14.14	0.01	26.76		0.56	0.10	0.16			100.21	0.61	0.32
KH18-02	D12-R12	Rice	0.00	0.02	38.35	19.65	0.26	14.05	0.00	27.43		0.39	0.13	0.17			100.44	0.61	0.32
KH18-02	D12-R12	Rice	0.01	0.00	42.80	18.52	0.23	14.89	0.00	23.19		0.64	0.12	0.18			100.59	0.63	0.27
KH18-02	D12-R12	Rice	0.00	0.00	38.89	19.28	0.28	13.70	0.01	26.76		0.46	0.14	0.13			99.64	0.60	0.32
KH18-02	D12-R12	Rice	0.00	0.02	38.26	17.94	0.22	14.77	0.00	28.35		0.29	0.11	0.13			100.09	0.64	0.33
KH18-02	D12-R12	Rice	0.00	0.00	42.33	16.38	0.24	16.33	0.00	24.80		0.30	0.12	0.20			100.69	0.69	0.28
KH18-02	D12-R12	Rice	0.00	0.06	41.00	17.27	0.21	15.49	0.00	25.98		0.33	0.14	0.21			100.70	0.66	0.30
KH18-02	D12-R12	Rice	0.00	0.00	39.13	17.55	0.27	15.19	0.01	28.17		0.41	0.15	0.14			101.02	0.65	0.33
KH18-02	D12-R12	Rice	0.00	0.00	32.73	20.51	0.28	13.05	0.00	33.21		0.32	0.12	0.11			100.32	0.58	0.40
KH18-02	D12-R12	Rice	0.04	0.08	32.75	21.01	0.30	12.40	0.00	33.29		0.47	0.13	0.12			100.58	0.56	0.41
KH18-02	D12-R12	Rice	0.00	0.00	37.93	18.94	0.24	13.99	0.01	28.55		0.38	0.13	0.16			100.33	0.61	0.34
KH18-02	D12-R12	Rice	0.00	0.14	43.39	16.37	0.16	17.70	0.00	22.98		0.20	0.11	0.24			101.27	0.73	0.26
KH18-02	D12-R12	Rice	0.00	0.09	43.54	16.40	0.17	17.57	0.02	22.72		0.36	0.13	0.28			101.28	0.73	0.26
KH18-02	D12-R12	Rice	0.00	0.11	43.46	16.66	0.19	17.21	0.00	22.61		0.14	0.10	0.25			100.74	0.71	0.26
KH18-02	D12-R12	Rice	0.01	0.06	42.88	16.67	0.16	17.30	0.00	23.12		0.19	0.16	0.22			100.76	0.72	0.27
KH18-02	D12-R12	Rice	0.01	0.06	43.17	17.87	0.22	16.24	0.00	23.06		0.29	0.10	0.27			101.29	0.68	0.26
KH18-02	D12-R14	Rice	0.02	0.03	37.83	19.10	0.22	13.73	0.00	28.72		0.37	0.08	0.16			100.26	0.60	0.34
KH18-02	D12-R14	Rice	0.00	0.03	34.98	19.78	0.22	12.79	0.03	30.42		0.45	0.10	0.11			98.90	0.57	0.37
KH18-02	D12-R14	Rice	0.00	0.05	30.78	21.16	0.22	11.51	0.03	34.54		0.56	0.10	0.02			98.97	0.53	0.43
KH18-02	D12-R14	Rice	0.02	0.01	37.17	19.73	0.24	13.09	0.00	28.44		0.59	0.13	0.19			99.62	0.58	0.34
KH18-02	D12-R14	Rice	0.03	0.06	37.58	19.06	0.22	13.76	0.00	28.40		0.50	0.11	0.13			99.85	0.60	0.34

Cruise ID	Sample	Lab	SiO_2	TiO_2	Al_2O_3	FeO*	MnO	MgO	CaO	Cr_2O_3	Fe_2O_3	ZnO	V_2O_3	NiO	Na_2O	K_2O	Total	Mg#	Cr#
KH18-02	D12-R14	Rice	0.00	0.05	33.47	20.98	0.24	12.01	0.00	32.06		0.50	0.08	0.11			99.50	0.54	0.39
KH18-02	D12-R14	Rice	0.00	0.08	35.33	19.37	0.25	12.83	0.01	30.66		0.40	0.12	0.16			99.22	0.57	0.37
KH18-02	D12-R14	Rice	0.01	0.02	31.30	22.47	0.26	11.08	0.00	33.15		0.37	0.08	0.11			98.85	0.51	0.42
KH18-02	D12-R14	Rice	0.01	0.06	31.90	20.94	0.24	11.67	0.06	33.40		0.45	0.15	0.04			98.92	0.53	0.41
KH18-02	D12-R14	Rice	0.00	0.02	29.35	23.80	0.32	10.35	0.07	34.65		0.51	0.14	0.11			99.32	0.48	0.44
KH18-02	D12-R14	Rice	0.06	0.05	31.65	21.66	0.24	11.32	0.02	33.65		0.41	0.10	0.06			99.22	0.52	0.42
KH18-02	D12-R14	Rice	0.00	0.05	30.97	22.73	0.24	10.98	0.07	33.10		0.45	0.08	0.07			98.74	0.51	0.42
KH18-02	D12-R14	Rice	0.00	0.07	30.71	22.46	0.27	10.91	0.03	34.35		0.25	0.10	0.12			99.28	0.50	0.43
KH18-02	D12-R14	Rice	0.00	0.05	35.04	20.15	0.24	12.61	0.01	30.76		0.49	0.09	0.15			99.58	0.56	0.37
KH18-02	D12-R14	Rice	0.00	0.08	33.37	20.85	0.21	12.20	0.00	32.64		0.56	0.12	0.13			100.17	0.55	0.40
KH18-02	D12-R14	Rice	0.05	0.02	30.88	21.14	0.28	11.47	0.04	34.11		0.38	0.08	0.09			98.54	0.53	0.43
KH18-02	D12-R14	Rice	0.02	0.01	31.61	20.89	0.28	11.79	0.03	33.89		0.59	0.10	0.14			99.34	0.54	0.42
KH18-02	D12-R15	Rice	0.00	0.10	35.64	17.15	0.23	14.48	0.01	33.30		0.16	0.21				101.27	0.62	0.39
KH18-02	D12-R15	Rice	0.00	0.11	32.08	19.29	0.27	12.65	0.00	35.87		0.13	0.14				100.55	0.56	0.43
KH18-02	D12-R15	Rice	0.00	0.09	34.12	17.79	0.29	13.75	0.00	34.46		0.22	0.13				100.84	0.60	0.40
KH18-02	D12-R15	Rice	0.00	0.09	32.98	18.97	0.29	12.77	0.00	34.43		0.13	0.17				99.82	0.57	0.41
KH18-02	D12-R15	Rice	0.01	0.12	26.32	24.07	0.36	9.94	0.01	38.61		0.58	0.15				100.16	0.47	0.50
KH18-02	D12-R15	Rice	0.00	0.07	23.53	26.16	0.39	8.44	0.00	39.26		0.57	0.15				98.57	0.41	0.53
KH18-02	D12-R15	Rice	0.00	0.05	25.49	23.83	0.40	9.60	0.00	38.78		0.32	0.17				98.65	0.46	0.51
KH18-02	D12-R15	Rice	0.00	0.11	24.41	25.57	0.36	9.17	0.01	39.03		0.37	0.16				99.18	0.44	0.52
KH18-02	D12-R15	Rice	0.00	0.11	24.84	24.89	0.42	9.17	0.00	39.71		0.27	0.13				99.55	0.43	0.52
KH18-02	D12-R15	Rice	0.00	0.03	27.47	21.76	0.32	11.10	0.00	39.40		0.50	0.16				100.74	0.51	0.49
KH18-02	D12-R15	Rice	0.00	0.03	25.81	24.51	0.32	10.15	0.00	38.10		0.66	0.13				99.70	0.48	0.50
KH18-02	D12-R17	Rice	0.00	0.06	46.60	14.84	0.15	16.98	0.00	21.29		0.21	0.16	0.28			100.57	0.70	0.23
KH18-02	D12-R17	Rice	0.00	0.04	46.99	14.61	0.12	16.97	0.00	21.42		0.27	0.15	0.25			100.82	0.70	0.23
KH18-02	D12-R17	Rice	0.00	0.12	46.15	14.42	0.21	16.70	0.02	21.69		0.28	0.17	0.29			100.04	0.69	0.24
KH18-02	D12-R17	Rice	0.00	0.06	46.42	14.42	0.12	16.99	0.01	21.80		0.09	0.16	0.23			100.31	0.70	0.24
KH18-02	D12-R17	Rice	0.00	0.00	41.59	17.09	0.23	15.24	0.00	25.40		0.32	0.12	0.22			100.22	0.65	0.29
KH18-02	D12-R17	Rice	0.00	0.03	41.29	16.74	0.22	15.35	0.00	26.32		0.31	0.14	0.29			100.69	0.65	0.30
KH18-02	D12-R17	Rice	0.00	0.02	34.71	19.41	0.25	13.41	0.00	32.00		0.41	0.12	0.21			100.54	0.59	0.38
KH18-02	D12-R17	Rice	0.00	0.02	34.48	19.48	0.26	12.98	0.01	31.69		0.21	0.11	0.16			99.40	0.58	0.38
KH18-02	D12-R18	Rice	0.00	0.05	41.50	17.32	0.19	14.85	0.00	25.12		0.40	0.20	0.19			99.83	0.64	0.29
KH18-02	D12-R18	Rice	0.02	0.03	36.20	18.56	0.24	13.65	0.05	30.28		0.30	0.14	0.12			99.59	0.60	0.36
KH18-02	D12-R18	Rice	0.00	0.04	39.22	18.04	0.20	14.23	0.02	27.38		0.36	0.15	0.14			99.78	0.62	0.32
KH18-02	D12-R18	Rice	0.00	0.01	31.67	21.93	0.27	10.88	0.00	33.64		0.49	0.17	0.15			99.20	0.50	0.42
KH18-02	D12-R18	Rice	0.05	0.07	31.88	22.87	0.31	10.12	0.00	33.27		0.65	0.12	0.11			99.44	0.47	0.41
KH18-02	D12-R18	Rice	0.03	0.01	32.62	19.26	0.25	13.00	0.01	34.30		0.21	0.11	0.10			99.90	0.58	0.41
KH18-02	D12-R18	Rice	0.00	0.00	32.57	20.13	0.28	12.51	0.01	34.57		0.38	0.13	0.14			100.71	0.56	0.42

Cruise ID	Sample	Lab	SiO_2	TiO_2	Al_2O_3	FeO*	MnO	MgO	CaO	Cr_2O_3	Fe_2O_3	ZnO	V_2O_3	NiO	Na_2O	K_2O	Total	Mg#	Cr#
KH18-02	D12-R18	Rice	0.02	0.03	33.84	18.63	0.24	13.53	0.00	33.22		0.27	0.13	0.15			100.07	0.60	0.40
KH18-02	D12-R18	Rice	0.04	0.03	31.33	19.59	0.29	12.50	0.00	34.52		0.14	0.08	0.15			98.68	0.57	0.43
KH18-02	D12-R18	Rice	0.00	0.00	31.90	20.02	0.29	12.07	0.02	34.57		0.22	0.11	0.02			99.23	0.55	0.42
KH18-02	D12-R18	Rice	0.00	0.07	35.62	18.89	0.21	13.25	0.02	30.72		0.35	0.18	0.12			99.43	0.59	0.37
KH18-02	D12-R18	Rice	0.00	0.05	36.43	19.65	0.28	12.54	0.00	30.35		0.37	0.15	0.16			99.98	0.56	0.36
KH18-02	D12-R18	Rice	0.00	0.01	36.76	19.39	0.23	12.78	0.00	29.74		0.33	0.16	0.12			99.52	0.57	0.35
KH18-02	D12-R18	Rice	0.00	0.00	35.71	20.03	0.23	12.12	0.00	29.33		0.34	0.14	0.11			98.02	0.55	0.36
KH18-02	D12-R19	Rice	0.00	0.03	41.76	17.82	0.21	15.12	0.00	23.72		0.09	0.10	0.26			99.11	0.65	0.28
KH18-02	D12-R19	Rice	0.00	0.00	43.49	17.31	0.15	15.41	0.02	21.85		0.26	0.07	0.21			98.77	0.66	0.25
KH18-02	D12-R19	Rice	0.00	0.07	43.61	17.93	0.20	15.06	0.00	21.68		0.47	0.08	0.25			99.35	0.64	0.25
KH18-02	D12-R19	Rice	0.00	0.05	34.60	21.17	0.26	12.62	0.01	29.95		0.51	0.14	0.15			99.46	0.57	0.37
KH18-02	D12-R19	Rice	0.01	0.05	36.12	20.53	0.26	12.90	0.00	28.23		0.34	0.12	0.13			98.69	0.57	0.34
KH18-02	D12-R19	Rice	0.00	0.02	28.61	24.05	0.28	10.51	0.04	34.06		0.27	0.12	0.10			98.06	0.49	0.44
KH18-02	D12-R19	Rice	0.00	0.01	25.20	24.91	0.31	9.92	0.04	37.42		0.35	0.14	0.06			98.38	0.47	0.50
KH18-02	D12-R19	Rice	0.01	0.02	23.77	25.78	0.39	9.12	0.04	37.97		0.42	0.15	0.07			97.75	0.44	0.52
KH18-02	D12-R19	Rice	0.00	0.06	22.79	28.00	0.40	8.21	0.11	37.56		0.30	0.11	0.10			97.64	0.40	0.53
KH18-02	D12-R19	Rice	0.00	0.05	43.91	17.06	0.23	15.85	0.00	21.90		0.31	0.08	0.29			99.68	0.67	0.25
KH18-02	D12-R19	Rice	0.00	0.00	41.88	18.56	0.19	14.36	0.00	22.98		0.15	0.08	0.17			98.37	0.62	0.27
KH18-02	D12-R19	Rice	0.00	0.00	43.17	18.45	0.25	15.19	0.01	22.34		0.26	0.11	0.26			100.04	0.64	0.26
KH18-02	D12-R19	Rice	0.00	0.00	43.10	18.18	0.17	15.25	0.00	22.33		0.33	0.10	0.27			99.73	0.65	0.26
KH18-02	D12-R19	Rice	0.01	0.04	40.67	19.68	0.23	13.65	0.00	24.56		0.37	0.07	0.17			99.44	0.59	0.29
KH18-02	D12-R19	Rice	0.01	0.02	40.04	20.33	0.22	13.38	0.01	25.27		0.36	0.08	0.18			99.88	0.58	0.30
KH18-02	D12-R19	Rice	0.00	0.04	44.23	16.02	0.19	16.20	0.00	22.29		0.20	0.17	0.18			99.52	0.68	0.25
KH18-02	D12-R19	Rice	0.01	0.02	44.55	16.68	0.19	15.66	0.00	22.29		0.27	0.08	0.25			100.00	0.66	0.25
KH18-02	D12-R19	Rice	0.00	0.05	41.11	18.09	0.25	14.34	0.02	24.93		0.38	0.09	0.19			99.45	0.62	0.29
KH18-02	D12-R19	Rice	0.00	0.01	43.74	16.83	0.19	16.50	0.01	22.05		0.43	0.08	0.16			100.00	0.69	0.25
KH18-02	D12-R19	Rice	0.00	0.00	43.41	17.01	0.18	15.71	0.00	22.24		0.16	0.11	0.25			99.07	0.67	0.26
KH18-02	D12-R19	Rice	0.00	0.03	22.86	28.83	0.50	7.32	0.04	37.97		0.48	0.10	0.09			98.22	0.36	0.53
KH18-02	D12-R19	Rice	0.02	0.06	17.64	31.03	0.51	5.94	0.07	41.80		0.47	0.09	0.07			97.69	0.30	0.61
KH18-02	D12-R19	Nagoya	0.01	0.12	44.15	15.31	0.15	16.67	0.00	22.26		0.19		0.33	0.01	0.00	99.19	0.70	0.25
KH18-02	D12-R19	Nagoya	0.00	0.10	43.81	15.15	0.17	16.81	0.02	22.57		0.23		0.30	0.00	0.00	99.17	0.70	0.26
KH18-02	D12-R19	Nagoya	0.00	0.13	43.80	17.04	0.16	15.73	0.00	21.88		0.18		0.27	0.00	0.00	99.20	0.66	0.25
KH18-02	D12-R19	Nagoya	0.02	0.09	43.58	16.81	0.18	15.69	0.00	22.40		0.21		0.30	0.00	0.00	99.27	0.66	0.26
KH18-02	D12-R19	Nagoya	0.00	0.09	43.94	17.02	0.20	15.54	0.00	22.14		0.24		0.32	0.00	0.00	99.50	0.65	0.25
KH18-02	D12-R19	Nagoya	0.02	0.09	43.74	15.35	0.13	16.95	0.01	22.55		0.20		0.31	0.00	0.00	99.34	0.71	0.26
KH18-02	D12-R19	Nagoya	0.00	0.10	43.87	15.24	0.18	16.85	0.00	22.32		0.19		0.29	0.00	0.00	99.03	0.70	0.25
KH18-02	D12-R19	Nagoya	0.02	0.08	43.94	15.28	0.18	16.94	0.00	22.38		0.19		0.27	0.00	0.00	99.28	0.70	0.25
KH18-02	D12-R19	Nagoya	0.01	0.08	42.71	17.95	0.20	15.18	0.01	22.39		0.24		0.26	0.00	0.00	99.03	0.64	0.26

Cruise ID	Sample	Lab	SiO_2	TiO_2	Al_2O_3	FeO*	MnO	MgO	CaO	Cr_2O_3	Fe_2O_3	ZnO	V_2O_3	NiO	Na_2O	K_2O	Total	Mg#	Cr#
KH18-02	D12-R19	Nagoya	0.02	0.11	42.83	18.25	0.24	15.00	0.00	22.28		0.26		0.29	0.00	0.00	99.28	0.63	0.26
KH18-02	D12-R19	Nagoya	0.00	0.08	44.09	15.25	0.16	16.91	0.02	22.46		0.21		0.31	0.00	0.00	99.48	0.70	0.25
KH18-02	D12-R19	Nagoya	0.01	0.07	43.80	15.37	0.18	17.10	0.01	22.51		0.23		0.27	0.00	0.00	99.54	0.71	0.26
KH18-02	D12-R20	Rice	0.03	0.17	36.60	16.90	0.25	14.42	0.01	30.13		0.31	0.25	0.09			99.16	0.63	0.36
KH18-02	D12-R20	Rice	0.00	0.12	34.12	18.40	0.26	13.63	0.04	32.05		0.20	0.33	0.09			99.25	0.60	0.39
KH18-02	D12-R20	Rice	0.03	0.14	38.18	17.21	0.23	14.68	0.02	28.30		0.22	0.32	0.11			99.43	0.64	0.33
KH18-02	D12-R20	Rice	0.04	0.11	34.52	19.51	0.21	13.50	0.00	31.11		0.40	0.27	0.14			99.81	0.60	0.38
KH18-02	D12-R20	Rice	0.01	0.08	33.86	19.75	0.29	13.43	0.01	31.33		0.41	0.26	0.10			99.52	0.60	0.38
KH18-02	D12-R20	Rice	0.02	0.07	29.98	21.40	0.25	11.28	0.01	35.05		0.44	0.20	0.02			98.70	0.52	0.44
KH18-02	D12-R20	Rice	0.02	0.14	32.04	19.09	0.26	12.51	0.00	35.11		0.19	0.20	0.07			99.63	0.56	0.42
KH18-02	D12-R33	Rice	0.00	0.02	51.21	12.52	0.12	18.53	0.00	17.67		0.30	0.13				100.50	0.74	0.19
KH18-02	D12-R33	Rice	0.02	0.02	51.39	12.82	0.13	18.22	0.02	17.43		0.32	0.12				100.48	0.73	0.19
KH18-02	D12-R33	Rice	0.00	0.03	52.82	12.63	0.11	18.49	0.00	16.50		0.30	0.11				100.98	0.73	0.17
KH18-02	D12-R33	Rice	0.03	0.07	48.84	12.88	0.16	18.09	0.01	19.76		0.17	0.12				100.13	0.73	0.21
KH18-02	D12-R33	Rice	0.00	0.06	49.09	13.00	0.17	18.15	0.03	19.59		0.21	0.14				100.42	0.73	0.21
KH18-02	D12-R33	Rice	0.00	0.00	49.99	12.72	0.13	18.36	0.00	18.83		0.23	0.06				100.33	0.74	0.20
KH18-02	D12-R33	Nagoya	0.00	0.07	48.99	13.70	0.16	17.68	0.00	19.06		0.29		0.31	0.02	0.00	100.29	0.71	0.21
KH18-02	D12-R33	Nagoya	0.00	0.08	48.94	13.87	0.18	17.97	0.00	18.96		0.25		0.28	0.02	0.01	100.55	0.72	0.21
KH18-02	D12-R33	Nagoya	0.00	0.09	48.89	13.08	0.16	18.29	0.00	19.26		0.19		0.28	0.03	0.00	100.27	0.74	0.21
KH18-02	D12-R34	Rice	0.00	0.16	41.28	15.84	0.16	16.34	0.00	25.55		0.24	0.18	0.24			99.99	0.69	0.29
KH18-02	D12-R34	Rice	0.01	0.04	41.86	16.34	0.19	15.95	0.01	25.52		0.07	0.13	0.26			100.38	0.67	0.29
KH18-02	D12-R34	Rice	0.00	0.10	41.35	16.57	0.21	15.71	0.01	25.46		0.21	0.09	0.27			99.98	0.67	0.29
KH18-02	D12-R34	Rice	0.00	0.12	41.54	16.65	0.23	16.03	0.00	25.14		0.21	0.12	0.29			100.33	0.68	0.29
KH18-02	D12-R34	Rice	0.00	0.17	41.58	16.43	0.18	16.17	0.00	25.18		0.19	0.11	0.25			100.27	0.68	0.29
KH18-02	D12-R34	Rice	0.00	0.09	41.39	16.33	0.20	16.32	0.00	25.35		0.06	0.14	0.23			100.10	0.69	0.29
KH18-02	D12-R34	Rice	0.00	0.12	41.43	16.15	0.19	15.92	0.01	25.52		0.22	0.14	0.21			99.91	0.67	0.29
KH18-02	D12-R34	Rice	0.00	0.13	41.59	16.54	0.13	15.68	0.00	25.35		0.29	0.13	0.25			100.09	0.66	0.29
KH18-02	D12-R34	Rice	0.00	0.10	41.70	16.35	0.19	15.89	0.00	25.55		0.22	0.09	0.26			100.37	0.67	0.29
KH18-02	D12-R34	Rice	0.00	0.11	41.76	16.17	0.21	15.56	0.00	25.74		0.25	0.14	0.17			100.11	0.66	0.29
KH18-02	D12-R34	Rice	0.00	0.09	41.80	17.78	0.22	14.72	0.03	25.39		0.33	0.12	0.17			100.64	0.63	0.29
KH18-02	D12-R34	Rice	0.00	0.09	42.33	15.80	0.18	16.10	0.00	25.83		0.24	0.14	0.15			100.85	0.67	0.29
KH18-02	D12-R34	Nagoya	0.01	0.14	40.78	16.67	0.21	16.33	0.01	25.26		0.17		0.28	0.00	0.01	99.87	0.69	0.29
KH18-02	D12-R34	Nagoya	0.00	0.13	40.21	16.49	0.23	16.47	0.01	25.48		0.21		0.25	0.00	0.02	99.49	0.70	0.30
KH18-02	D12-R34	Nagoya	0.02	0.15	38.65	18.73	0.22	15.24	0.01	25.36		0.23		0.30	0.00	0.02	98.94	0.66	0.31
KH18-02	D12-R34	Nagoya	0.04	0.13	38.80	18.99	0.26	15.39	0.00	25.39		0.27		0.25	0.00	0.03	99.54	0.66	0.31
KH18-02	D12-R34	Nagoya	0.02	0.14	38.99	17.86	0.22	15.79	0.02	25.74		0.19		0.31	0.00	0.02	99.28	0.67	0.31
KH18-02	D12-R34	Nagoya	0.01	0.11	39.13	18.17	0.19	15.53	0.02	25.83		0.25		0.28	0.00	0.02	99.55	0.66	0.31
KH18-02	D12-R34	Nagoya	0.04	0.11	38.86	18.33	0.18	15.50	0.00	25.91		0.26		0.26	0.00	0.03	99.47	0.66	0.31

Cruise ID	Sample	Lab	SiO_2	TiO_2	Al_2O_3	FeO*	MnO	MgO	CaO	Cr_2O_3	Fe_2O_3	ZnO	V_2O_3	NiO	Na_2O	K_2O	Total	Mg#	Cr#
KH18-02	D12-R34	Nagoya	0.01	0.11	38.24	19.63	0.22	14.75	0.01	25.89		0.35		0.32	0.00	0.02	99.55	0.63	0.31
KH18-02	D12-R34	Nagoya	0.01	0.10	40.61	18.03	0.24	15.65	0.00	24.61		0.23		0.28	0.00	0.02	99.77	0.66	0.29
KH18-02	D12-R34	Nagoya	0.03	0.05	40.76	17.02	0.18	16.45	0.02	24.46		0.18		0.29	0.00	0.01	99.44	0.69	0.29
KH18-02	D12-R34	Nagoya	0.03	0.11	40.73	17.30	0.19	16.04	0.01	24.60		0.16		0.26	0.00	0.02	99.45	0.68	0.29
KH18-02	D12-R34	Nagoya	0.01	0.13	40.28	17.62	0.20	15.66	0.00	25.68		0.22		0.25	0.01	0.01	100.07	0.66	0.30
KH18-02	D12-R34	Nagoya	0.01	0.11	39.45	18.60	0.24	14.94	0.00	26.04		0.39		0.23	0.00	0.02	100.03	0.64	0.31
KH18-02	D12-R34	Nagoya	0.01	0.12	39.88	18.03	0.25	15.36	0.01	25.62		0.25		0.22	0.00	0.01	99.76	0.65	0.30
KH18-02	D12-R34	Nagoya	0.01	0.12	39.47	17.34	0.17	15.66	0.01	26.06		0.20		0.23	0.00	0.02	99.27	0.67	0.31
KH18-02	D12-R34	Nagoya	0.03	0.08	39.69	17.59	0.22	15.21	0.00	25.59		0.20		0.21	0.01	0.01	98.84	0.65	0.30
KH18-02	D12-R34	Nagoya	0.02	0.13	39.98	17.50	0.22	15.51	0.03	25.45		0.27		0.25	0.01	0.02	99.39	0.66	0.30
KH18-02	D12-R34	Nagoya	0.01	0.10	39.46	18.54	0.21	14.95	0.01	25.48		0.32		0.26	0.00	0.02	99.35	0.64	0.30
KH18-02	D12-R34	Nagoya	0.01	0.07	39.35	18.50	0.23	14.54	0.00	25.70		0.33		0.27	0.01	0.01	99.02	0.63	0.30
KH18-02	D12-R34	Nagoya	0.03	0.07	39.07	17.82	0.20	15.61	0.02	25.55		0.25		0.29	0.00	0.03	98.95	0.67	0.30
KH18-02	D12-R34	Nagoya	0.00	0.13	39.78	17.15	0.22	15.63	0.02	25.92		0.18		0.26	0.00	0.03	99.30	0.67	0.30
KH18-02	D12-R34	Nagoya	0.01	0.11	39.86	16.91	0.18	15.99	0.00	25.79		0.18		0.26	0.00	0.00	99.27	0.68	0.30
KH18-02	D12-R34	Nagoya	0.01	0.10	39.61	17.65	0.24	15.59	0.01	25.87		0.18		0.26	0.00	0.02	99.53	0.66	0.30
KH18-02	D12-R34	Nagoya	0.01	0.09	39.79	16.85	0.18	16.38	0.01	25.78		0.20		0.24	0.02	0.03	99.57	0.69	0.30
KH18-02	D12-R34	Nagoya	0.04	0.14	39.67	16.69	0.18	16.26	0.03	25.63		0.19		0.21	0.01	0.01	99.06	0.69	0.30
KH18-02	D12-R34	Nagoya	0.01	0.13	39.91	16.67	0.20	16.27	0.00	25.82		0.15		0.25	0.00	0.03	99.44	0.69	0.30
KH18-02	D12-R34	Nagoya	0.02	0.12	39.94	16.70	0.19	16.15	0.00	25.85		0.21		0.23	0.01	0.02	99.43	0.68	0.30
KH18-02	D12-R34	Nagoya	0.02	0.13	39.92	16.59	0.21	16.03	0.00	25.78		0.20		0.24	0.00	0.01	99.12	0.68	0.30
KH18-02	D12-R34	Nagoya	0.00	0.11	39.57	17.58	0.21	15.59	0.00	25.66		0.21		0.27	0.02	0.01	99.22	0.66	0.30
KH18-02	D12-R34	Nagoya	0.03	0.08	39.58	19.69	0.27	14.32	0.00	25.06		0.43		0.26	0.03	0.00	99.75	0.61	0.30
KH18-02	D12-R34	Nagoya	0.02	0.09	39.24	19.05	0.21	14.65	0.02	25.28		0.28		0.22	0.00	0.01	99.06	0.63	0.30
KH18-02	D12-R34	Nagoya	0.02	0.08	39.66	19.18	0.24	14.72	0.01	24.90		0.36		0.26	0.01	0.03	99.46	0.63	0.30
KH18-02	D12-R34	Nagoya	0.01	0.06	39.49	18.30	0.24	15.04	0.01	25.42		0.33		0.25	0.00	0.02	99.18	0.64	0.30
KH18-02	D12-R34	Nagoya	0.01	0.09	39.35	17.95	0.24	15.16	0.00	25.84		0.20		0.24	0.02	0.02	99.11	0.65	0.31
KH18-02	D12-R34	Nagoya	0.02	0.09	38.75	18.83	0.24	14.88	0.00	26.44		0.32		0.22	0.00	0.01	99.81	0.64	0.31
YK18-07	6K-1515-R02	Rice	0.00	0.05	50.18	12.54	0.12	17.84	0.00	18.09		0.13	0.14	0.32			99.41	0.73	0.19
YK18-07	6K-1515-R02	Rice	0.02	0.04	50.93	12.40	0.15	18.10	0.00	17.27		0.17	0.16	0.39			99.62	0.74	0.19
YK18-07	6K-1515-R02	Rice	0.00	0.02	50.82	12.43	0.11	18.12	0.00	17.31		0.17	0.14	0.30			99.42	0.74	0.19
YK18-07	6K-1515-R02	Rice	0.03	0.05	50.10	13.37	0.17	17.78	0.01	17.58		0.21	0.14	0.28			99.71	0.72	0.19
YK18-07	6K-1515-R02	Rice	0.00	0.06	49.40	13.39	0.18	17.26	0.00	18.47		0.18	0.09	0.23			99.26	0.71	0.20
YK18-07	6K-1515-R02	Rice	0.00	0.05	51.63	13.31	0.16	17.61	0.00	16.18		0.21	0.11	0.26			99.52	0.72	0.17

Cruise ID	Sample	Lab	SiO_2	TiO_2	Al_2O_3	FeO*	MnO	MgO	CaO	Cr_2O_3	Fe_2O_3	ZnO	V_2O_3	NiO	Na_2O	K_2O	Total	Mg#	Cr#
YK18-07	6K-1515-R02	Rice	0.00	0.01	52.25	12.74	0.15	17.95	0.00	16.55		0.16	0.13	0.29			100.23	0.72	0.18
YK18-07	6K-1515-R02	Rice	0.00	0.03	51.32	12.99	0.14	17.77	0.00	16.81		0.13	0.13	0.22			99.54	0.72	0.18
YK18-07	6K-1515-R02	Rice	0.03	0.01	47.36	18.98	0.22	14.50	0.00	17.72		0.65	0.11	0.23			99.82	0.61	0.20
YK18-07	6K-1515-R02	Rice	0.00	0.01	47.79	19.38	0.23	14.80	0.00	17.69		0.60	0.13	0.28			100.91	0.62	0.20
YK18-07	6K-1515-R02	Rice	0.00	0.01	46.43	19.57	0.23	14.35	0.00	18.03		0.59	0.09	0.18			99.48	0.61	0.21
YK18-07	6K-1515-R02	Rice	0.00	0.00	46.09	19.13	0.20	14.22	0.00	17.93		0.63	0.08	0.26			98.54	0.61	0.21
YK18-07	6K-1515-R03	Rice	0.00	0.03	48.99	14.35	0.13	17.17	0.00	17.47		0.33	0.13	0.28			98.87	0.71	0.19
YK18-07	6K-1515-R03	Rice	0.00	0.05	49.28	14.72	0.16	17.00	0.01	18.18		0.36	0.12	0.30			100.18	0.70	0.20
YK18-07	6K-1515-R03	Rice	0.01	0.04	48.36	14.81	0.17	16.80	0.02	18.26		0.30	0.11	0.30			99.19	0.70	0.20
YK18-07	6K-1515-R03	Rice	0.00	0.05	39.34	19.71	0.26	12.99	0.00	25.66		0.55	0.11	0.18			98.85	0.57	0.30
YK18-07	6K-1515-R03	Rice	0.00	0.01	48.44	15.19	0.19	17.19	0.00	18.21		0.30	0.12	0.36			100.02	0.71	0.20
YK18-07	6K-1515-R03	Rice	0.12	0.02	47.74	15.04	0.15	16.32	0.02	19.10		0.39	0.08	0.31			99.28	0.68	0.21
YK18-07	6K-1515-R03	Rice	0.00	0.04	49.13	13.39	0.17	17.54	0.00	18.75		0.13	0.10	0.33			99.58	0.72	0.20
YK18-07	6K-1515-R03	Rice	0.00	0.06	49.54	13.22	0.15	17.95	0.00	18.56		0.12	0.11	0.29			100.00	0.73	0.20
YK18-07	6K-1515-R03	Rice	0.00	0.10	48.49	13.72	0.15	17.39	0.00	19.12		0.17	0.13	0.27			99.54	0.71	0.21
YK18-07	6K-1515-R03	Rice	0.00	0.06	48.94	13.34	0.16	17.63	0.00	18.58		0.18	0.09	0.26			99.25	0.72	0.20
YK18-07	6K-1515-R03	Rice	0.00	0.04	49.59	14.15	0.17	17.73	0.01	18.05		0.39	0.18	0.28			100.59	0.72	0.20
YK18-07	6K-1515-R03	Rice	0.00	0.07	49.56	13.77	0.12	17.67	0.00	18.06		0.34	0.18	0.22			99.99	0.72	0.20
YK18-07	6K-1515-R03	Rice	0.00	0.04	38.33	15.26	0.20	14.74	0.00	28.16		0.28	0.25	0.21			97.48	0.65	0.33
YK18-07	6K-1515-R03	Rice	0.00	0.05	40.28	16.41	0.23	15.20	0.00	27.04		0.29	0.21	0.18			99.90	0.65	0.31
YK18-07	6K-1515-R03	Rice	0.00	0.04	32.19	18.68	0.24	13.35	0.01	34.44		0.23	0.25	0.13			99.56	0.60	0.42

Cruise ID	*Sample*	*Lab*	*SiO_2*	*TiO_2*	*Al_2O_3*	*FeO**	*MnO*	*MgO*	*CaO*	*Cr_2O_3*	*Fe_2O_3*	*ZnO*	*V_2O_3*	*NiO*	*Na_2O*	*K_2O*	*Total*	*Mg#*	*Cr#*
YK18-07	6K-1515-R03	Rice	0.00	0.08	48.52	13.33	0.13	17.53	0.00	19.31		0.15	0.17	0.26			99.48	0.72	0.21
YK18-07	6K-1515-R03	Rice	0.00	0.07	47.63	13.26	0.12	17.38	0.00	20.19		0.14	0.15	0.31			99.25	0.72	0.22
YK18-07	6K-1515-R06	Rice	0.00	0.14	17.55	38.68	0.71	3.05	0.00	37.06		0.95	0.11	0.12			98.38	0.16	0.59
YK18-07	6K-1515-R09	Rice	0.00	0.59	23.27	37.63	0.47	4.50	0.00	31.54		0.60		0.13			98.97	0.22	0.48
YK18-07	6K-1515-R09	Rice	0.01	0.51	25.35	36.70	0.44	4.68	0.00	30.27		0.81		0.27			99.26	0.23	0.44
YK18-07	6K-1515-R09	Rice	0.01	0.60	16.23	38.13	0.68	2.89	0.00	39.19		0.84		0.11			98.92	0.15	0.62
YK18-07	6K-1515-R09	Rice	0.01	0.62	15.89	38.35	0.86	2.94	0.00	38.74		0.93		0.11			98.73	0.15	0.62
YK18-07	6K-1515-R10	Rice	0.00	0.07	20.69	35.55	0.68	3.71	0.00	36.83		0.79		0.06			98.47	0.19	0.54
YK18-07	6K-1515-R10	Rice	0.00	0.09	23.65	34.53	0.78	4.01	0.00	35.73		0.91		0.00			99.81	0.20	0.50
YK18-07	6K-1515-R10	Rice	0.00	0.17	16.83	35.19	0.84	2.94	0.01	41.70		0.68		0.07			98.62	0.16	0.62
YK18-07	6K-1515-R10	Rice	0.03	0.01	33.68	24.68	0.34	9.91	0.00	29.99		0.86		0.14			99.77	0.46	0.37
YK18-07	6K-1515-R10	Rice	0.00	0.00	34.41	27.55	0.43	8.34	0.00	27.80		0.86		0.16			99.64	0.39	0.35
YK18-07	6K-1515-R10	Rice	0.01	0.13	20.54	34.74	0.65	4.04	0.00	38.25		0.70	0.15	0.07			99.28	0.21	0.56
YK18-07	6K-1515-R15	Rice	0.00	0.00	51.57	13.46	0.18	17.45	0.00	16.37		0.27	0.09	0.30			99.69	0.71	0.18
YK18-07	6K-1515-R15	Rice	0.01	0.00	51.74	14.30	0.14	16.67	0.00	15.60		0.29	0.12	0.33			99.20	0.68	0.17
YK18-07	6K-1515-R15	Rice	0.00	0.00	50.08	14.09	0.12	17.29	0.00	17.31		0.29	0.09	0.28			99.55	0.71	0.19
YK18-07	6K-1515-R15	Rice	0.00	0.00	48.29	14.12	0.15	16.87	0.04	18.92		0.34	0.10	0.24			99.08	0.70	0.21
YK18-07	6K-1515-R15	Rice	0.00	0.02	49.72	15.79	0.16	16.25	0.02	17.35		0.60	0.06	0.33			100.30	0.67	0.19
YK18-07	6K-1515-R15	Rice	0.00	0.00	50.09	14.86	0.17	16.76	0.00	17.24		0.66	0.09	0.34			100.21	0.69	0.19
YK18-07	6K-1515-R15	Rice	0.00	0.02	47.45	17.39	0.23	14.84	0.00	19.53		0.69	0.09	0.35			100.59	0.62	0.22
YK18-07	6K-1515-R15	Rice	0.00	0.01	51.61	12.87	0.12	17.71	0.01	16.30		0.27	0.12	0.30			99.32	0.72	0.17

Cruise ID	*Sample*	*Lab*	*SiO_2*	*TiO_2*	*Al_2O_3*	*FeO**	*MnO*	*MgO*	*CaO*	*Cr_2O_3*	*Fe_2O_3*	*ZnO*	*V_2O_3*	*NiO*	*Na_2O*	*K_2O*	*Total*	*Mg#*	*Cr#*
YK18-07	6K-1515-R15	Rice	0.01	0.04	52.31	13.01	0.16	18.24	0.02	15.67		0.27	0.07	0.23			100.03	0.73	0.17
YK18-07	6K-1515-R15	Rice	0.00	0.03	50.38	12.80	0.12	18.03	0.00	17.12		0.25	0.07	0.33			99.13	0.74	0.19
YK18-07	6K-1515-R15	Rice	0.00	0.00	51.38	12.51	0.19	18.10	0.00	16.72		0.26	0.07	0.32			99.55	0.74	0.18

Supplementary Table S2 D: Major element composition of amphiboles

Cruise ID	*Sample*	*SiO_2*	*TiO_2*	*Al_2O_3*	*FeO**	*MnO*	*MgO*	*CaO*	*Cr_2O_3*	*NiO*	*Na_2O*	*K_2O*	*Total*	*Si (a.p.f.u. for O = 23)*	*Na + K (a.p.f.u. for O = 23)*	*Comment*
KH18-02	D12-R05	44.88	0.53	12.75	3.16	0.04	16.94	12.35	2.60	0.09	3.01	0.24	96.57	6.38	0.87	Replacement over Pyroxene
KH18-02	D12-R05	46.10	0.38	11.75	4.64	0.09	20.37	9.07	2.26	0.09	2.53	0.21	97.49	6.43	0.72	Replacement over Pyroxene
KH18-02	D12-R05	44.61	1.43	12.39	3.25	0.07	17.51	12.17	1.93	0.10	2.52	0.41	96.40	6.35	0.77	Replacement over Pyroxene
KH18-02	D12-R05	44.72	1.34	12.52	3.22	0.10	17.64	11.91	2.01	0.07	2.55	0.42	96.50	6.35	0.78	Replacement over Pyroxene
KH18-02	D12-R17	45.94	0.55	11.24	3.59	0.04	19.32	12.55	1.65	0.08	2.24	0.13	97.32	6.46	0.63	Replacement over Pyroxene
KH18-02	D12-R17	46.64	0.63	10.83	3.54	0.05	18.61	13.05	1.63	0.12	2.26	0.13	97.48	6.55	0.64	Replacement over Pyroxene
KH18-02	D12-R17	45.95	1.13	11.13	3.57	0.11	18.41	12.67	1.06	0.15	2.03	0.16	96.36	6.51	0.59	Replacement over Pyroxene
YK18-07	6K-1515-R03	47.18	0.29	11.14	3.20	0.06	19.50	12.59	1.42	0.09	1.99	0.00	97.46	6.58	0.54	Replacement over Pyroxene
YK18-07	6K-1515-R03	47.14	0.19	6.58	4.20	0.11	23.85	9.54	0.56	0.09	1.34	0.04	93.64	6.80	0.38	Replacement over Pyroxene
YK18-07	6K-1515-R03	46.70	0.38	12.04	3.40	0.06	18.61	12.32	1.40	0.05	2.24	0.02	97.22	6.53	0.61	Replacement over Pyroxene
YK18-07	6K-1515-R03	46.60	0.70	11.93	3.27	0.05	18.61	12.72	1.14	0.08	2.34	0.03	97.47	6.51	0.64	Replacement over Pyroxene
YK18-07	6K-1515-R03	46.68	0.59	11.29	3.43	0.04	19.30	12.84	1.08	0.08	2.28	0.02	97.63	6.52	0.62	Replacement over Pyroxene
YK18-07	6K-1515-R03	46.98	0.49	11.45	3.20	0.07	19.37	12.52	1.69	0.05	2.22	0.05	98.10	6.53	0.61	Replacement over Pyroxene

Cruise ID	*Sample*	*SiO_2*	*TiO_2*	*Al_2O_3*	*FeO**	*MnO*	*MgO*	*CaO*	*Cr_2O_3*	*NiO*	*Na_2O*	*K_2O*	*Total*	*Si (a.p.f.u. for O = 23)*	*Na + K (a.p.f.u. for O = 23)*	*Comment*
YK18-07	6K-1515-R03	45.98	0.50	11.87	3.37	0.05	19.24	12.56	1.84	0.01	2.31	0.07	97.80	6.43	0.64	Replacement over Pyroxene
YK18-07	6K-1515-R03	46.67	0.47	11.71	3.42	0.07	19.20	12.39	1.34	0.08	2.18	0.04	97.56	6.51	0.60	Replacement over Pyroxene
YK18-07	6K-1515-R03	46.44	0.60	11.74	3.35	0.08	18.71	12.37	1.63	0.02	2.34	0.06	97.34	6.50	0.65	Replacement over Pyroxene
YK18-07	6K-1515-R03	46.54	0.50	12.09	3.38	0.05	18.99	12.36	1.37	0.08	2.29	0.06	97.71	6.49	0.63	Replacement over Pyroxene
YK18-07	6K-1515-R03	48.34	0.41	10.16	3.28	0.05	19.44	12.71	0.95	0.11	2.01	0.05	97.50	6.73	0.55	Replacement over Pyroxene
YK18-07	6K-1515-R03	47.11	0.48	11.31	3.28	0.08	18.92	12.42	1.59	0.07	2.26	0.07	97.59	6.57	0.62	Replacement over Pyroxene
YK18-07	6K-1515-R06	46.76	0.73	10.44	7.05	0.08	18.07	11.13	0.02	0.11	2.10	0.11	96.60	6.60	0.59	Vein
YK18-07	6K-1515-R06	45.79	0.70	11.71	7.45	0.14	17.46	11.21	0.00	0.04	2.36	0.19	97.04	6.45	0.68	Vein
YK18-07	6K-1515-R06	47.83	1.14	9.15	6.92	0.11	18.42	10.95	0.02	0.10	2.20	0.22	97.06	6.71	0.64	Vein
YK18-07	6K-1515-R06	46.22	1.14	10.43	6.65	0.11	18.01	11.16	0.00	0.10	2.37	0.20	96.40	6.55	0.69	Vein
YK18-07	6K-1515-R06	47.12	2.25	7.14	10.97	0.20	14.43	10.39	0.02	0.10	2.23	0.21	95.06	6.81	0.66	Vein
YK18-07	6K-1515-R06	47.58	2.16	7.00	10.70	0.16	16.28	10.63	0.03	0.01	2.05	0.26	96.86	6.75	0.61	Vein
YK18-07	6K-1515-R06	45.58	0.31	11.38	7.89	0.18	17.53	10.77	0.01	0.00	2.43	0.20	96.28	6.47	0.70	Vein
YK18-07	6K-1515-R06	44.81	0.36	12.52	8.23	0.13	16.94	10.99	0.00	0.09	2.55	0.16	96.79	6.35	0.73	Vein
YK18-07	6K-1515-R06	43.71	1.04	11.30	9.79	0.16	16.19	10.82	0.80	0.02	2.49	0.11	96.44	6.26	0.71	Vein
YK18-07	6K-1515-R06	43.82	0.95	11.27	9.52	0.15	16.29	10.69	0.91	0.00	2.52	0.11	96.23	6.28	0.72	Vein
YK18-07	6K-1515-R06	45.12	1.49	9.96	10.45	0.16	15.78	10.68	0.70	0.12	2.50	0.17	97.14	6.42	0.72	Vein
YK18-07	6K-1515-R06	46.20	1.70	9.00	10.41	0.20	16.31	10.37	0.20	0.13	2.34	0.20	97.06	6.55	0.68	Vein
YK18-07	6K-1515-R06	45.15	1.38	10.31	9.58	0.15	15.87	10.71	0.77	0.10	2.30	0.16	96.48	6.44	0.67	Vein
YK18-07	6K-1515-R06	45.98	0.21	10.61	6.75	0.12	17.89	11.09	1.09	0.07	2.38	0.15	96.34	6.53	0.68	Replacement over Pyroxene

Cruise ID	*Sample*	*SiO_2*	*TiO_2*	*Al_2O_3*	*FeO**	*MnO*	*MgO*	*CaO*	*Cr_2O_3*	*NiO*	*Na_2O*	*K_2O*	*Total*	*Si (a.p.f.u. for O = 23)*	*Na + K (a.p.f.u. for O = 23)*	*Comment*
YK18-07	6K-1515-R06	45.05	0.23	11.45	7.10	0.12	17.39	11.10	1.55	0.04	2.45	0.18	96.66	6.40	0.71	Replacement over Pyroxene
YK18-07	6K-1515-R06	46.00	0.18	10.64	6.68	0.13	17.81	11.10	1.20	0.12	2.49	0.19	96.54	6.53	0.72	Replacement over Pyroxene
YK18-07	6K-1515-R09	49.36	0.46	8.53	3.78	0.08	19.80	12.57	0.49	0.08	1.90	0.18	97.23	6.89	0.55	Replacement over Pyroxene
YK18-07	6K-1515-R09	48.23	0.23	9.18	4.43	0.10	19.26	11.76	1.46	0.07	2.11	0.20	97.03	6.77	0.61	Replacement over Pyroxene
YK18-07	6K-1515-R09	48.01	0.18	9.34	4.33	0.10	19.30	12.02	1.46	0.09	2.05	0.19	97.07	6.74	0.59	Replacement over Pyroxene
YK18-07	6K-1515-R10	49.29	1.36	7.33	5.88	0.13	19.23	11.13	0.65	0.18	2.01	0.12	97.31	6.89	0.57	Vein
YK18-07	6K-1515-R10	51.51	0.92	5.65	5.59	0.12	20.11	11.01	0.22	0.15	1.53	0.11	96.92	7.17	0.43	Vein
YK18-07	6K-1515-R10	48.49	1.09	8.19	6.07	0.11	18.78	11.01	0.37	0.18	2.13	0.13	96.55	6.83	0.60	Vein
YK18-07	6K-1515-R10	49.17	1.22	7.63	5.29	0.12	19.35	11.11	0.24	0.09	2.02	0.14	96.37	6.91	0.58	Vein

Supplementary Table S2 E: Trace element concentration (in ppm) in clinopyroxenes

Cruise ID	*Sample*	*La*	*Ce*	*Pr*	*Nd*	*Sm*	*Eu*	*Gd*	*Tb*	*Dy*	*Ho*	*Er*	*Tm*	*Yb*	*Lu*	*Comments*
KH18-02	D12-R01	0.11	0.08	0.02	0.13	0.09	0.06	0.35	0.10	0.86	0.23	0.64	0.10	0.72	0.10	
KH18-02	D12-R01	0.08	0.13	0.02	0.12	0.19	0.07	0.54	0.13	1.20	0.29	0.91	0.13	0.92	0.13	
KH18-02	D12-R01	0.12	0.08	0.03	0.12	0.17	0.07	0.53	0.12	1.03	0.24	0.79	0.12	0.77	0.12	
KH18-02	D12-R01	0.07	0.10	0.01	0.11	0.13	0.07	0.46	0.14	1.16	0.25	0.88	0.15	0.80	0.12	
KH18-02	D12-R01	0.05	0.09	0.01	0.05	0.12	0.05	0.42	0.11	0.90	0.22	0.67	0.10	0.70	0.07	
KH18-02	D12-R01	0.09	0.13	0.04	0.11	0.18	0.09	0.61	0.15	1.30	0.34	1.02	0.14	0.90	0.14	
KH18-02	D12-R01	0.05	0.22	0.04	0.10	0.14	0.08	0.50	0.13	1.02	0.24	0.81	0.11	0.75	0.13	
KH18-02	D12-R01	0.08	0.10	0.03	0.12	0.14	0.07	0.54	0.15	1.20	0.26	0.94	0.13	0.86	0.14	
KH18-02	D12-R01	0.07	0.08	0.01	0.10	0.25	0.07	0.56	0.14	1.14	0.28	0.86	0.13	0.91	0.14	
KH18-02	D12-R01	0.11	0.11	0.02	0.11	0.27	0.10	0.75	0.17	1.55	0.33	1.15	0.16	1.18	0.17	
KH18-02	D12-R01	0.06	0.07	0.02	0.10	0.18	0.10	0.53	0.16	1.09	0.26	0.76	0.12	0.92	0.12	
KH18-02	D12-R01	0.12	0.09	0.02	0.14	0.20	0.11	0.49	0.15	1.08	0.28	0.85	0.13	0.81	0.11	
KH18-02	D12-R01	0.10	0.15	0.02	0.12	0.18	0.07	0.52	0.13	1.03	0.24	0.83	0.11	0.83	0.12	
KH18-02	D12-R01	0.08	0.12	0.01	0.15	0.25	0.12	0.94	0.23	1.93	0.48	1.53	0.22	1.44	0.18	

Cruise ID	*Sample*	*La*	*Ce*	*Pr*	*Nd*	*Sm*	*Eu*	*Gd*	*Tb*	*Dy*	*Ho*	*Er*	*Tm*	*Yb*	*Lu*	*Comments*
KH18-02	D12-R01	0.06	0.09	0.03	0.14	0.28	0.10	0.82	0.18	1.51	0.36	1.04	0.17	1.20	0.14	
KH18-02	D12-R01	0.04	0.10	0.01	0.10	0.18	0.09	0.42	0.14	1.08	0.24	0.87	0.13	0.84	0.11	
KH18-02	D12-R01	0.09	0.06	0.05	0.11	0.20	0.09	0.64	0.15	1.36	0.31	1.03	0.14	1.08	0.14	
KH18-02	D12-R01	0.16	0.23	0.03	0.12	0.20	0.11	0.58	0.15	1.18	0.29	0.96	0.14	1.14	0.16	
KH18-02	D12-R01	0.07	0.08	0.03	0.14	0.24	0.10	0.83	0.17	1.54	0.36	1.19	0.18	1.24	0.16	
KH18-02	D12-R01	0.09	0.13	0.02	0.14	0.32	0.11	0.77	0.18	1.65	0.37	1.23	0.16	1.24	0.17	
KH18-02	D12-R01	0.10	0.22	0.02	0.15	0.26	0.10	0.77	0.21	1.44	0.36	1.10	0.18	1.20	0.17	
KH18-02	D12-R01	0.05	0.05	0.01	0.11	0.14	0.08	0.61	0.14	1.13	0.24	0.89	0.13	0.94	0.12	
KH18-02	D12-R05	2.44	8.80	1.18	4.53	1.26	0.29	1.70	0.33	2.49	0.63	1.97	0.28	2.19	0.28	Enriched
KH18-02	D12-R05	2.59	8.76	1.05	3.73	1.04	0.27	1.49	0.31	2.32	0.54	1.78	0.26	1.81	0.28	Enriched
KH18-02	D12-R06	2.52	9.33	1.23	4.55	1.24	0.27	1.72	0.39	2.80	0.69	2.14	0.34	2.34	0.31	Enriched
KH18-02	D12-R06	3.00	10.58	1.27	4.41	1.14	0.29	1.57	0.35	2.68	0.61	1.99	0.30	2.11	0.31	Enriched
KH18-02	D12-R06	0.01	0.04	0.01	0.16	0.28	0.13	1.04	0.22	1.76	0.44	1.30	0.22	1.40	0.22	
KH18-02	D12-R06	0.03	0.05	0.01	0.15	0.31	0.15	1.13	0.24	2.01	0.47	1.36	0.23	1.47	0.20	
KH18-02	D12-R06	0.02	0.08	0.01	0.18	0.33	0.13	1.01	0.21	1.87	0.42	1.23	0.21	1.32	0.18	
KH18-02	D12-R06	0.11	0.39	0.08	0.27	0.34	0.15	0.77	0.21	1.71	0.39	1.27	0.20	1.31	0.16	
KH18-02	D12-R06	0.15	0.48	0.06	0.29	0.31	0.12	0.83	0.20	1.79	0.42	1.16	0.21	1.17	0.17	
KH18-02	D12-R06	0.08	0.22	0.02	0.22	0.31	0.14	0.88	0.19	1.65	0.40	1.04	0.17	1.28	0.18	
KH18-02	D12-R07	2.30	7.78	0.99	4.01	0.98	0.26	1.64	0.30	2.55	0.62	1.82	0.27	1.98	0.27	Enriched
KH18-02	D12-R07	2.59	8.15	0.98	3.70	1.01	0.30	1.41	0.32	2.47	0.55	1.92	0.30	2.07	0.28	Enriched
KH18-02	D12-R08	3.25	14.36	2.50	11.03	2.94	0.78	3.48	0.65	4.27	0.99	2.95	0.46	3.02	0.39	Enriched
KH18-02	D12-R08	3.19	10.80	1.55	6.58	1.98	0.52	2.67	0.55	3.76	0.86	2.74	0.38	2.58	0.35	Enriched
KH18-02	D12-R09	2.58	9.10	1.33	5.73	1.73	0.47	2.24	0.46	3.29	0.74	2.23	0.36	2.05	0.27	Enriched
KH18-02	D12-R09	2.68	9.03	1.26	5.32	1.37	0.47	1.81	0.38	2.66	0.62	1.95	0.29	1.90	0.27	Enriched
KH18-02	D12-R10	2.63	8.77	1.13	4.65	1.24	0.45	1.60	0.33	2.37	0.58	1.75	0.25	1.63	0.23	Enriched
KH18-02	D12-R19	0.16	0.17	0.01	0.06	0.12	0.07	0.42	0.11	0.96	0.22	0.79	0.13	0.81	0.12	
KH18-02	D12-R19	0.18	0.17	0.01	0.09	0.14	0.09	0.51	0.13	1.06	0.24	0.76	0.13	0.85	0.12	
KH18-02	D12-R19	0.16	0.25	0.02	0.13	0.16	0.11	0.54	0.12	1.00	0.23	0.76	0.14	0.73	0.12	
KH18-02	D12-R19	0.11	0.12	0.03	0.09	0.17	0.08	0.57	0.14	1.00	0.26	0.81	0.12	0.85	0.11	
KH18-02	D12-R19	0.27	0.45	0.05	0.14	0.14	0.06	0.35	0.09	0.67	0.16	0.53	0.09	0.57	0.09	
KH18-02	D12-R20	0.07	0.37	0.09	0.18	0.13	0.07	0.51	0.24	1.10	0.26	0.85	0.13	0.80	0.11	
KH18-02	D12-R20	0.04	0.13	0.03	0.13	0.25	0.21	0.70	0.17	1.36	0.33	1.04	0.16	0.99	0.13	
KH18-02	D12-R20	0.04	0.04	0.01	0.12	0.24	0.07	0.72	0.15	1.29	0.29	0.88	0.14	0.83	0.12	
KH18-02	D12-R20	0.04	0.25	0.02	0.13	0.24	0.07	0.81	0.20	1.54	0.37	1.11	0.18	1.10	0.15	
KH18-02	D12-R20	0.02	0.02	0.02	0.08	0.21	0.09	0.63	0.18	1.29	0.31	1.02	0.14	0.80	0.14	
KH18-02	D12-R20	0.07	0.04	0.03	0.11	0.17	0.06	0.48	0.15	1.04	0.23	0.75	0.11	0.79	0.11	
KH18-02	D12-R20	0.04	0.16	0.12	0.14	0.24	0.10	0.72	0.21	1.49	0.38	1.27	0.17	1.01	0.15	
KH18-02	D12-R20	0.03	0.02	0.04	0.13	0.19	0.07	0.61	0.16	1.20	0.28	0.92	0.14	0.72	0.11	

Cruise ID	*Sample*	*La*	*Ce*	*Pr*	*Nd*	*Sm*	*Eu*	*Gd*	*Tb*	*Dy*	*Ho*	*Er*	*Tm*	*Yb*	*Lu*	*Comments*
KH18-02	D12-R20	0.06	0.18	0.03	0.11	0.21	0.09	0.48	0.14	1.14	0.27	0.84	0.14	0.79	0.12	
KH18-02	D12-R20	0.06	0.08	0.01	0.11	0.17	0.10	0.53	0.14	1.15	0.28	0.89	0.12	0.73	0.11	
KH18-02	D12-R20	0.10	0.05	0.05	0.13	0.17	0.10	0.48	0.14	0.98	0.27	0.82	0.12	0.75	0.12	
KH18-02	D12-R20	0.03	0.12	0.02	0.10	0.23	0.10	0.50	0.14	1.17	0.26	0.84	0.12	0.72	0.11	
KH18-02	D12-R20	0.06	0.12	0.02	0.12	0.23	0.08	0.73	0.18	1.54	0.35	1.06	0.17	1.05	0.14	
KH18-02	D12-R20	0.07	0.09	0.01	0.17	0.29	0.12	0.87	0.22	1.71	0.40	1.31	0.19	1.17	0.15	
KH18-02	D12-R20	0.09	0.27	0.06	0.11	0.20	0.11	0.65	0.17	1.40	0.32	1.04	0.17	0.83	0.13	
KH18-02	D12-R20	0.05	0.08	0.14	0.11	0.27	0.11	0.58	0.19	1.45	0.33	1.07	0.17	0.86	0.15	
KH18-02	D12-R20	0.06	0.24	0.04	0.14	0.22	0.08	0.61	0.14	1.13	0.29	0.88	0.13	0.73	0.10	
KH18-02	D12-R20	0.02	0.28	0.05	0.09	0.17	0.11	0.58	0.17	1.25	0.30	0.96	0.14	0.81	0.13	
KH18-02	D12-R20	0.05	0.04	0.01	0.15	0.18	0.08	0.54	0.15	1.32	0.31	0.93	0.14	0.94	0.11	
KH18-02	D12-R33	0.16	0.36	0.05	0.27	0.35	0.15	0.99	0.23	1.71	0.37	1.21	0.18	1.09	0.20	
KH18-02	D12-R33	0.17	0.50	0.07	0.36	0.36	0.17	0.79	0.19	1.53	0.39	1.17	0.17	1.15	0.16	
KH18-02	D12-R33	0.06	0.22	0.04	0.29	0.32	0.13	0.75	0.18	1.45	0.34	1.03	0.15	1.04	0.15	
KH18-02	D12-R33	0.14	0.39	0.09	0.32	0.25	0.15	0.83	0.23	1.71	0.38	1.17	0.19	1.11	0.19	
KH18-02	D12-R33	0.15	0.35	0.05	0.34	0.34	0.14	0.88	0.19	1.64	0.40	1.23	0.17	1.15	0.17	
KH18-02	D12-R33	0.22	0.78	0.10	0.64	0.45	0.15	0.95	0.23	1.74	0.41	1.30	0.20	1.33	0.20	
KH18-02	D12-R33	0.14	0.51	0.06	0.31	0.33	0.12	0.76	0.19	1.41	0.35	1.11	0.18	0.97	0.15	
KH18-02	D12-R33	0.22	0.89	0.09	0.41	0.35	0.13	0.85	0.20	1.78	0.37	1.19	0.17	1.27	0.16	
KH18-02	D12-R33	0.14	0.29	0.03	0.22	0.35	0.12	0.76	0.16	1.37	0.30	0.88	0.14	0.89	0.14	
KH18-02	D12-R33	0.30	0.67	0.07	0.31	0.28	0.15	0.82	0.19	1.44	0.34	1.11	0.15	1.11	0.16	
KH18-02	D12-R33	0.24	0.68	0.09	0.45	0.38	0.17	0.85	0.20	1.54	0.36	1.20	0.15	1.10	0.15	
KH18-02	D15-R01	0.08	0.12	0.03	0.08	0.12	0.08	0.52	0.13	1.24	0.31	1.09	0.16	1.05	0.15	
KH18-02	D15-R01	0.08	0.37	0.02	0.20	0.16	0.08	0.69	0.17	1.27	0.31	1.16	0.17	1.16	0.16	
KH18-02	D15-R01	0.07	0.28	0.04	0.12	0.17	0.12	0.40	0.12	1.05	0.24	0.84	0.12	0.83	0.11	
KH18-02	D15-R01	0.06	0.12	0.04	0.08	0.16	0.09	0.45	0.12	1.04	0.26	0.73	0.12	0.80	0.14	
KH18-02	D15-R01	0.02	0.34	0.01	0.05	0.17	0.08	0.56	0.14	1.22	0.32	0.98	0.15	0.86	0.12	
KH18-02	D15-R01	0.06	0.22	0.08	0.11	0.12	0.09	0.62	0.16	1.40	0.36	1.20	0.18	1.09	0.17	
KH18-02	D12-R17	1.88	6.72	1.24	6.81	2.30	0.63	3.05	0.60	3.79	0.85	2.58	0.43	2.68	0.40	Enriched
KH18-02	D12-R17	1.85	6.19	1.15	6.48	2.38	0.61	3.08	0.55	3.95	0.88	2.48	0.42	2.45	0.34	Enriched
KH18-02	D12-R17	1.75	5.57	0.85	4.02	1.14	0.31	1.28	0.25	1.84	0.41	1.28	0.21	1.39	0.21	Enriched
KH18-02	D12-R17	1.22	4.26	0.59	2.71	0.77	0.24	0.92	0.19	1.28	0.28	0.88	0.17	1.05	0.14	Enriched
KH18-02	D12-R17	1.51	5.50	1.07	6.31	2.64	0.65	4.17	0.75	4.82	1.04	2.80	0.41	2.29	0.30	Enriched
KH18-02	D12-R17	2.45	8.66	1.71	10.81	4.23	1.03	5.86	1.07	7.07	1.58	4.63	0.63	3.75	0.53	Enriched
KH18-02	D12-R17	1.86	7.42	1.30	7.60	2.99	0.77	4.43	0.77	5.07	1.10	2.91	0.45	2.50	0.33	Enriched
KH18-02	D12-R33	1.24	5.83	1.12	6.83	2.45	0.56	3.16	0.59	4.00	0.79	2.27	0.31	1.77	0.25	Enriched
KH18-02	D12-R33	1.62	8.10	1.64	9.10	3.48	0.86	4.44	0.86	5.60	1.09	2.96	0.40	2.28	0.30	Enriched
KH18-02	D12-R33	1.41	6.36	1.27	7.39	2.80	0.54	4.09	0.70	4.69	0.86	2.37	0.32	1.76	0.26	Enriched

Cruise ID	*Sample*	*La*	*Ce*	*Pr*	*Nd*	*Sm*	*Eu*	*Gd*	*Tb*	*Dy*	*Ho*	*Er*	*Tm*	*Yb*	*Lu*	*Comments*
YK18-07	6K-1515-R02	0.37	0.79	0.05	0.20	0.22	0.15	0.76	0.20	1.38	0.33	1.00	0.16	1.03	0.14	
YK18-07	6K-1515-R02	0.16	0.19	0.03	0.21	0.32	0.18	0.87	0.19	1.44	0.41	1.27	0.16	1.05	0.16	
YK18-07	6K-1515-R02	0.08	0.05	0.02	0.22	0.27	0.15	0.74	0.20	1.35	0.34	1.14	0.18	1.03	0.17	
YK18-07	6K-1515-R02	0.05	0.04	0.01	0.15	0.25	0.13	0.64	0.16	1.13	0.31	0.99	0.15	0.92	0.11	
YK18-07	6K-1515-R02	0.11	0.10	0.03	0.21	0.30	0.14	0.67	0.19	1.50	0.37	1.27	0.18	1.19	0.17	
YK18-07	6K-1515-R02	0.12	0.40	0.02	0.19	0.27	0.14	0.90	0.20	1.52	0.34	1.21	0.19	1.12	0.17	
YK18-07	6K-1515-R02	0.09	0.13	0.05	0.18	0.32	0.14	0.80	0.21	1.45	0.34	1.21	0.18	1.01	0.17	
YK18-07	6K-1515-R02	0.11	0.16	0.02	0.20	0.33	0.13	0.76	0.19	1.36	0.36	1.08	0.17	0.95	0.14	
YK18-07	6K-1515-R02	0.08	0.09	0.03	0.18	0.25	0.13	0.77	0.16	1.24	0.30	1.00	0.14	0.90	0.12	
YK18-07	6K-1515-R02	0.02	0.02	0.02	0.21	0.32	0.19	0.88	0.23	1.75	0.39	1.32	0.19	1.23	0.17	
YK18-07	6K-1515-R02	0.02	0.02	0.01	0.12	0.20	0.13	0.53	0.15	1.20	0.27	0.88	0.13	0.79	0.12	
YK18-07	6K-1515-R02	0.05	0.14	0.02	0.22	0.22	0.15	0.77	0.18	1.47	0.33	1.08	0.14	0.93	0.13	
YK18-07	6K-1515-R02	0.01	0.02	0.00	0.09	0.30	0.12	0.70	0.15	1.25	0.30	0.88	0.13	0.86	0.11	
YK18-07	6K-1515-R02	0.01	0.01	0.01	0.14	0.29	0.16	0.91	0.20	1.66	0.38	1.12	0.16	1.02	0.15	
YK18-07	6K-1515-R02	0.01	0.01	0.01	0.12	0.24	0.13	0.80	0.17	1.57	0.32	1.02	0.15	0.90	0.14	
YK18-07	6K-1515-R03	0.26	0.59	0.08	0.60	0.65	0.26	1.95	0.44	3.39	0.84	2.58	0.40	2.47	0.37	
YK18-07	6K-1515-R03	0.23	0.56	0.07	0.53	0.65	0.27	1.68	0.38	3.16	0.73	2.35	0.35	2.20	0.32	
YK18-07	6K-1515-R03	0.18	0.35	0.05	0.37	0.43	0.20	1.17	0.28	2.25	0.54	1.64	0.26	1.70	0.25	
YK18-07	6K-1515-R06	1.03	3.77	0.67	4.89	2.46	0.59	4.26	0.80	5.26	1.08	2.88	0.40	2.26	0.35	Enriched
YK18-07	6K-1515-R06	1.61	5.09	0.93	5.41	2.50	0.74	3.90	0.75	4.94	1.06	2.76	0.40	2.40	0.36	Enriched
YK18-07	6K-1515-R06	0.86	3.38	0.72	4.30	2.36	0.55	3.95	0.73	5.13	1.07	2.91	0.38	2.36	0.36	Enriched

Cruise ID	*Sample*	*La*	*Ce*	*Pr*	*Nd*	*Sm*	*Eu*	*Gd*	*Tb*	*Dy*	*Ho*	*Er*	*Tm*	*Yb*	*Lu*	*Comments*
YK18-07	6K-1515-R06	0.92	2.94	0.57	3.93	1.92	0.49	3.30	0.72	4.51	0.95	2.61	0.38	2.08	0.32	Enriched
YK18-07	6K-1515-R15	0.29	0.41	0.08	0.20	0.18	0.10	0.49	0.15	1.03	0.26	0.70	0.11	0.71	0.09	
YK18-07	6K-1515-R15	0.34	0.61	0.06	0.28	0.20	0.09	0.47	0.12	0.99	0.23	0.78	0.12	0.81	0.13	
YK18-07	6K-1515-R15	0.14	0.19	0.02	0.18	0.29	0.14	0.82	0.21	1.57	0.39	1.09	0.17	1.14	0.16	
YK18-07	6K-1515-R15	0.05	0.16	0.01	0.17	0.35	0.15	0.80	0.20	1.44	0.36	1.12	0.16	1.00	0.16	
YK18-07	6K-1515-R15	0.05	0.07	0.03	0.21	0.29	0.15	0.78	0.17	1.34	0.31	0.88	0.15	0.97	0.13	
YK18-07	6K-1515-R15	0.26	0.51	0.03	0.18	0.23	0.13	0.66	0.17	1.38	0.28	0.91	0.13	0.84	0.16	
YK18-07	6K-1515-R15	0.20	0.39	0.04	0.35	0.33	0.15	0.98	0.24	1.86	0.45	1.29	0.19	1.41	0.18	
YK18-07	6K-1515-R15	0.16	0.26	0.05	0.26	0.34	0.15	0.82	0.19	1.55	0.36	1.17	0.15	1.07	0.17	
YK18-07	6K-1515-R15	0.34	0.49	0.12	0.44	0.29	0.34	0.85	0.19	1.58	0.37	1.10	0.15	1.09	0.16	
YK18-07	6K-1515-R15	0.18	0.37	0.03	0.26	0.29	0.20	0.82	0.19	1.64	0.33	1.05	0.14	1.01	0.17	
YK18-07	6K-1515-R15	0.05	0.10	0.01	0.23	0.21	0.13	0.65	0.14	1.16	0.30	0.86	0.14	0.93	0.15	
YK18-07	6K-1515-R15	0.04	0.08	0.01	0.22	0.36	0.16	0.84	0.19	1.40	0.37	1.03	0.17	1.03	0.18	
YK18-07	6K-1515-R15	0.04	0.19	0.01	0.17	0.26	0.15	0.82	0.17	1.24	0.34	0.94	0.16	0.94	0.16	
YK18-07	6K-1515-R15	0.07	0.05	0.03	0.15	0.20	0.12	0.58	0.14	1.20	0.27	0.91	0.12	0.90	0.15	
YK18-07	6K-1515-R15	0.31	0.62	0.08	0.36	0.31	0.17	0.94	0.22	1.52	0.40	1.08	0.21	1.07	0.15	
YK18-07	6K-1515-R15	0.10	0.24	0.02	0.24	0.27	0.15	0.96	0.21	1.63	0.41	1.18	0.20	1.24	0.18	
YK18-07	6K-1515-R15	0.02	0.04	0.01	0.20	0.27	0.16	0.89	0.23	1.65	0.40	1.23	0.20	1.14	0.20	

Supplementary Table S2 F: Major element compositional (wt.%) of zoned spinels

Cruise ID	*Sample*	*SiO_2*	*TiO_2*	*Al_2O_3*	*FeO**	*MnO*	*MgO*	*CaO*	*Cr_2O_3*	*ZnO*	*V_2O_3*	*NiO*	*Total*	*Mg#*	*Cr#*	*Comment*

KH18-02	D12-R14	0.02	0.01	37.17	19.73	0.24	13.09	0.00	28.44	0.59	0.13	0.19	99.62	0.58	0.34	Core
KH18-02	D12-R14	0.03	0.06	37.58	19.06	0.22	13.76	0.00	28.40	0.50	0.11	0.13	99.85	0.60	0.34	Core
KH18-02	D12-R14	0.00	0.05	33.47	20.98	0.24	12.01	0.00	32.06	0.50	0.08	0.11	99.50	0.54	0.39	Core
KH18-02	D12-R14	0.00	0.08	35.33	19.37	0.25	12.83	0.01	30.66	0.40	0.12	0.16	99.22	0.57	0.37	Core
KH18-02	D12-R14	0.00	0.05	35.04	20.15	0.24	12.61	0.01	30.76	0.49	0.09	0.15	99.58	0.56	0.37	Core
KH18-02	D12-R14	0.00	0.08	33.37	20.85	0.21	12.20	0.00	32.64	0.56	0.12	0.13	100.17	0.55	0.40	Core
KH18-02	D12-R14	0.01	0.02	31.30	22.47	0.26	11.08	0.00	33.15	0.37	0.08	0.11	98.85	0.51	0.42	Boundary
KH18-02	D12-R14	0.01	0.06	31.90	20.94	0.24	11.67	0.06	33.40	0.45	0.15	0.04	98.92	0.53	0.41	Boundary
KH18-02	D12-R14	0.00	0.02	29.35	23.80	0.32	10.35	0.07	34.65	0.51	0.14	0.11	99.32	0.48	0.44	Boundary
KH18-02	D12-R14	0.06	0.05	31.65	21.66	0.24	11.32	0.02	33.65	0.41	0.10	0.06	99.22	0.52	0.42	Boundary
KH18-02	D12-R14	0.00	0.05	30.97	22.73	0.24	10.98	0.07	33.10	0.45	0.08	0.07	98.74	0.51	0.42	Boundary
KH18-02	D12-R14	0.00	0.07	30.71	22.46	0.27	10.91	0.03	34.35	0.25	0.10	0.12	99.28	0.50	0.43	Boundary
KH18-02	D12-R14	0.05	0.02	30.88	21.14	0.28	11.47	0.04	34.11	0.38	0.08	0.09	98.54	0.53	0.43	Boundary
KH18-02	D12-R14	0.02	0.01	31.61	20.89	0.28	11.79	0.03	33.89	0.59	0.10	0.14	99.34	0.54	0.42	Boundary
YK18-07	6K-1515-R03	0.00	0.04	49.59	14.15	0.17	17.73	0.01	18.05	0.39	0.18	0.28	100.59	0.72	0.20	Core
YK18-07	6K-1515-R03	0.00	0.07	49.56	13.77	0.12	17.67	0.00	18.06	0.34	0.18	0.22	99.99	0.72	0.20	Core
YK18-07	6K-1515-R03	0.00	0.04	38.33	15.26	0.20	14.74	0.00	28.16	0.28	0.25	0.21	97.48	0.65	0.33	Boundary
YK18-07	6K-1515-R03	0.00	0.05	40.28	16.41	0.23	15.20	0.00	27.04	0.29	0.21	0.18	99.90	0.65	0.31	Boundary

Chapter 3: Termination of back-arc spreading and magmatic activity at the Shikoku basin revealed from zircon bearing amphibole veins in peridotites from the Mado Megamullion

3.1. Introduction

Oceanic core complexes (OCCs) are formed by the exhumation of lithosphere along low angle detachment faults at slow spreading rates. The Mado Megamullion is a recently discovered OCC in the back-arc spreading environment of the Shikoku Basin in the Philippine Sea Plate (Figure 2.1). The Shikoku Basin has undergone changes in spreading rate and direction. Magnetic anomaly data suggest that spreading in the Shikoku basin ceased after 15 Ma. Based on thermal anomalies it was proposed that a later spreading phase of nearly N-S spreading existed between 15 to 12 Ma. The age of volcanism in the Kinan Seamount chain which is situated in the center of the graben reveals an ^{40}Ar-^{39}Ar age of 15-10 Ma. Since these basalts revealed enriched signatures they were interpreted to be formed during the final stages or post-cessation of back-arc spreading by mantle-upwelling that continued after cessation of back-arc spreading.

The age of termination of spreading is not constrained from geochronologic evidence yet. We dated zircons from amphibole-chlorite bearing veins that crosscut the mantle peridotites of the Mado Megamullion. These zircons do not show compositional zoning. Titanium in zircon geothermometer reveals a crystallization temperature ranging between 650 to 828 ºC. We dated zircons from amphibole bearing veins from a peridotite sample. These zircons reveal a U-Pb age of 13.37 ± 0.24 Ma in Sensitive High Resolution Ion Microprobe (SHRIMP). The U-Pb zircon

ages constrain magmatic activity at least until 13 Ma. The trace and REE chemistry of the zircons and the amphiboles and the calculated crystallization temperature suggests that these are igneous-mafic zircons that could have crystallized from a hydrous gabbroic melt. Since these high temperature zircons are associated with magmatic veins and gabbros we suggest that mantle upwelling and magmatism continued until 13 Ma while magnetic anomaly data suggest spreading was terminated at 15 Ma our study reveals the possibility that back-arc spreading continued till 13 Ma.

The Shikoku basin was created by back-arc spreading as a result of the westward subduction of the Pacific plate (Karig 1971; Okino et al., 1994). The rifting was initiated at the Shikoku basin after the cessation of arc volcanism at the Kyushu-Palau ridge. The age of initiation of rifting at the Shikoku basin cannot be clearly constrained due to the subduction of the older crust along Nankai Trough. Assuming a similar age for rifting of the Parece Vela basin and the Shikoku basin a Middle Miocene age of 30 Ma could be inferred (Kasuga & Ohara, 1997; Okino et al., 1994). The rifting was followed by the opening of the Shikoku basin from 26Ma. The northwestward propagation of the Philippine Sea Plate at a velocity of 3.5 cm/year (Seno and Maruyama, 1984) and the eastward retreat of the Izu-Bonin-Mariana Trench led to the formation of the Shikoku basin between 30-17 Ma (Okino et al., 1994). At 23 Ma there was a clockwise rotation of the spreading axis and decrease of spreading rate from 4.5 cm/year to 2.3 cm/year after which the direction of spreading changed again at 19 Ma from E-W to NE-SW. This change in the spreading rate was slow which was determined by the curved transform faults (Okino et al., 1994). Lineation of the magnetic anomalies, 5E and 5B reflects an age of 15 Ma after which spreading is considered to

have ceased in the Shikoku Basin. Based on heat flow versus age measurements based on standard heat flow laws (Parsons and Sclater 1977) it was seen that the measured values underestimate the actual heat flux of the oceanic crust. Thermal modelling also showed that the plate subducting beneath the Nankai trough was hot (Yamano et al., 1984). Based on these observations it was proposed that a later spreading phase of nearly N-S spreading existed between 15 to 12Ma (Rooke et al., 1987). The Kinan Seamount chain situated in the graben in the centre of the basin reveals an ^{40}Ar-^{39}Ar age of 15-10 Ma (Ishii et al., 2000). Since these seamounts were situated on transform faults, they are interpreted to be created by the upwelling of magmas between the remnant spreading center and the fracture zones (Okino et al., 1994). Based on the enriched geochemical signatures and comparison to other enriched post-spreading basalts from back-arc basins indicated that geochemically enriched basalts are commonly formed during the final stages or post-cessation of back-arc spreading (Sato et al., 2002). This was explained by the process of mantle upwelling induced by back-arc spreading that continued post cessation of back-arc spreading.

Although the age of termination of back-arc spreading in the Shikoku Basin is considered to be at 15 Ma from magnetic anomaly data, this age is not well constrained by geochemical evidence. In this study we report ages of zircon grains from amphibole-chlorite bearing veins that crosscut the peridotites of the Mado Megamullion. In combination with trace element chemistry of zircon and amphibole grains we try to constrain the process of mantle upwelling at the termination stage and the age of cessation of back-arc spreading at the Shikoku basin.

3.2. Petrography

Peridotites were recovered from the Mado Megamullion by dredging and submersible dives on cruises KH18-02 and YK18-07. Some of the peridotites contains leucocratic veins that crosscut the peridotitic framework. In this study we study zircon grains from a leucocratic vein bearing peridotite sample, YK18-07 6K1515-R10 (Figure 3-1A). These veins are amphibole-chlorite bearing, with traces of zircon and apatites and Fe-Ti oxides (Figure 3-1B). Similar veins cross-cutting the peridotites are present in other samples, but zircon grains were only found in sample YK18-07 6K1515-R10. The amphiboles associated with the zircon grains are pleochroic from green to brown and does not exhibit any signature of deformation (Figure 3-1C). The zircon grains range in diameter from 10μ to 120μ. The zircons are homogeneous under back scattered electron (BSE) and cathode-luminescence (CL) and do not display oscillatory zoning or overgrowth (Figure 3-2A). Some of the zircon grains have cracks and display patchy zoning (Figure 3-2B). Zircons were also found in some of the gabbro samples from KH-18-02 dredging cruise.

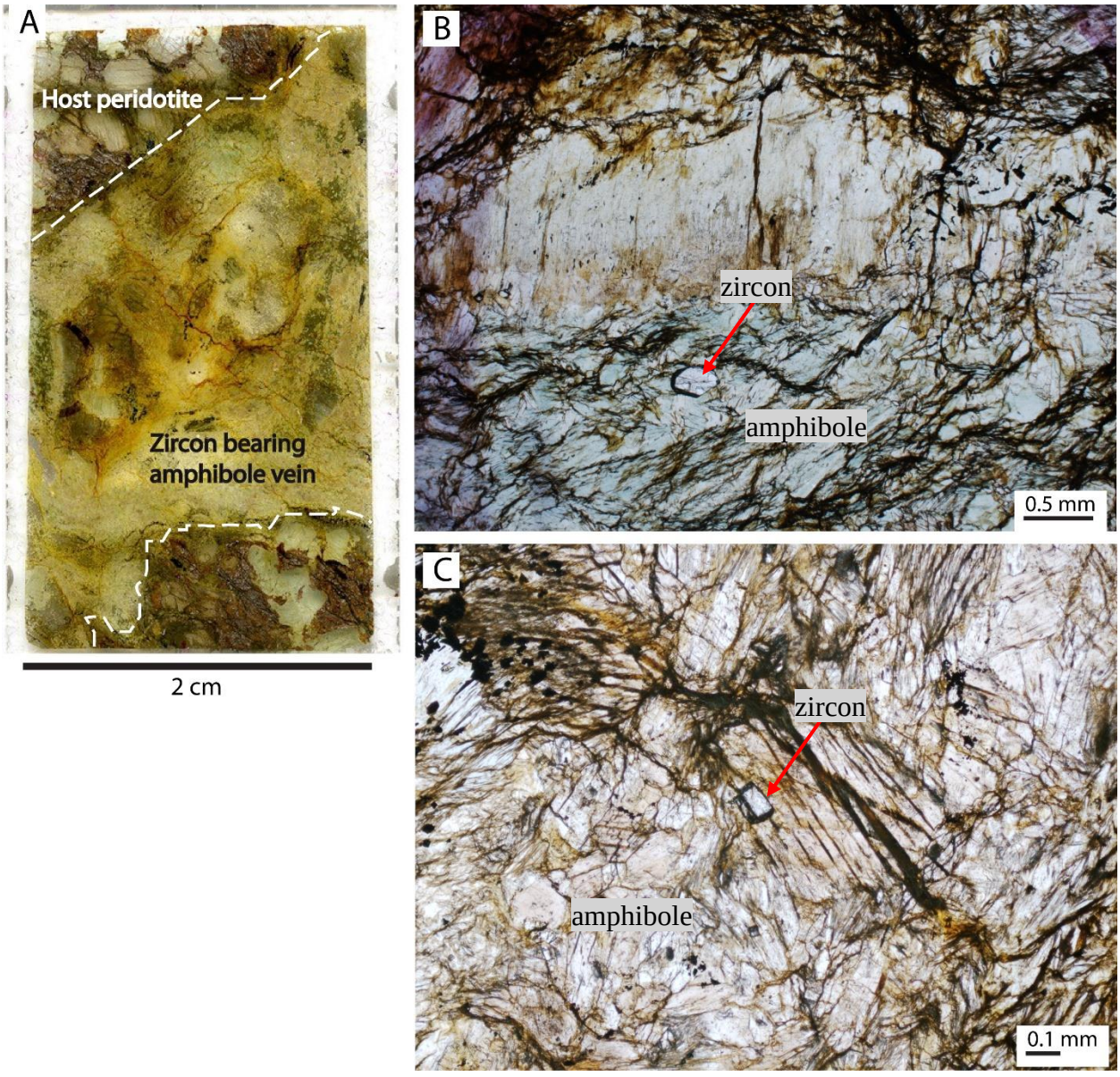

Figure 3-1: Thin section image and photomicrographs illustrating the textural relationships between zircon-bearing veins and peridotite. A. Thin section image showing a zircon-bearing amphibole vein cross-cutting the peridotite. B. Photomicrographs illustrating the association of zircon grains with amphibole grains. C. Pleochroic (between green to brown) amphiboles associated with zircons and Fe-Ti oxides.

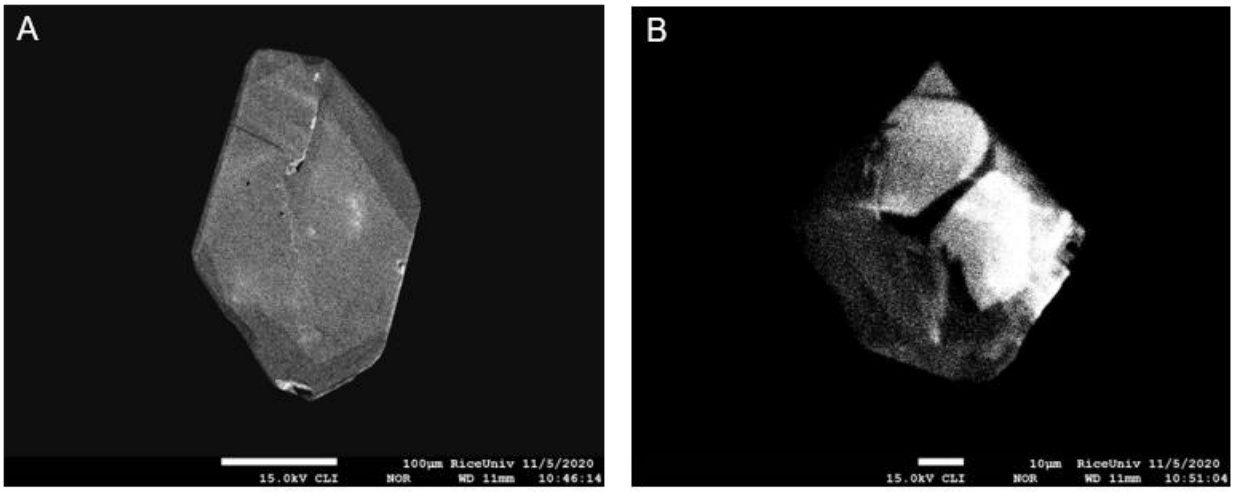

Figure 3-2: Monochromatic cathode-luminiscense (CL) images. A. Homogeneous zircon grain (almost euhedral) that does not display zoning. B. Small zircon grain (~20 microns) showing patchy zoning and cracks.

3.3. Analytical Methods

3.3.1. Trace element chemistry of zircons and amphiboles

Laser ablation inductively coupled plasma mass spectrometry (LA-ICP-MS) analyses of zircons and amphiboles were accomplished using a Thermo-iCAP Q quadrupole mass spectrometer (Thermo Scientific, Bremen, Germany) coupled with a New Wave/ESI 193 nm laser ablation system (Elemental Scientific Lasers, Huntingdon, UK) at the University of Arkansas Trace Element and Radiogenic Isotope Laboratory (TRAIL) (Supplementary Table S3 A and Supplementary Table S3 C). Laser ablation analyses utilized a 50 µm laser spot diameter, 10 Hz repetition rate over 20 s, laser fluence of ≈4.3 J/cm2, and the application of a He carrier gas flow rate of 0.800 L/min. Instrumental settings were adjusted to maintain UO and ThO < 1.0%. The standard NIST 612 was used for calibration (Jochum et al., 2011) with 43Ca as the internal

standard in all analyses. Standards NIST 610 and NIST 612 were cycled prior to and at the end of each analytical session and were bracketed once more after each set of ten analyses during the analytical run. Masses investigated for included: ^{139}La, ^{140}Ce, ^{141}Pr, ^{146} Nd, ^{147}Sm, ^{153}Eu, ^{157}Gd, ^{159}Tb, ^{163}Dy, ^{165}Ho, ^{166}Er, ^{169}Tm, ^{172}Yb, ^{175}Lu, ^{232} Th, and ^{238}U. Data reduction was carried out using the Iolite v4.4.3 software package the Trace Element data reduction scheme (Paton et al., 2011).

3.3.2. Analytical conditions in SHRIMP

All zircon grains were imaged in backscatter and cathodoluminescence using a using a XM-26740PCLI Panchromatic Cathodoluminescence (PCL) detector integrated into the JEOL JXA8530F Hyperprobe at Rice University. It images light intensity emitted from regions of the sample in the visible range and provides a wide view of the sample at a 40° take-off angle. The standard photon detector range is from 300 to 900 nm. Mounts were prepared for secondary ion mass spectrometry (SIMS), to identify grain structure, compositional zoning, and inclusions or physical defects. To prepare the section for secondary ion mass spectrometry (SIMS) U-Pb analyses, first the carbon coating was removed using ethanol and light polishing with 1-µm polycrystalline diamond suspension. The thin section slide was trimmed and partitioned using a diamond band saw, and the section pieces containing zircon grains were mounted face down on double-sided tape on a glass slide along with a pre-polished epoxy block of U-Pb and composition zircon standards. The thin section pieces and standards were then cast in an epoxy “mega-mount” to accommodate the size limitations of the SHRIMP-RG (reverse geometry) sample holders, measuring 37.5 mm in diameter with a 24 mm diameter working area on the surface where the

zircons were centered. After curing, the mount was cleaned with a 10% EDTA (ethylenediaminetetraacetic acid) wash, thoroughly rinsed with distilled water, and dried at 50°C in a vacuum oven for 30 minutes. The sample surface was coated with ~10nm of gold for conductivity.

Zircon U-Pb analyses were conducted on the SHRIMP-RG ion microprobe in the co-operated Stanford and U. S. Geological Survey SUMAC facility at Stanford University. Analytical procedure and data reduction follows methods developed by (Williams, 1997) and Ireland and Williams (2003). An O_2- primary beam with accelerating voltage of 10 kV was used to sputter secondary ions from the sample surface with a 4-5 nA primary beam current focused to ~25-30 µm. Prior to analysis, spots were pre-sputtered for 100 seconds using a 50 µm raster to remove gold coating and surface contamination, and the primary and secondary beams were auto tuned to maximize transmission. Nine masses were measured, including 90Zr216O+, 204Pb+, a background measured at 0.045 mass units above the ^{204}Pb+ peak, ^{206}Pb+, ^{207}Pb+, ^{208}Pb+, ^{238}U+, ^{232}Th^{16}O+, and ^{238}U^{16}O+, for count times of 2s, 10s, 10s, 30s, 30s, 2s, 8s, 2s, and 4s, respectively. Data were collected over 5 scans per spot, for a total run time of 18 minutes.Mass resolution (M/DM) was set to ~5000-5500 for all masses, sufficient to resolve any interfering molecular species.

Zircon U and Th concentration data were standardized against the well-characterized MAD-559 zircon standard (4196 ppm U; Barth et al., 2010; Coble et al., 2018). The U-Pb calculated ages are standardized relative to Temora-2 (416.8 Ma; Black et al., 2003) using standard-sample bracketing, analyzed after every three unknown spot analyses. For data reduction, we used the

Microsoft Excel add-in program Squid2.51 and Isoplot3.76 from (Ludwig, 2001; 2003). Due to the low abundance of ^{204}Pb, the measured $^{206}Pb/^{238}U$ was corrected for common Pb based on measured ^{207}Pb, assuming a common Pb composition according to the model by (Stacey et al., 1975). All reported $^{206}Pb/^{238}U$ model ages and uncertainties include the propagated error from the external reproducibility of the Temora standard. The 1s standard error of the mean for standard analyses was 0.88% during the approximately 9-hour session. Some analyses were omitted from the final dataset based on run quality, contamination, or surface topography (cracks or inclusions).

3.4. Results

3.4.1. Trace and REE chemistry of zircons

Trace and rare earth elements (REEs) in zircons from YK18-07 6K1515-R10 were analysed by LA-ICPMS (Supplementary Table S3 A). Th, U and Pb concentrations were also measured in SHRIMP (Supplementary Table S3 B) and the concentrations measured in SHRIMP are mostly comparable to those measured in LA-ICPMS. The ^{49}Ti content in zircons range between 2-24 ppm. All the zircon grains exhibit a negative Eu anomaly and a positive Ce anomaly (

Figure 3-3A). The chondrite normalized plot of all the zircon grains show consistent enrichment in HREEs with respect to LREEs. The zircon grains that do not exhibit any patchy zones or presence of micro-inclusions exhibit a consistent distribution of trace elements. In the Th vs U plot, most of the grains have low U and Th content ranges between 10 to 60 ppm and 5 to 40 ppm respectively (

Figure 3-3B).

Crystallization temperature for zircons were calculated using the uptake of Ti in zircon (Watson et al., 2006). The thermometer was calibrated for natural and experimental zircons in a wide range of temperature and pressure ranging from 580 to 1450 ºC and 0.7 to 3GPa respectively.

A log-linear dependence of equilibrium temperature with the inverse of Ti content in zircons could be established. In this study the zircon grains were analysed for ^{49}Ti using LA-ICPMS. The calculated temperature ranges from 650 to 828ºC (Watson et al., 2006).

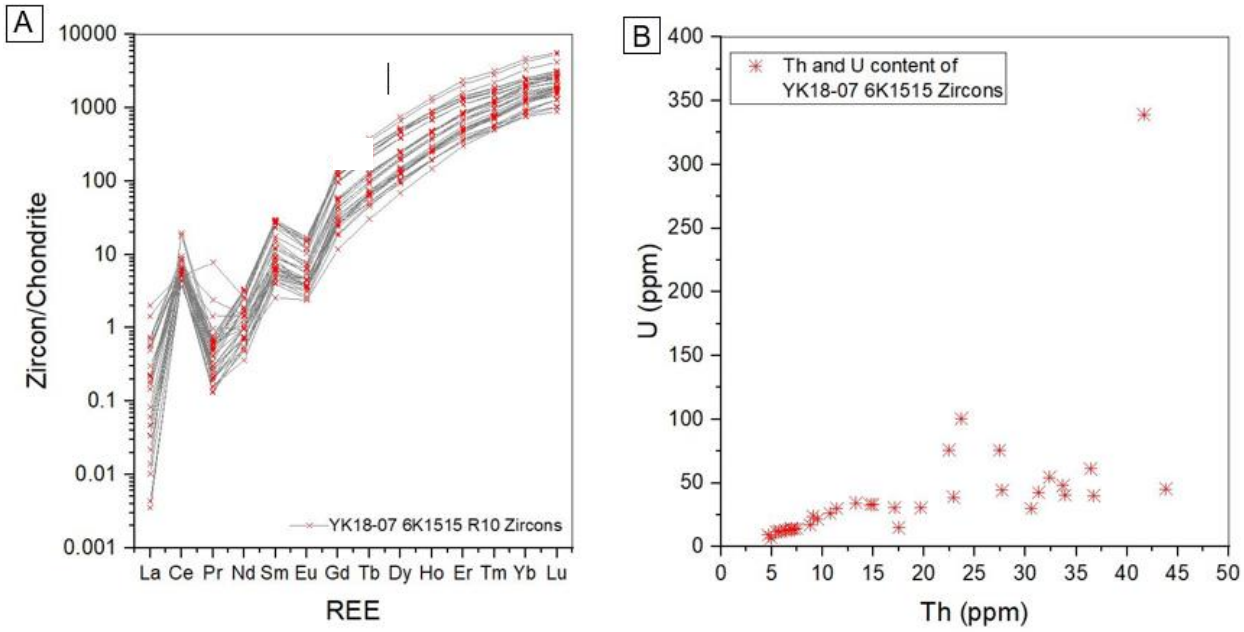

Figure 3-3: Trace and REE composition of zircons. A. Chondrite normalized (Sun and MacDonough 1989) plots of zircons from the leucocratic veins exhibiting a positive Ce ad negative Eu anomaly. B. Th (ppm) vs U(ppm) plot of zircons shows that these zircons are low in U and Th with the exception of one analysis which could be a U-rich inclusion.

3.4.2. U-Pb Geochronology

We obtained U-Pb ages from 21 zircon grains from one peridotite sample that contains zircon-apatite bearing amphibole veins. The $^{206}Pb/^{238}U$ data are given in Supplementary Table S3 B. The

$^{232}Th/^{238}U$ ratio ranges from 0.36 to 0.65. There is an exception of 2 analyses with the $^{232}Th/^{238}U$ ratio of 1.17 and 1.83 that have significantly higher proportion of Th with respect to U. One analysis has a $^{232}Th/^{238}U$ ratio of 0.17 where is 556 ppm with respect to 91 ppm Th. The $^{206}Pb/^{238}U$ ranges from 11.4±1 Ma to 15.6±0.5 Ma. The zircons form a cluster with an intercept age of 13.30±.24 Ma with 2.3 MSWD (

Figure 3-4). Three analyses that yield a slightly younger age in the range of 11 to 12 Ma could be due to Pb loss as some of the grains have cracks or alteration signatures in the form of patchy zones.

Figure 3-4: Tera-Wasserburg plot for zircons from sample YK 18-07 6K-1515. MSWD- Mean square weighted deviation. Error on the $^{206}U/^{238}Pb$ are 95% confidence.

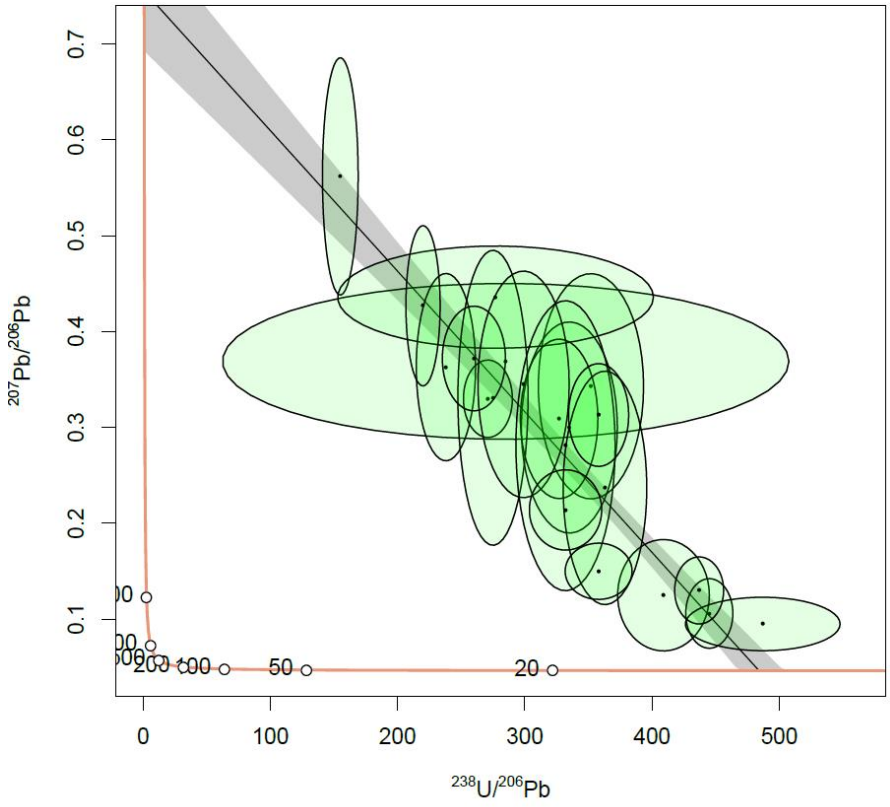

3.4.3. Trace and REE chemistry of amphiboles

The amphiboles from the zircon bearing veins exhibit a flat rare earth element pattern with a negative Eu-anomaly in a chondrite normalized plot (Figure 3-5A). In a Zr vs Nb normalized plot the amphiboles have a narrow range and plot at higher values of Zr and Nb (Figure 3-5B). Their composition is similar to the composition of the bleb, coronitic and deformed amphiboles from the gabbro mylonites of the Godzilla Megamullion (Harigane et al., 2019).

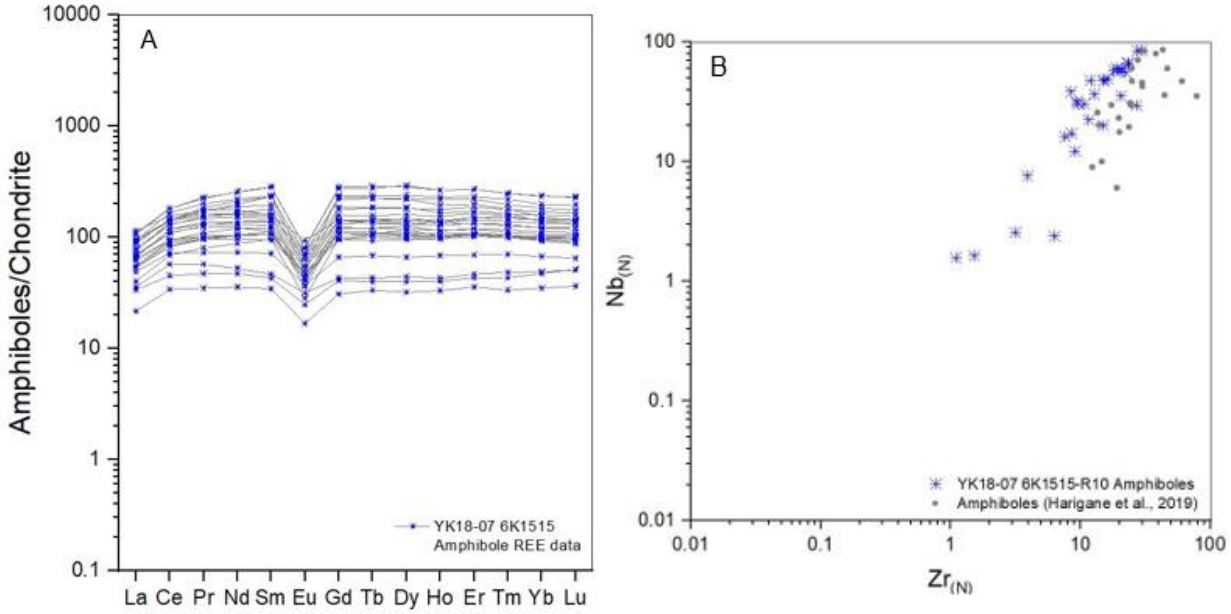

Figure 3-5: Trace ad REE composition of amphiboles. A. REE composition of amphiboles (Chondrite normalized) from the zircon bearing amphibole veins reveals a negative Eu anomaly. B. Chondrite normalized plot of Zr vs Nb shows that the amphibole from the veins have similar composition to the bleb and coronitic amphiboles from the Godzilla Megamullion.

3.5. Discussion

3.5.1. Origin of amphibole veins

Zircons are present within amphibole veins. It is crucial to find the origin of the amphiboles to understand the origin of the zircons. Amphiboles in oceanic gabbros may form by crystallization from a hydrous melt (Basch et al., 2020). It was observed that the Mado Megamullion gabbros had primary amphiboles that crystallized from a hydrous melt in a back-ac spreading center. Amphiboles are also ubiquitous in the peridotites (Sen et., 2021 under review). These amphiboles are either present as a replacement of host clinopyroxenes or within leucocratic veins. Amphiboles in oceanic peridotites within interstitial spaces of minerals are inferred to be the products of reaction of the peridotites with hydrous fluids (Agrinier et al., 1993). Disseminated amphiboles and vein amphiboles are interpreted to be a result of reaction between clinopyroxene and metasomatic melt (Bonadimann et al., 2014; Coltorti et al., 2004). The relationship of amphiboles within clinopyroxenes grains or cracks and the pyroxenes were established from the amphiboles in gabbro mylonites of the Godzilla Megamullion (Harigane et al., 2019). We calculated the composition of the melt in equilibrium with the Mado Megamullion amphiboles using Damp/melt (Chazot et al., 1996; Harigane et al., 2019). It is observed that the composition of the calculated melts (normalized to N-MORB) show an overall similar compositional trend like the melts in equilibrium with the bleb amphiboles in the mylonitic gabbros from the Godzilla Megamullion (Figure 3-6A). These melts are more enriched in terms of both, the LREE and the HREE content compared to the Godzilla Megamullion melts in equilibrium with the bleb amphiboles (Figure 3-6B). Although the REE trends of both the oceanic core complexes are similar with negative Sr,

Eu and Yb anomalies, the positive Zr anomaly in the Godzilla Megamullion melt composition is not observed from the melts in equilibrium with the amphiboles from the Mado Megamullion (Figure 3-6A). Since zircon crystallized as a separate phase depleting the associated amphiboles in Zr and hence the calculated melts associated with these Zr-depleted amphiboles do not exhibit the positive Zr-anomaly. It is reported from previous studies that the Shikoku basin and Mado basalts are more enriched in comparison to N-MORB (Ishizuka et al., 2009; Basch et al., 2020; Sen et al., 2021 under review). It is also observed that the composition of the calculated melts in equilibrium with the enriched clinopyroxenes (Sen et al., 2021 under review) shows a similar trend in the REE compositions to the calculated melts from the amphiboles but exhibit more enrichment in REEs in comparison to the enriched melt in equilibrium with the clinopyroxenes (Figure 3-6B). As these amphiboles are present in the veins within the peridotites the enrichment could be due to crystallization from a more evolved hydrous silicate melt. From the trace element composition of the amphiboles, it could be inferred that the melts were more enriched compared to the differentiated melts from the Godzilla Megamullion that formed the oxide gabbros (Harigane et al., 2019). The enriched clinopyroxenes (Sen et al., 2021 under review) and the amphiboles could be derived from the same source but the amphiboles in the veins crystallized from a more evolved melt composition after the crystallization of the enriched clinopyroxenes.

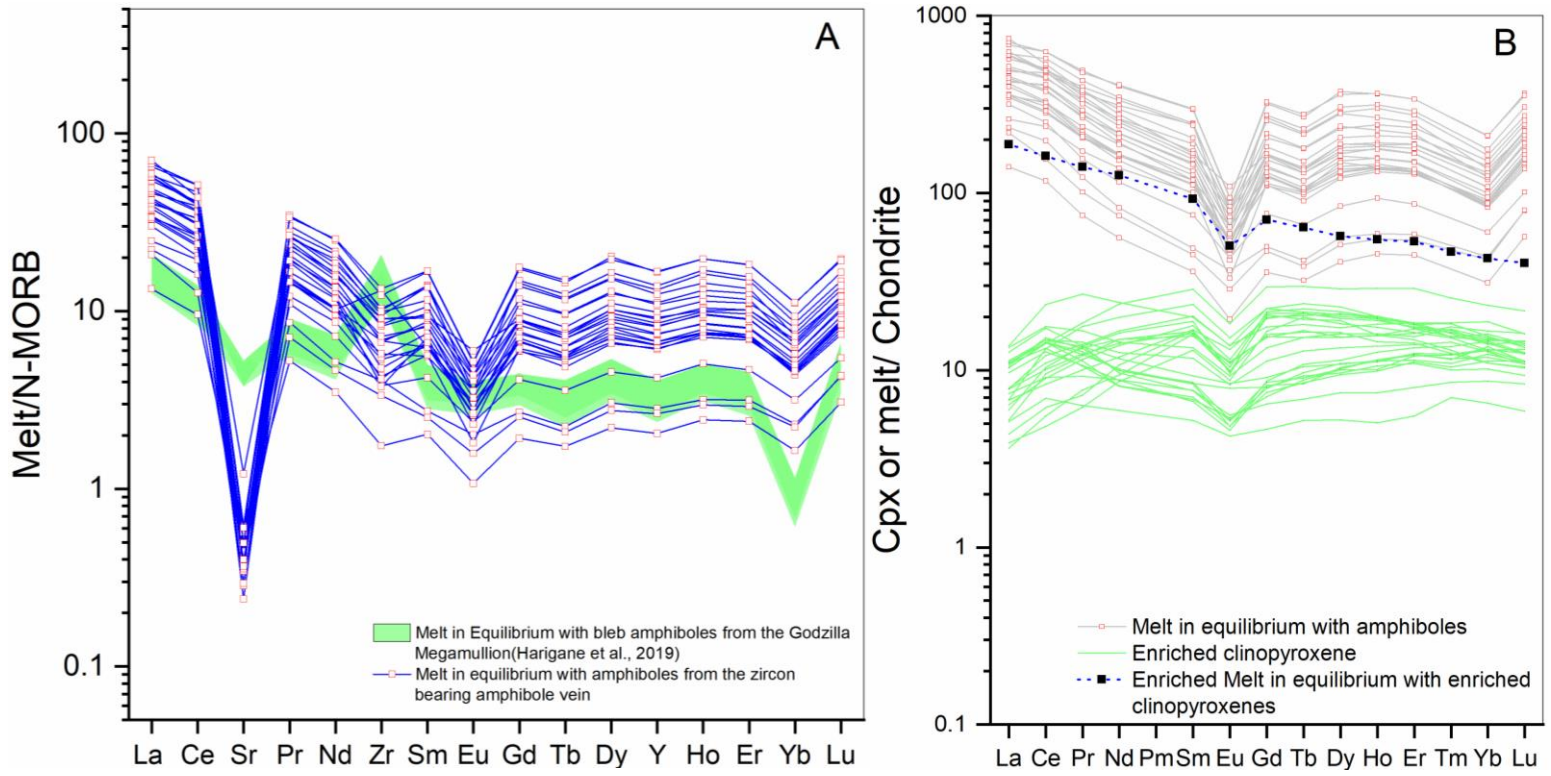

Figure 3-6: Calculated composition of melt in equilibrium with amphiboles. A. N-MORB normalized melt composition shows that the melt in equilibrium with bleb amphiboles from the Godzilla Megamullion have similar compositional trend to that calculated from the Mado Megamullion amphiboles (from the zircon bearing veins). Although the Sr anomaly is more prominent in the Mado amphiboles and the positive Zr-anomaly is absent. B. Chondrite normalized REE plot of calculated melt composition from the amphiboles with respect to the calculated melt composition from the enriched clinopyroxenes (Sen et al., in review).

3.5.2. Zircon age distribution

Some of the zircons preserve euhedral crystal faces (Figure 3-2A) but do not display any oscillatory zoning. Some of the grains are fractured and have patchy zones (Figure 3-2B). These factures could correspond to dislocation structures (Reddy et al., 2006; Timms et al., 2006). Deformation could lead to the formation of sub-grains that have a lower intensity in CL due to the changes in structure and chemistry during deformation. The patchy zones observed in some of the zircon grains could be due to the formation of the sub-grains as a result of syn/post-magmatic deformation during exhumation of the lithosphere along a low angle detachment fault. The ages range from 11.4±1 Ma to 15.6±0.5 Ma (Supplementary Table S3 B). The three younger ages of 11.4, 11.8 and 12.1 Ma respectively could be due to Pb loss during post-magmatic deformation. The deformation could alter the structural integration and isotopic configuration of the zircon grains revealing a younger age from some of the grains. The distribution of the ages revealed from the zircons from a single sample gives a MSWD of 2.3.

3.5.3. Implications of zircon chemistry and thermometry

The zircons yield a high Th/U ratio ~0.5 with a few exceptions lower Th/U (0.17 and 0.39) and a single analysis that has significantly higher U with respect to Th and might be a result of a U-rich inclusion in the zircon (Figure 3-3B). The high Th/U content of most of the zircons >=0.5 which is comparable to those observed in magmatic zircons from mafic rocks (Corfu et al., 2003; Rubatto and Gebauer, 2000; Paul et al., 2003; Kaczmarek et al., 2008). The Th/U ratio of the zircons also show that most of these zircons are not re-crystallized as recrystallization leads to significant

decrease in Th/U ratios as the eight-fold co-ordinated of Th^{4+} has a higher ionic radius than U^{4+} and therefore gets preferentially removed during re-crystallization (Paul et al., 2003). The steep slope of REEs from LREEs to HREEs with a negative Eu-anomaly suggests crystallization from a melt after plagioclase fractionation. These indicate that the zircons associated with the amphibole veins formed by magmatic process and the age of ~13Ma obtained from these zircons are crystallization ages.

The Ti in zircon thermometer (Watson et al., 2006) reveal temperatures ranging from 650 to 828ºC. The calculated temperatures are comparable to previous studies of zircons from oceanic gabbros from Lanzo in the Italian Alps that revealed crystallization temperatures between 751 to 822 ºC (Kaczmarek et al., 2008). These temperatures are lower than the crystallization temperature of gabbros (Kelemen et al., 1998; Leuthold et al., 2018; Sanfilippo et al., 2019). The lower calculated temperature from geothermometric calculations could result from the zircon Ti-content reflecting the composition of a local trapped melt, zircon being a late crystallizing phase. (Coogan and Hinton 2006; Hiess et el., 2006).

3.5.4. Termination of back-arc spreading and magmatism at the Mado Megamullion

E-W spreading continued for a few million years and generated magnetic lineations 6B through 5E (19 Ma). 5E lies close to the geometrical center of the basin. The spreading axis, anomaly 5B which corresponds to 15 Ma is half-way between the base of the Kyushu-Palau Ridge and the base of the Izu-Ridge (Rooke et al., 1987) and is off-centered to the east. Similar asymmetric development is also observed in other back-arc basins. Such geometry implies either asymmetric spreading or later destruction of that part of the oceanic crust which is next to the volcanic arc.

Magnetic anomaly data from 5E and 5B magnetic anomalies revealed that spreading terminated in the Shikoku basin at 15 Ma (Okino et al., 1994). This was debated based on heat flow measurements and thermal modelling and proposed that spreading existed between 15 Ma and 12 Ma (Yamano et al., 1984; Rooke et al., 1987). Zircon ages from this study has revealed an age of 13.3±0.24 Ma (Figure 3-4). It is also interpreted from the distribution of the trace elements and thermometric calculations that this is a magmatic age. Although magnetic anomaly younger than 15 Ma has not been reported from the Shikoku basin, geochemical evidence suggest that magmatism continued at least until ~13 Ma in the Mado Megamullion even if spreading ceased at 15 Ma in the Shikoku back-arc basin. Thus, the Mado Megamullion records magmatic activity until ~13 Ma that post-dates spreading termination.

3.6. Conclusions

The chemistry of the amphiboles in terms of their enrichments in REEs suggests that they crystallized from an evolved hydrous melt. The positive Zr-anomaly that is observed from the amphiboles in the Godzilla Megamullion is not present in the Mado Megamullion zircon-bearing amphibole veins. This could be due to the crystallization of zircon as an individual phase that depletes the associated amphiboles of Zr. The trace and REE chemistry of the zircons and high temperature of crystallization suggests a magmatic origin of the zircons that could be associated with a gabbroic melt. The zircon grains reveal an age of 13.3±0.24 Ma. The MSWD of 2.3 could be due to the wide distribution ages where some of the grains reveal a younger age of ~11-12 Ma. This could be due to syn/post magmatic deformation that altered some of the zircon grains.

Magnetic data had showed that spreading at the Shikoku basin terminated at 15 Ma but our study suggests that magmatism continued at the Mado Megamullion until ~13 Ma.

3.7. Supplementary Data

Supplementary Table S3 A: Trace and REE composition (in ppm) of zircons from sample YK18-07 6K1515-R10

	La	*Ce*	*Pr*	*Nd*	*Sm*	*Eu*	*Gd*	*Tb*	*Dy*	*Ho*	*Er*	*Tm*	*Yb*	*Lu*	*Ti*	*Th*	*U*
R10.01A	nd	3.48	0.05	1.39	3.91	0.87	24.03	9.05	119.13	43.96	210.92	41.73	390.50	70.70		6.91	13.75
R10.02	0.04	3.33	0.04	0.86	2.36	0.41	19.76	8.25	117.73	49.38	257.36	54.30	538.83	102.83		9.49	21.74
R10.03	0.01	3.33	0.02	0.47	1.27	0.21	8.57	3.60	52.14	21.65	112.16	24.52	240.27	46.97		8.77	17.10
R10.04	0.00	12.08	0.07	1.52	4.30	0.70	33.94	13.72	184.30	74.83	378.33	78.11	752.94	140.01		33.67	48.11
R10.01B	0.00	3.08	0.72	1.18	3.40	0.67	19.77	7.62	96.71	37.19	178.95	36.19	343.30	60.17		5.71	11.66
R10.01C	0.03	3.77	0.06	1.48	3.87	0.91	24.59	9.18	113.63	43.99	207.29	41.37	387.25	66.93		6.93	14.08
R10.01D	0.00	3.43	0.05	1.19	4.06	0.86	24.79	9.16	114.78	43.59	202.80	40.75	381.03	64.19		6.39	12.69
R10.16	0.01	3.54	0.03	0.34	1.35	0.35	11.05	4.58	63.00	26.58	132.05	28.40	267.95	49.52		5.91	12.06
R10.08	0.05	4.08	0.07	0.87	1.13	0.26	6.82	2.66	33.33	13.41	66.05	14.18	136.97	25.52		17.52	14.99
R10.07	0.04	4.06	0.04	0.45	0.71	0.18	4.71	1.87	26.36	10.79	55.03	12.38	122.38	21.97		4.96	6.98
R10.11A	0.00	2.77	0.01	0.25	0.68	0.15	5.35	2.18	32.62	14.00	75.56	18.81	198.56	38.95		9.07	24.01
R10.11B	nd	2.68	0.01	0.33	0.78	0.20	5.29	2.16	30.98	13.42	72.71	18.37	197.39	38.76		11.43	30.16
R10.25A	0.18	5.79	0.06	0.75	1.76	0.40	11.35	4.39	61.59	25.40	127.87	29.90	299.13	54.49		30.58	30.12
R10.25B	0.02	5.15	0.03	0.47	1.51	0.31	9.91	4.12	58.82	25.07	133.39	31.28	331.67	62.62		17.10	30.69
R10.22	0.12	4.35	0.22	0.68	1.36	0.32	8.92	3.53	49.04	20.37	104.41	24.44	256.87	47.23		36.72	40.22
R10.23	0.00	2.75	0.01	0.22	0.72	0.20	5.02	2.17	30.76	13.45	72.59	18.17	192.56	36.52		10.76	26.27
R10.24	0.01	3.48	0.02	0.32	1.01	0.21	5.82	2.31	34.74	14.68	79.70	19.15	197.95	38.68		14.72	33.07
R10.27	0.01	2.66	0.01	0.17	0.58	0.14	3.67	1.64	24.23	10.63	59.32	14.48	154.28	31.69		23.70	100.66
R10.31	0.14	4.03	0.03	0.44	1.01	0.25	7.78	3.31	47.88	20.26	111.96	27.09	302.11	56.12		22.93	38.97
R10.3.31	0.05	3.14	0.02	0.23	1.02	0.20	5.77	2.50	36.01	15.45	84.22	19.76	211.59	45.48	2.78	19.68	30.61
R10.4.4	nd	11.00	0.06	1.21	4.30	0.66	30.01	12.45	165.39	67.62	331.02	70.21	680.05	132.83	7.38	27.69	44.23
R10.4.1A	nd	3.25	0.03	0.85	2.60	0.58	19.19	7.31	95.06	37.72	178.33	37.54	345.72	68.16	4.54	5.44	11.79
R10.4.1B	nd	3.20	0.06	1.12	3.56	0.84	23.46	8.96	113.81	43.22	208.98	42.00	378.01	73.37	3.29	6.67	13.19
R10.4.1C	0.01	3.69	0.06	1.50	4.12	0.96	26.75	10.10	124.50	47.72	223.01	45.34	406.05	76.96	5.04	7.48	14.31
R10.4.1D	nd	3.56	0.07	1.48	4.44	0.96	27.66	10.34	128.85	49.25	231.17	46.25	407.68	78.62	3.80	7.24	13.88

R10.1.16	0.01	3.54	0.02	0.31	1.17	0.21	8.59	3.60	51.54	21.62	112.65	23.77	241.89	44.06	3.49	4.66	9.04
R10.1.11A	nd	2.64	0.02	0.22	0.61	0.18	5.70	2.42	32.31	14.33	81.04	18.83	203.83	43.46	5.88	13.31	34.29
R10.1.11B	0.01	3.16	0.02	0.34	0.85	0.21	5.87	2.44	32.14	14.89	81.78	19.18	198.14	42.61	4.14	14.97	33.20
R10.1.7	0.05	4.77	0.06	0.51	0.94	0.21	5.30	1.84	25.27	10.83	58.00	12.77	126.82	25.16	6.15	32.36	54.63
R10.1.8	0.13	3.83	0.06	0.58	0.90	0.25	5.84	2.40	32.85	14.06	76.67	17.45	184.16	38.88	4.54	33.91	40.54
R10.2.24	0.48	3.30	0.13	0.66	0.79	0.22	3.83	1.75	22.94	10.55	58.52	13.61	146.40	31.58	24.92	22.49	75.93
R10.2.27	0.07	2.25	0.03	0.31	0.38	0.13	2.33	1.09	16.94	8.03	48.38	12.29	140.88	32.45	13.79	41.67	339.03
R10.2.25A	0.17	5.20	0.04	0.79	2.14	0.36	10.83	4.48	61.70	25.57	140.30	31.60	323.59	65.55	4.62	43.84	45.25
R10.2.25B	0.05	5.30	0.05	0.67	1.84	0.44	11.89	4.85	61.21	26.10	139.33	30.62	314.68	65.19	2.35	31.29	42.84
R10.2.23	0.34	3.32	0.09	0.44	0.78	0.26	5.27	2.34	31.29	14.09	75.98	17.83	195.26	41.47	10.21	27.44	75.55
R10.2.22	0.18	3.63	0.06	0.45	0.95	0.26	6.37	2.67	37.71	16.36	91.29	21.31	222.53	46.29	6.10	36.42	61.18

Supplementary Table S3 B: Concentration of U, Th & Pb of zircons measured in SHRIMP

Grain Spot	*U(ppm)*	*Th(ppm)*	*Th/U*	*207/206 uncorrected*	*% error*	*238/206 uncorrected*	*% error*	*Ages 206Pb/238U 207 corrected*	*1 σ error*
Zircon1_1	33	16	0.49	0.369	9	285	31.9	13.7	4
Zircon1_2	37	18	0.51	0.343	14	352	4.8	11.6	1
Zircon_1rim_1	33	16	0.50	0.300	15	335	4.6	13.3	1
Zircon1_3	34	17	0.50	0.562	9	155	3.7	15.4	3
Zircon_3_1	50	32	0.65	0.436	5	277	18.3	12.1	2
Zircon_2_1	52	20	0.39	0.309	11	327	3.8	13.4	1.0
Zircon_11_1	76	29	0.39	0.125	19	409	3.6	14.2	0.7
Zircon_11_2	36	12	0.33	0.363	11	238	4.0	16.6	1
Zircon_10_1	75	28	0.38	0.330	5	271	2.9	15.5	0.7
Zircon_13_1	619	1093	1.83	0.106	14	445	1.7	13.4	0.4
Zircon_14_1	96	59	0.63	0.427	8	220	2.5	15.6	1
Zircon_8_1	38	43	1.17	0.331	19	275	4.1	15.3	2
Zircon_7_1	45	42	0.97	0.372	6	260	3.9	14.9	0.9
Zircon_16_1	37	17	0.47	0.345	14	299	4.9	13.7	1

Zircon_16_2	39	17	0.45	0.281	22	332	4.8	13.8	2
zircon 28_1	91	47	0.53	0.095	12	487	5.1	12.4	0.7
Zircon_22_1	66	33	0.52	0.237	21	363	3.7	13.6	1
Zircon_23_1	105	37	0.36	0.150	8	358	3.0	15.7	0.5
Zircon_25_1	76	41	0.56	0.214	8	332	3.5	15.4	0.7
Zircon_27_1	556	91	0.17	0.130	11	437	1.8	13.2	0.4
Zircon_31_1	120	82	0.71	0.313	7	358	2.7	12.1	0.6

Supplementary Table S3 C: Trace and REE composition (in ppm) of amphiboles from sample YK18-07 6K1515-R10

Grain/Spot	*Sr*	*Y*	*Zr*	*Nb*	*La*	*Ce*	*Pr*	*Nd*	*Sm*	*Eu*	*Gd*	*Tb*	*Dy*	*Ho*	*Er*	*Tm*	*Yb*	*Lu*
R10ZRC1.01	9.36	49.98	14.97	1.82	5.13	20.85	3.24	16.23	5.09	0.94	6.13	1.20	7.89	1.80	5.70	0.82	5.61	0.89
R10ZRC1.02	7.01	148.53	58.33	4.82	15.14	58.59	9.55	48.07	15.70	2.61	18.91	3.66	23.86	5.44	16.80	2.47	15.28	2.24
R10ZRC1.03	8.36	102.82	32.71	4.15	11.58	44.54	6.75	33.50	10.60	2.09	13.11	2.48	16.24	3.73	11.09	1.73	10.82	1.59
R10ZRC1.05	7.29	157.22	45.85	5.36	14.55	57.47	9.27	48.09	15.89	2.69	21.26	3.87	26.24	5.59	17.00	2.47	14.98	2.16
R10ZRC2.01	7.22	321.61	86.95	16.02	22.26	101.99	18.61	100.61	35.04	3.95	45.91	8.20	54.95	11.97	35.19	4.86	29.45	4.30
R10ZRC2.02	7.55	157.95	41.00	7.28	16.60	68.00	11.56	55.72	16.66	3.13	21.50	3.79	25.16	5.53	17.03	2.56	16.44	2.53
R10ZRC10.01	3.66	180.65	47.02	11.39	15.61	72.19	12.14	59.74	18.85	2.53	24.38	4.37	29.31	6.30	19.18	2.89	18.05	2.73
R10ZRC10.02	5.85	150.89	49.46	8.77	13.18	54.94	8.99	44.34	13.98	2.62	19.10	3.37	23.44	5.26	16.32	2.46	15.95	2.51
R10ZRC10.03	7.30	68.91	34.90	2.92	8.52	35.04	5.31	24.00	6.89	1.77	8.58	1.56	10.89	2.34	7.49	1.20	7.88	1.25
R10ZRC08.01	5.75	239.88	70.67	13.92	20.76	90.21	15.23	75.07	24.28	3.77	31.45	5.64	39.58	8.40	26.35	3.94	25.62	3.84
R10ZRC08.03	4.33	198.72	59.01	11.57	15.49	72.69	12.69	63.22	20.94	2.45	26.59	4.86	32.17	7.10	21.44	3.22	19.47	2.93
R10ZRC16.01	6.21	338.32	80.81	14.22	17.73	85.02	15.87	90.68	34.47	3.11	47.31	8.64	58.81	12.56	36.98	5.44	31.89	4.82
R10ZRC16.02	6.74	272.74	72.26	14.42	18.26	79.16	14.39	76.11	26.67	3.02	35.41	6.64	44.77	9.69	29.92	4.39	27.38	4.05
R10ZRC16.03	4.48	156.39	36.95	7.31	9.53	42.41	7.45	40.26	14.20	1.60	19.56	3.76	25.49	5.61	16.63	2.55	15.56	2.33
R10ZRC25.01	5.23	208.13	57.32	11.27	18.83	80.52	13.81	69.42	21.94	3.12	28.38	5.04	34.79	7.35	22.88	3.45	21.41	3.24
R10ZRC25.03	7.51	220.00	77.59	13.58	21.70	86.10	14.60	72.64	22.92	3.55	28.55	5.20	36.34	7.67	24.17	3.64	23.48	3.55
R10ZRC23.01	7.56	163.77	112.24	7.07	12.64	50.57	8.86	47.30	15.70	2.29	21.70	3.88	28.77	5.60	17.43	2.61	15.91	2.42
R10ZRC23.02	5.39	182.46	32.32	9.20	12.98	57.72	10.22	54.55	17.89	2.03	23.82	4.38	31.19	6.24	19.01	2.75	17.07	2.59
R10ZRC22.01	8.60	403.54	105.27	20.12	25.04	111.55	21.23	116.20	41.85	4.51	55.00	10.04	72.19	14.48	43.36	6.13	37.87	5.74
R10ZRC22.02	9.44	408.39	114.59	20.41	25.91	111.75	20.71	117.93	42.21	4.57	56.18	10.38	69.62	14.51	43.27	6.14	38.14	5.61
R10ZRC22.03	5.57	164.50	35.55	7.60	12.95	51.79	8.99	47.81	16.66	2.33	22.47	4.01	27.28	5.82	17.44	2.45	15.79	2.45
R10ZRC27.02	6.08	64.71	28.75	3.87	7.98	27.66	4.38	21.54	6.33	1.39	8.10	1.45	9.85	2.19	6.91	1.07	7.61	1.26
R10ZRC27.03	7.57	201.50	61.84	11.78	16.21	66.72	11.85	62.79	20.51	2.86	28.03	4.86	33.30	7.03	21.31	3.14	19.58	3.01
R10ZRC31.01	7.53	302.82	88.85	15.70	21.88	87.71	17.12	96.87	34.18	4.07	44.04	8.03	54.14	10.62	31.80	4.45	24.73	3.45
R10ZRC31.02	18.46	265.66	84.88	13.36	22.83	87.61	16.36	86.39	28.91	3.84	37.19	6.72	45.91	9.04	27.55	4.06	22.15	3.34
R10ZRC31.03	9.17	223.90	77.80	8.45	27.12	95.06	16.34	80.55	23.51	5.27	28.74	5.06	36.48	7.47	24.09	3.82	22.66	3.51

Chapter 4: Conclusions

We record melt-rock reaction in terms of the textural morphology and chemical composition of spinels and silicates from both two different tectonic regions. The Hess Deep and Mado Megamullion plagioclase-bearing peridotites exhibit domains of altered plagioclase. A hybrid sample from the Hess Deep have regions of plagioclase-spinel symplectite intergrowths that record the intermediate reaction pathways of breakdown of spinel to plagioclase. Both, the Mado Megamullion and Hess Deep peridotites have Ti-enrichment in spinels in the melt reacted peridotites, although it is more significant in the Hess Deep samples. Spinel composition (Cr#, Mg# and TiO_2 wt%) can be used as a petrogenetic indicator to estimate the degree of melting and melt-rock interaction. We could successfully model the degree of partial melting at Hess Deep and the Mado Megamullion using MELTS. Our partial melting models show that the Hess Deep harzburgites underwent high degrees of partial melting between 17-20% while the Mado Megamullion lherzolites record a wide range of partial melting ranging from 6 to 18 %. This agrees with the degree of partial melting calculated from the empirical formula by Hellebrand et al. (2001). We modelled the melt-rock reaction textures seen in the plagioclase-bearing peridotites from the Hess Deep using AFC mechanism. Our AFC models explain the TiO_2 enrichment trend in spinels from the melt-reacted rocks with the advent of plagioclase crystallization. The models also explain the early appearance of orthopyroxene in the liquidus in contrast to fractional crystallization models. The existing fractional melting models that could not explain the ubiquitous

presence of orthopyroxene in crustal gabbros from the Hess Deep and other mid-oceanic ridge environments.

In addition to the texture and chemistry of spinels, clinopyroxenes from the Mado Megamullion also exhibit enriched signatures that cannot be explained by fractional melting. Our open system models with moderate degrees of melting (between 7-10%) closely approximates the composition of the residual clinopyroxenes with moderate influx rates (β)=0.01 and melt porosity (α)=0.01. The composition of the accumulated melts from these open system models also approximates the composition of Shikoku basin and Mado basalts. The multiple generations of amphiboles in zircon-chlorite bearing amphibole veins and as replacement of anhydrous silicates suggest the involvement of water at different stages of exhumation of the Mado Megamullion. The compositional similarity between the pargasitic amphiboles to the magmatic amphiboles in the Mado Megamullion gabbros (Basch et al., 2020) suggests a genetic relationship between them. Back-arc mantle could be hydrated by reaction of the peridotites with hydrous melt. The enrichment in fluid mobile elements in the back-arc basalts with respect to N-MORB also indicates the presence of hydrous melts in the system that acted as carriers of these fluid-mobile elements. We infer that reaction of refractory mantle with enriched hydrous melts played an important role in the evolution of the Mado Megamullion mantle peridotites and crustal basalts in the back-arc spreading system.

We analyzed zircon grains in SHRIMP for their U-Pb isotopic configuration to determine the crystallization of zircons in the zircon bearing amphibole veins that cut through the peridotite matric in sample YK18-07-R10. The trace and REE chemistry of the amphiboles and zircons and

their crystallization temperatures indicate a magmatic origin of the veins that could be associated with evolved gabbros. The zircon grains reveal an age of 13.3±0.24 Ma. This geochronologic evidence suggests that magmatism continued at the Mado Megamullion until ~13 Ma although magnetic anomaly data had previously suggested that spreading at the Shikoku basin terminated at 15 Ma.

Our studies indicate that partial melting and melt-rock reaction is operative in different tectonic regions although the degree of melting, melt-rock reaction and the involvement of water determines the chemistry of the mantle phases (spinels and silicates). These can be successfully modelled using partial melting and melt-rock reaction mechanisms. The evolution of the peridotites in the Mado Megamullion OCC of the Shikoku back-arc basin is different from the evolutionary trend of mid-oceanic ridge mantle peridotites. This is also revealed by the chemistry of the Shikoku basin basalts that show significant enrichment in trace elements with respect to N-MORB and high abundances of fluid mobile elements. These indicate the involvement of hydrous melts in the evolutionary trends of back-arc systems in contrast to dry-magmas at mid-oceanic ridges.

Bibliography

Agrinier, P., Mével, C., Bosch, D., & Javoy, M. (1993). Metasomatic hydrous fluids in amphibole peridotites from Zabargad Island (Red Sea). *Earth and Planetary Science Letters*, *120*(3–4), 187–205.

Akizawa, N., Ohara Y., Okino, K., Ishizuka, O., Yamashita, H., Machida, S., Snow, J. E., Sen, A., Sanfilippo, A., Basch, V., Michibayashi, K., Harigane, Y., Hirauchi, K., Fujii, M., Asanuma, H., and Hirata, T. Geochemical characteristics of back-arc basin lower crust and upper mantle final spreading stage of Shikoku Basin: an example of Mado Megamullion. *Island Arc (under review).*

Allan, J. F., & Dick, H. J. B. (1996). Cr-Rich Spinel as a Tracer for Melt Migration and Melt-Wall Rock Interaction in the Mantle: Hess Deep, Leg 147. *Proceedings of the Ocean Drilling Program, 147 Scientific Results*.

Allan, J. F., Falloon, T., Pedersen, R. B., Shankar Lakkapragada, B., Natland, J. H., & Malpas, J. (1996). Petrology of Selected Leg 147 Basaltic Lavas and Dikes. *Proceedings of the Ocean Drilling Program, 147 Scientific Results*, *147*.

Arai, S. (1994). Characterization of spinel peridotites by olivine-spinel compositional relationships: Review and interpretation. *Chemical Geology*, *113* (3–4), 191–204.

Baines, G.A., Cheadle, M. J., Dick, H. J. B., Scheirer, H. A., John, B. E., Kusznir, N. J., & Matsumoto, T. (2003). Mechanism for generating the anomalous uplift of oceanic core complexes: Atlantis Bank, southwest Indian Ridge. *Geology*, *31* (12), 1105.

Barth, A. P., Wooden, J. L., Barth, A. P., & Wooden, J. L. (2010). Coupled elemental and isotopic analyses of polygenetic zircons from granitic rocks by ion microprobe, with implications for melt evolution and the sources of granitic magmas. *Chemical Geology*, *277*(1–2), 149–159.

Basch, V., Rampone, E., Borghini, G., Ferrando, C., & Zanetti, A. (2019). Origin of pyroxenites in the oceanic mantle and their implications on the reactive percolation of depleted melts. *Contributions to Mineralogy and Petrology*, *174* (12), 97.

Basch, V., Sanfilippo, A., Sani, C., Ohara, Y., Snow, J., Ishizuka, O., et al. (2020). Crustal accretion in a slow-spreading back-arc basin: Insights from the Mado Megamullion oceanic core complex in the Shikoku Basin. *Geochemistry, Geophysics, Geosystems*, *21*(11).

Basch, V., Sanfilippo, A., Sani, C., Ohara, Y., Snow, J., Ishizuka, O., et al. (2020). Crustal accretion in a slow-spreading back-arc basin: Insights from the Mado Megamullion oceanic core complex in the Shikoku Basin. *Geochemistry, Geophysics, Geosystems, 21* (11).

Batanova, V. G., Belousov, I. A., Savelieva, G. N., & Sobolev, A. v. (2011). Consequences of Channelized and Diffuse Melt Transport in Supra-subduction Zone Mantle: Evidence from the Voykar Ophiolite (Polar Urals). *Journal of Petrology*, *52*(12), 2483–2521.

Berndt, J. (2004). An Experimental Investigation of the Influence of Water and Oxygen Fugacity on Differentiation of MORB at 200 MPa. *Journal of Petrology*, *46*(1), 135–167.

Bertrand, P., & Mercier, J. C. C. (1985). The mutual solubility of coexisting ortho- and clinopyroxene: toward an absolute geothermometer for the natural system? *Earth and Planetary Science Letters*, *76* (1–2), 109–122.

Black, L. P., Kamo, S. L., Allen, C. M., Aleinikoff, J. N., Davis, D. W., Korsch, R. J., & Foudoulis, C. (2003). TEMORA 1: a new zircon standard for Phanerozoic U–Pb geochronology. *Chemical Geology*, *200*(1–2), 155–170.

Blackman, D. K., Canales, J. P., & Harding, A. (2009). Geophysical signatures of oceanic core complexes. *Geophysical Journal International*. Oxford Academic.

Blackman, D.K., Ildefonse, B., John, B. E., Ohara, Y., Miller, D. J., MacLeod, C. J., et al. (2005). IODP Expeditions 304 and 305: Oceanic core complex formation, Atlantis Massif. *Scientific Drilling*, *1*, 28–31.

Blackman, D.K., Ildefonse, B., John, B.E., Ohara, Y., MacLeod, C.J., Expedition 304/305 Scientists (2006) *Proceedings of the Integrated Ocean Drilling Program* 304–305.
Blundy, J., & Wood, B. (1994). Prediction of crystal-melt partition coefficients from elastic moduli. *Nature*, *372*(6505), 452–454.

Bodinier, J.-L., Menzies, M. A., & Thirlwall, M. F. (1991). Continental to Oceanic Mantle Transition: REE and Sr-Nd Isotopic Geochemistry of the Lanzo Lherzolite Massif. *Journal of Petrology*, *Special Volume* (2), 191–210.

Bonadiman, C., Nazzareni, S, Coltorti, M, Comodi, P, Giuli, G, & Faccini, B. (2014). Crystal chemistry of amphiboles: implications for oxygen fugacity and water activity in lithospheric mantle beneath Victoria Land, Antarctica. *Contributions to Mineralogy and Petrology* (167), 984.

Boudreau, A. (1999). Fluid Fluxing of Cumulates: The J-M Reef and Associated Rocks of the Stillwater Complex, Montana. *Journal of Petrology*, *40*(5), 755–772.

Brey, G. P., & Köhler, T. (1990). Geothermobarometry in four-phase lherzolites II. new thermobarometers, and practical assessment of existing thermobarometers. *Journal of Petrology*, *31* (6), 1353–1378.

Brice, J. C. (1975). Some thermodynamic aspects of the growth of strained crystals. *Journal of Crystal Growth*, *28*(2), 249–253.

Brunelli, D., Paganelli, E., & Seyler, M. (2014). Percolation of enriched melts during incremental open-system melting in the spinel field: A REE approach to abyssal peridotites from the Southwest Indian Ridge. *Geochimica et Cosmochimica Acta*, *127*, 190–203.

Cann, J. R., Blackman, D. K., Smith, D. K., McAllister, E., Janssen, B., Mello, S., et al. (1997). Corrugated slip surfaces formed at ridge-transform intersections on the Mid-Atlantic Ridge. *Nature*, *385*(6614), 329–332.

Cannat, M., Bideau, D., & Hébert, R. (1990). Plastic deformation and magmatic impregnation in serpentinized ultramafic rocks from the Garrett transform fault (East Pacific Rise). *Earth and Planetary Science Letters*, *101*(2–4), 216–232.

Cannat, M., Mevel, C., Maia, M., Deplus, C., Durand, C., Gente, P., et al. (1995). Thin crust, ultramafic exposures, and rugged faulting patterns at the Mid-Atlantic Ridge (22°–24°N). *Geology*, *23* (1), 49–52.

Chamot-Rooke, N., Renard, V., & le Pichon, X. (1987). Magnetic anomalies in the Shikoku Basin: a new interpretation. *Earth and Planetary Science Letters*, *83*(1–4), 214–228.

Chazot, G., Menzies, M. A., & Harte, B. (1996). Determination of partition coefficients between apatite, clinopyroxene, amphibole, and melt in natural spinel lherzolites from Yemen: Implications for wet melting of the lithospheric mantle. *Geochimica et Cosmochimica Acta*, *60*(3), 423–437.

Coble, M. A., Vazquez, J. A., Barth, A. P., Wooden, J., Burns, D., Kylander-Clark, A., et al. (2018). Trace Element Characterisation of MAD-559 Zircon Reference Material for Ion Microprobe Analysis. *Geostandards and Geoanalytical Research*, *42*(4), 481–497.

Coltorti, M., Beccaluva, L., Bonadiman, C., Faccini, B., Ntaflos, T., & Siena, F. (2004). Amphibole genesis via metasomatic reaction with clinopyroxene in mantle xenoliths from Victoria Land, Antarctica. *Lithos*, *75*(1–2), 115–139.

Constantin, M. (1999). Gabbroic intrusions and magmatic metasomatism in harzburgites from the Garrett transform fault: implications for the nature of the mantle-crust transition at fast-spreading ridges. *Contributions to Mineralogy and Petrology*, *136*(1–2), 111–130.

Coogan, L. A., & Hinton, R. W. (2006). Do the trace element compositions of detrital zircons require Hadean continental crust? *Geology*, (8), 633.

Coogan, L. A., Gillis, K. M., MacLeod, C. J., Thompson, G. M., & Hekinian, R. (2002). Petrology and geochemistry of the lower ocean crust formed at the East Pacific Rise and exposed at Hess Deep: A synthesis and new results. *Geochemistry, Geophysics, Geosystems*, *3*(11), 1–30.

Corfu, F., Hanchar, J. M., Hoskin, P. W. O., & Kinny, P. (2003). Atlas of Zircon Textures. *Reviews in Mineralogy and Geochemistry*, *53*(1), 469–500.

Crawford, W. C., & Webb, S. C. (2002). Variations in the distribution of magma in the lower crust and at the Moho beneath the East Pacific Rise at 9°-10°N. *Earth and Planetary Science Letters*, *203*(1), 117–130.

Detrick, R. S., Buhl, P., Vera, E., Mutter, J., Orcutt, J., Madsen, J., & Brocher, T. (1987). Multi-channel seismic imaging of a crustal magma chamber along the East Pacific Rise. *Nature*, *326*(6108), 35–41.

Dick, H. J. B. (1977). Partial melting in the Josephine Peridotite; I, The effect on mineral composition and its consequence for geobarometry and geothermometry. *American Journal of Science*, *277*(7), 801–832.

Dick, H. J. B. (1989). Abyssal peridotites, very slow spreading ridges and ocean ridge magmatism. *Geological Society, London, Special Publications*, *42*(1), 71–105.

Dick, H. J. B., Fisher, R. L., & Bryan, W. B. (1984). Mineralogic variability of the uppermost mantle along mid-ocean ridges. *Earth and Planetary Science Letters 69(1)*, 88-106.

Dick, H. J. B., Lissenberg, J. C., & Warren, J. M. (2010). Mantle Melting, Melt Transport, and Delivery Beneath a Slow-Spreading Ridge: The Paleo-MAR from 23.815º N to 23.845º N. *Journal of Petrology*, *51*(1–2), 425–467.

Dick, H. J. B., MacLeod, C. J., Blum, P., Abe, N., Blackman, D. K., Bowles, J. A., et al. (2019). Dynamic Accretion Beneath a Slow-Spreading Ridge Segment: IODP Hole 1473A and the Atlantis Bank Oceanic Core Complex. *Journal of Geophysical Research: Solid Earth*, *124*(12), 12631–12659.

Dick, H. J.B., & Bullen, T. (1984). Chromian spinel as a petrogenetic indicator in abyssal and alpine-type peridotites and spatially associated lavas. *Contributions to Mineralogy and Petrology*, *86* (1), 54–76.

Dick, H.J.B., & Natland, J. H. (1996). Late-Stage Melt Evolution and Transport in the Shallow Mantle beneath the East Pacific Rise. *Proceedings of the Ocean Drilling Program, 147 Scientific Results*.

Dick, H.J.B., Kvassnes, A. J. S., Robinson, P. T., MacLeod, C. J., & Kinoshita, H. (2019). The Atlantis Bank Gabbro Massif, Southwest Indian Ridge. *Progress in Earth and Planetary Science*, *6*(1), 1–70.

Dick, H.J.B., Lin, J. & Schouten, H. (2003) An ultraslow-spreading class of ocean ridge. *Nature* **426,** 405–412.

Dick, H.J.B., Lissenberg, C. J., & Warren, J. M. (2010). Mantle Melting, Melt Transport, and Delivery Beneath a Slow-Spreading Ridge: The Paleo-MAR from 23º15'N to 23º45'N. *Journal of Petrology*, *51* (1–2), 425–467.

Dick, H.J.B., Ozawa, K., Meyer, P. S., Niu, Y., Robinson, P. T., Constantin, M., et al. (2002). Primary silicate mineral chemistry of a 1.5-km section of very slow spreading lower ocean crust: ODP Hole 735B, Southwest Indian Ridge. In *Proceedings of the Ocean Drilling Program, 176 Scientific Results*. Ocean Drilling Program.

Dick, H.J.B., Tivey, M. A., & Tucholke, B. E. (2008). Plutonic foundation of a slow-spreading ridge segment: Oceanic core complex at Kane Megamullion, 23°30′N, 45°20′W. *Geochemistry, Geophysics, Geosystems*, *9*(5).

Dien, H., Arai, S., Doucet, L. S., Li, Z. X., Kil, Y., Fougerouse, D., et al. (2019). Cr-spinel records metasomatism not petrogenesis of mantle rocks. *Nature Communications*, *10*(1).

Drouin, M., Godard, M., Ildefonse, B., Bruguier, O., & Garrido, C. J. (2009). Geochemical and petrographic evidence for magmatic impregnation in the oceanic lithosphere at Atlantis Massif, Mid-Atlantic Ridge (IODP Hole U1309D, 30ºN). *Chemical Geology*, *264*(1–4), 71–88.

Dunn, R. A., Toomey, D. R., & Solomon, S. C. (2000). Three-dimensional seismic structure and physical properties of the crust and shallow mantle beneath the East Pacific Rise at 9°30'N. *Journal of Geophysical Research: Solid Earth*, *105*(B10), 23537–23555.

Edwards, S. J., & Malpas, J. (1996). Melt-Peridotite Interactions in Shallow Mantle at the East Pacific Rise: Evidence from ODP Site 895 (Hess Deep). *Mineralogical Magazine*, *60*(398), 191–206.

Elardo, S. M., McCubbin, F. M., & Shearer, C. K. (2012). Chromite symplectites in Mg-suite troctolite 76535 as evidence for infiltration metasomatism of a lunar layered intrusion. *Geochimica et Cosmochimica Acta*, *87*, 154–177.

Elthon, D., Stewart, M., & Ross, D. K. (1992). Compositional trends of minerals in oceanic cumulates. *Journal of Geophysical Research*, *97*(B11), 15189–15199.

Escartín, J., & Canales, J. P. (2011). Detachments in Oceanic Lithosphere: Deformation, Magmatism, Fluid Flow, and Ecosystems. *Eos, Transactions American Geophysical Union*, *92*(4), 31–31.

Escartín, J., Mével, C., MacLeod, C. J., & McCaig, A. M. (2003). Constraints on deformation conditions and the origin of oceanic detachments: The Mid-Atlantic Ridge core complex at 15°45′N. *Geochemistry, Geophysics, Geosystems*, *4* (8).

Escartín, J., Smith, D. K., Cann, J., Schouten, H., Langmuir, C. H., & Escrig, S. (2008). Central role of detachment faults in accretion of slow-spreading oceanic lithosphere. *Nature*, *455*(7214), 790–794.

Francheteau, J., Armijo, R., Chemine, J. L., Hekinian, R., Lonsdale, P., & Blum, N. (1990). 1 Ma East Pacific Rise oceanic crust and uppermost mantle exposed by rifting in Hess Deep (equatorial Pacific Ocean). *Earth and Planetary Science Letters*, *101*(2–4), 281–295.

Frost, B. R. (1976). Limits to the assemblage forsterite-anorthite as inferred from peridotite hornfelses, Icicle Creek, Washington. *American Mineralogist*, 61(7-8), 732-750.

Ghiorso, M. S., & Sack, R. O. (1995). Chemical mass transfer in magmatic processes IV. A revised and internally consistent thermodynamic model for the interpolation and extrapolation of liquid-solid equilibria in magmatic systems at elevated temperatures and pressures. *Contributions to Mineralogy and Petrology*, *119*(2–3), 197–212.

Ghiorso, M. S., Hirschmann, M. M., Reiners, P. W., & Kress, V. C. (2002). The pMELTS: A revision of MELTS for improved calculation of phase relations and major element partitioning related to partial melting of the mantle to 3 GPa. *Geochemistry, Geophysics, Geosystems*, *3*(5), 1–35.

Gillis, K, Mevel, C., & Allan, J. (1993). Hess Deep Rift Valley. *ODP Preliminary Report*.

Gillis, K. M., Snow, J. E., Klaus, A., Abe, N., Adrião, Á. B., Akizawa, N., et al. (2014). Primitive layered gabbros from fast-spreading lower oceanic crust. *Nature*, *505*(7482), 204–207.

Godard, M., Awaji, S., Hansen, H., Hellebrand, E., Brunelli, D., Johnson, K., et al. (2009). Geochemistry of a long in-situ section of intrusive slow-spread oceanic lithosphere: Results from IODP Site U1309 (Atlantis Massif, 30°N Mid-Atlantic-Ridge). *Earth and Planetary Science Letters*, *279*(1–2), 110–122.

Godard, M., Jousselin, D., & Bodinier, J.-L. (2000). Relationships between geochemistry and structure beneath a palaeo-spreading centre: a study of the mantle section in the Oman ophiolite. *Earth and Planetary Science Letters*, *180*(1–2), 133–148.

Goodrich, C. A., Herd, C. D. K., & Taylor, L. A. (2003). Spinels and oxygen fugacity in olivine-phyric and lherzolitic shergottites. *Meteoritics & Planetary Science*, *38*(12), 1773–1792.

Guo, B., Wang, Y., Xie, H., & Zhou, G. (2020). Mineralogy and geochemistry of the peridotites and high-Cr podiform chromitites from the Tangbale Ophiolite Complex, West Junggar (NW China): Implications for the origin and tectonic environment of formation. *Ore Geology Reviews, 44(10),* 855-858.

Hamlyn, P. R., & Bonatti, E. (1980). Petrology of mantle-derived ultramafics from the Owen fracture zone, northwest Indian ocean: Implications for the nature of the oceanic upper mantle. *Earth and Planetary Science Letters*, *48* (1), 65–79.

Harigane, Y., Abe, N., Michibayashi, K., Kimura, J.-I., & Chang, Q. (2016). Melt-rock interactions and fabric development of peridotites from North Pond in the Kane area, Mid-Atlantic Ridge: Implications of microstructural and petrological analyses of peridotite samples from IODP Hole U1382A. *Geochemistry, Geophysics, Geosystems*, *17* (6), 2298–2322.

Harigane, Y., Michibayashi, K., & Ohara, Y. (2008). Shearing within lower crust during progressive retrogression: Structural analysis of gabbroic rocks from the Godzilla Mullion, an oceanic core complex in the Parece Vela backarc basin. *Tectonophysics*, *457*(3–4), 183–196.

Harigane, Y., Michibayashi, K., & Ohara, Y. (2011). Deformation and hydrothermal metamorphism of gabbroic rocks within the Godzilla Megamullion, Parece Vela Basin, Philippine Sea. *Lithos*, *124*(3–4), 185–199.

Harigane, Y., Okamoto, A., Morishita, T., Snow, J. E., Tamura, A., Yamashita, H., et al. (2019). Melt–fluid infiltration along detachment shear zones in oceanic core complexes: Insights from amphiboles in gabbro mylonites from the Godzilla Megamullion, Parece Vela Basin, the Philippine Sea. *Lithos*, *344–345*, 217–231.

Hekinian, R., Bideau, D., Francheteau, J., Cheminee, J. L., Armijo, R., Lonsdale, P., & Blum, N. (1993). Petrology of the East Pacific Rise crust and upper mantle exposed in Hess deep (eastern equatorial Pacific). *Journal of Geophysical Research: Solid Earth*, *98*(B5), 8069–8094.

Hellebrand, E., & Snow, J. E. (2003). Deep melting and sodic metasomatism underneath the highly oblique-spreading Lena Trough (Arctic Ocean). *Earth and Planetary Science Letters*, *216*(3), 283–299.

Hellebrand, E., Snow, J. E., Dick, H. J. B., & Hofmann, A. W. (2001). Coupled major and trace elements as indicators of the extent of melting in mid-ocean-ridge peridotites. *Nature*, *410*(6829), 677–681.

Hellebrand, E., Snow, J. E., Hoppe, P., & Hofmann, A. W. (2002). Garnet-field Melting and Late-stage Refertilization in "Residual" Abyssal Peridotites from the Central Indian Ridge. *Journal of Petrology* (Vol. 43). Oxford Academic.

Hellebrand, E., Snow, J. E., Mostefaoui, S., & Hoppe, P. (2005). Trace element distribution between orthopyroxene and clinopyroxene in peridotites from the Gakkel Ridge: A SIMS and NanoSIMS study. *Contributions to Mineralogy and Petrology*, *150*(5), 486–504.

Hey, R. N., Deffeyes, K. S., Johnson, G. L., & Lowrie, A. (1972). The galapagos triple junction and plate motions in the east Pacific. *Nature*, *237*(5349), 20–22.

Hiess, J., Nutman, A. P., Bennett, V. C., & Holden, P. (2008). Ti-in-zircon thermometry applied to contrasting Archean metamorphic and igneous systems. *Chemical Geology*, *247*(3–4), 323–338.

Hirauchi, K., Segawa, Kouketsu, Y., Harigane, Y., Ohara, Y., Snow, J. E., Sen, A., Fujii, M., & Okino, K. (2021). Alteration processes recorded by back-arc mantle peridotites from oceanic core complexes, Shikoku Basin, Philippine Sea. *Island Arc, 30(1),* 1-13.

Hirth, G., & Kohlstedt, D. L. (1996). Water in the oceanic upper mantle: implications for rheology, melt extraction and the evolution of the lithosphere. *Earth and Planetary Science Letters*, *144 (1-2),* 94-108.

Hooft, E. E. E., Detrick, R. S., & Kent, G. M. (1997). Seismic structure and indicators of magma budget along the Southern East Pacific Rise. *Journal of Geophysical Research B: Solid Earth*, *102* (12), 27319–27340.

Hoskin, P. W. O., & Schaltegger, U. (2003). The Composition of Zircon and Igneous and Metamorphic Petrogenesis. *Reviews in Mineralogy and Geochemistry*, *53*(1), 27–62.

Hussenoeder, S. A., Collins, J. A., Kent, G. M., & Detrick, R. S. (1996). Seismic analysis of the axial magma chamber reflector along the southern East Pacific Rise from conventional reflection profiling. *Journal of Geophysical Research: Solid Earth*, *101*(10), 22087–22105.

Ildefonse, B., Blackman, D. K., John, B. E., Ohara, Y., Miller, D. J., MacLeod, C. J., et al. (2007). Oceanic core complexes and crustal accretion at slow-speading ridges. *Geology*, *35*(7), 623–626.

Ildefonse, B., Blackman, D.K., John, B. E., Ohara, Y., Miller, D. J., MacLeod, C. J., et al. (2006). IODP expeditions 304 & 305 characterize the lithology, structure, and alteration of an oceanic core complex. *Scientific Drilling*, *1* (3), 4–11.

Ishii, T., Sato, H., Machida, S., Haraguchi, S., Usui, A., Ishizuka, O., Taniguchi, H., Y. K. (2000). Geological and petrological studies of the Kinan and Izu-Ogasawara-back arc-echelon Seamount Chains. *Bulletin of the Geological Survey of Japan*, *51*(12), 615–630.

Ishizuka, O., Yuasa, M., Taylor, R. N., & Sakamoto, I. (2009). Two contrasting magmatic types coexist after the cessation of back-arc spreading. *Chemical Geology*, *266*(3–4), 274–296.

Jochum, K. P., Weis, U., Stoll, B., Kuzmin, D., Yang, Q., Raczek, I., et al. (2011). Determination of Reference Values for NIST SRM 610–617 Glasses Following ISO Guidelines. *Geostandards and Geoanalytical Research*, *35*(4), 397–429.

Johnson, K. T. M., Dick, H. J. B., & Shimizu, N. (1990). Melting in the oceanic upper mantle: an ion microprobe study of diopsides in abyssal peridotites. *Journal of Geophysical Research*, *95*(B3), 2661–2678.

Kaczmarek, M. A., Müntener, O., & Rubatto, D. (2007). Trace element chemistry and U–Pb dating of zircons from oceanic gabbros and their relationship with whole rock composition (Lanzo, Italian Alps). *Contributions to Mineralogy and Petrology 2007 155:3*, *155*(3), 295–312.

Karig, D. E. (1971). Origin and development of marginal basins in the western Pacific. *Journal of Geophysical Research*, *76*(11), 2542–2561.

Karson, J. A., & Dick, H. J. B. (1983). Tectonics of ridge-transform intersections at the Kane fracture zone. *Marine Geophysical Researches*, *6*(1), 51–98.

Karson, J.A. (1990) Seafloor spreading on the Mid-Atlantic Ridge: implications for the structure of ophiolites and oceanic lithosphere produced in slow-spreading environments. *Ophiolites and Oceanic Crustal Analogues: Proceedings of the Symposium "Troodos 1987". Geol. Surv. Dept., Nicosia, Cyprus*, 125–130.

Kasuga, S., & Ohara, Y. (1997). A new model of back-arc spreading in the Parece Vela Basin, northwest Pacific margin. *Island Arc*, *6*(3), 316–326.

Kelemen, P. B., & Aharonov, E. (1998). Periodic Formation of Magma Fractures and Generation of Layered Gabbros in the Lower Crust Beneath Oceanic Spreading Ridges. *Geophysical Monograph Series*, *106*, 267–289.

Kelemen, P. B., & Dick, H. J. B. (1995). Focused melt flow and localized deformation in the upper mantle: Juxtaposition of replacive dunite and ductile shear zones in the Josephine peridotite, SW Oregon. *Journal of Geophysical Research: Solid Earth*, *100*(B1), 423–438.

Kelemen, P. B., Braun, M., & Hirth, G. (2000). Spatial distribution of melt conduits in the mantle beneath oceanic spreading ridges: Observations from the Ingalls and Oman ophiolites. *Geochemistry, Geophysics, Geosystems*, *1*(7).

Kelemen, P. B., Shimizu, N., & Salters, V. J. M. (1995). Extraction of mid-ocean-ridge basalt from the upwelling mantle by focused flow of melt in dunite channels. *Nature*, *375*(6534), 747–753.

Kelemen, P.B., Kikawa, E., Miller, D.J., Expedition 209 Scientist (2004) Proceedings of the Ocean Drilling Program, Initial Reports.

Kinzler, R. J., & Grove, T. L. (1992). Primary magmas of mid-ocean ridge basalts 1. Experiments and methods. *Journal of Geophysical Research*, *97*(B5), 6885–6906.

Kirby, S. H., & Etheridge, M. A. (1981). Exsolution of Ca-clinopyroxene from orthopyroxene aided by deformation. *Physics and Chemistry of Minerals*, *7*(3), 105–109.

Korenaga, J., & Kelemen, P. B. (1998). Melt migration through the oceanic lower crust: A constraint from melt percolation modeling with finite solid diffusion. *Earth and Planetary Science Letters*, *156*(1–2), 1–11.

Leake, B. E., Woolley, A. R., Arps, C. E. S., Birch, W. D., Gilbert, M. C., Grice, J. D., et al. (1997). Nomenclature of amphiboles: Report of the subcommittee on amphiboles of the international mineralogical association, commission on new minerals and mineral names. *American Mineralogist*, *82* (9–10), 1019–1037.

Lenaz, D., Velicogna, M., Hålenius, U. & O'Driscoll, B. (2016). Structural parameters of Cr-bearing spinels and pleonaste from the Cuillin Igneous Complex (Isle of Skye, Scotland): Implications for metamorphic and cooling history. *Mineralogical Magazine, 80,* 749-763.

Leuthold, J., Lissenberg, C. J., O'Driscoll, B., Karakas, O., Falloon, T., Klimentyeva, D. N., & Ulmer, P. (2018). Partial Melting of Lower Oceanic Crust Gabbro: Constraints from Poikilitic Clinopyroxene Primocrysts. *Frontiers in Earth Science*, *0*, 15.

Liang, Y., Schiemenz, A., Hesse, M. A., Parmentier, E. M., & Hesthaven, J. S. (2010). High-porosity channels for melt migration in the mantle: Top is the dunite and bottom is the harzburgite and lherzolite. *Geophysical Research Letters*, *37(15).*

Liang, Y., Sun, C., & Yao, L. (2013). A REE-in-two-pyroxene thermometer for mafic and ultramafic rocks. *Geochimica et Cosmochimica Acta*, *102*, 246–260.

Liati, A., & Seidel, E. (1996). Metamorphic evolution and geochemistry of kyanite eclogites in central Rhodope, northern Greece. *Contributions to Mineralogy and Petrology*, *123*(3), 293–307.

Lissenberg, C. J., MacLeod, C. J., Howard, K. A., & Godard, M. (2013). Pervasive reactive melt migration through fast-spreading lower oceanic crust (Hess Deep, equatorial Pacific Ocean). *Earth and Planetary Science Letters*, *361*, 436–447.

Lonsdale, P. (1988). Structural pattern of the Galapagos microplate and evolution of the Galapagos triple junctions. *Journal of Geophysical Research*, *93*(B11), 13551–13574.

Loocke, M., Snow, J. E., & Ohara, Y. (2013). Melt stagnation in peridotites from the Godzilla Megamullion Oceanic Core Complex, Parece Vela Basin, Philippine Sea. *Lithos*, *182–183*, 1–10.

Loocke, M., Snow, J. E., & Ohara, Y. (2013). Melt stagnation in peridotites from the Godzilla Megamullion Oceanic Core Complex, Parece Vela Basin, Philippine Sea. *Lithos*, *182–183*, 1–10.

Lundstrom, C. C., Gill, J., Williams, Q., & Perfit, M. R. (1995). Mantle Melting and Basalt Extraction by Equilibrium Porous Flow. *Science*, *270*(5244), 1958–1961.

Maaløe, S. (1982). Geochemical aspects of permeability controlled partial melting and fractional crystallization. *Geochimica et Cosmochimica Acta*, *46*(1), 43–57.

Macleod, C. J., Banerji, D., Banks, G. J., Irving, D. H. B., Lilly, R. M., Mccaig, A. M., & Smith, D. K. (2002). Direct geological evidence for oceanic detachment faulting: The Mid-Atlantic Ridge, 1545N. *Geology, 30(10),* 879-88.

Macleod, C. J., Searle, R. C., Murton, B. J., Casey, J. F., Mallows, C., Unsworth, S. C., et al. (2009). Life cycle of oceanic core complexes. *Earth and Planetary Science Letters, 287 (3-4),* 333-344.

McDonough, W. F., & Sun, S. s. (1995). The composition of the Earth. *Chemical Geology*, *120*(3–4), 223–253.

Michael, P. J., & Bonatti, E. (1985). Peridotite composition from the North Atlantic: regional and tectonic variations and implications for partial melting. *Earth and Planetary Science Letters*, *73*(1), 91–104.

Michibayashi, K., Harigane, Y., Ohara, Y., Muto, J., & Okamoto, A. (2014). Rheological properties of the detachment shear zone of an oceanic core complex inferred by plagioclase flow law: Godzilla Megamullion, Parece Vela back-arc basin, Philippine Sea. *Earth and Planetary Science Letters*, *408*, 16–23.

Michibayashi, K., Harigane, Y., Ohara, Y., Muto, J., & Okamoto, A. (2014). Rheological properties of the detachment shear zone of an oceanic core complex inferred by plagioclase flow

law: Godzilla Megamullion, Parece Vela back-arc basin, Philippine Sea. *Earth and Planetary Science Letters, 408,* 16–23.

Morishita, T., Hara, K., Nakamura, K., Sawaguchi, T., Tamura, A., Arai, S., et al. (2009). Igneous, alteration and exhumation processes recorded in abyssal peridotites and related fault rocks from an oceanic core complex along the Central Indian Ridge. *Journal of Petrology, 50* (7), 1299–1325.

Natland, J. H., & Dick, H. J. B. (1996). Melt Migration through High-Level Gabbroic Cumulates of the East Pacific Rise at Hess Deep: The Origin of Magma Lenses and the Deep Crustal Structure of Fast-Spreading Ridges. *Proceedings of the Ocean Drilling Program, 147 Scientific Results*.

Niu, Y. (1997). Mantle melting and melt extraction processes beneath ocean ridges: Evidence from abyssal peridotites. *Journal of Petrology*, *38*(8), 1047–1074.

Niu, Y., & Hékinian, R. (1997). Spreading-rate dependence of the extent of mantle melting beneath ocean ridges. *Nature, 385* (6614), 326–328.

Ohara, Y, Fujioka, K., Ishii, T., & Yurimoto, H. (2003). Peridotites and gabbros from the Parece Vela backarc basin: Unique tectonic window in an extinct backarc spreading ridge. *Geochemistry, Geophysics, Geosystems, 4*(7), 8611.

Ohara, Y, Okino, K., & Kasahara, J. (2007). Seismic study on oceanic core complexes in the Parece Vela back-arc basin. *Island Arc, 16*(3), 348–360.

Ohara, Y. (2016). The Godzilla Megamullion, the largest oceanic core complex on the earth: a historical review. *Island Arc, 25*(3), 193–208.

Ohara, Y., Fujioka, K., Ishii, T., & Yurimoto, H. (2003). Peridotites and gabbros from the Parece Vela backarc basin: Unique tectonic window in an extinct backarc spreading ridge. *Geochemistry, Geophysics, Geosystems, 4* (7), 8611.

Ohara, Y., Kato, Y., Yoshida, T., & Nishimura, A. (2015). Geoscientific Characteristics of the Seafloor of the Southern Ocean of Japan Revealed by Japan's Continental Shelf Survey. *Journal of Geography (Chigaku Zasshi), 124* (5), 687–709.

Ohara, Y., Okino, K., Akizawa, N., Fujii, M., Harigane, Y., Hirano, N., et al. (2018). A new tectonic window into the backarc basin lower oceanic crust and upper mantle: Mado Megamullion in the Shikoku Basin. *AGUFM, 2018,* T32C-05B. Retrieved from AGUFM. T32C.05B (abstract).

Ohara, Y., Okino, K., Akizawa, N., Fujii, M., Harigane, Y., Hirano, N., Hirauchi, K., Ishizuka, O., Machida, S., Michibayashi, K., Sanfilippo, A., Snow, J.E., and Yamashita, H. Introducing an oceanic core complex in the Shikoku Basin: Mado Megamullion, JpGU 2019, SMP30-07.

Ohara, Y., Okino, K., Akizawa, N., Fujii, M., Harigane, Y., Hirauchi, K. I., et al. (2019). Crustal accretion in a backarc spreading ridge: the oceanic core complexes in the Shikoku Basin and their tectonic implications. *AGUFM*, *2019*, T13A-07. Retrieved from 2019AGUFM.T13A07O(abstract).

Ohara, Y., Stern, R. J., Ishii, T., Yurimoto, H., & Yamazaki, T. (2002). Peridotites from the Mariana Trough: First look at the mantle beneath an active back-arc basin. *Contributions to Mineralogy and Petrology*, *143*(1), 1–18.

Ohara, Y., Yoshida, T., Kato, Y., & Kasuga, S. (2001). Giant Megamullion in the Parece Vela Backarc Basin. *Marine Geophysical Researches*, *22*(1), 47–61.

Okamura, F. P., McCallum, I. S., Stroh, J. M., Ghose, S., Okamura, F. P., McCallum, I. S., et al. (1976). *Pyroxene-spinel intergrowths in lunar and terrestrial pyroxenes. LPSC* (Vol. 2).

Okino, K. (2015). Magnetic Anomalies in the Philippine Sea: Implications for Regional Tectonics. *Journal of Geography (Chigaku Zasshi)*, *124* (5), 729–747.

Okino, K., & Shimakawa, Y. (1994). Evolution of the Shikoku Basin. *Journal of Geomagnetism and Geoelectricity*, *46*(6), 463–479.

Okino, K., Ohara, Y., Kasuga, S., & Kato, Y. (1999). The Philippine Sea: New survey results reveal the structure and the history of the marginal basins. *Geophysical Research Letters*, *26*(15), 2287–2290.

Ozawa, K., & Shimizu, N. (1995). Open-system melting in the upper mantle: constraints from the Hayachine-Miyamori ophiolite, northeastern Japan. *Journal of Geophysical Research*, *100*(B11), 22315–22335.

Parkinson, IJ; Pearce, JA (1998): Geochemistry of ODP Leg 125 peridotites.

Parnell-Turner, R., Escartín, J., Olive, J. A., Smith, D. K., & Petersen, S. (2018). Genesis of corrugated fault surfaces by strain localization recorded at oceanic detachments. *Earth and Planetary Science Letters*, *498*, 116–128.

Parsons, B., & Sclater, J. G. (1977). An analysis of the variation of ocean floor bathymetry and heat flow with age. *Journal of Geophysical Research*, *82*(5), 803–827.

Paton, C., Hellstrom, J., Paul, B., Woodhead, J., & Hergt, J. (2011). Iolite: Freeware for the vizualisation and processing of mass spectrometric data. *Journal of Analytical Atomic Spectrometry*, *26*(12), 2508–2518.

Pedersen, R. B., Malpas, J., & Falloon, T. (1996). Petrology and Geochemistry of Gabbroic and Related Rocks from Site 894, Hess Deep. *Proceedings of the Ocean Drilling Program, 147 Scientific Results*.

Perk, N. W., Coogan, L. A., Karson, J. A., Klein, E. M., & Hanna, H. D. (2007). Petrology and geochemistry of primitive lower oceanic crust from Pito Deep: implications for the accretion of the lower crust at the Southern East Pacific Rise. *Contributions to Mineralogy and Petrology*, *154*(5), 575–590.

Pirnia, T., Saccani, E., & Arai, S. (2018). Spinel and plagioclase peridotites of the Nain ophiolite (Central Iran): Evidence for the incipient stage of oceanic basin formation. *Lithos, 310–311*, 1–19.

Poldervaart, A., & Hess, H. H. (1951). Pyroxenes in the Crystallization of Basaltic Magma. *The Journal of Geology*, *59* (5), 472–489.

Posner, E. S., Ganguly, J., & Hervig, R. (2016). Diffusion kinetics of Cr in spinel: Experimental studies and implications for 53 Mn‐ 53 Cr cosmochronology. *Geochimica et Cosmochimica Acta, 175*, 20–35.

Quick, J. E. (1982). The origin and significance of large, tabular dunite bodies in the Trinity peridotite, northern California. *Contributions to Mineralogy and Petrology*, *78*(4), 413–422.

Rampone, E., Borghini, G., & Basch, V. (2020). Melt migration and melt-rock reaction in the Alpine-Apennine peridotites: Insights on mantle dynamics in extending lithosphere. *Geoscience Frontiers*, 11 (1), 151-166.

Reddy, S. M., Timms, N. E., Trimby, P., Kinny, P. D., Buchan, C., & Blake, K. (2006). Crystal-plastic deformation of zircon: A defect in the assumption of chemical robustness. *Geology*, *34*(4), 257–260.

Rehfeldt, T., Obst, K., & Johansson, L. (2007). Petrogenesis of ultramafic and mafic xenoliths from Mesozoic basanites in southern Sweden: Constraints from mineral chemistry. *International Journal of Earth Sciences*, *96*(3), 433–450.

Renna, M. R., & Tribuzio, R. (2011). Olivine-rich Troctolites from Ligurian Ophiolites (Italy): Evidence for Impregnation of Replacive Mantle Conduits by MORB-type Melts. *Journal of Petrology*, *52*(9), 1763–1790.

Rioux, M., Lissenberg, C. J., Mclean, N. M., Bowring, S. A., Macleod, C. J., Hellebrand, E., & Shimizu, N. (2012). Protracted timescales of lower crustal growth at the fast-spreading East Pacific Rise. *Nature Geoscience, 5*, 275-278.

Ross, K., & Elthon, D. (1997). Extreme incompatible trace-element depletion of diopside in residual mantle from south of the Kane fracture zone. *Scientific Results* (153).

Roux, V. L., Dasgupta, R., Lee, C. A. (2015). Recommended mineral-melt partition coefficients for FRTEs (Cu), Ga, and Ge during mantle melting. *American Mineralogist*, 100 (11-12), 2533–2544.

Rubatto, D., & Gebauer, D. (2000). Use of Cathodoluminescence for U-Pb Zircon Dating by Ion Microprobe: Some Examples from the Western Alps. *Cathodoluminescence in Geosciences*, 373–400.

Saal, A. E., Hauri, E. H., Langmuir, C. H., & Perfit, M. R. (2002). Vapour undersaturation in primitive mid-ocean-ridge basalt and the volatile content of Earth's upper mantle. *Nature*, *419*(6906), 451–455.

Salters, V. J. M., & Stracke, A. (2004). Composition of the depleted mantle. *Geochemistry, Geophysics, Geosystems*, *5*(5), 5–07.

Sanfilippo, A., Dick, H. J. B., & Ohara, Y. (2013). Melt-Rock Reaction in the Mantle: Mantle Troctolites from the Parece Vela Ancient Back-Arc Spreading Center. *Journal of Petrology*, *54*(5), 861–885.

Sanfilippo, A., Dick, H. J. B., Marschall, H. R., Lissenberg, C. J., & Urann, B. (2019). Emplacement and High-Temperature Evolution of Gabbros of the 16.5°N Oceanic Core Complexes (Mid-Atlantic Ridge): Insights Into the Compositional Variability of the Lower Oceanic Crust. *Geochemistry, Geophysics, Geosystems*, *20*(1), 46–66.

Sanfilippo, A., Morishita, T., Kumagai, H., Nakamura, K., Okino, K., Hara, K., et al. (2015). Hybrid troctolites from mid-ocean ridges: inherited mantle in the lower crust. *Lithos*, *232*, 124–130.

Sato, H., Machida, S., Kanayama, S., Taniguchi, H., & Ishii, T. (2002). Geochemical and isotopic characteristics of the Kinan Seamount Chain in the Shikoku Basin. *Geochemical Journal*, *36*(5), 519–526.

Saumur, B. M., & Hattori, K. (2013). Zoned Cr-spinel and ferritchromite alteration in forearc mantle serpentinites of the Rio San Juan Complex, Dominican Republic. *Mineralogical Magazine*, *77* (1), 117–136.

Sauter, D., Cannat, M., Rouméjon, S., Andreani, M., Birot, D., Bronner, A., et al. (2013). Continuous exhumation of mantle-derived rocks at the Southwest Indian Ridge for 11 million years. *Nature Geoscience*, *6*(4), 314–320.

Scott, J. M., Konrad-Schmolke, M., O'brien, P. J., & Günter, C. (2013). High-T, Low-P Formation of Rare Olivine-bearing Symplectites in Variscan Eclogite. *Journal of Petrology*, *54*(7), 1375–1398.

Sdrolias, M., Roest, W. R., & Müller, R. D. (2004). An expression of philippine sea plate rotation: The parece vela and shikoku basins. *Tectonophysics*, *394* (1–2), 69–86.

Sen, A., Snow, J. E., Ohara, Y., Hirauchi, K., Kouketsu, Y., Sanfilippo, A., Basch, V., Harigane, Y., Fujii, M., Okino, K., Akizawa, N. (2021). Melting and evolution of amphibole-rich back-arc abyssal peridotites at the Mado Megamullion, Shikoku Basin. *Geochemistry, Geophysics, Geosystems (under review)*

Sen, A., Snow, J. E., & Ohara, Y. (2020). Melt-Rock Reaction in the Late Stages of Back Arc Spreading Forming the Mado Megamullion in Shikoku Basin, Goldschmidt Conference, 2336–2336.

Sen, A., Snow, J.E., Ohara, Y., Sanfilippo, A., Basch, V., and Okino, K. (2020). Melt-Rock Reaction during back-arc spreading forming the Mado Megamullion in the Shikoku Basin, AGU Fall Meeting, T026-0016.

Seno, T., & Maruyama, S. (1984). Paleogeographic reconstruction and origin of the Philippine Sea. *Tectonophysics, 102*(1–4), 53–84.

Seyler, M., & Bonatti, E. (1997). Regional-scale melt-rock interaction in lherzolitic mantle in the Romanche Fracture Zone (Atlantic Ocean). *Earth and Planetary Science Letters*, *146*(1–2), 273–287.

Seyler, M., Lorand, J. P., Dick, H. J. B., & Drouin, M. (2007). Pervasive melt percolation reactions in ultra-depleted refractory harzburgites at the Mid-Atlantic Ridge, 15° 20′N: ODP Hole 1274A. *Contributions to Mineralogy and Petrology*, *153*(3), 303–319.

Seyler, M., Lorand, J. P., Toplis, M. J., & Godard, G. (2004). Asthenospheric metasomatism beneath the mid-ocean ridge: Evidence from depleted abyssal peridotites. *Geology*, *32*(4), 301–304.

Shaw, D. M. (1970). Trace element fractionation during anatexis. *Geochimica et Cosmochimica Acta*, *34*(2), 237–243.

Shervais, J. W., Reagan, M., Haugen, E., Almeev, R. R., Pearce, J. A., Prytulak, J., et al. (2019). Magmatic Response to Subduction Initiation: Part 1. Fore-arc Basalts of the Izu-Bonin Arc from IODP Expedition 352. *Geochemistry, Geophysics, Geosystems*, *20*(1), 314–338.

Smith, D. K., Escartín, J., Schouten, H., & Cann, J. R. (2008). Fault rotation and core complex formation: Significant processes in seafloor formation at slow-spreading mid-ocean ridges (Mid-Atlantic Ridge, 13°-15°N). *Geochemistry, Geophysics, Geosystems*, *9*(3).

Sobolev, A. V., & Shimizu, N. (1993). Ultra-depleted primary melt included in an olivine from the Mid-Atlantic Ridge. *Nature*, *363*(6425), 151–154.

Spencer, J. E., & Ohara, Y. (2014). Curved grooves at the Godzilla Megamullion in the Philippine Sea and their tectonic significance. *Tectonics*, *33*(6), 1028–1038.

Stacey, J. S., Kramers, J. D., Stacey, J. S., & Kramers, J. D. (1975). Approximation of terrestrial lead isotope evolution by a two-stage model. *Earth and Planetary Science Letters*, *26*(2), 207–221.

Stracke, A., Zindler, A., Salters, V. J. M., McKenzie, D., Janne, B. T., Albarède, F., & Grönvold, K. (2003). Theistareykir revisited. *Geochemistry, Geophysics, Geosystems*, *4*(2), 8507.

Sun, C., & Liang, Y. (2012). Distribution of REE between clinopyroxene and basaltic melt along a mantle adiabat: Effects of major element composition, water, and temperature. *Contributions to Mineralogy and Petrology*, *163*(5), 807–823.

Sun, S. S., & McDonough, W. F. (1989). Chemical and isotopic systematics of oceanic basalts: Implications for mantle composition and processes. *Geological Society Special Publication*, *42*(1), 313–345.

Tani, K., Dunkley, D. J., & Ohara, Y. (2011). Termination of backarc spreading: Zircon dating of a giant oceanic core complex. *Geology*, *39*(1), 47–50.

Tartarotti, P., Susini, S., Nimis, P., & Ottolini, L. (2002). Melt migration in the upper mantle along the Romanche Fracture Zone (Equatorial Atlantic). *Lithos*, *63*(3–4), 125–149.

Timms, N. E., Kinny, P. D., & Reddy, S. M. (2006). Enhanced diffusion of Uranium and Thorium linked to crystal plasticity in zircon. *Geochemical Transactions 2006 7:1*, *7*(1), 1–16.

Tucholke, B. E., Behn, M. D., Buck, W. R., & Lin, J. (2008). Role of melt supply in oceanic detachment faulting and formation of megamullions. *Geology*, *36* (6), 455–458.

Tucholke, B. E., Lin, J., & Kleinrock, M. C. (1998). Megamullions and mullion structure defining oceanic metamorphic core complexes on the Mid-Atlantic Ridge. *Journal of Geophysical Research: Solid Earth*, *103* (5), 9857–9866.

Uenver-Thiele, L., Woodland, A. B., Downes, H., & Altherr, R. (2014). Oxidation State of the Lithospheric Mantle below the Massif Central, France. *Journal of Petrology*, *55*(12), 2457–2480.

Wan, Z., Coogan, L. A., & Canil, D. (2008). Experimental calibration of aluminum partitioning between olivine and spinel as a geothermometer. *American Mineralogist*, *93*(7), 1142–1147.

Wang, C., Liang, Y., & Xu, W. (2021). Formation of Amphibole-Bearing Peridotite and Amphibole-Bearing Pyroxenite Through Hydrous Melt-Peridotite Reaction and In Situ Crystallization: An Experimental Study. *Journal of Geophysical Research: Solid Earth*, *126*(3).

Warren, J. M., & Shimizu, N. (2010). Cryptic Variations in Abyssal Peridotite Compositions: Evidence for Shallow-level Melt Infiltration in the Oceanic Lithosphere. *Journal of Petrology*, *51*(1–2), 395–423.

Watson, E. B., Wark, D. A., & Thomas, J. B. (2006). Crystallization thermometers for zircon and rutile. *Contributions to Mineralogy and Petrology*, *151*(4), 413–433.

Williams, I. S. (1997). U-Th-Pb Geochronology by Ion Microprobe. *Applications of Microanalytical Techniques to Understanding Mineralizing Processes*, 1–35.

Workman, R. K., & Hart, S. R. (2005). Major and trace element composition of the depleted MORB mantle (DMM). *Earth and Planetary Science Letters*, *231*(1–2), 53–72.

Xiong, F., Dilek, Y., Wirth, R., Xu, X., & Yang, J. (2020). Opx–Cpx exsolution textures in lherzolites of the Cretaceous Purang Ophiolite (S. Tibet, China), and the deep mantle origin of Neotethyan abyssal peridotites. *International Geology Review*, *62* (6), 665–682.

Yamano, M., Honda, S., & Uyeda, S. (1984). Nankai Trough: A hot trench? *Marine Geophysical Researches 1984 6:2*, *6*(2), 187–203.

Yang, K., & Seccombe, P. K. (1993). Chemical variation of chromitite in the ultramafic cumulates of the great sepentinite belt, Upper Bingamto-Doonba, New South Wales, Australia. *Canadian Mineralogist*, *31*, 75–87.

Zhang, W.-Q., Liu, C.-Z., & Dick, H. J. B. (2021). Evidence for Multi-stage Melt Transport in the Lower Ocean Crust: the Atlantis Bank Gabbroic Massif (IODP Hole U1473A, SW Indian Ridge). *Journal of Petrology*, *61* (9).

Zhu, Y., Chen, J., Xue, Y., Feng, W., & Jiang, J. (2018). Spinel and orthopyroxene exsolved from clinopyroxene in the Haladala pluton in the middle Tianshan (Xinjiang, China). *Mineralogy and Petrology*, 112 (4), 465–479.